ANALYSIS OF CREEP BEHAVIOR AND PARAMETRIC MODELS FOR 2124 AL AND 2124 AL + SiC$_\text{w}$ COMPOSITE

Karen M. B. Taminger

Thesis submitted to the Faculty of the

Virginia Polytechnic Institute and State University

in partial fulfillment of the requirements for the degree of

MASTER OF SCIENCE

IN

MATERIALS SCIENCE AND ENGINEERING

Robert W. Hendricks, Chair
William D. Brewer
Alex O. Aning
Michael Hyer

February 11, 1999

Blacksburg, Virginia

Keywords: Creep, Discontinuously Reinforced, Metal Matrix Composite, Aluminum, Parametric Models, Manson-Haferd Parameter

Analysis of Creep Behavior and Parametric Models for 2124 Al and 2124 Al + SiC$_w$ Composite

Karen M. B. Taminger

(Abstract)

The creep behavior of unreinforced 2124 aluminum and 2124 aluminum reinforced with 15 wt% silicon carbide whiskers was studied at temperatures from 250°F to 500°F. Tensile tests were conducted to determine the basic mechanical properties, and microstructural and chemical analyses were performed to characterize the starting materials. The creep, tensile, and microstructural data for the 2124+SiC$_w$ composite were compared with a similarly processed unreinforced 2124 aluminum alloy. Applying the basic theories for power law creep developed for common metals and alloys, the creep stress exponents and activation energies for creep were determined from the experimental data. These results were used to identify creep deformation mechanisms and compared to predicted values based on a parametric approach for creep analysis. The results demonstrate the applicability of traditional creep analyses on non-traditional materials.

ACKNOWLEDGEMENTS

There are numerous people who were instrumental in assisting me to finally complete this degree. First, I would like to thank my committee chairman, Dr. Robert W. Hendricks for his guidance and enthusiasm for my research. I would like to thank my committee, Dr. Robert W. Hendricks, Dr. Michael W. Hyer, Dr. Alex O. Aning, and Mr. William D. Brewer for having faith in my abilities, for being willing to tackle a graduate student from 300 miles away, and for exercising infinite patience with my timetable. I would also like to thank Mr. William D. Brewer of NASA Langley Research Center for serving as a mentor as well as an adjunct advisor for this degree, (even though he preferred a root canal to my defense). This degree would never have materialized (no pun intended) without the help of Ms. Jan Doran in the Materials Engineering Department at VPI&SU, who rescued my student file from certain oblivion on several occasions. My gratitude is also extended to Mr. George Allison of NASA Langley Research Center for his assistance with the tuition side of this degree. Finally, I would be remiss in failing to mention my husband, Brian, for all of his love and support, for picking up more than his share of the slack so that I could work on this thesis, and for always helping me to see the hope of a rainbow through a little black rain cloud.

CONTENTS

LIST OF TABLES

LIST OF FIGURES

LIST OF EQUATIONS

INTRODUCTION

Whiskers have been added to some aluminum alloys to enhance the alloys' room and elevated temperature properties. However, the creep properties of whisker reinforced composites are not well understood. Thus, it is of interest to determine the creep properties and mechanisms in whisker reinforced aluminum. It is impractical to perform creep tests for the entire projected lifetime of real-life applications, particularly when the lifetimes can range from 20,000 to 120,000 hours. Therefore, determining an acceptable, conservative method for extrapolating long term properties from short term tests is a significant goal. The data also must be presented to the structural designers in a format which is easy to understand and use.

The objectives of this research program were threefold. First, the creep properties were measured for 2124+SiC$_w$ over a temperature range of 250°F to 500°F. Creep was also performed on unreinforced 2124 as a baseline. Second, creep parameters of stress exponent and activation energy for creep were calculated based on the empirical data. This information was used to deduce the active damage mechanisms for creep. Third, the creep data were extrapolated using a parametric model for creep. An appropriate creep parametric model, the Manson-Haferd model, was selected to extrapolate the experimental data. Error analysis has been performed to give a reliability factor to the extrapolated data.

There are many markets for aluminum alloys, such as the aircraft, automobile, and aerospace industries. Commercial subsonic aircraft operate in a temperature regime in which creep is not a significant problem. (Collins, 1981; Dieter, 1986) However, with

1

the increasing demand for air travel over long distances, such as across the Atlantic or Pacific Oceans, the demand to push civil transport capabilities into the supersonic regime has also increased. The increase in temperature associated with these supersonic speeds have brought an entire new problem to the design of airframe structures. In the aerospace and defense industries, rocket and missile fins require high stiffness and resistance to high temperatures for short periods of time. As the automobile industry competes to reduce weight and improve fuel-efficiency, durable, lightweight materials for elevated temperature applications in engines are necessary. Increasing the temperatures in the engine components and reducing the total weight of the automobiles will both impact the fuel efficiency. As can be seen, there are numerous demands for improved materials for use in elevated temperature environments in many different industries.

1.1   DEVELOPMENT OF AIRFRAME APPLICATIONS

Leonardo da Vinci, although he lived nearly four centuries before humans ever traveled in a flying machine, understood the importance of material selection for use in aircraft. In 1505, da Vinci wrote, "Its joints should be of strong tanned leather and its sinews of raw silk of great strength; and let not anyone hamper himself with fittings of iron, because they burst easily in twisting, or waste away, for which reasons they are not to be used," regarding construction materials for his flying machine. (Murphy, 1972) Da Vinci recognized the most important properties of the times for structural design were strength and weight. He also recognized there are additional properties that are important and may exclude the use of some materials with otherwise good properties, as in the weak torsion and corrosion tendencies of iron and steel. This philosophy in material selection is still being used today in mechanical and structural design.

Humans have always dreamed of flying, and materials issues have always been an integral part of this desire to design and build flying machines. In Ancient Greek

mythology, Daedalus fabricated wings from wax and goose feathers for himself and his son, Icarus, to escape from the Labyrinth by flying. (Hamilton, 1942) In 1505, da Vinci recommended the use of leather and silk for the joints of his flying machine. Three hundred years later, Sir George Cayley, a British aerodynamicist, suggested that bamboo had properties that would be excellent for aerial navigation purposes. It is only natural then that when the first flying machines did emerge, they were built of common raw materials : wood and canvas -- from the lighter-than-air balloons to the Wright flyer. (Murphy, 1972)

Wooden construction dominated the first several decades of heavier-than-air aircraft design because of the availability, cost, and most important, density. At the turn of the century, metal was considered too expensive, unreliable in quality, and too heavy. Ironically, the ratios of strength or modulus of elasticity to density, (specific strength or specific modulus), in commonly used woods such as spruce and birch are quite similar to the specific properties in strong aluminum alloys and some steels. (Budinski, 1983; Murphy, 1972)

More demands on aircraft performance and payload capabilities, in conjunction with the development of better engines, led to the eventual transition from wooden airframes to metal. The first practical metal aircraft were built in Germany. In 1915 the Junkers were built of iron and steel, and in 1917, the Junkers J4 were aluminum. Metal airframes progressed slowly, however, and up through World War II all-wooden aircraft were still flying, such as the de Havilland Mosquito. The transition from wooden to metal airframes occurred slowly because the specific properties of the different materials were not much different, and it took time to recognize some of the advantages of metal airframes. (Murphy, 1972)

As history has shown, the most important material properties required for aircraft have been strength and density. As material properties and aircraft designs have become better understood, the list of important properties has increased. Aircraft designers now recognize the most important properties required are dependent on the function and

specific loading conditions of various parts on the aircraft, such as the wings, fuselage, and vertical tail. The material requirements for a specific body point are driven by the loading conditions during take-off, flight, and landing. (Hyatt & Axter, 1991; Murphy, 1972; Rougier, Mace, Ferton, Sainfort & Albert, 1993) For example, the upper wing skin requires high compressive yield strength because the wing flexes upwards due to lift, putting the upper wing skin in compression during most of the flight. (Hyatt & Axter, 1991) In this same loading scenario, the lower wing skin is put into a state of tension during the flight, which requires high strength for the lower wing skin. (Murphy, 1972) The fuselage also requires high strength because it undergoes internal pressurization, which places hoop stresses along the length of the aircraft body. (Hyatt & Axter, 1991) The vertical tail requires high stiffness to maintain a rigid structure for ease of control and to help avoid developing flutter conditions. (Hyatt & Axter, 1991) These properties are the most important of those considered in material selection. Some of these properties can be accomplished with the structural design, but tailoring the material properties to the design requirements can increase the aircraft efficiency and decrease the aircraft weight while achieving the same property goals.

There are several material properties not specific to a location on the aircraft, but which are required throughout the aircraft for safety in design. These properties are generally more applicable to the lifetime of the aircraft rather than the loading conditions. The fuselage and wings are critical parts of the airplane when it comes to passenger safety, so in addition to the strength requirements, safe design also requires good fracture toughness and fatigue resistance, even with large amounts of damage present. (Hyatt & Axter, 1991) The vertical tail is not considered a critical structural member, so some of the damage tolerance and fatigue resistance requirements are not as stringent for this application. Corrosion resistance is another important property. Poor corrosion resistance can be circumvented by applying protective corrosion-resistant coatings if necessary, but the penalty paid is a significant contribution from the coatings to the total aircraft weight. Any of these properties is not sufficient by itself to merit selection of a material for a

specific application.   Ideally, the designer would select a material in which these properties are as high as possible, but realistically, a trade-off in properties is usually required. (Hyatt & Axter, 1991; Murphy, 1972)

Trade-offs in properties is a fact of material selection; the aircraft designer must compare the service environment to the properties of candidate materials to make an educated decision.   Another trade-off in material selection is cost versus material properties.   In military aircraft, cost is secondary to the performance of the aircraft. Therefore, materials such as titanium and metal matrix composites have been used on military aircraft for many years because they have the best combination of properties for the job.   However, with commercial aircraft, economic viability is essential in a competitive market.   The materials used in subsonic aircraft must be inexpensive, yet capable of performing the required tasks.

There are two major factors which figure into the cost. The first is direct costs, such as the price of the raw materials and their fabrication, manufacturing, and machining costs. These costs result in the actual cost to produce a manufactured good. The second is indirect costs, which are the operating costs of the aircraft. Density can be a large factor in reducing the weight of the aircraft, making it more efficient and using less fuel. However, this savings cannot be offset by a material that is extremely expensive to implement or to process. (Hyatt & Axter, 1991) Improving the mechanical properties of aluminum alloys is a great desire, due to increasing demands on performance, as long as the increase in direct costs is not too great and can be offset by the reduction in indirect costs.   Improvements in material properties can be offset using near-net forming techniques to replace the expense of a significant amount of machining. In some cases, this trade-off between higher material costs and lower manufacturing and forming costs can result in equivalent direct costs, but the integration of improved alloys into existing aircraft design has been severely limited by the numerous requirements for changing design specifications. (Hyatt & Axter, 1991)

Designers of commercial transports have long been interested in supersonic speeds to

significantly reduce the time spent in flight on long distance trips. In the 1950's, the Soviet Union built the Tu 144 Charger, a commercial transport that operated at speeds up to Mach 2.35 (2.35 times the speed of sound) until its recent retirement. The Tu 144 was constructed of high-strength aluminum-lithium alloys. (Quist, 1990) Relatively little technical information is available on that aircraft because of the classified nature of Russian technology. In the early 1960's, the French and the English developed the Concorde. The Concorde's maximum speed was Mach 2.2, with a cruising speed of Mach 2.0. Much information is known about the Concorde, and a significant database is available from the material selection issues as well as performance standards of the airframe. (Quist, 1990; Sertour, 1968) Design data are also available from the U.S. Supersonic Transport (SST) program from the 1960's. This program was canceled in 1970 because it did not appear to be economically viable at the time. (Quist, 1990)

Increasing its speed to supersonic levels significantly changes the service environment and thereby the design of the aircraft. The nose and leading edges must be contoured to minimize the effects of drag and to maximize aerodynamic efficiency. (Sweetman, 1979) Kinetic heating from the high-speed boundary layer is also increased with higher airspeeds. Figure 1 shows the skin temperature as a function of the airspeed. (Harpur, 1967) Note that at Mach 2.0, the skin temperature is approximately 200-225°F. On an absolute temperature scale, this is near 50% of the melting temperature of aluminum, which is a temperature regime in which creep becomes significant. (Collins, 1981; Dieter, 1986) The increase in temperature introduced by supersonic speeds has a major impact on the selection of materials for structural applications. Many aspects of the service environment have been predicted by computer models. There are also two decades of actual flight data and design criteria for the Concorde. Flight data from a typical flight of the Concorde, shown in Figure 2, depicts the thermal profile of the aircraft, taking into account the temperature of the atmospheric layers and airspeed. (Harpur, 1967) This graph shows that much of the thermal profile is above 200°F, (93°C) primarily because of the cruising airspeed of Mach 1.8 to 2.2. Using this profile as a baseline service

environment for the design of a supersonic airframe structure, the temperature becomes a significant factor in the design of aluminum structures, whereas in subsonic design the temperature is not really considered a factor. (Harpur, 1967; Hyatt & Axter, 1991)

Elevated temperatures in the presence of applied stresses may create additional design problems because of thermal expansion, thermal stresses (due to differences in thermal expansion and constraint of an expanding member), and thermal energy causing metallurgical changes to occur. For aluminum, an increase of temperature from 75°F to 250°F is sufficient to cause overaging and creep over long periods of time. In designing a commercial or a military aircraft that will experience thermal cycles, it is important to examine temperature-related deformations as well as the classic properties used for aircraft design. Creep was considered such an important property that the alloy selected for the Concorde structure (RR58 or CM.001; modifications of the alloy currently designated 2618 in the ANSI numbering system) was originally developed to have high creep strength for elevated temperature applications in gas turbines. (Rougier, et al., 1993) (Murphy, 1972) This alloy, and the thermo-mechanical processing developed, were specifically selected for use on the Concorde because of creep resistance, damage tolerance, and durability. (Sertour, 1968)

1.2   MATERIALS AND PROPERTIES

During the 1920's, aided by the success of a few all-metal airplanes of the time, aluminum became more conventional for use on aircraft structures. Aluminum alloys began to be developed, and basically three different categories of aluminum alloys emerged: the Al-Cu-Mg (2XXX) alloys, the Al-Cu-Mg-T (2XXX or 6XXX) alloys where T was some transition element, and the Al-Cu-Mg-Zn (7XXX) alloys. It was in the 1930's that such alloys as 2024 (Al-Cu-Mg) and 7075 (Al-Cu-Mg-Zn) were developed, and these alloys are still the main ones used in aircraft today. (Hyatt & Axter, 1991;

Murphy, 1972)

Since alloys such as 2024 and 7075 have such a long and successful history for structural applications, they are hard to displace with new alloys. The commercial aircraft industry requires an extremely complete characterization of any material before it is certified for use on commercial vehicles. This process takes a long time and extensive testing to ensure the safety of materials used in commercial aircraft. Even after certification, many new materials are not incorporated as replacement parts for existing aircraft because there are numerous drawings with the original alloy specified. In order to change an alloy, modifications to all of these drawings is necessary; therefore, it is simply easier to leave the existing alloys in place, regardless of the missed opportunities. With the advent of completely new generations of aircraft comes the best chance for newly developed alloys and metal matrix composites to realize use on airframes. (Hyatt & Axter, 1991)

One major drawback to aluminum alloys is their low melting points and corresponding rapid loss in mechanical properties. The ultimate tensile strength, yield strength, and modulus of elasticity decrease and the elongation to failure and reduction in area increase as a result of elevated temperatures in a simple tensile test. (Collins, 1981) These changes in mechanical properties may be attributed to a number of different mechanisms. Atom and vacancy mobility increase and diffusion-controlled processes accelerate due to the added thermal energy. Elevated temperatures also provide sufficient energy to enable dislocations to climb, and may activate different slip systems in some metals. (Dieter, 1986) Alloy stability, especially in the age-hardenable alloys, also becomes a problem after long exposures at elevated temperatures: phases change, grains coarsen, precipitates change structure or coarsen, or entirely new precipitates form. These problems can preclude the use of aluminum for many hot structure applications. As aircraft are developed to operate at higher airspeeds, the surface temperature of the airframe structure correspondingly increases. (Toaz, 1987) Presently, denser materials, such as titanium and steels, are required to sustain elevated temperatures for these applications. Improvements

in the elevated temperature properties of aluminum alloys could open up an entirely new range of potential applications.

The creep resistance of an aluminum alloy can be affected by adding elements to form stable strengthening phases which will not coarsen over prolonged periods of time at elevated temperatures. This was the approach used in developing an appropriate alloy for use on the Concorde. Iron additions were made to form fine dispersion of Fe-Al intermetallic particles throughout the matrix. There are two mechanisms that helped improve these properties: increased dislocation densities which form networks that impede dislocation motion; and hard particles which serve to impede dislocation motion and pin dislocations because of the strain fields associated with the presence of the intermetallic particles in the aluminum matrix. (Harpur, 1967; Sertour, 1968)

Researchers are developing new solutions to improve the properties of conventional aluminum alloys. Innovative processing techniques such as rapid solidification, superplastic forming, and powder metallurgy have produced some interesting aluminum alloys with improved properties, especially in room and elevated temperature strength. New alloying combinations, such as Al-Li or Al-Fe-X alloys, are introducing different precipitate phases, which offer promising mechanical properties over a wider range of temperatures. Another solution involves the addition of extrinsic reinforcement, either in the form of dispersoids, particulates, whiskers, or continuous fibers. The addition of a reinforcement phase can help to overcome these current limitations in aluminum alloys and expand the practical service parameters for aluminum. (Schoutens, 1981)

The latter solution to improving properties resulted in the development of metal matrix composites (MMC). Metal matrix composites typically involve a relatively ductile metal matrix that transfers load to a high strength reinforcing phase. The metal matrix is designed to absorb energy, which provides impact resistance, ductility, toughness, and plastic deformation. The role of the matrix depends on the form of the reinforcement, but in general, the matrix transfers load to the reinforcing phase. The reinforcement phase is designed to be the load-bearing phase to increase the strength, stiffness, and creep

resistance of the metal matrix. Reinforcements can be effective in many different forms, and the strengthening mechanisms are dependent upon the morphology of the reinforcing phase. (Dieter, 1986; Kelly & Davies, 1965; Schoutens, 1981)

Dispersoids are often metal oxides and are extremely fine, spherical-shaped particles measuring in the range of 0.01 to 0.1 micrometer in diameter. Ideally, these are uniformly distributed and have a relatively low volume fraction (1-15%). Particulates are coarser, equiaxed particles, generally greater than 1.0 micrometer in diameter. The volume fraction for particulate reinforced materials is typically greater than 25%. Dispersoids and particulates reinforce metals by obstructing dislocation motion. The second phase particles are incoherent in the matrix, so dislocations must climb over or bend around the dispersed particles. In addition, strengthening also occurs due to the presence of the hard second-phase particles which result in a compressive strain field in the surrounding aluminum matrix. Artz and Wilkinson hypothesized that there is an attractive interaction between the dislocations and the hard particles, due to the difference in the microscopic strain fields associated with the dislocations and the hard particles. This is expected to cause the dislocations to be attracted to the hard particles to reduce the strain energy in the matrix. The dislocations are pinned because they cannot pass through the incoherent reinforcing phase. This form of reinforcement is effective at reducing creep that occurs at high temperatures by dislocation glide. (Artz & Wilkinson, 1986) Dislocation creep still occurs, because vacancy diffusion to the hard particles allows the dislocations to climb around the particles. If uniformly distributed, this type of reinforcement is more effective at strengthening the alloy than precipitate hardening, because the hard particles are generally thermally stable in the matrix. (Hertzberg, 1989; Nardone & Tien, 1986)

Whiskers are typically single crystals with a diameter of 0.25 to 1.0 micrometer and an aspect ratio of 4:1 to 7:1 (length-to-diameter). Silicon carbide is often used in whisker form. Chopped fibers are manufactured as continuous fibers which are subsequently chopped into short lengths. The lengths depend a great deal on the intended applications

of the material, and the distribution of lengths can be controlled to a high degree. The orientation of these short fibers or whiskers can be tailored to the requirements of the application. The short fibers can be aligned in predominantly one direction or randomly oriented, depending upon the manufacturing and forming practices used. (Brewer & Sarkar, 1984) Whisker and short chopped fiber reinforced composites strengthen the matrix both intrinsically and extrinsically. Extrinsically, applied loads are transferred to the whiskers or fibers so that the matrix remains under a lower state of stress and the higher strength reinforcements take most of the stress. Intrinsically, high dislocation densities cause the matrix strength to increase by inhibiting the mobility of the dislocations. High dislocation densities are located at the ends of the whiskers or fibers, and are a result of the large difference in coefficients of thermal expansion between the metal matrix and the reinforcing phase. These dislocation dense fields do not need to be introduced by any special processing techniques; they are formed during cooling from normal consolidation and processing temperatures for the composite materials as a result of the coefficient of thermal expansion mismatch between the reinforcement and matrix phases. (Hertzberg, 1989; Nardone & Strife, 1987; Papazian & Adler, 1990)

The final form of extrinsic reinforcement used in metal matrix composites is continuous filaments. Continuously reinforced metals are designed such that the fibers are oriented in the direction of the applied loading. This takes greatest advantage of the strength of the fibers. The metal matrix absorbs energy and transfers essentially all of the load to the fibers. These composites display high degrees of anisotropy, depending on the orientation of the fibers, and typical fiber volume fractions range from 0.30 to greater than 0.50. High residual stresses in the matrix due to the large mismatch in coefficients of thermal expansion also aid in strengthening in some cases. (Brown, Brewer & Hendricks, 1990) High strength is retained at high temperatures almost to the melting temperature of the metal matrix in the direction of the length of the fibers. (Kelly & Davies, 1965; McDanels, 1985; Schoutens, 1981)

Of the various forms of reinforcement available, whiskers are considered a prime

candidate for reinforcing aluminum alloys for several reasons. Whiskers offer better stiffness than particulate or dispersoid reinforced composites, especially if the whiskers are aligned. Cost is also a key factor. Continuous reinforced MMCs have far better directional strength and stiffness than any discontinuous MMCs. However, the raw materials, fabrication, and subsequent post-fabrication processing and machining costs are extremely high compared to discontinuous MMCs. Discontinuous reinforcements are attractive for cost effectiveness and machinability considerations: conventional manufacturing and processing methods such as extrusion, casting, rolling, and machining can still be used with whisker reinforcement. (Divecha, Fishman & Karmarkar, 1981)

Although some properties are adversely affected, many are enhanced by the addition of SiC whiskers to aluminum. By controlling such factors as the volume content of whiskers, alignment of the whiskers, matrix alloy, and temper, it is possible to tailor some of the properties to best suit the application. This is an exciting concept in engineered materials that allows the feasibility of many specific applications. Ideally, the composite properties will follow the rule of mixtures, but in reality, often one constituent will influence certain properties more than the others. The bonding characteristics also play an important role in determining the composite properties. (Lee, Vaudin, Handwerker, & Kattner, 1988; Peteves, et al., 1990; Schoutens, 1981)

One of the most obvious effects of the reinforcement on the matrix properties is observed in the mechanical properties. Whiskers increase the modulus of elasticity; the actual amount of the increase in modulus is determined by the alignment and the volume fraction of the whiskers. The yield or flow stress and the ultimate tensile strength experience up to 60% increase over the unreinforced alloy. (Lederich & Sastry, 1982; Rack, Barusch & Cook, 1982) The reinforcement generally has an embrittling effect which reduces the ductility and fracture toughness of the aluminum alloys. (Nutt & Needleman, 1987) This effect is influenced by the volume fraction of whiskers and the strength of the aluminum alloy: ductile alloys with lower whisker loadings maintain good ductility, whereas high strength alloys or greater whisker contents tend to cause brittle

fracture with only 1-2% elongation to failure. (McDanels, 1985) The reinforced composite tends to have better strength and stiffness at high temperatures also, although the difference between the reinforced and unreinforced strength properties become less as the temperature increases. (Nardone & Strife, 1987; Nieh, 1984; Nieh, Xia & Langdon, 1988)

One subject of debate in the literature is the actual mechanism which increases the room temperature properties of discontinuous MMCs above those of the matrix. One theory proposes that the MMC strengthening is due to the increased work hardening coefficient of the matrix due to high dislocation densities from the difference in the coefficients of thermal expansion between the matrix and the whiskers. (Arsenault, 1991; Nardone & Strife, 1987; Nardone & Tien, 1986) Another suggests that the strengthening is a result of an attractive interaction between the particles and dislocations because dislocations at the interface reduce the strain field and will not climb. (Artz & Wilkinson, 1986; Nardone & Strife, 1987; Nardone & Tien, 1986) Orowan bowing around particles is another theorized strengthening mechanism in which additional deformation energy is required to cause the dislocations to bypass the reinforcement phases. (Ledrich & Sastry, 1982; Park, Lavernia & Mohamed, 1990) In contrast to these theories, a different group of researchers claim that an increase in the dislocation density does not add much to strengthening. (Suresh, Christman & Sugimura, 1989)

The addition of SiC whiskers also has a significant impact on the microstructure. Highly aligned whiskers, achieved by secondary mechanical processing such as extrusion or rolling, tend to anisotropically increase the modulus of elasticity and the ultimate tensile strength in the direction of the length of the whisker. (McDanels, 1985) Cross-rolling can be used to obtain a more random orientation of the SiC whiskers which results in improved planar isotropy in a plate or sheet material. (Brewer & Sarkar, 1984; Divecha, Fishman & Karmarkar, 1981; Toaz, 1987) Uniform distribution of the whiskers throughout the composite is also important, because fiber-poor areas are too dependent on matrix properties and have no fibers to transfer load to, and fiber agglomerates can

initiate cracking because adjacent fibers may not have sufficient matrix infiltration to effectively transfer load to the fibers, and voids between fibers become precracks. (Birt & Johnson, 1990) During consolidation or casting, the whiskers provide more nucleation sites for grain development and precipitation. Fine grain size in an alloy tends to increase the room temperature strength, but can be a hinderance at elevated temperatures where grain boundary sliding is significant. (Birt & Johnson, 1990) In powder metallurgy MMCs, it is desirable to have a fine powder size to enable better mixing of the aluminum matrix and the SiC whiskers. This leads to an inherently fine grain size. (Rack, 1988; Sarkar, Brewer & Lisagor, 1984) Solute segregation to the whisker-matrix interface, due to long exposures at elevated temperatures, can result in precipitate-free zones which will decrease the MMC properties. (Strangewood, Hippsley & Lewandowski, 1990) High dislocation densities and voids nucleate at the fiber ends in a whisker reinforced composite as a result of high stress concentrations, residual stresses, and coefficient of thermal expansion mismatch between the matrix and the reinforcing whiskers during processing. Void coalescence to initiate cracking and high dislocation densities impeding dislocation mobility are considered to be the most direct reasons for poor ductility and fracture toughness in SiC whisker reinforced MMCs. (Nutt & Needleman, 1987; Papazian & Adler, 1990)

The creep properties of whisker and particulate reinforced MMCs have been studied, but most of the studies done to date have been at significantly higher temperatures and stresses than the expected service environment for a supersonic aircraft. (Barth, Morton & Tien, 1990; Morimoto, Taya, Yamaoka & Lilholt, 1988; Nardone & Strife, 1987; Nieh, 1984) Elevating the temperatures and shortening the times too much will lead to two problems when trying to predict actual creep properties for the service life of an aircraft. First, test temperatures significantly higher than the anticipated service conditions cause changes in the material and its mechanical properties as previously mentioned in this section. This can put the material into a different creep deformation regime, as can be seen in creep deformation maps, which may produce erroneous data because it does not

accurately reproduce the deformation mechanisms active under service conditions. This can also cause large changes in the precipitates which results in a non-representative material. It is difficult to separate overaging effects from creep effects, particularly if they are both occurring in a short test. Second, elevating the temperature and stress so that creep tests only last a few hours results in the problem of extrapolating the data from a test of less than ten hours to a service life of 100,000 hours. The reliability of extrapolating such data is questionable, for the reasons given above. (Collins, 1981; Larson & Miller, 1952; Manson & Haferd, 1953)

Aluminum alloy 2024 is among the class of Al-Cu-Mg age hardenable alloys developed for use in airframe structures. The alloy 2024 is used on Boeing commercial aircraft for the damage critical areas such as the fuselage and the wing lower surfaces. This correlates to approximately 40% of the total aircraft structure. (Hyatt & Axter, 1991) The alloy 2024 can be heat-treated to achieve moderately high strength, and maintains good ductility and toughness. In addition, 2024 also has good fatigue life, corrosion resistance, and relatively good creep resistance at temperatures below approximately 60% of the absolute melting temperature of the alloy. (Lampman, Zorc, et al., Eds., 1990)

Alloy 2124 has the same nominal composition as 2024, but the tolerances are held tighter to improve quality. In ingot metallurgy, the quality of the alloy is not as critical as with powder metallurgy. Oxygen and impurity pick-up is inherent in the production of aluminum powders for powder metallurgy. However, powder metallurgy offers advantages, such as extremely fine grain sizes and improved blending with discontinuous reinforcement, unattainable with ingot metallurgy. Therefore, the tighter tolerances are necessary to ensure the quality and thus the properties of the alloy. The good all-around properties of 2024 and 2124 were key to the selection of this alloy as the matrix alloy for a silicon carbide whisker reinforced composite. (Hyatt & Axter, 1991) The tighter tolerances in 2124 helped to reduce impurity levels that could be a further detriment to the ductility and toughness, which are already decreased as a result of the SiC whisker additions. (Brewer & Sarkar, 1984; Rack, 1988) The alloy compositions and tolerances

for 2024 and 2124 are shown in Table 1. (Lampman, Zorc, et al., Eds., 1990)

Manufacturing discontinuously reinforced metal matrix composites using an alloy that has a history in the aircraft field is a logical selection. Alloy 2024 is readily available and has already been proven in flight environments. Recently, several parts on military aircraft have been manufactured from discontinuously reinforced aluminum matrix composites for non-critical parts such as cargo bay doors and floors. (Brewer & Sarkar, 1984)

There are numerous applications for materials such as these SiC whisker reinforced composites. The aerospace industry is examining SiC reinforced aluminum for use in airframes, missile fins, and airplane engine applications. The flexibility of tailoring properties such as thermal expansion and stiffness of SiC reinforced aluminum also makes this material attractive for use in satellites, antennas, and reflective mirrors for optical sensing and transmission. Also, the automotive industry is interested in using discontinuously reinforced aluminum alloys in automobile engines, which requires good high temperature properties, wear resistance, and good fatigue life. (Toaz, 1987) The automotive industry is already using cast reinforced composites for pistons. The strength and wear resistance are important properties for this application. This material is also being considered for use in connecting rod because of its high stiffness and strength. The additional wear resistance from the addition of the SiC is also making this material a candidate for use in brake disks and drums. There are many potential applications for inexpensive materials with combined higher specific stiffness and strength in many other industries as well. (Brewer & Sarkar, 1984)

1.3   Creep Deformation Mechanisms and Parametric Models

One material challenge in elevated temperature applications is the prevention of creep.

Creep is a permanent deformation resulting from an applied stress in a material over a long duration of time. Creep strains of engineering significance are typically not encountered until 35 to 70% of the melting temperature of an alloy. (Collins, 1981; Dieter, 1986) The creep process is accelerated and far more detrimental at elevated temperatures, because the additional thermal energy activates different mechanisms for creep. (Collins, 1981; Garafalo, 1965)

There are generally three different stages of creep in unreinforced alloys. Primary creep is transient creep during which the creep rate decreases over time. As the material deforms, the material strengthens via strain hardening, thus increasing the creep resistance and causing the decreasing creep rate observed. This is the dominant form of creep observed at low stresses and at low temperatures with respect to the melting point of the material. (Dieter, 1986; Garafalo, 1965; Hertzberg, 1989; Reed-Hill, 1973; Sherby & Burke, 1967) Primary creep gradually transitions into the second stage, called secondary or steady-state creep. During secondary creep, the strain hardening of the material during deformation balances against the creep deformation mechanisms in the material. In an ideal material, the strain hardening rate is exactly proportional to the deformation rate. The difference between these two rates produces a linear creep rate which is typically identified as the steady-state creep rate. In reality, many materials do not exhibit a truly linear secondary creep rate because the strain hardening rate never becomes exactly proportional to the deformation rate. In these cases, the material will demonstrate a continuously decreasing creep rate which reaches a minimum inflection point then accelerates into tertiary creep. In these materials, the region within approximately 10% of the minimum creep rate has been considered to be the secondary creep regime. It has been documented that this behavior can be assumed to be linear for the purposes of conventional creep analyses with little impact on the quality of the subsequent results. (Barth, Morton & Tien, 1990; Garafalo, 1965; Lilholt & Taya, 1987; McLean, 1988; Mishra & Pandey, 1990; Nieh, Xia & Langdon, 1988) The secondary creep transitions into the third stage, typically identified as tertiary creep. Tertiary creep is characterized

by an increasing creep rate, and is mainly observed in constant load tests at high temperatures and high stresses when an effective reduction in area due to necking or void formation occurs. This phase of creep is the final stage of creep before rupture occurs. (Dieter, 1986; Garafalo, 1965; Hertzberg, 1989; Reed-Hill, 1973; Sherby & Burke, 1967)

At lower temperatures, (relative to the melting temperature of the metal), creep is dominated by the diffusion of vacancies. This involves either Nabarro-Herring creep in which the bulk vacancy flux is directed by the orientation of the stress such that vacancies diffuse from grain boundaries in tension to grain boundaries in compression; or Coble creep (also called pipe diffusion) in which vacancies diffuse along the grain boundaries. (Frost & Ashby, 1982; Hertzberg, 1989; Sherby & Burke, 1967) These types of creep can be identified when the calculated activation energy for creep is approximately equivalent to the activation energy for vacancy diffusion in the alloy. At higher stress levels and temperatures greater than approximately half of the melting temperature, dislocation creep is dominant. In this stage, dislocation motion is enhanced by the diffusion of vacancies so as to allow easier dislocation climb and the formation of dislocation jogs and kinks. At higher temperatures, vacancy diffusion is as rapid as dislocation motion, resulting in vacancy diffusion no longer being the rate-controlling mechanism for creep. At this point, dislocation glide independent of vacancy diffusion is the controlling deformation mechanism. (Dieter, 1986; Reed-Hill, 1973; Sherby & Burke, 1967)   Other creep mechanisms involve complex synergism of different deformation modes and result in extremely inhomogeneous deformation. Examples include the formation of subgrains, segregation of thermodynamically stable voids to the grain boundaries, or an effective sliding of adjacent grains at the grain boundaries. (Davies, Evans, Williams & Wilshire, 1969; Dieter, 1986) Fine-grained alloys are more sensitive to grain boundary sliding because of the overall increase in grain boundary area. Grain boundary sliding is generally not significant until creep enters the tertiary stage. (Ghahremani, 1980; Sherby & Burke, 1967) In general, plastic deformation due to creep is a result of movement of lattice defects (ions, vacancies, and dislocations) as a result

of the deviatoric shear stresses on the material. (Frost & Ashby, 1982)

These are generally accepted as the controlling deformation mechanisms in creep of unreinforced engineering alloys. Creep in MMCs is more complex than creep in a monolithic alloy. The mechanisms described for unreinforced alloys can occur in both constituent phases. Creep will have a far smaller effect in the reinforcement phase than in the matrix because the melting temperature of SiC is approximately 4900°F. Thus, at temperatures below 500°F, the creep effects within SiC whiskers can be considered negligible. (Simon & Bunsell, 1983) As a result, the SiC whiskers can be described as creep-resistant, and the aluminum matrix creep-compliant. The extent of primary creep is dependent on the volume fraction of the reinforcement phase due to load redistribution between fibers and matrix during creep. As the matrix creeps, the stress in the matrix decreases. The fibers deform elastically, so the stress in the fibers increases, resulting in an overall decrease in the creep rate as compared to the unreinforced alloy. Other local mechanisms also occur which combine to create the overall creep response of the composite. (Lilholt & Taya, 1987) Reinforced phases increase the creep resistance of the MMC matrix by obstructing dislocation, atom, or vacancy motion. However, the reinforcement phase may not be capable of impeding other deformation mechanisms active within different temperature or stress regimes. Reinforcement phases can also introduce new creep mechanisms which do not occur in monolithic alloys.

There are several opposing theories of the creep mechanisms which occur in whisker reinforced aluminum alloys. More highly-stressed regions, such as in the matrix in the vicinity of the whisker ends, are the most likely locations for initiation and accumulation of creep damage. (Lilholt & Taya, 1987) One theory proposes that microcracks form at the interface and whisker ends where the bond strength is lower. (Cao, et al., 1988) Another theory proposes that void nucleation due to interface decohesion at the whisker ends is responsible for creep in whisker reinforced MMCs. (Nieh, Xia, & Langdon, 1988; Nutt & Needleman, 1987) Yet another theory is that the loss in high temperature properties is due to a reduction in matrix shear strength, thus reducing the effectiveness

of the matrix to transfer the load to the whiskers. Therefore, the whiskers end up not contributing to the elevated temperature strength above certain levels. (Schueller & Wawner, 1991) These proposed mechanisms of creep in composites operate in conjunction with the bulk creep mechanisms due to the movement of defects within the metal matrix. The proliferation of different theories indicates that there is much disagreement about the actual mechanism(s) occurring in MMCs. The difficulty of identifying a mechanism is due, in part, to the fact that properties and microstructures can be interpreted many different ways.

One tool used in identifying creep mechanisms is microstructural evaluation. This typically requires detailed transmission electron microscopy (TEM), and as can be seen from the above discussion, may lead to subjective interpretation. In addition, TEM samples an extremely limited volume of the specimen, and can be misrepresentative of the conditions in the bulk material.

Another useful tool in identifying creep mechanisms is the use of deformation maps. Deformation maps have been developed by solving constitutive equations for different deformation mechanisms, then plotting the different regions in stress-temperature space. (Hertzberg, 1989) These maps are not absolute, but can be used as a first approximation to determine potential creep deformation regimes. A deformation map developed by Frost and Ashby for pure aluminum is shown in Figure 3. (Frost & Ashby, 1982)

Another technique which sheds light on the active mechanisms is to determine the activation energy for creep and compare this value to known activation energies for different mechanisms. In the steady-state regime of the creep relationship, the creep rate is given by a simple power law:

$$\dot{\varepsilon}_{ss} = A_1 \, \sigma^n \, e^{-\left(\frac{Q_{app}}{RT}\right)} \tag{1}$$

where $\dot{\varepsilon}_{ss}$ is the steady-state creep rate, A_1 is a constant for all stresses and temperatures, σ is the applied stress, n is the creep stress exponent, Q_{app} is the apparent activation energy for creep, R is the universal gas constant, and T is the absolute creep test temperature. The activation energy is designated as the apparent energy for creep because it is empirically determined. Many different mechanisms may be interacting to cause the observed Q_{app}, but cannot be separated based only on the experimental data. (Mishra & Pandey, 1990)

Creep stress exponents and activation energies can be used to identify possible creep mechanisms.   The understanding of creep deformation mechanisms in materials is fundamental in identifying innovative solutions to increase the creep resistance of a material. For example, the creep properties of candidate aluminum alloys were examined in selecting appropriate materials for use on the Concorde.   The alloy finally used, CM.001, was developed to meet the various material properties required, including creep resistance.   The addition of iron to the alloy and the development of new thermo-mechanical processing parameters resulted in a fine dispersion of Al-Fe intermetallic particles which improved the creep resistance to meet the design allowable criterion. (Sertour, 1968)

Creep strength is important in considering the life of structures to be exposed to elevated temperatures and stresses for extended periods of time. Typically, in locations where creep is a potential problem, strict restrictions are placed on the allowable stresses in order to maintain the creep strain well below creep rupture.   This often results in overdesigned structures to minimize the stresses. However, in aircraft there is a tradeoff between weight and overdesigning the structure to minimize creep.   The creep design criterion specified for the Concorde is a maximum of 0.1% permanent strain over the lifetime of the aircraft. (Harpur, 1967; Murphy, 1972; Sertour, 1968) This is conservative from the standpoint of time, since the design lifetime of the Concorde is 50,000 flight hours, but only 20,000 to 30,000 hours may be spent at elevated temperatures. (Harpur, 1967; Murphy, 1972; Sertour, 1968)

It is unrealistic to perform creep tests for the exact service life of an aircraft because that would take seven to ten years of uninterrupted creep testing for a single test! There are many recognized methods for extrapolating creep data. Two major types of extrapolation techniques have emerged: linear extrapolation of the steady-state regime, and parametric models. The following paragraphs describe each of these different techniques.

Data from creep tests should extend at least 1 to 10% of actual lifetimes to give meaningful extrapolation. Linear extrapolation of the creep strain along the steady-state creep rate is considered valid for no more than one to two orders of magnitude, although this method is generally unacceptable because it does not account for the possibility of entering tertiary creep. Using the abridged method of extrapolation, tests are performed at several stress levels at the anticipated service temperature. The creep strain versus time at constant temperature results in a family of creep curves, each curve representing a different stress level. Extrapolation of the creep rate out to the design life will provide an estimate to the actual creep life, but will not predict if creep rupture will occur prior to reaching the design life. (Collins, 1981)

Acceleration of creep tests is sometimes necessary to shorten the length of the tests to reasonable times. The mechanical acceleration method uses stress levels significantly higher than the anticipated service stresses to reach the limiting strain faster. The design life is again determined by developing a family of creep curves at constant stress and temperature and extrapolating the appropriate steady-state creep rate out to the design life. (Collins, 1981) Accelerated tests can also use the thermal acceleration method in which the temperatures in the tests are significantly higher than the anticipated service temperatures. A plot of the stress versus time for a constant creep strain and temperature will develop a family of creep curves from which extrapolation out to the design lifetime can be made. (Collins, 1981) As with the abridged method above, neither of these accelerated test methods will predict if creep rupture will occur prior to reaching the design life. (Collins, 1981) In addition, increasing the temperature or the stress significantly can change which creep deformation mechanism is active, which makes the

creep data developed from these tests relatively meaningless to the actual service environment conditions. (Garafalo, 1965)

Because of uncertainties in extrapolating creep data to determine the design lifetime, parametric models have been developed. There is more certainty to extrapolating data using a parametric model, because many different test conditions are superimposed to create a master curve. The guidelines for extrapolating data using a parametric method allow an additional order of magnitude extrapolation with more certainty than simple linear extrapolation allows. The most common and universally recognized parametric model developed is the Larson-Miller method. This model assumes that the steady-state regime follows power law creep as shown in Equation (1). Larson and Miller developed this time-temperature relationship for prediction rupture and creep stresses:

$$T \ (\ C \ + \ \log t \ ) \ = P_{L\text{-}M} \tag{2}$$

where $P_{L\text{-}M}$ is the Larson-Miller parameter, T is the absolute creep test temperature, C is the Larson-Miller constant, and t is time to either creep rupture or to a given creep strain level. Whichever time is used for determining the constant will determine the lifetime extrapolated for this method. In addition, minimum creep rate can be substituted for time, allowing the prediction of creep rates instead of lifetimes. Typically, the Larson-Miller constant, C, has been forced to be approximately 20 if the time is shown in hours. (Larson & Miller, 1952) This constant can also be empirically determined using a plot of log time to creep rupture versus the inverse of the absolute temperature. Extrapolating these isostress lines of data back to the point where the inverse of the absolute temperature approaches zero (the ordinate) will graphically determine the appropriate value for C. (Larson & Miller, 1952) This is useful for extrapolating test parameters to determine the maximum allowable stress levels for a given application. This relationship will not be valid if a major phase change occurs in the material, but it does account for

metallurgical changes involving diffusion.

Manson and Haferd developed a linear time-temperature relation for the extrapolation of creep and stress-rupture data, as an improvement to the Larson-Miller method. This was developed to eliminate errors introduced in the Larson-Miller method by assuming *C=20* for the Larson-Miller constant. The Manson-Haferd method assumes the same starting point of steady-state creep dominated by power law behavior. However, the Manson-Haferd parameter determines two constants in lieu of the one proposed by Larson and Miller. The Manson-Haferd parameter is:

$$\frac{(T - T_a)}{(\log t - \log t_a)} = P_{M\text{-}H} \tag{3}$$

where $P_{M\text{-}H}$ is the Manson-Haferd parameter, T is the absolute creep test temperature, T_a is the Manson-Haferd temperature constant, t is time, and t_a is the Manson-Haferd time constant. As with the Larson-Miller method, the time can either be the time to creep rupture or the time to a given creep strain level. The Manson-Haferd parameter is derived graphically from the intersection point of extrapolated isostress lines when plotted on a log of minimum creep rate versus absolute temperature (instead of the inverse of temperature, which is used in the Larson-Miller parameter). The intersection point will identify the constants T_a and t_a. By plotting the Manson-Haferd parameter versus stress, all creep data will collapse onto a single master curve. The equation of this curve can be determined by curve fitting, which yields an equation relating time to a given percent creep, temperature, and stress. (Manson & Haferd, 1953) The Manson-Haferd parameter can be used for a variety of different materials and times to either a certain percent creep strain or creep rupture. The Manson-Haferd method tends to be more conservative by underestimating the creep extrapolations, as compared to the Larson-Miller method.

One of the difficulties of designing structures for elevated temperature applications is

the potential for creep. As a result, oftentimes the structure and/or the material selected is overdesigned so that creep is not an issue, either because the temperatures are too low for the material selected to experience creep, or the design stresses are low enough to prevent appreciable creep. In some designs, such as for aircraft and spacecraft, weight and efficiency of design are important considerations, such that aircraft designers may be forced to design in an area where it cannot be assumed that creep is not an issue. If a single equation which relates time to a given percent permanent creep strain, temperature, and stress could provide information to aircraft designers, extrapolated creep data may be applied to the design of aircraft structures. This approach would provide the designer with useful creep information so that creep can be effectively factored into the design.

THESIS JUSTIFICATION

The previous chapter has established that the important properties of an alloy for aircraft use are based on the service environment. Properties include strength, damage tolerance, and modulus for subsonic aircraft. When the design speed of an aircraft is increased to supersonic, the temperature of the airframe structure correspondingly increases. Thus, additional material properties such as creep become more significant to the airframe designers. To integrate new materials with improved properties into mechanical and structural designs, the cost effectiveness of the materials and their fabrication techniques must be viable.

The material used in this study, 2124 aluminum reinforced with silicon carbide whiskers, is made of inexpensive constituents and is designed to improve the modulus, strength, and elevated temperature properties of an alloy that already is extremely common in commercial aircraft structures. This study measures the creep properties of 2124+SiC$_w$ and unreinforced 2124 over relatively short test times, and then applies predictive creep models to predict their creep parameters. In addition, this study attempts to determine standard creep parameters, such as creep stress exponents and activation energies for creep, by applying traditional creep analyses. Finally, this study also attempts to simplify creep data so that designers can incorporate the results of this program directly into structural designs.

PROCEDURES

3.1 EXPERIMENTAL DESIGN

This section summarizes the entire test matrix for this research study. More complete details on materials, test equipment, procedures, and analysis follow in the remaining sections of this chapter. This research is focused primarily on the 2124+SiC$_w$ discontinuously reinforced aluminum matrix composite. Selected tests were performed on unreinforced 2124 for comparison to the reinforced material.

Microstructural analysis and phase identification were used to characterize the as-received material. These techniques were also used to identify changes that occurred after the test materials were exposed to elevated temperatures with or without applied stress. Optical microscopy, scanning electron microscopy (SEM), and transmission microscopy (TEM) were used for imaging microstructures, and SEM was used to examine fracture surfaces. Phase identification was primarily conducted by x-ray diffraction analysis; some x-ray dispersive spectrometry (XDS) was also used to identify chemistries of phases in the SEM. The specific materials and conditions examined in detail are shown in Table 2a.

Tensile tests were conducted at room temperature and various elevated temperatures to determine the mechanical properties of unreinforced 2124 and 2124+SiC$_w$ materials at the different creep test temperatures. The number of replicates performed at each of the

27

test temperatures are shown in Table 2b.

Creep tests were conducted at eight temperatures and six stress levels on unreinforced 2124 and 2124+SiC$_w$. Due to limitations in material quantities and equipment availability, only selected combinations of these temperatures and stress levels were tested to provide sufficient data for subsequent analyses. The ultimate tensile strengths at the test temperatures were also used to identify appropriate stress levels for different test temperatures. All creep tests were single specimens, no replicates were performed in creep. All of the conditions tested for unreinforced 2124 are shown in Table 2c, and for 2124+SiC$_w$ are shown in Table 2d.

3.2   MATERIAL AND PROCESSING HISTORY

The material tested for this research program was powder metallurgy 2124 aluminum reinforced with SiC whiskers. This material was produced by Advanced Composite Materials Corporation (ACMC) in Greer, South Carolina. The alloying elements in the matrix alloy, 2124, are Al, Cu, Mg, Mn, and Si. The nominal composition is shown in Table 1. This alloy is essentially the same as the commonly used alloy 2024, except that the allowances on the impurity levels are smaller for 2124. The lower impurity levels helped to improve the quality of the alloy powders, since the powder metallurgy process inherently picks up impurities during powder production and processing. (Brewer & Sarkar, 1984; Rack, 1988)

The reinforcement phase was 15 vol% (18 wt%) silicon carbide whiskers. These whiskers were designated F-9 by the manufacturer. (Brewer & Sarkar, 1984; Dvorak & Goodman, 1982; Rack, Baruch & Cook, 1982) The reinforcement is inexpensive to produce because it is manufactured using pyrolization, an inexpensive processing technique, on rice hulls. Due to this manufacturing process, the resulting whiskers are either β-SiC (BCC structure) or a mixture of β-SiC and α-SiC (HCP structure).

Pyrolizing rice hulls does result in slightly lower quality whiskers than the single crystal whiskers, because it results in some polycrystalline whiskers in addition to a significant volume fraction of SiC and/or SiO_2 particulates and some larger irregularly shaped SiC particles. In addition, an SiO_2 layer often forms on the SiC whiskers, which can result in silicon being absorbed into solid solution with the aluminum matrix. (Lee, et al., 1988; Peteves, et al., 1990; Rack, 1988) In general, the whiskers started with a diameter of 0.5 μm and an aspect ratio (length to diameter) prior to consolidation of 10 to 60. Whisker breakage during processing resulted in the lower aspect ratio observed in the material. (Brewer & Sarkar, 1984; Rack, 1988)

The $2124+SiC_w$ was manufactured using powder metallurgy techniques. The 2124 aluminum matrix was gas atomized to form a pre-alloyed powder. This powder was mechanically blended with the silicon carbide whiskers. The composite, in powder form, was cold isostatically pressed, degassed, then consolidated by hot isostatic pressing into a billet. Next the billet was extruded into a one-inch thick plate. The plate was hot rolled in a direction perpendicular to the extrusion direction to randomize the whisker orientation. The plate was rolled to its final thickness of 0.0525 inch thick, then solutionized and naturally aged (T4 condition). (Brewer & Sarkar, 1984; Rack, 1988) For consistency, the unreinforced 2124 examined in this study was processed using the same procedure as just described for the composite. This eliminated variability in the test results from the processing of the materials.

Solutionizing was conducted per manufacturing recommended practices for the standard 2024 and 2124 ingot alloys. The same aging conditions (times and temperatures) were used for solutionizing the unreinforced material and for the whisker reinforced composite. Microstructural evaluation showed large intermetallic constituent particles, even after the solutionizing step. Using an energy dispersive spectrometer attached to the SEM, these large particles were determined to be primarily copper-rich phases. These particles were too large to go into solution during solutionizing. It is thought that these constituent particles are a result of residual impurities and inclusions from the powder

process. Since this material was procured, the material supplier has worked to clean up its powder as a result of early analysis done on this material by other researchers. (Brewer & Sarkar, 1984; Rack, 1988)

The materials for this study were all tested in the naturally aged condition, or T4 temper. This temper was selected because the material in this temper exhibits a good strength/toughness combination while maintaining some degree of ductility. For the SiC whisker reinforced 2124, the T4 temper actually has higher strength and good ductility as compared to either artificially aged or stretched plus artificially aged materials. (Papazian & Adler, 1990; Zhao & Huang, 1989) This is attributed to the dislocation substructure and Guinier-Preston zones which develop upon quenching from the solutionizing temperature. Stretching and artificial aging to produce a peak age temper (T8) results in precipitation of S' (Al_2CuMg), refines the precipitate distribution, and increases the dislocation density to pin mobile dislocations. In the $2124+SiC_w$, these effects result in inferior tensile strength. The full tensile strength is not realized because the whiskers and other inclusions provide numerous crack initiation locations, which lead to lower ductility and premature tensile failure. (Papazian & Adler, 1990)

Finally, it is anticipated that $2124+SiC_w$ would be used in either the T4 (solutionized and naturally aged) or T6 (solutionized and artificially aged) conditions. Stretching to introduce additional dislocations is not necessary because the presence of the whiskers achieves the same result. For some applications such as missile fins, the actual service temperatures would far exceed the heat treating temperature, which would accelerate aging regardless of the initial condition. Further overaging and potential losses in the toughness and ductility will occur at these service temperatures, not allowing the advantages of aging to be fully realized.

3.3   MICROSTRUCTURAL ANALYSIS

For microstructural analysis, specimens were sectioned for examining in the rolling plane (L-T plane) and mounted in epoxy mounts which were cured at room temperature. The mounted specimens were polished using a diamond slurry on an automatic polishing wheel to achieve a mirror finish. Next, the specimens were attack-polished using Keller's etch to highlight the grain structure and morphology. The optical micrographs were taken using bright field on an inverted stage microscope. These same specimens were also examined in a scanning electron microscope.

The specimen surfaces were anodized using an electrochemical approach with Barker's etch to measure the grain sizes in the specimen. This causes a difference in oxide thicknesses on differently oriented grains. When observed under polarized light, the different grains have good bright/dark contrast, thus simplifying the measurement of the grain size. The grain sizes were measured using the intercept method on several micrographs, then averaged to calculate the average grain size and aspect ratio. The grain size in the unreinforced 2124 is 250 μm, with an aspect ratio of 4.7. The average grain size of the composite is 77 μm, with an aspect ratio of 2.6.

Figure 4 shows optical micrographs in the plane of the sheet (L-T plane) for unreinforced 2124 and 2124+SiC$_w$ composite, both in the T4 condition. An inhomogeneous distribution of coarse Θ or Θ' (Al$_2$Cu) particles appear as dark spots in the unreinforced material in Figure 4c. The silicon carbide whiskers dominate the field of view in both optical (Figures 4a and 4b) and scanning electron (Figure 5) micrographs, which prevents observation of precipitates in the aluminum matrix of the composite. It can be seen that cross-rolling of the composite was successful at establishing a fairly random and homogeneous distribution of the SiC whiskers within the aluminum matrix. In some regions, clustering of the SiC whiskers is evident, and a few SiC particulates inherently present in the whisker production method used are also present. Figure 5 shows a scanning electron image of the 2124+SiC$_w$ composite in the T4 condition. As

can be seen in this figure, the whiskers are randomly distributed in the Al matrix. The average length of the whiskers is 8.2 ± 2.4 μm, which yields an aspect ratio of approximately 6.3.

A limited amount of transmission electron microscopy (TEM) was also performed to examine the whisker-matrix interface and the internal substructure of the material. Electropolishing the TEM specimens using a cooled ethanol-nitric acid bath was attempted, but the whiskers were impervious to the solution, and were not thinned. In addition, when perforation was achieved using the electropolishing technique, the aluminum was etched out around the SiC whiskers, and the entire thinned section tended to fracture, leaving no good areas for viewing in the specimen. So instead of electropolishing, mechanical thinning and ion milling was used to achieve a useable TEM sample. Specimens were prepared by slicing a thin section using a diamond wafering saw. The specimens were cut from the L-T plane, since the TEM specimen must be a 0.114 inch (3 mm) diameter disk, and the thickness of the material used in this study was only 0.0525 inch thick. A 0.114 inch diameter disk was punched from the saw-cut wafer. This was dimpled from both sides using diamond paste and a dimpler, until the dimple diameter indicated near-perforation. Then, the specimen was placed in an ion-milling machine with a cryogenic stage, and ion-milled until perforation was achieved. The cryogenic stage helped prevent the specimen from heating to minimize the effect of sample preparation on the resulting microstructure.

Four TEM micrographs from a single 2124+SiC$_w$ creep tested specimen are shown in Figure 6. This specimen was exposed to 143 hours at 350°F and 35 ksi stress, and stopped in secondary creep. Within the SiC whiskers, stacking faults appear as parallel lines normal to the long axis of the whiskers in Figures 6a and 6b. In addition, whiskers in Figures 6a and 6d are cracked, although it is difficult to tell if the cracking occurred during processing or during creep. It is concluded that the cracks are a result of the rolling and processing, since the applied stress during creep for this specimen was significantly lower that the strength of the SiC whiskers. It appears as though voids are

initiating at these cracks in the SiC whiskers. Voids can also be observed along the SiC-Al interface as observed in Figures 6a, 6b, and 6d at the corners and along the edges of the whiskers. Deformation contours and dislocations also appear to be emanating from the stress concentration of the SiC whisker corners in Figure 6a. Finally, precipitates can be seen in the aluminum matrix as dark slanted lines. These are either Θ or S' particles, which typically have a platelet shape, appearing on edge in Figures 6a and 6c.

3.4   PHASE IDENTIFICATION

X-ray diffraction was performed to identify the existing phases present in the 2124+SiC$_w$ and unreinforced 2124 specimens analyzed. Scans were performed on a Siemens D5000 θ-θ system using copper Kα radiation and a position sensitive detector. The scans were performed using a count rate of 200 seconds per step, at a step size of 0.02° 2θ over the 2θ angular range of 15°-140°. The position sensitive detector produced measurable diffraction peaks from the precipitates and second phases formed with good signal-to-noise ratios. Peak locations and integrated intensities were identified using the peak fitting routine on the Siemens software, which uses the Pearson VII technique. Phases were identified by comparing the experimentally determined 2θ peak locations to theoretical peak locations based on known structures and atom positions of possible phases present. (Villars & Calvert, 1985)

X-ray diffraction scans were performed on 2124+SiC$_w$ and unreinforced 2124 in the as-received condition (T4 temper). X-ray diffraction scans on the as-received materials are shown in Figure 7 to demonstrate the differences between the unreinforced 2124 and the 2124+SiC$_w$. Typically, Θ', which is a metastable precipitate, is formed at room temperature in 2XXX series alloys after the solutionizing heat treatment. Other precipitates form in 2XXX series alloys during artificial aging, and coherent Θ' precipitates tend to transform into the equilibrium non-coherent Θ phase, depending on

the temperature of the aging and on the proportions of alloy additions in the alloy. (Mondolfo, 1976; Starke, 1989) The composite material has an increased amount of silicon in solution due to some dissolution of the SiC whiskers and SiO_2 contaminants during the composite manufacturing process. (Rack, 1988) The aluminum-silicon binary phase diagram shown in Figure 8 reveals that these two elements exhibit complete solid solubility over most of the composition range shown. (Moffatt, 1977; Mondolfo, 1976) Although aluminum does not form silicides, the presence of silicon in solid solution with the aluminum may favor formation of silicides with alloying additions instead of the anticipated precipitate phases in the absence of the silicon. Therefore, the precipitates in the unreinforced alloy may not be expected to be the same precipitates that form in the composite after exposure to elevated temperatures. In addition, the high state of localized stress and stress concentrations about the SiC whiskers may provide more sites for heterogeneous nucleation of precipitates in the composite material. (Zhao & Huang, 1989)

Several post-creep and post-aging specimens of unreinforced 2124 and 2124+SiC_w were also examined using x-ray diffraction to identify phases which were precipitated during the exposure to creep conditions. All of the conditions which were examined are shown in Table 2a. Figure 9 shows the scans performed on 2124+SiC_w after 143 hours at 350°F with zero, 25, and 35 ksi applied load. In addition, the as-received 2124+SiC_w data are shown in Figure 9 for comparison.   Peak identification was used to determine which precipitate phases were present in the different specimens examined. Scans were performed on various specimens with different exposure temperatures and stresses to determine the effects of temperature and/or stress on the precipitation in these materials. In addition, line broadening was studied by examining the full width at half maximum and the $K\alpha_1$-$K\alpha_2$ peak resolution at high 2θ angle peaks for aluminum. This was done to understand how the aluminum lattice was affected by the different temperature and stress combinations applied for long periods of time.

3.5   TENSILE TESTS

Tensile tests were performed on unreinforced 2124 and on 2124+SiC$_w$, following guidelines in ASTM Standard E8-91. Tensile tests were performed using a screw-driven Instron machine and a hydraulically actuated MTS tensile testing machine, both at a constant strain rate of 0.005 in/min. Data were taken every 0.5 seconds and recorded in a file on an IBM computer. The specimens were machined per ASTM Standard E8-91 for subsize tensile specimens with a gage length of 1.0 inch. The reduced cross-section was nominally 0.25 inch wide by 0.0525 inch thick. Specimens were gripped using serrated wedge grips with two alignment pins in a tapered clevis. The specimens and grip assembly were heated in a forced air oven. Two thermocouples were attached to the grips near the specimen to monitor the temperature. The oven heating rate was set so that the temperature would reach the test temperature in one hour. Prior to initiating the tensile test, the temperature was allowed to equilibrate between the control thermocouple in air and the thermocouples on the specimen by soaking for 30 minutes after heating to the test temperature.   The temperature and overshoot was controlled to within ±5°F for the isothermal soak and tensile test.

Specimens were instrumented with back-to-back strain gages in the longitudinal direction. The strain gages, type WK-13-125AD-350 from Micromeasurements, Inc., were specifically selected to match the coefficient of thermal expansion of the aluminum matrix to minimize temperature effects. The strain gages were rated to temperatures up to 500°F and were attached to the specimens using M600 epoxy with an elevated temperature cure to minimize creeping of the adhesive during the tensile test.   The maximum strain measurable was approximately 0.02 inch. These strain gages did not measure total elongation to failure, but gave an accurate measure of strain for determining the modulus, yield point, and shape of the stress-strain relationships for the unreinforced 2124 and the 2124+SiC$_w$.

Tensile tests were performed at room temperature and at 250°F, 300°F, 350°F, 400°F,

450°F, and 500°F. A typical stress-strain relationship for $2124+SiC_w$ at 300°F is shown in Figure 10. Typical tensile data for the unreinforced 2124 at room temperature is shown in Figure 11. These two figures include the 0.02% offset construction for determining the yield strength. Individual stress-strain data for each test temperature performed in this study are in Appendix B. In some tests, back-to-back MTS extensometers were also attached to the specimens in addition to the strain gages. These extensometers were used to determine the total elongation to failure. The strain in Figure 10 is based on the average of back-to-back strain gages. Since the strain gages fail at higher strains, this figure only includes data up to the failure of the strain gages. The strain in Figure 11 is based upon the average of back-to-back extensometers, so the ultimate tensile strength and total elongation to failure is also captured in this data. Note that not all of the tests were conducted using extensometers, so the total elongation was not obtained accurately for all of the tests.

Raw data voltages from the test instrumentation (strain gages and load cell) were converted to engineering units of stress and strain, based on the gage factors for the strain gages, the calibration factor for the load cell, and the initial cross-sectional area of the reduced section on the specimen. Calculation of the tensile test information was performed per ASTM Standard E8-91. All calculation of tensile information, ultimate tensile strength, proportional limit, yield strength, modulus of elasticity, and total elongation to failure, were performed in Symphony, version 2.0 on an IBM PC. These values are shown for the unreinforced 2124 in Table 3 and for $2124+SiC_w$ in Table 4 for each test conducted.

The ultimate tensile strength is defined as the maximum stress achieved in the test. The ultimate tensile strength of the reinforced and unreinforced alloy tested was determined by taking the maximum load measured in the test divided by the initial cross-sectional area of the specimen. This is the engineering stress, not the true stress. There was little difference between the engineering and true stresses due to the low ductility and imperceptible reduction in area measured for the reinforced material. (Dieter, 1986;

Hertzberg, 1989)   The effect of temperature on the ultimate tensile strength of unreinforced 2124 and 2124+SiC$_w$ is shown in Figure 12.

The proportional limit is identified as the stress where the stress-strain relationship first deviates from linearity. The proportional limit was determined by superimposing a line having identical slope to the modulus of elasticity on the stress-strain relationship. The value of the proportional limit was taken as the last point before the constructed line and the stress-strain relationship diverge. (Dieter, 1986; Hertzberg, 1989) The effect of the test temperature on the proportional limit is shown in Figure 13.

The yield strength is defined as the stress at which plastic deformation begins, nominally taken as the 0.02% offset stress. The 0.02% offset yield strength was calculated by constructing a line parallel to the elastic region of the stress-strain relationship, offset by 0.02% strain. The yield strength was identified as the stress at which the constructed line intersects the stress-strain data. (Dieter, 1986; Hertzberg, 1989) The effect of the test temperature on the 0.02% offset yield strength for unreinforced 2124 and 2124+SiC$_w$ is shown in Figure 14.

The modulus of elasticity is defined as the slope of the elastic portion of the stress-strain relationship, which is typically linear. The modulus was calculated by performing a linear regression using the method of least squares on the linear portion of the stress-strain relationship.   No preload was used, so the modulus was calculated starting at the origin and using data to the proportional limit. (Dieter, 1986; Hertzberg, 1989) The standard deviation and the goodness-of-fit (r^2) statistics were also calculated from the experimental data set. These values are shown in Tables 3 and 4 for each test conducted. The effect of temperature on the modulus for the unreinforced 2124 and 2124+SiC$_w$ is shown in Figure 15.

Total elongation to failure could not be determined from the strain gages because they failed before reaching the end of the test. However, strain measurements were made using strain gages because they are more accurate, and are therefore better suited for calculating the modulus of elasticity. The total elongation to failure was taken to be the

final strain value before the specimen failed, on specimens tested using back-to-back MTS extensometers. This combines the elastic and the plastic portions of the strain.

The data points shown in Figures 12 through 15 are the arithmetic means of the tests performed at each temperature. Error bars shown in Figures 12 through 15 are the range of data acquired during the testing to demonstrate the amount of scatter and variability in the measured properties. Data for each specimen are shown in Tables 3 and 4 for the unreinforced 2124 and 2124+SiC$_w$ respectively.

The ultimate tensile strengths at the different test temperatures for the 2124+SiC$_w$ were used to identify the stress levels for the creep tests. Tensile and creep properties of the unreinforced alloy, fabricated using the same procedures as the composite, were measured in order to have direct comparability of data. The tensile strengths measured for the unreinforced 2124 tested in this study are statistically significantly lower than the handbook data on 2124 ingot included in Table 3 for reference. (Lampman, Zorc, et al., Eds., 1990)

Except for some room temperature tensile tests, all specimens were tested parallel to the extrusion (longitudinal) direction. Since this material was cross-rolled to achieve planar isotropy, similar properties were anticipated in the transverse direction as well. A few tests were performed on transverse specimens to compare the different directions and to measure the effectiveness of the cross-rolling technique to achieve planar isotropy. There was statistically no difference measured in the tensile properties in either unreinforced or composite specimens tested, as seen by comparing the data shown in Tables 3 and 4 respectively.

3.6 CREEP TESTS

Creep tests were conducted on SATEC Model D creep frames, with Applied Test Systems model 2691 three-zone clamshell furnaces controlled by a Micricon

programmable PID temperature controller. The creep frames were used with a 3:1 lever arm ratio. The specimens were the same as for the tensile testing: ASTM subsize dogbone specimens with a gage length of 1.00 inch, gage width of 0.25 inch, and nominal thickness of 0.0525 inch. (ASTM Standard-E8-91) The specimen was centered in the center zone of the furnace to maintain a constant temperature along the gage length of the specimen. Thermocouples to monitor the specimen temperature throughout the creep test were attached to the top and the bottom of the specimen using aluminum tape. The specimens were gripped using wedge grips in a clevis assembly. The wedge grips had two 0.125-inch diameter alignment pins in the grip area to ensure proper alignment and unidirectional loading of the specimen during the tests.

The specimens were instrumented with back-to-back strain gages, type WK-13-125AD-350 manufactured by Micromeasurements, Inc. The strain gages were specifically selected to have a coefficient of thermal expansion approximately equal to that of aluminum, and have temperature compensation built in to minimize the effect of the elevated temperatures on the electronic signals. The strain gages were also selected because of their design for use at temperatures up to 500°F without degradation of their strain-measuring capabilities. The primary reason for using strain gages is the fact that they do not add significant load to the specimen as is the case with the transducer-type extensometers typically used for creep testing. Also, some of the strains were anticipated to be small, and traditional mechanical extensometry with transducers extended below the furnace is not as sensitive in the expected strain range. Alignment of mechanical extensometers on the small creep specimens is also difficult, and alignment is critical in acquiring good quality data with transducer-type extensometers.

Miniature load cells made by Interface with a 1000-pound capacity were placed in line in the load train to measure the load throughout the creep test. Although the creep tests were dead weight loaded, load cell data was used to identify the point at which all of the load was applied to the specimen to identify the true start of the creep test. This is important in identifying the primary creep regime as well as for comparison between the

reinforced and unreinforced materials. The load cells were also used to identify the exact time of failure for those tests that proceeded into tertiary creep and creep rupture.

The creep tests were conducted using the following procedure, which is primarily based on the standard practice described in ASTM E139-83(1990). First, the specimen was loaded to the full creep weight at room temperature to seat the specimen in the wedge grips and to check the instrumentation to ensure it was working properly. The specimen was centered in the center zone of the three-zone furnace. The lever arm was leveled at this point by adjusting the front crosshead height. The specimen was then unloaded, leaving a nominal weight (5-10 pounds) on the specimen to keep the load train in tension during the heating of the furnace. Due to the thermal mass of the furnace, two to three hours were required to stabilize the specimen temperature. The temperature overshoot was less than 5°F with PID tuning. The specimen was allowed to stabilize at the test temperature, then was slowly loaded by lowering the elevator beneath the load pan. The lever arm was again checked with a level and adjusted as necessary using the front crosshead height adjustment. Data was taken at five-second intervals during the loading and unloading at room temperature and during the loading at the test temperature. Data were taken every ten minutes during the heating. During the first few hours of the creep test, data was collected every 30 seconds to capture the shape of the initial stages of the primary creep. After this initial period, the data rate was slowed to 15-minute intervals to reduce the size of the data file. Data were taken and stored in an IBM compatible computer, then transferred into Symphony for data reduction after the tests were complete.

Some creep tests were stopped after a given length of time, instead of continuing the tests until creep rupture occurred. Typically this length of time was approximately 140 hours (6 days), when the specimen was believed to have entered steady-state creep. Other specimens were allowed to continue through tertiary creep to rupture. The minimum creep rate was measured as the minimum rate established during the test -- in some cases, the minimum creep rate reported may not be the true steady-state creep rate because the

creep rate was continuing to decrease up to the point where the tests were terminated. This would be a conservative measure of creep rate, since the rates reported would always err on the high side, given the nature of typical creep behavior. The minimum creep rate for each specimen is included on the plots of the creep data shown in Appendix C, and is also shown in Table 5 for the unreinforced 2124 and Table 6 for the 2124+SiC$_w$.

Some early tests resulted in specimens breaking at the alignment pinhole, due to improper gripping of the wedges in front of the alignment pins. This invalidated the data from those tests because the specimens were being loaded locally at a higher stress than in the gage section. These data were discarded and not used in any of the analyses performed.

Creep tests were conducted on the 2124+SiC$_w$ at temperatures between 200°F and 500°F, at every 50°F increment. Stress levels at any given temperature did not exceed 50% of the ultimate tensile strength at that temperature for the 2124+SiC$_w$. Other stress levels were selected to provide tests at several temperatures and the same stress levels, and at several stress levels at the same temperature in order to generate creep information and for use with the predictive models. The stress levels were as follows: 10, 17, 20, 25, 35, and 37 ksi. To reduce the size of the test matrix and maximize the amount of information to be acquired with a limited number of specimens, not all of the stress levels were tested at all of the temperatures. Due to limitations in the availability of the unreinforced 2124 material, creep tests were conducted at fewer temperatures and stresses. All test conditions are shown in the test matrix in Tables 2c and 2d.

The creep data were converted from the raw voltage signals to engineering units by the data acquisition system. These conversions were periodically checked to ensure proper conversion of the data. The thermocouple data were examined to ensure that the temperature on the specimen remained constant throughout the entire creep test. The equations relating the thermal output of the strain gages and the gage factor to the test temperature were provided with the strain gages. This information was used in conjunction with the specimen temperature from the thermocouples to correct for the

thermal response of the strain gages. A copy of this information sheet is shown in Figure 16. The front and back strain gage data were averaged to eliminate any anomalies in the data as a result of bending in the specimen. In general, the differences between the front and back strain gages were minimal, except for the initial zero point. The strain measured at the first point at which the entire load was applied was subtracted from all subsequent strain gage data to determine the strain solely due to creep in the specimens. This also helped to eliminate apparent strain as a result of slight differences in the coefficients of thermal expansion between the aluminum specimen and the polymer foil strain gages.

Once the raw data were converted into engineering units and normalized to the starting conditions of the creep test, the data were plotted on a linear scale using the creep strain on the ordinate, and the time on the abscissa. Representative creep curves for unreinforced 2124 and 2124+SiC$_w$ are shown in Figures 17 through 24. Individual creep curves for each test conducted are shown in Appendix C. The graphs were examined to identify the linear portion which indicates a minimum or steady-state creep rate. The minimum creep rate was calculated by performing a least squares linear regression to the data along the portion of the creep relationship in which the data was linear at the lowest slope. Linear regressions were performed over several different ranges to identify the minimum creep rate. The r^2 goodness-of-fit and error bars for the slopes were also calculated with the linear regression. All data points were used without applying smoothing techniques to the data sets which demonstrated random line fluxuations and noise. The electronic noise in the data acquisition system was on the order of ±0.075 millivolts, which corresponds to a measured strain value of ±0.000025 in/in (25 microstrain). This noise was a much more significant problem in tests at low temperatures (see curves shown at 250°F and 37 ksi in Figure 17) and low stresses because the strain levels being measured were so small. Since the noise was random, performing the linear regression through the entire data was used in lieu of significant alterations to the data to artificially remove the noise. The slopes calculated for these

data sets appear to be reasonable, and fit with the observed trends in other data sets which did not exhibit significant noise problems. However, the regression statistics calculated were poor for these tests with significant noise because most of the data lay above and below the regression line. The calculated slopes were superimposed on the creep relationships to identify the portion of the creep data used to calculate the minimum creep rates. Tables 5 and 6 contain data from each creep test on the unreinforced 2124 and the 2124+SiC$_w$ respectively.

DISCUSSION OF RESULTS

4.1   MICROSTRUCTURAL ANALYSIS

Microstructural evaluation and x-ray diffraction analyses were used to characterize the as-received microstructure.   The silicon carbide whisker reinforced 2124 has a significantly smaller grain structure than the unreinforced 2124, indicating that under similar processing procedures, the presence of the silicon carbide whiskers helps to refine the grain size by preventing grain growth during the solutionizing and subsequent hot pressing and hot rolling processes. This finer grain size can improve the tensile strength of the material, but can also be a potential problem in creep. In the latter stages of creep and at relatively high temperatures (as compared to the material's melting temperature) creep is facilitated by grain boundary diffusion and eventually grain boundary sliding. (Garafalo, 1965; Hertzberg, 1989) Since the 2124+SiC$_w$ composite material has a finer grain size than the unreinforced 2124, there is significantly more grain boundary area to assist with these creep deformation mechanisms in the composite. The unknown in this case is the effect of the silicon carbide whiskers. One of the objectives of this research is to determine what the effect of the silicon carbide whiskers is on the creep properties of unreinforced 2124.   The improvements due to load transfer to the silicon carbide whiskers may offset the detriment of the finer grain size in the composite.

The silicon carbide does not have an effect on the starting precipitates in the 2124

matrix, as identified by x-ray diffraction scans shown in Figure 7. In the as-received condition, both unreinforced and composite materials contained Θ' Al_2Cu particles and Al_7Cu_2Fe, Mg_2Si, and $(Al,Si)_{19}Mn_4$ intermetallic particles, in addition to large undissolved particles which were not reabsorbed during solutionizing. These constituent particles are copper-rich phases, as determined by XDS in the SEM; the specific phase was not identified. These large undissolved constituent particles are undesirable because they can cause high strains in the matrix alloy, thereby initiating cracks from the induced strain field leading to premature failure under tension. Also, these particles demonstrate brittle fracture when stressed, (as shown in the tensile fracture surface for $2124+SiC_w$ in Figure 25), thus introducing a crack which can subsequently propagate into the matrix.

After thermal exposure to either aging or creep, changes in the precipitation were identified in the 2124 unreinforced alloy as well as the $2124+SiC_w$ composite. The post-creep exposure specimens demonstrate a higher state of stress than the aged coupons, as evidenced by the broadening of the aluminum (422) peak (Figure 9). For the specimens exposed to creep conditions at any of the creep temperatures, the peaks were significantly broader and the $K\alpha_1$-$K\alpha_2$ splitting was less defined than that for coupons exposed only to elevated temperatures without stress. This was true for both unreinforced 2124 and $2124+SiC_w$ specimens examined using x-ray diffraction. In addition, the post-exposure x-ray diffraction scans (Figure 9) show evidence of precipitate formation, thereby verifying that this alloy is not thermally stable. Figure 9 shows x-ray diffraction data for as-received $2124+SiC_w$, in addition to $2124+SiC_w$ exposed to 350°F for 143 hours with no stress (aging) and with 25 and 35 ksi (creep). This figure reveals that the Al_7Cu_2Fe, Mg_2Si, and $(Al,Si)_{19}Mn_4$ phases are still present after aging and creep. In addition, some of the Θ' (Al_2Cu) phase remained after the thermal exposure, and S' (Al_2CuMg) is also precipitating out during the thermal exposures. The S' phase was more prevalent at the exposures at higher temperatures (350°F and above), and was not observed in the specimens exposed at 250°F either with or without stress. The precipitation of S' occurs at the elevated temperatures in both aging and creep specimens, but may be enhanced

further by the applied stress in creep. Recall that some creep mechanisms occur by atom and vacancy diffusion. (Garafalo, 1965; Hertzberg, 1989) However, it is not anticipated that this caused significant changes in the creep properties of this material. Larson and Miller concluded that the creep modes are not directly affected by precipitation, or by precipitate coarsening or redistribution. (Larson & Miller, 1952)

4.2   TENSILE DATA

The addition of silicon carbide whiskers improved the tensile strength and modulus of the unreinforced 2124. At room temperature, the strength and modulus of the 2124+SiC$_w$ were significantly higher than for the unreinforced alloy. Addition of 15 vol% of silicon carbide whiskers increased the ultimate tensile strength of the unreinforced 2124 by 25%, from 61 ksi to 76 ksi. This is a direct result of the 2124 matrix alloy transferring load to the silicon carbide whisker strengthening phase. The modulus of elasticity was also enhanced 25% over the unreinforced 2124 by the addition of the silicon carbide whiskers.

The increase in properties due to the addition of silicon carbide whiskers is significant, but not as large an improvement as could have been realized. Notice the ultimate and yield strengths of the unreinforced 2124 measured in these tests are below handbook data reported in the ASM Metals Handbook, and shown in Table 3 for comparison purposes. (Lampman, Zorc, et al., Eds., 1990) This is a result of the powder metallurgy process and the quality of the alloy powders used to produce both the reinforced and the unreinforced alloys tested in this study. The lower strengths are partially attributed to the large copper-rich constituent particles observed in the micrographs creating failure initiation locations. The surface of the fracture specimens substantiate this; numerous constituent particles were observed on the fracture surface of the tensile specimens, as seen in Figure 25. In several cases, the constituent particles were located in the bottom of a ductile dimple, and were often cracked. This brittle phase is attributed to reducing

the strengths of both the unreinforced 2124 powder metallurgy alloy and the 2124+SiC$_w$ composite by serving as a crack initiation site.

The processing used was successful at achieving planar isotropy. Although there appears to be a preferential orientation of whiskers in the composite (Figure 4a), visual examination of the higher magnification (Figure 4b) and the SEM image (Figure 5) show that there is fairly random orientation of the whiskers. The data in Tables 3 and 4 show that there was no significant difference between the longitudinal and transverse tensile properties.

Figure 12 shows the ultimate tensile strength of both the unreinforced 2124 and 2124+SiC$_w$ as a function of the test temperature, from room temperature up to 500°F. The ultimate tensile strength decreases for both the unreinforced 2124 and the 2124+SiC$_w$ composite with increasing temperature. This decrease proceeds in a smooth relationship as the test temperature increases. Furthermore, the rate of decrease increases at an accelerating rate with the increasing temperature such that the reduction in ultimate tensile strength is substantial at 500°F. This trend is generally true for both unreinforced and composite materials. However, at higher temperatures, the composite appears to lose strength faster than the unreinforced alloy, such that the strength of the composite ends up approaching the ultimate tensile strength of the unreinforced alloy at 500°F. The strengthening effect of the silicon carbide whiskers is thus more significant at lower temperatures. At 500°F, the whiskers are apparently of little benefit to the ultimate tensile strength of the composite.

Figures 13 and 14 show the proportional limit and the yield strength of both the unreinforced 2124 and the 2124+SiC$_w$ as a function of the test temperature from room temperature up to 500°F. The effect of temperature on the 0.2% offset yield strength and the proportional limit is not as substantial as it is on the ultimate tensile strength. Both the yield strength and the proportional limit decrease at elevated temperatures, but the rate of decrease is much smaller and more gradual than with the ultimate tensile strength. Again, this trend is generally true for both the unreinforced 2124 and the 2124+SiC$_w$.

The temperature affects the modulus of elasticity in a similar fashion to the yield strength and proportional limit. In Figure 15, the modulus of the composite remains higher than for the unreinforced alloy over the entire temperature range tested. For both reinforced and unreinforced alloys, the modulus remains fairly constant up to about 350°F and then decreases at higher temperatures. However, unlike the ultimate tensile strength, the ratio of the composite modulus to the unreinforced modulus remains approximately constant over the entire temperature range. This would seem to indicate that the active mechanism causing the reduction in the strength is not as effective at causing changes in the modulus.

4.3 CREEP

The individual creep curves from each test performed (Appendix C) show the creep strain as a function of time for a variety of different temperatures and stress levels. In addition, Figures 17 through 24 show representative creep curves for several different temperatures and stress levels for both unreinforced 2124 and 2124+SiC$_w$. The tertiary creep stage was not captured well in these tests because this is the stage where localized deformation occurs, typically by necking. Since the strain shown was measured using strain gages, the non-uniform tertiary creep strain was not captured when necking occurred in a region outside of where the strain gages were located on the specimen. However, the strain gages were able to successfully capture the uniform strain (up through the "steady-state" regime) very well.

The unreinforced 2124 demonstrated short primary and steady-state regimes, and a longer tertiary regime, as shown in Figure 18. Addition of the silicon carbide whiskers increased the length of the primary regime as compared to the unreinforced alloy. The 2124+SiC$_w$ did not demonstrate a linear steady-state regime; rather it demonstrated a long primary creep that gradually made a transition directly into a longer tertiary regime. This

type of behavior has been documented before. (McLean, 1988; Nieh, 1984; Nieh, Xia & Langdon, 1988) As was discussed in the Introduction, it is still valid to use these data in conventional creep analyses. Instead of using the slope of the linear steady-state regime, the minimum creep rate can be used, and the secondary creep regime is considered to cover the range of data where the creep rate falls within 10% of the minimum creep rate.

For both the unreinforced 2124 and 2124+SiC$_w$, as the temperature and stress increase, the amount of primary creep strain measured also increases. (See Figures 21 through 24.) Also at the higher temperatures and stresses, the primary creep made a transition into steady state creep faster, and has a higher steady-state creep rate than tests conducted at lower temperatures and stresses. However, for the same temperature and stress level, as shown for 350°F and 25 ksi (Figure 18) and 500°F and 17 ksi (Figure 19), the creep curve for unreinforced 2124 is shifted towards significantly shorter times and smaller strains as compared to 2124+SiC$_w$. The primary regime for the composite tended to last for significantly longer times and higher strains than for comparable temperatures and stresses for the unreinforced alloy. In addition, for similar temperatures and applied stresses, the 2124+SiC$_w$ exhibited creep strain rates similar or slightly higher than the minimum creep rate determined for the unreinforced 2124.

This may not be an entirely valid comparison, since the strength and stiffness of the composite is significantly enhanced by the presence of the silicon carbide whiskers. Therefore, comparisons are also made for relative values, normalizing the applied stress level in the creep tests to the ultimate tensile strength of the material being tested. This allows the comparison of the two materials on a more even basis, looking at the percentage of the tensile strengths of the two materials rather than the absolute applied stress. Comparing, then, by the ratio of the applied stress to the ultimate tensile strength of the material at the chosen test temperature, yields an interesting point. Although the total accumulated strains are significantly larger for the total creep curve in the composite than for the unreinforced alloy, the minimum creep rates determined are nearly an order

of magnitude smaller for the unreinforced 2124 than for the 2124+SiC_w. (See Figure 20, at 350°F and a stress ratio of 0.5.) Also, for those tests which terminated in creep rupture, the time to rupture was not significantly different between the reinforced and unreinforced alloys.

Creep curves are shown in Appendix C for all tests performed. Tables 5 and 6 contain summaries of all of the creep data determined from each specimen tested. The unreinforced alloy demonstrated different creep characteristics and properties than ingot metallurgy 2124 as compared to data found in ASM Metals Handbook. (See Table 3.) This is primarily due to the powder metallurgy processing used in the production of this unreinforced alloy tested.

The general equation relating steady-state creep to temperature and stress also incorporates a number of material and structure factors. This equation is based on a model of stress and diffusion-assisted dislocation motion in a three-dimensional substructure: (Dieter, 1986)

$$\dot{\varepsilon}_{ss} = \frac{16 \ \pi^3 \ c_j \ D_v \ G \ b}{k \ T} \left(\frac{\sigma}{G} \right)^n \tag{4}$$

where $\dot{\varepsilon}_{ss}$ is the steady-state creep rate, c_j is the concentration of dislocation jogs, D_v is the bulk or lattice self-diffusion coefficient, G is the shear modulus, b is the burgers vector of the dislocation, k is Boltzmann's constant, T is the absolute temperature, σ is the applied stress, and n is the creep stress exponent. According to Equation (4), almost all of the strain is due to dislocation glide, but the rate-limiting factor is dislocation climb around an obstacle. Since dislocation climb requires either atom or vacancy diffusion, the rate controlling step is atomic diffusion. (Dieter, 1986) This power law relation can be simplified to its more common form, repeated below, but also shown in the introduction as Equation (1):

$$\dot{\varepsilon}_{ss} = A_1 \; \sigma^n \; e^{-\left(\frac{Q_{app}}{RT}\right)} \tag{1}$$

where $\dot{\varepsilon}_{ss}$ is the steady-state creep rate, A_1 is a constant for all stresses and temperatures, σ is the applied stress, n is the creep stress exponent, Q_{app} is the apparent activation energy for creep, R is the universal gas constant, and T is the absolute creep test temperature. Many different mechanisms may be interacting to cause the observed Q_{app}, but cannot be separated out strictly on the experimental data collected. Therefore, the activation energy is designated as the apparent activation energy because it is empirically determined.

The stress exponent can be calculated directly, although a graphical representation is easier to understand. By plotting the logarithm of the minimum creep strain rate on the ordinate, against the logarithm of the applied stress on the abscissa, isothermal plots will plot as straight lines for simple power law creep. The slope of these lines is the creep exponent, n.

Since the 2124+SiC$_w$ did not exhibit classic steady-state creep, the minimum creep rate was used to determine the creep stress exponent, n, and the apparent activation energy for creep, Q_{app}. The minimum creep regime of the creep curve appears to behave like simple power law creep with no threshold stress. The stress exponent was determined by plotting the logarithm of the minimum creep strain rate on the ordinate, against the logarithm of the applied stress on the abscissa. (See Figures 26 and 27.) For the unreinforced alloy (Figure 27), the creep stress exponent was determined to be 2.76 at 350°F and 7.54 at 500°F. The creep stress exponent for the reinforced alloy (Figure 26) was also determined to be a function of temperature: at 250°F, n was calculated to be 2.00, which increased to a value of 6.99 at 500°F. The values for n as well as error bars and goodness of fit statistics from the least squares linear regression fit to the data are shown in Table 7. Plotting the creep stress exponent as a function of test temperature,

shown in Figures 28 and 29, the relationship between the two variables can be quantified by an empirical curve fit. The 2124+SiC$_w$ data appears to behave linearly (Figure 28), but the unreinforced 2124 does not (Figure 29). Examining the curve fitting statistics of different functions reveals that both the unreinforced 2124 and the 2124+SiC$_w$ best fit a linear relationship, although the fit for the unreinforced 2124 has large error bars due to fitting a limited number of data points. The equation developed to relate stress exponent to test temperature for the silicon carbide whisker reinforced 2124 is:

$$n_{2124+SiC_w} = 0.021 \cdot T - 3.71 \tag{5}$$

where $n_{2124+SiCw}$ is the stress exponent for the composite, and T is the creep test temperature in °F. Examination of the calculated error bars reveals that the corresponding linear equation developed for the unreinforced 2124 is not statistically significantly different from that developed for the 2124+SiC$_w$:

$$n_{UR\ 2124} = 0.028 \cdot T - 5.99 \tag{6}$$

where $n_{UR\ 2124}$ is the stress exponent for the unreinforced 2124, and T is the creep test temperature in °F. These values for stress exponent are comparable to values reported in the literature for similar materials. (Krajewski, Allison & Jones, 1993; Park, Mohamed & Lavernia, 1988)

Using the empirical values determined for n, it is possible to identify the existence of a threshold stress. The threshold stress is defined as a stress level below which no creep occurs at a given temperature. Substituting a correction to account for a threshold stress in Equation (1) results in the following equation:

$$\dot{\varepsilon}_{ss} = A \ (\ \sigma - \sigma_{th}\ )^n \ e^{-\left(\frac{Q}{R\,T}\right)} \tag{7}$$

where $\dot{\varepsilon}_{ss}$ is the steady-state creep rate, A is a constant for all stresses and temperatures, σ is the applied stress, σ_{th} is the threshold stress, n is the creep stress exponent, Q is the activation energy for creep, R is the universal gas constant, and T is the absolute creep test temperature. The existence of a threshold stress can be verified graphically and the threshold stress determined by plotting isothermal lines of the minimum creep rate to the *1/n* power versus the applied stress, on a bilinear plot. It can be seen that when $\dot{\varepsilon}_{ss}^{1/n}$ is equal to zero, the applied stress is equal to the threshold stress. Extrapolating the data back to the stress axis where the strain rate is equal to zero results in the threshold stress for that particular temperature. If the threshold stress is calculated to be zero or negative, the material does not demonstrate the existence of a threshold stress. (Cadek & Sustek, 1993, Dieter, 1986; Mishra & Pandey, 1990)

Figure 30 shows the plot of minimum creep strain rate to the *1/n* power as a function of stress for the 2124+SiC$_w$ composite. The isothermal lines all extrapolate back to zero or negative stress values, which indicates for the composite that no threshold stress exists. Likewise, Figure 31 shows the plot of minimum creep strain rate to the *1/n* power as a function of stress for the unreinforced 2124. It can be seen that extrapolating these data back to the x-axis produces a zero intercept, and therefore indicates there is no threshold stress in the unreinforced material. This is reasonable, because typically the stress exponent will appear inflated when a threshold stress exists. The typical range of stress exponent values is 3 to 8 for metallic materials. When a threshold stress exists, the stress exponent can reach values near 40. (Nardone & Tien, 1986)

The activation energy for creep can be determined three different ways. The first method is to use the creep stress exponents determined above, then the activation energy is calculated directly from experimental parameters using Equation (1). This method will

yield the apparent activation energy, Q_{app}, and will magnify any errors or uncertainties introduced when determining the creep stress exponent. Second, Q_{app} can be determined graphically by plotting the natural logarithm of the minimum creep rate on the ordinate against the inverse of the absolute temperature on the abscissa. The slope of the isostress lines is equal to $-Q_{app}/R$, where R is the universal gas constant. The third method for evaluating the activation energy for creep uses a modulus-compensated stress. This method calculates the activation energy by normalizing the stress by the shear modulus at the test temperature, which recognizes the effect of temperature on the modulus of the material. This too can magnify uncertainties introduced in the determination of the stress exponent, but yields a value for the true activation energy for creep, Q_c, instead of Q_{app}. Making this substitution yields the following equation:

$$\dot{\varepsilon}_{ss} = A_2 \left(\frac{\sigma}{E(T)}\right)^n \cdot e^{-\left(\frac{Q_c}{RT}\right)} \tag{8}$$

where $\dot{\varepsilon}_{ss}$ is the steady-state creep rate, A_2 is a constant for all stresses and temperatures, σ is the applied stress, $E(T)$ is the temperature-dependent elastic modulus, n is the creep stress exponent, Q_c is the true activation energy for creep, R is the universal gas constant, and T is the absolute creep test temperature. In Equation (8), A_2 is a different constant from A_1 in Equation (1) because it incorporates the factor related to the modulus as a function of temperature. The true activation energy for creep, Q_c, can be defined as:

$$Q_c = -R \left(\frac{\partial \ln \dot{\varepsilon}_{ss}}{\partial \left(\frac{1}{T}\right)}\right)_\sigma - n\,R \left(\frac{\partial \ln E(T)}{\partial \left(\frac{1}{T}\right)}\right) \tag{9}$$

This equation can also be written as:

$$Q_c = Q_{app} + Q_E \tag{10}$$

in which the apparent activation energy, Q_{app}, becomes:

$$Q_{app} = -R \left(\frac{\partial \ln \dot{\varepsilon}_{ss}}{\partial \left(\frac{1}{T} \right)} \right)_\sigma \tag{11}$$

and the contribution of the change in the modulus as a function of the exposure temperature, Q_E, is defined as:

$$Q_E = -n\ R \left(\frac{\partial \ln E(T)}{\partial \left(\frac{1}{T} \right)} \right) \tag{12}$$

In Equation (9), notice that the first term is the Q_{app} from Equation (1), which is now corrected by the variations in the modulus with temperature. If the temperature effect on the modulus is small, then this term, Q_E, is quite small and can be assumed to be equal to zero. In this case, Equation (8) is simplified to its more common form, shown as Equation (1). Sherby (Sherby, 1968) has shown that this analysis is valid for pure metals and many alloys. It has been proposed that this analysis is also valid for dispersion-strengthened alloys. (Cadek & Sustek, 1993; Lund & Nix, 1975)

The activation energies, calculated using all three methods described above, are shown in Table 8 for the unreinforced and reinforced alloys. The values shown for all three methods of calculating activation energy are within the error of calculation or

measurement, and therefore are not significantly different. Since activation energies calculated using three independent methods provided similar results, this adds confidence to the values determined. The similarity in activation energies calculated by different methods also indicates that there is not a significant effect on the creep properties due to the temperature dependence of the modulus of elasticity.

In general, the activation energy for creep was lower for the $2124+SiC_w$ than for the unreinforced alloy. In addition, the activation energy for creep was determined to increase with increasing temperature and stress, in both the unreinforced 2124 and the $2124+SiC_w$. This observation is consistent with activation energies reported in the literature for similar discontinuously reinforced aluminum alloys. (Barth, Morton & Tien, 1990; Morimoto, Taya, Yamaoka & Lilholt, 1988; Nardone & Strife, 1987; Nieh, 1984) This increase in temperature and stress apparently activates additional deformation mechanisms such that the rate-controlling mechanism shifts from grain boundary diffusion to lattice diffusion within the range of parameters tested. The controlling creep deformation mechanisms, either grain boundary diffusion at the lower temperatures and stresses or lattice diffusion at the higher temperatures and stresses, also correlate well with the creep mechanisms as shown in the creep deforation map for aluminum. (See Figure 3.)

The activation energy for creep determined by plotting the natural logarithm of the minimum creep rate on the ordinate against the inverse of the absolute temperature on the abscissa is shown in Figures 32 and 33. The reinforced data (Figure 32) exhibited a break in the isostress lines, which is an indication that the apparent activation energy for creep is changing, possibly due to a change in creep mechanisms. (Lund & Nix, 1975) The first slope, over the lower temperature ranges, was similar to that of pipe diffusion in aluminum, approximately 23 kcal/mol in the lower temperature regime. Pipe diffusion, or grain boundary diffusion, is typically associated with dislocation glide, and is more common at lower temperatures. (Lund & Nix, 1975) The second slope, over the higher portion of the temperature range tested, was steeper than the first, resulting in a higher

activation energy. This second slope for the $2124+SiC_w$ was comparable to the activation energies determined for the unreinforced 2124, which were near or above the activation energy for self-diffusion in pure aluminum (approximately 35 kcal/mol). The activation energy for self-diffusion does not change significantly with the addition of alloying elements. This mechanism is associated with dislocation climb, because diffusion of vacancies or atoms is required to facilitate the climbing mechanism. At higher temperatures when dislocations begin to climb more easily, annihilation of dislocations also becomes more common. (Lund & Nix, 1975)

The mechanisms described above, as related to the activation energies calculated, can be compared to those identified from a creep deformation mechanism map for aluminum. Examining the creep deformation map for pure aluminum shown in Figure 3, the temperature and stress levels used in this program fall within the power law creep region of the deformation mechanisms map. (Frost & Ashby, 1982) The low temperature, low stress region is typically controlled by dislocation creep in which dislocation glide is aided by vacancy diffusion. This includes creep mechanisms such as Coble creep at the lower temperatures, and Nabarro-Herring creep at the higher temperatures. Coble creep is grain boundary diffusion, and is the primary mechanism active at lower temperatures. Since these materials are powder metallurgy alloys with fine grain sizes, there is a significant amount of grain boundary area for grain boundary diffusion (Coble creep) to occur. At temperatures closer to the melting temperature of the material, Nabarro-Herring creep becomes active. Nabarro-Herring creep is controlled by lattice diffusion, where vacancies drift from grain boundaries in compression to grain boundaries in tension. The atoms diffuse in the opposite direction, towards the grain boundaries in compression. This eventually results in elongation of the grains which is measured as creep. (Garafalo, 1965; Hertzberg, 1989)

In the $2124+SiC_w$, it is assumed that all of the creep will occur in the 2124 matrix in the temperature regime tested. As far as the dislocations are concerned, the silicon carbide whiskers are large and far apart, which will not significantly impede dislocation

motion directly. However, the whiskers do act as dislocation sources, producing high dislocation densities in the aluminum matrix due the coefficient of thermal expansion mismatch. The presence of the silicon carbide whiskers also effectively reduces the stress on the aluminum matrix because the 2124 matrix transfers the stress to the whiskers via shear mechanisms.

In summary, there is evidence from several different portions of this creep study to indicate that the creep is progressing by atom migration or diffusion. First, the x-ray diffraction data shows evidence of precipitation occurring during creep in the creep specimens. The atoms must migrate to enable this precipitation. Second, the calculated activation energies for creep are approximately the same as for self-diffusion in aluminum for the unreinforced 2124. In the $2124+SiC_w$, the calculated activation energies for creep are approximately equal to the activation energy for pipe diffusion at the lower temperatures tested, and slightly higher than the activation energy for self-diffusion over the higher temperatures tested. These activation energies indicate not only the potential creep mechanisms, but also a change in the mechanisms for the $2124+SiC_w$ over the temperature and stress range tested. Finally, these data are consistent with deformation maps and information found in the literature.

4.4   PREDICTIVE CREEP MODELS

The empirical creep data was fit using two different predictive creep models. This is desirable to allow extrapolation of the data to longer times with more certainty, and interpolation between test conditions to determine creep parameters at any temperature or stress within a reasonable proximity of the experimental envelope. The unreinforced 2124 and the $2124+SiC_w$ data generated under this research program were first fit using the Larson-Miller parameter. The Larson-Miller parameter was selected first because it is traditionally the most widely used parameter for creep. To determine the Larson-Miller

constant, isostress lines were plotted on a log-time or log-rate scale as a function of the inverse of the absolute temperature. The data did not converge to a point on the ordinate axis for either material as required by Equation (2). Rather, when the lines were extrapolated to the ordinate axis, they were actually diverging instead of converging to a single point. (See Figures 34 and 35 for 2124+SiC$_w$ and unreinforced 2124 respectively.) As a result, this method was not considered to be accurate at predicting the creep data for this material system because the data did not fit the model. The creep data could be predicted using the general value of 20 for the Larson-Miller constant, but this approach would introduce more error and uncertainty in the creep data than if a constant were determined using the method described above had been used.

Therefore, another creep parametric model was examined. The Manson-Haferd parameter is defined in the introduction by Equation (3), and is repeated below:

$$P_{M\text{-}H} = \frac{(T - T_a)}{(\log t - \log t_a)} = constant \tag{3}$$

where T is the absolute creep temperature, T_a is the Manson-Haferd temperature constant, t is time, and t_a is the Manson-Haferd time constant. The time used in Equation (3) can either be the time to creep rupture, or the time to a given creep strain level. The Manson-Haferd model uses a similar premise as the Larson-Miller approach, except that the isostress lines are plotted on a log-time or log-rate scale as a function of absolute temperature instead of the inverse of absolute temperature. When the 2124+SiC$_w$ data was plotted in this fashion, the data converged to nearly a single point, as shown in Figures 36 and 38. Figures 37 and 39 show the unreinforced 2124 data, which behaved in a similar fashion to the 2124+SiC$_w$. The Manson-Haferd constants T_a and either t_a or r_a are derived graphically from the intersection point of extrapolated isostress lines when plotted on a log-time or log-rate scale versus absolute temperature (instead of the inverse

of temperature, which is used in the Larson-Miller parameter). With this data set, the isostress lines converged to a single point, but the intersections of the different lines did not all occur at precisely the same point. Therefore, the Manson-Haferd parameters T_a and either t_a or r_a were determined by taking the arithmetic mean of the intersection points for each combination of paired isostress lines. The Manson-Haferd parameters calculated for the time to 0.05% creep strain and for the minimum creep rate are shown in Table 9 for both materials tested, along with calculations of the associated error bars.

Once the Manson-Haferd parameters were determined, the master curve could be developed based on the relationship shown in Equation (3). The Manson-Haferd parameter is plotted versus the applied stress. The resulting curve is called a master curve because all of the data collapses onto a single curve, regardless of the test parameters. This curve can be used to predict any creep value, assuming conditions for two of the three unknowns (stress, temperature, and either strain rate or time to a given percent strain). The amount of strain is fixed to the experimental data and is the basis for selecting the times or rates used in developing this curve.

Figure 40 shows the master curves determined for 2124+SiC$_w$ and unreinforced 2124, based on the time required to reach 0.05% creep strain. Notice that all of the creep data for the reinforced alloy collapse onto a single curve. In addition, all of the unreinforced alloy also fall along a single curve, which lies below that of the reinforced data. This entire curve is derived from the experimental data and can be used to predict parameters. Using this curve and Equation (3), and knowing two of the three parameters (temperature, stress, or time to 0.05% percent strain) the third can be determined. (Manson & Haferd, 1953)

Once the master curves were generated, all of the "normalized" creep data in the master curves were fit to generate an empirical relationship relating rate, stress, and temperature in one equation. The Manson-Haferd master curves based on the time to 0.05% creep strain data for both the unreinforced 2124 and 2124+SiC$_w$ were best fit using a hyperbolic equation. Initially, these equations were developed fitting the applied stress

to the Manson-Haferd parameter. The equations shown below have further substituted the empirical relationship on which the Manson-Haferd parameter is based in order to develop an equation based strictly on the creep parameters of temperature, stress, and time to 0.05% permanent creep strain. The resulting relationship developed for unreinforced 2124 is shown below in Equation (13):

$$P_{M\text{-}H} = \frac{(T + 459.69 - 367)}{(\log t_{0.05\%} - 12.30)} = \frac{-35.15 \cdot \sigma}{-3.682 + \sigma} \tag{13}$$

where $P_{M\text{-}H}$ is the Manson-Haferd parameter for the time to 0.05% creep strain in the unreinforced 2124, T is the creep test temperature, °F, $t_{0.05\%}$ is the time to 0.05% creep strain, hours, and σ is the applied creep stress, ksi. The corresponding equation developed based entirely on the times to 0.05% creep strain for 2124+SiC$_w$ is shown below in Equation (14):

$$P_{M\text{-}H} = \frac{(T + 459.69 - 736)}{(\log t_{0.05\%} - 3.05)} = \frac{-34.71 \cdot \sigma}{-5.914 + \sigma} \tag{14}$$

where $P_{M\text{-}H}$ is the Manson-Haferd parameter for the time to 0.05% creep strain in the 2124+SiC$_w$, T is the creep test temperature, °F, $t_{0.05\%}$ is the time to 0.05% creep strain, hours, and σ is the applied creep stress, ksi.

Equations (13) and (14) compile all of the creep data collected in this study and combine it into a form that is easily understood and used. This tool can be used by designers to determine creep values, to adjust the stress and/or temperature on a given part to avoid exceeding a creep design allowable, or to determine a lifetime based on creep. These equations are also effective for predicting maximum stress levels for design,

if the design temperature and lifetime are known. In addition, the lifetime of the material can be accurately predicted if the design temperatures and stresses are stipulated. If time to a different percent creep strain is desired, the creep data can be reanalyzed to develop the appropriate equations for the desired maximum creep strain. Either using the master curve or an empirical curve fit to the master curve would work for these predictions. However, use of the master curve may be safer because limits to the extrapolations can be built into the limits of the stress axis on the curve shown. If the equations fit to the master curves are used instead of the master curves, then the limitations on extrapolating data must accompany the equations. This will prevent extrapolation of data far beyond the temperature and stress ranges used to develop the master curve, or extrapolating the time to 0.05% creep strain more than two orders of magnitude from the longest tests included in this data set.

Of less interest to aircraft designers, but significantly more important for the materials engineers are the master curves developed based on the minimum creep rate. The minimum creep rate contains information such as the stress exponent and the activation energy for creep, when used in conjunction with the power law equation. The Manson-Haferd parametric method was also used to extrapolate the minimum creep rate instead of time to a given percent creep strain. In this case, the t and t_a are replaced with $\dot{\varepsilon}_{min}$ (or $\dot{\varepsilon}_{ss}$) and r_a in Equation (3). The data were well-behaved enough to determine the Manson-Haferd constants, r_a and T_a. Using these constants, a master curve was developed using the entire experimental data set, shown in Figure 41. Even data not used to calculate the Manson-Haferd constants fell along a single curve.

The Manson-Haferd master curves based on the minimum creep rate data for both the unreinforced 2124 and 2124+SiC$_w$ were best fit using an exponential decay equation. The equations shown below incorporate the basis for the Manson-Haferd parameter, resulting in an empirical equation relating the creep parameters of temperature, stress, and minimum creep rate. The relationship developed for unreinforced 2124 is shown below in Equation (15):

$$P_{M-H} = \frac{(T + 459.69 - 728)}{(\log \dot{\varepsilon}_{min} + 11.59)} = 123.7 \; e^{\, (-0.0536 \; \sigma)} \tag{15}$$

where P_{M-H} is the Manson-Haferd parameter for the unreinforced 2124 minimum creep rate, T is the creep test temperature, °F, $\dot{\varepsilon}_{min}$ is the minimum creep rate, in/in/sec, and σ is the applied creep stress, ksi. The corresponding equation developed based entirely on the 2124+SiC$_w$ creep data is shown below in Equation (16):

$$P_{M-H} = \frac{(T + 459.69 - 559)}{(\log \dot{\varepsilon}_{min} + 13.68)}$$
$$= 140.9 \; e^{\, (-0.2112 \; \sigma)} + 64.88 \; e^{\, (-0.0108 \; \sigma)} \tag{16}$$

where P_{M-H} is the Manson-Haferd parameter for the 2124+SiC$_w$ minimum creep rate, T is the creep test temperature, °F, $\dot{\varepsilon}_{min}$ is the minimum creep rate, in/in/sec, and σ is the applied creep stress, ksi.

Empirical Equations (15) and (16) can be used to extrapolate creep data within the boundaries of the experimental data on which the equations were based. Data should not be extrapolated significantly beyond the temperatures and stresses used in the experimental data set, and creep rates should not be extrapolated more than two orders of magnitude from what was actually measured.

Using Equations (15) and (16), the minimum creep rates were predicted for unreinforced 2124 and 2124+SiC$_w$ for the range of temperatures and stresses tested. These data were then used to predict the creep stress exponent, n, at different temperatures, and the activation energy for creep, Q_{app}, at different stress levels. The predicted values for n are shown in Table 10 in comparison to the values empirically

determined based on the slopes of isothermal lines on a log minimum creep rate versus log stress plot. Two of the predicted values for the unreinforced 2124 are within the margin of error calculated for the creep stress exponents determined using conventional creep analysis. There is a large deviation between the empirical and predicted stress exponents for the unreinforced 2124 at 400°F. The empirical value was determined to be 6.94, while the predicted value was only 3.43. However, these data are based upon a very small sample of specimens, and are therefore susceptible to a large amount of scatter. Comparison of the values for *n* predicted for 2124+SiC$_w$ with the slopes of the log minimum creep rate versus log stress shows that most of the values are within the error bars for the empirically determined values of stress exponent. The predicted stress exponents are plotted along with the experimental data in Figures 42 and 43, to demonstrate graphically the excellent agreement between the predicted and experimental data. The predicted *n* values are also shown as a function of temperature, in comparison to the experimentally determined values in Figures 44 and 45. The Manson-Haferd results predict a straight line correlation of stress exponent as a function of temperature, although the slope is a little different from that determined experimentally.

The Manson-Haferd method was also able to accurately predict the activation energy slopes, as well as the change in slopes resulting from the change in deformation mechanisms, as shown in Figures 46 and 47. Again using Equations (15) and (16), the minimum creep rates were predicted, then apparent activation energies were predicted based upon the slope of the natural log of the minimum creep rate versus the inverse of the absolute temperature. The predicted values for Q_{app} are shown in Table 11 in comparison to the empirical slopes shown in Table 8 (method 2). As was the case with the stress exponent data, the predicted values for the unreinforced 2124 show generally good agreement with the experimental data. The activation energy predicted at 10 ksi was significantly different from the experimental value. This error is considered an anomaly due to the limited number of tests performed on the unreinforced 2124 material. For the 2124+SiC$_w$, the predicted values generally fall within the error bars for the

experimentally determined activation energies.

These excellent correlations between empirical data and predicted values demonstrate the suitability of using the Manson-Haferd technique for predicting creep properties. This proves that the use of conventional creep analysis such as the power law equation in conjunction with the Manson-Haferd parameter is suitable for application with the non-conventional discontinuously reinforced 2124+SiC$_w$ composite data.

CONCLUSIONS

1. Creep in P/M 2124+SiC$_w$ and unreinforced 2124 can be analyzed using the Manson-Haferd parametric model developed for standard metals and alloys.

2. Conventional creep analysis and Manson-Haferd analysis compare well. Except for the highest temperature tested, the predicted steady-state creep rates agree well with experimentally determined values.

3. Manson-Haferd model prediction of time to 0.05% creep strain correlates well with experimental data. Manson-Haferd parameter proves useful for predicting creep parameters (time to a given percent creep strain) and creep rate (to determine other creep properties such as creep stress exponent and activation energy) for 2124+SiC$_w$.

4. Creep stress exponents for 2124+SiC$_w$ and unreinforced 2124 indicate power law creep with no threshold stress for the temperature and stress range tested.

5. At higher stresses and temperatures, the activation energy for creep for both the unreinforced 2124 and the 2124+SiC$_w$ indicates lattice (self) diffusion is the creep deformation rate-controlling process. At lower temperatures and stresses, the activation energy for creep for the 2124+SiC$_w$ indicates grain boundary (pipe) diffusion may be the creep deformation rate-controlling process.

6. Creep of 2124+SiC$_w$ exhibits primary creep over significantly longer times and higher strains than unreinforced 2124.

REFERENCES

Annual Book of ASTM Standards, Vol. 03.01, Standard # E 8-91, "Test Methods of Tension Testing of Metallic Materials," 1991.

Annual Book of ASTM Standards, Vol. 03.01, Standard # E 139-83(1990), "Practice for Conducting Creep, Creep-Rupture, and Stress-Rupture Tests of Metallic Materials," 1990.

Arsenault, R. J. (1991). Strengthening and deformation mechanisms of discontinuous metal matrix composites. In Strength of Metals and Alloys, 1, (pp. 31-46). London: Freung Publishing House, Ltd.

Arzt, E., & Wilkinson, D. S. (1986). Threshold stresses for dislocation climb over hard particles : the effect of an attractive interaction. Acta Metallurgica, 34, 1893-1898.

Barth, E. P., Morton, J. T., & Tien, J. K. (1990). Threshold for creep resistance in a silicon carbide reinforced aluminum alloy. In M. N. Gungor & P. K. Liaw (Eds.), Fundamental Relationships Between Microstructure and Mechanical Properties of Metal-Matrix Composites (pp. 839-846). Warrendale, PA: The Metallurgical Society.

Birt, M. J., & Johnson, W. S. (1990). Characterization of the tensile and microstructural properties of an aluminum metal matrix composite. In M. N. Gungor & P. K. Liaw (Eds.), Fundamental Relationships Between Microstructure and Mechanical Properties of Metal-Matrix Composites (pp. 71-88). Warrendale, PA: The Metallurgical Society.

Brewer, W. D., & Sarkar, B. (1984). Directionality of mechanical and microstructural properties of extruded and rolled 2124 PM aluminum alloy and SiC whisker reinforced 2124 aluminum composites. Metal Matrix, Carbon, and SiC Composites (NASA CP 2357, pp. 25-41). Hampton, VA: National Aeronautics and Space Administration.

Brown, K. M., Brewer, W. D., & Hendricks, R. W. (1990). X-ray diffraction measurements of residual stresses in SiC/Ti composites. In M. N. Gungor & P. K. Liaw (Eds.), Fundamental Relationships Between Microstructure and Mechanical Properties of Metal-Matrix Composites (pp. 269-286). Warrendale, PA: The Metallurgical Society.

Budinski, K. G. (1983). Engineering Materials : Properties and Selection (2nd ed.). Reston, VA: Reston Publishing Co., Inc.

Cadek, J., & Sustek, V. (1993). Comment on "creep behavior of discontinuous SiC-Al composites." Scripta Metallurgica, 29, 1397-1401.

Cao, L., Jiang, C. P., Wang, B., Geng, L., Yao, C. K., & Lei, T. C. (1988). The fracture processes of SiC_w/Al composites. Proceedings of the MRS International Meeting on Advanced Materials, 4, 59-66.

Collins, J. A. (1981). Failure of Materials in Mechanical Design (pp. 31-32, 435-478). New York: John Wiley & Sons, Inc.

Davies, P. W., Evans, W. J., Williams, K. R., & Wilshire, B. (1969). An equation to represent strain/time relationships during high temperature creep. Scripta Metallurgica, 3, 671-674.

Dieter, G. E. (1986). Mechanical Metallurgy (3rd ed., pp. 275-334, 432-470). New York: McGraw-Hill Book Co.

Divecha, A. P., & Fishman, S. G. (1980). Progress in the development of SiC/Al alloys. In Proceedings of the 12th National SAMPE Technical Conference, 656-663.

Divecha, A. P., Fishman, S. G., & Karmarkar, S. D. (1981). Silicon carbide reinforced aluminum - a formable composite. Journal of Metals, 12-17.

Dvorak, G. J., & Goodman, E. C. (1982). Static and fatigue testing of 2024 Al-SiC (F-9) T-4. In Proceedings of the ASME Winter Annual Meeting (ASME Paper 82-WA/AERO-2). Fairfield, NJ: American Society of Mechanical Engineers.

Frost, H. J., & Ashby, M. F. (1982). Deformation-Mechanism Maps : The Plasticity and Creep of Metals and Ceramics (pp. 1-5, 20-29). Oxford: Pergamon Press.

Garafalo, F. (1965). Fundamentals of Creep and Creep-Rupture in Metals. New York: The Macmillan Company.

Ghahremani, F. (1980). Effect of grain boundary sliding on steady creep of polycrystals. <u>International Journal of Solids and Structures, 16,</u> 847-862.

Gilman, P. S. (1991). Discontinuously reinforced aluminum : ready for the 1990s. <u>Journal of Metals,</u> (8) 7.

Hamilton, E. (1942). <u>Mythology</u> (p. 193). Boston: Little, Brown and Company.

Harpur, N. F. (1967). Concorde structural development. <u>Journal of Aircraft, 5,</u> 176-183.

Hertzberg, R. W. (1989). <u>Deformation and Fracture Mechanics of Engineering Materials</u> (3rd ed., pp. 145-192). New York: John Wiley & Sons, Inc.

House, M. B., Meinert, K. C., & Bhagat, R. B. (1991). The aging response and creep of DRA composites. <u>Journal of Metals,</u> (8) 24-28.

Hyatt, M. V., & Axter, S. E. (1991). Aluminum alloy development for subsonic and supersonic aircraft. In <u>Science and Engineering of Light Metals</u> (pp. 273-280). Tokyo: Japan Institute of Light Metals.

Jones, R. M. (1975). <u>Mechanics of Composite Materials</u> (pp. 2-3, 91). New York: Hemisphere Publishing Corporation.

Kelly, A., & Davies, G. J. (1965). The principles of the fibre reinforcement of metals. <u>Metallurgical Reviews, 10,</u> (37) 1-77.

Krajewski, P. E., Allison, J. E., & Jones, J. W. (1993). The influence of matrix microstructure and particle reinforcement on the creep behavior of 2219 aluminum. <u>Metallurgical Transactions A, 24A,</u> 2731-2741.

S. R. Lampman, T. B. Zorc, et al., (Eds.). (1990). <u>ASM Metals Handbook, 2,</u> (10th ed., pp. 70-78). Materials Park, OH: ASM International.

Larson, F. R., & Miller, J. (1952). A time-temperature relationship for rupture and creep stresses. <u>Transactions of the ASME, 74,</u> 765-775.

Lederich, R. J., & Sastry, S. M. L. (1982). Deformation behavior of silicon-carbide-whisker-reinforced aluminum composites. <u>Materials Science and Engineering, 55,</u> 143-146.

Lee, D., Vaudin, M. D., Handwerker, C. A., & Kattner, U. R. (1988). Phase stability and interface reactions in the Al-SiC system. In <u>High Temperature/High Performance Composites</u> (pp. 357-365). Pittsburgh: Materials Research Society.

Lilholt, H., & Taya, M. (1987). Creep behaviour of the metal matrix composite Al 2124 with SiC fibres. In <u>Proceedings of the 6th International Conference on Composite Materials, 2,</u> (pp. 2.234-2.244). New York: Elsevier Applied Sciences.

Lund, R. W., & Nix, W. D. (1975). On high creep activation energies for dispersion strengthened metals. <u>Metallurgical Transactions A, 6A,</u> 1329-1333.

Manson, S. S., & Haferd, A. M. (1953). <u>A Linear Time-Temperature Relation for Extrapolation of Creep and Stress-Rupture Data</u> (NACA Technical Note 2890). Hampton, VA: National Advisory Committee for Aeronautics.

McDanels, D. L. (1985). Analysis of stress-strain, fracture, and ductility behavior of aluminum matrix composites containing discontinuous silicon carbide reinforcement. <u>Metallurgical Transactions A, 16A,</u> 1105-1115.

McDanels, D. L., Serafini, T. T., & DiCarlo, J. A. (1986). Polymer, metal, and ceramic matrix composites for advanced aircraft engine applications. <u>Journal for Energy Systems, 8,</u> (1) 80-91.

McLean, M. (1988). Mechanisms and models of high temperature deformation of composites. In <u>High Temperature/High Performance Composites</u> (pp. 67-79). Pittsburgh: Materials Research Society.

Mishra, R. S., & Pandey, A. B. (1990). Some observations on the high-temperature creep behavior of 6061 Al-SiC composites. <u>Metallurgical Transactions A, 21A,</u> 2089-2090.

Moffatt, W. G. (1977). <u>The Handbook of Binary Phase Diagrams, 1.</u> Schenectady, NY: The General Electric Company.

Mondolfo, L. F. (1976). <u>Aluminum Alloys: Structure and Properties.</u> Boston: Butterworth (Publishers) Inc.

Morimoto, T., Taya, M., Yamaoka, T., & Lilholt, H. (1988). Second stage creep of SiC whisker/6061 aluminum composite at 573 K. <u>Journal of Engineering Materials and Technology, 110,</u> 70-76.

Murphy, A. J. (1972). Metals in flight. <u>Tech Air, 28,</u> 15-21.

Nardone, V. C., & Strife, J. R. (1987). Analysis of the creep behavior of silicon carbide whisker reinforced 2124 Al (T4). <u>Metallurgical Transactions A, 18A,</u> 109-114.

Nardone, V. C., & Tien, J. K. (1986). On the creep rate stress dependence of particle strengthened alloys. <u>Scripta Metallurgica, 20,</u> 797-802.

Nieh, T. G. (1984). Creep rupture of a silicon carbide reinforced aluminum composite. <u>Metallurgical Transactions A, 15A,</u> 139-146.

Nieh, T. G., Xia, K., & Langdon, T. G. (1988). Mechanical properties of discontinuous SiC reinforced aluminum composites at elevated temperatures. <u>Journal of Engineering Materials and Technology, 110,</u> 70-82.

Nutt, S. R., & Needleman, A. (1987). Void nucleation at fiber ends in Al-SiC composites. <u>Scripta Metallurgica, 21,</u> 705-710.

Orr, R. L., Sherby, O. D., & Dorn, J. E. (1954). Correlations of rupture data for metals at elevated temperatures. <u>Transactions of ASM, 46,</u> 113-128.

Papazian, J. M., & Adler, P. N. (1990). Tensile properties of short fiber-reinforced SiC/Al composites : part 1. effects of matrix precipitates. <u>Metallurgical Transactions A, 21A,</u> 401-410.

Park, K., Lavernia, E. J., & Mohamed, F. A. (1990). High temperature creep of silicon carbide particulate reinforced aluminum. <u>Acta Metallurgica, 38,</u> 2149-2159.

Park, K., Mohamed, F. A., & Lavernia, E. J. (1988). The stress dependence of creep rate in silicon carbide particulate reinforced 6061 aluminum. <u>Israel Journal of Technology, 24,</u> 369-374.

Peteves, S. D., Tambuyser, P., Helbach, P., Audier, M., Laurent, V., & Chatain, D. (1990). Microstructure and microchemistry of the Al/SiC interface. <u>Journal of Materials Science, 25,</u> 3765-3772.

Quist, W. E. (1990, November). Advanced materials for a high speed civil transport. Presented to the Capital Metals and Materials Forum, Boeing Commercial Aircraft Group, Seattle, WA.

Rack, H. J. (1988). Fabrication of high performance powder-metallurgy aluminum matrix composites. Advanced Materials and Manufacturing Processes, 3, 327-358.

Rack, H. J., Baruch, T. R., & Cook, J. L. (1982). Mechanical behavior of silicon carbide whisker reinforced aluminum alloys. In Proceedings of the Fourth International Conference on Composite Materials (pp. 1465-1472).

Reed-Hill, R. E. (1973). Physical Metallurgy Principles (2nd ed., pp. 827-887). Boston: PWS Engineering.

Rougier, M., Mace, R., Ferton, D., Sainfort, P., & Albert, D. (1993). Perspectives in the development and applications of aluminum alloys for aeronautical structures. In Materiaux Pour L'Aeronautique et L'Espace [Materials for Aeronautics and Space] (pp. 404-417). Paris: Aeronautique Espace.

Sarkar, B., Brewer, W. D., & Lisagor, W. B. (1984). Improvements in mechanical properties of SiC-whisker-reinforced aluminum composites through increased microstructural uniformity. In Proceedings of TMS-AIME Annual Meeting pp. 65-71.

Schoutens, J. E. (1981). Particulate, whisker, and fiber-reinforced metals: a comparison and discussion. (Department of Defense Metal Matrix Composites Information Analysis Center (MMCIAC) Report # MMC 063). West Lafayette, IN: Purdue University, Center for Information and Numerical Data Analysis and Synthesis (CINDAS).

Schueller, R. D., & Wawner, F. E. (1991). An analysis of high-temperature behavior of AA2124/SiC whisker composites. Composites Science and Technology, 40, 213-223.

Sertour, G. (1968). Les materiaux utilises sur Concorde [The materials used in the Concorde]. L'Aeronautique et l'Astronautique, 4, 35-51.

Sherby, O. D. (1968). Mechanical behavior of crystalline solids at elevated temperature. Progress in Materials Science, 13, (7) 325-390.

Sherby, O. D., & Burke, P. M. (1967). Mechanical Behavior of Crystalline Solids at Elevated Temperature (NASA Technical Report # SC-NGR-05-020-084). Washington DC: National Aeronautics and Space Administration.

Simon, G., & Bunsell, A. R. (1983). The creep of silicon carbide fibres. Journal of Materials Science Letters, 2, 80-82.

Starke, Jr., E. A. (1989). Heat-treatable aluminum alloys. In A. K. Vasudevan & R. D. Doherty (Eds.), <u>Treatise on Materials Science and Technology: Aluminum Alloys -- Contemporary Research and Applications, 31,</u> (pp. 35-63). Boston: Academic Press Inc.

Strangewood, M., Hippsley, C. A., & Lewandowski, J. J. (1990). Segregation to SiC/Al interfaces in Al based metal matrix composites. <u>Scripta Metallurgica, 24,</u> 1483-1487.

Suresh, S., Christman, T., & Sugimura, Y. (1989). Accelerated aging in cast Al alloy-SiC particulate composites. <u>Scripta Metallurgica, 23,</u> 1599-1602.

Sweetman, B. (1979). The next supersonic transport. <u>Flight International, 116,</u> 1772-1779.

Toaz, M. W. (1987). Discontinuous ceramic fiber MMCs. In <u>Engineered Materials Handbook: Vol. 1. Composites,</u> (pp. 903-910). Metals Park, OH: ASM International.

Villars, P., & Calvert, L. D. (1985). <u>Pearson's Handbook of Crystallographic Intermetallic Phases, 2.</u> Metals Park, OH: American Society for Metals.

Wang, J. B., Geng, L., & Yao, C. K. (1989). The fracture processes of SiC_w/Al composites. In <u>Composites Corrosion/Coating of Advanced Materials, 4,</u> (pp. 59-64). Pittsburgh: Materials Research Society.

Wilson, R. N. (1973). Creep fracture mechanisms in aluminum alloys. In <u>The Practical Implications of Fracture Mechanisms</u> (pp. 103-111). London: Institution of Metallurgists.

Yoo, Y. C., Jang, B. L., Han, H. K., & Lee, H. I. (1991). High temperature deformation behavior of SiC_w/Al 2024 composite. In <u>Strength of Metals and Alloys,1,</u> (pp. 511-518). London: Freung Publishing House, Ltd.

Zhao, X., & Huang, D. (1989). Heat-treatment strengthening effect of SiC whisker reinforced aluminum composites. In <u>Proceedings of the Seventh International Conference on Composite Materials, 1,</u> (pp. 411-416). Oxford: Pergamon Press.

TABLES

LIST OF TABLES

Table 1. Typical alloy composition ranges (values shown in weight percent). (Lampman, Zorc, et al., Eds., 1990)

Alloy	Al	Cu	Mg	Mn	Si	Fe	Zn	Ti	Cr	Other
2024	bal	3.8-4.9	1.2-1.8	0.30-0.9	0.5 max	0.50 max	0.25 max	0.15 max	0.10 max	0.05 max (each) 0.15 max (total)
2124	bal	3.8-4.9	1.2-1.8	0.30-0.9	0.20 max	0.30 max	0.25 max	0.15 max	0.10 max	0.05 max (each) 0.15 max (total)

Table 2. Test matrix for all work performed on unreinforced 2124 and 2124+SiC$_w$ in this research study. This test matrix is subdivided into three different sections: microstructural analysis and phase identification, tensile testing, and creep testing.

(a)   Microstructural Analysis and Phase Identification

X-ray diffraction scans were performed on creep and aging specimens. *(R)* indicates specimen failed in creep rupture. Otherwise, creep specimens shown were stopped in secondary creep.

Analysis Technique	Material	Condition
Optical Microscopy	unreinforced 2124	as-received
	2124+SiC$_w$	as-received
SEM / XDS	2124+SiC$_w$	as-received
TEM	2124+SiC$_w$	350°F/143 hrs/35 ksi
X-Ray Diffraction	unreinforced 2124	as-received 350°F/137 hrs/25 ksi 400°F/182 hrs/17 ksi
	2124+SiC$_w$	as-received 250°F/137 hrs/0 & 17 ksi 350°F/143 hrs/0, 25 & 35 ksi 400°F/143 hrs/17 ksi 450°F/60 hrs (R)/17 ksi 500°F/84 hrs (R)/10 ksi

Table 2. (b) Tensile Tests

Room temperature tensile tests were performed in both longitudinal *(L)* and transverse *(T)* directions, with the longitudinal direction defined as parallel to the extrusion direction. All elevated temperature tensile tests were performed only in the longitudinal direction. Specimens were held at the aging temperature less than one hour prior to performing the tensile test.

Material	Test Temperature (°F)	# of Specimens Tested
unreinforced 2124	75	2 (L), 2 (T)
	250	2
	300	2
	350	2
	400	2
	450	2
	500	2
2124+SiC$_w$	75	5 (L), 3 (T)
	250	4
	300	5
	350	5
	400	5
	450	5
	500	12

Table 2. (c) Creep Tests on Unreinforced 2124

Single specimens were tested at each of the test conditions listed below. Time indicates the time at which the test was stopped; *(R)* indicates the test was terminated by creep rupture. Stress:UTS is the ratio of the applied stress to the UTS at the given test temperature.

Material	Temperature (°F)	Stress (ksi)	Stress:UTS Ratio	Time (hrs)
unreinforced 2124	250	39	0.65	100
	350	17	0.33	142
		25	0.49	137
		25	0.49	215 (R)
		35	0.68	66 (R)
	400	17	0.36	182
		20	0.43	34 (R)
		25	0.53	20 (R)
		35	0.75	3.5 (R)
	450	10	0.24	142
	500	10	0.38	182
		17	0.65	1.7 (R)
		20	0.76	0.8 (R)

Table 2. (d) Creep Tests on 2124+SiC$_w$

Single specimens were tested at each of the test conditions listed below. Time indicates the time at which the test was stopped; *(R)* indicates the test was terminated by creep rupture. Stress:UTS is the ratio of the applied stress to the UTS at the given test temperature.

Material	Temperature (°F)	Stress (ksi)	Stress:UTS Ratio	Time (hrs)
2124+SiC$_w$	200	35	0.47	1035
	250	17	0.23	137
		35	0.47	199
		35	0.47	401
	300	25	0.35	211
	350	17	0.25	142
		17	0.25	233
		25	0.37	148
		25	0.37	286
		35	0.52	143
		35	0.52	219 (R)
	400	10	0.16	142
		10	0.16	311
		17	0.27	143
		17	0.27	231
		25	0.40	161
	450	10	0.20	143
		17	0.34	60 (R)
		25	0.50	5 (R)
	475	10	0.23	143
		17	0.40	28 (R)
	500	10	0.28	84 (R)
		14	0.39	36 (R)
		17	0.47	1.6
		20	0.56	3 (R)

Table 3. Tensile data for unreinforced 2124 alloy. Individual tests are shown, in addition to average values. *(T)* indicates transverse orientation, *(L)* or unmarked indicates longitudinal orientation.

Temp. (°F)	UTS (ksi)	0.2% YS (ksi)	Prop. Limit (ksi)	% el (%)	E (Msi)
RT *	68	47	--	19	10.5
RT (T)	63.5	41.7	--	≈20	10.7
	58.5	34.9	--	>15	9.7
avg RT (T)	61.0 ± 2.5	38.3 ± 3.4	--	>15	10.2 ± 0.5
RT (L)	61.5	38.5	--	--	10.5
	57.2	34.3	--	>15	10.1
avg RT (L)	59.3 ± 2.1	36.4 ± 2.1	--	>15	10.3 ± 0.2
250	59.3	41.3	27.6	11.2	11.8
	60.8	42.7	30.7	15.7	10.7
avg 250	60.1 ± 0.7	42.0 ± 0.7	29.1 ± 1.6	13.5 ± 2.2	11.3 ± 0.5
300	57.1	40.1	28.1	17.2	9.8
	55.3	39.5	32.2	10.9	9.9
avg 300	56.2 ± 0.9	39.8 ± 0.3	30.1 ± 2.1	14.1 ± 3.1	9.9 ± 0.1

* Data from (Lampman, Zorc, et al., Eds., 1990)

Table 3. Tensile data for unreinforced 2124 alloy (continued).

Temp. (°F)	UTS (ksi)	0.2% YS (ksi)	Prop. Limit (ksi)	% el (%)	E (Msi)
350	51.2 51.5	34.4 35.0	23.7 24.7	16.5 17.1	10.8 10.6
avg 350	51.3 ± 0.1	34.7 ± 0.3	24.2 ± 0.5	16.8 ± 0.3	10.7 ± 0.1
400	47.2 46.4	33.8 32.1	27.7 27.5	8.8 8.9	9.3 10.1
avg 400	46.8 ± 0.4	32.9 ± 0.9	27.6 ± 0.1	8.9 ± 0.1	9.7 ± 0.4
450	42.5 41.6	39.4 37.9	25.4 23.4	5.1 5.4	8.9 9.5
avg 450	42.1 ± 0.5	38.7 ± 0.7	24.4 ± 1.0	5.3 ± 0.1	9.2 ± 0.3
500	25.7 26.8	23.0 24.2	17.7 16.9	14.5 11.4	8.5 8.8
avg 500	26.3 ± 0.5	23.6 ± 0.6	17.3 ± 0.4	12.9 ± 1.5	8.7 ± 0.1

Table 4. Tensile data for 2124+SiC$_w$ composite. Individual tests are shown, in addition to average values. *(T)* indicates transverse orientation, *(L)* or unmarked indicates longitudinal orientation.

Temp. (°F)	UTS (ksi)	0.2% YS (ksi)	Prop. Limit (ksi)	% el (%)	E (Msi)
RT (T)	78.2	51.4	--	3.3	13.4
	77.0	51.9	--	4.4	12.9
	72.9	53.3	--	3.1	12.7
avg RT (T)	76.0 ± 2.8	52.2 ± 1.0	--	3.6 ± 0.7	13.0 ± 0.4
RT (L)	72.4	53.1	--	4.3	13.3
	74.4	51.6	--	7.4	12.5
	70.2	52.1	--	1.8	13.1
	78.0	57.0	--	4.0	13.1
	75.3	50.7	--	4.4	12.7
avg RT (L)	74.1 ± 2.9	52.9 ± 2.5	--	4.4 ± 2.0	12.9 ± 0.3
250	74.0	46.5	35.9	--	13.1
	74.7	46.0	34.2	--	13.1
	76.0	47.1	33.0	--	13.7
	74.7	46.6	31.6	--	13.1
avg 250	74.9 ± 0.8	46.5 ± 0.5	33.7 ± 1.8	--	13.3 ± 0.3
300	69.5	45.1	33.3	--	13.1
	71.7	46.9	33.3	--	13.2
	69.8	46.5	32.1	--	13.0
	70.8	46.7	34.8	--	13.3
	71.9	48.2	36.0	--	13.2
avg 300	70.7 ± 1.1	46.7 ± 1.1	33.9 ± 1.5	--	13.2 ± 0.1

Table 4. Tensile data for 2124+SiC$_w$ composite (continued).

Temp. (°F)	UTS (ksi)	0.2% YS (ksi)	Prop. Limit (ksi)	% el (%)	E (Msi)
350	65.7	46.4	34.6	--	12.9
	68.2	46.7	34.2	--	13.3
	66.2	46.9	35.9	--	12.8
	68.0	47.1	32.3	--	13.4
	67.3	46.6	34.8	--	13.2
avg 350	67.1 ± 1.1	46.7 ± 0.3	34.4 ± 1.3	--	13.1 ± 0.3
400	63.8	46.3	32.2	--	13.2
	68.1	46.5	33.7	--	13.1
	59.8	45.2	31.1	--	12.8
	61.2	46.0	33.2	--	12.9
	59.9	45.6	31.8	--	12.7
avg 400	62.6 ± 3.5	45.9 ± 0.5	32.4 ± 1.1	--	12.9 ± 0.2
450	50.0	44.8	31.5	--	12.2
	50.3	44.4	28.9	--	11.9
	49.9	43.4	31.9	--	11.6
	48.2	41.1	28.6	--	11.9
	51.6	44.1	31.0	--	12.1
avg 450	50.0 ± 1.2	43.6 ± 1.5	30.4 ± 1.5	--	11.9 ± 0.2

Table 4. Tensile data for 2124+SiC$_w$ composite (continued).

Temp. (°F)	UTS (ksi)	0.2% YS (ksi)	Prop. Limit (ksi)	% el (%)	E (Msi)
500	37.8	34.4	18.6	--	11.2
	39.4	36.0	15.7	--	11.3
	36.8	33.7	17.5	--	11.2
	35.6	32.4	18.2	--	11.0
	35.6	32.6	17.9	--	10.9
	35.3	31.9	16.9	--	11.0
	33.1	30.5	16.0	--	11.2
	34.4	31.4	16.8	--	11.1
	33.1	29.5	14.8	--	11.0
	36.3	33.5	18.2	--	11.3
	36.3	33.3	16.3	--	11.2
	37.2	33.7	18.4	--	11.2
avg 500	35.9 ± 1.8	32.7 ± 1.8	17.1 ± 1.2	--	11.1 ± 0.1

Table 5. Creep data for unreinforced 2124. Each line represents a single test. *Time End* is the time at which the creep test was terminated. No note beside the number indicates the test was terminated, but the specimen was still intact. *(R)* indicates the test was terminated because creep rupture occurred.

Temp. (°F)	Stress (ksi)	Stress/ UTS Ratio	Time End (hrs)	Max. Strain (%)	Min. Creep Rate (in/in/sec)	Error for Rate (in/in/sec)
250	39.2	0.65	100	0.037	1.74×10^{-10}	$\pm 2.11 \times 10^{-11}$
351	17.3	0.34	142	0.041	3.19×10^{-10}	$\pm 8.30 \times 10^{-11}$
350	24.9	0.48	137	0.091	4.44×10^{-10}	$\pm 1.57 \times 10^{-10}$
348	25.6	0.50	215 (R)	0.182	9.55×10^{-10}	$\pm 1.06 \times 10^{-10}$
355	35.5	0.69	66 (R)	0.211	2.29×10^{-9}	$\pm 8.36 \times 10^{-11}$
390	18.1	0.39	182 (R)	0.097	8.18×10^{-10}	$\pm 4.22 \times 10^{-13}$
394	20.3	0.43	34 (R)	0.058	2.40×10^{-9}	$\pm 4.99 \times 10^{-10}$
393	25.0	0.54	19.8 (R)	0.328	2.63×10^{-8}	$\pm 6.62 \times 10^{-11}$
402	35.0	0.75	3.5 (R)	0.358	9.01×10^{-8}	$\pm 9.44 \times 10^{-10}$
457	11.1	0.27	142	0.079	8.42×10^{-10}	$\pm 2.99 \times 10^{-11}$
502	10.0	0.38	182	0.512	5.98×10^{-9}	$\pm 4.54 \times 10^{-12}$
505	18.1	0.69	1.7 (R)	0.660	6.30×10^{-7}	$\pm 1.93 \times 10^{-8}$
510	19.7	0.75	0.8 (R)	0.365	8.76×10^{-7}	$\pm 2.87 \times 10^{-8}$

Table 6. Creep data for 2124+SiC$_w$ composite. Each line represents a single test. *Time End* is the time at which the creep test was terminated. No note beside the number indicates the test was terminated, but the specimen was still intact. *(R)* indicates creep rupture occurred.

Temp. (°F)	Stress (ksi)	Stress/ UTS Ratio	Time End (hrs)	Max. Strain (%)	Min. Creep Rate (in/in/sec)	Error for Rate (in/in/sec)
201	36.8	0.49	1035	0.011	6.81 x 10^{-12}	± 3.51 x 10^{-13}
246	16.9	0.23	137	0.013	1.20 x 10^{-11}	± 8.80 x 10^{-12}
258	33.0	0.44	199	0.030	6.35 x 10^{-11}	± 6.58 x 10^{-12}
249	37.2	0.50	401	0.025	4.78 x 10^{-11}	± 8.29 x 10^{-12}
302	28.7	0.37	211	0.059	1.98 x 10^{-10}	± 8.12 x 10^{-12}
348	16.8	0.25	142	0.071	4.31 x 10^{-10}	± 4.30 x 10^{-11}
352	23.6	0.35	132	0.136	1.40 x 10^{-9}	± 3.86 x 10^{-11}
333	25.1	0.37	286	0.224	1.21 x 10^{-9}	± 2.16 x 10^{-11}
349	25.2	0.37	148	0.206	2.12 x 10^{-9}	± 5.02 x 10^{-11}
354	34.6	0.52	143	0.668	9.62 x 10^{-9}	± 1.79 x 10^{-10}
350	35.5	0.53	219 (R)	1.99+	6.96 x 10^{-9}	± 1.58 x 10^{-9}
361	16.4	0.24	233	0.223	1.18 x 10^{-9}	± 3.65 x 10^{-11}
411	10.4	0.17	142	0.095	2.97 x 10^{-10}	± 2.74 x 10^{-11}
394	10.8	0.17	311	0.089	2.05 x 10^{-10}	± 7.68 x 10^{-12}
400	16.4	0.26	231	0.245	1.18 x 10^{-9}	± 3.65 x 10^{-11}
393	17.1	0.27	143	0.131	1.01 x 10^{-9}	± 4.10 x 10^{-12}
394	25.1	0.40	161	1.45	1.55 x 10^{-8}	± 2.07 x 10^{-11}

Table 6. Creep data for 2124+SiC$_w$ composite (continued).

Temp. (°F)	Stress (ksi)	Stress/ UTS Ratio	Time End (hrs)	Max. Strain (%)	Min. Creep Rate (in/in/sec)	Error for Rate (in/in/sec)
453	10.3	0.21	143	0.140	8.92×10^{-10}	$\pm 7.57 \times 10^{-11}$
451	16.6	0.33	60 (R)	0.584	1.99×10^{-8}	$\pm 8.97 \times 10^{-11}$
448	27.1	0.54	5 (R)	0.846	3.68×10^{-7}	$\pm 6.65 \times 10^{-9}$
473	10.1	0.18	143	0.236	2.16×10^{-9}	$\pm 1.18 \times 10^{-11}$
464	17.1	0.30	28 (R)	1.14	6.72×10^{-8}	$\pm 1.06 \times 10^{-10}$
488	8.5	0.24	143	0.145	1.19×10^{-9}	$\pm 6.28 \times 10^{-12}$
515	10.3	0.29	84 (R)	0.573	1.30×10^{-8}	$\pm 1.03 \times 10^{-10}$
500	13.8	0.39	36 (R)	1.07	5.21×10^{-8}	$\pm 6.00 \times 10^{-11}$
498	17.3	0.48	1.6	0.204	2.06×10^{-7}	$\pm 1.05 \times 10^{-9}$
515	19.2	0.53	3 (R)	0.955	5.89×10^{-7}	$\pm 2.11 \times 10^{-8}$

Table 7. Creep stress exponents calculated from experimental creep data (slope of isothermal lines on log strain rate vs. log stress plot).

Unreinforced 2124			
Temperature (°F)	Stress Exponent, n	r^2	# Obs
350	2.76 ± 0.81	.850	4
400	6.94 ± 0.27	.997	4
500	7.54 ± 0.42	.997	3
$2124+SiC_w$			
Temperature (°F)	Stress Exponent, n	r^2	# Obs
250	2.00 ± 0.62	.912	3
350	3.20 ± 0.68	.948	7
400	4.50 ± 0.69	.950	5
450	6.22 ± 0.16	.999	3
475	6.53	1	2
500	6.99 ± 0.67	.974	5

Table 8. Activation energy for creep as calculated (1) as calculated using the stress exponents calculated and shown in Table 7; (2) from slope of isostress lines on natural log minimum creep rate vs. inverse of absolute temperature plot; and (3) as calculated using stress normalized by the shear modulus of the material.

Stress (ksi)	Temperature Range (°F)	Activation Energy[1] (kcal/mol)	Activation Energy[2] (kcal/mol)	Activation Energy[3] (kcal/mol)
Unreinforced 2124				
10	450-500	42.4	42.4	42.8
17	350-400	27.1 ± 8.7	29.0 ± 15.3	34.8 ± 8.4
17	400-500	49.3 ± 3.3	49.4 ± 3.3	49.9 ± 3.3
25	350-400	65.6 ± 8.4	64.3 ± 13.2	72.9 ± 8.6
35	350-400	60.6	60.7	67.3
2124+SiC$_w$				
10	400-450	20.3 ± 2.5	21.7 ± 1.3	21.9 ± 3.8
10	450-500	42.3 ± 0.6	38.8 ± 16.6	42.9 ± 0.6
17	250-400	19.4 ± 4.1	20.5 ± 2.7	19.7 ± 4.1
17	400-500	47.0 ± 5.6	48.4 ± 1.9	49.2 ± 6.3
25	300-350	33.3 ± 5.0	30.0 ± 6.2	33.4 ± 5.1
25	350-450	43.2 ± 6.8	43.7 ± 3.8	44.4 ± 7.3
35	200-250	19.7 ± 1.4	20.7 ± 0.4	19.7 ± 1.4
35	250-350	33.2 ± 0.5	33.3 ± 0.7	33.4 ± 0.5

Activation energy for self (bulk) diffusion in aluminum = 35 kcal/mol
Activation energy for pipe (grain boundary) diffusion in aluminum = 23 kcal/mol

Table 9. Manson-Haferd constants for unreinforced 2124 and 2124+SiC$_w$, determined empirically based on the intersection of isostress lines on *log t$_{0.1\%}$* or *log $\dot{\varepsilon}_{ss}$* versus absolute temperature (Basis).

Material	Basis	T_a (°R)	*log t$_a$* (hrs) or *log r$_a$* (in/in/sec)
2124+SiC$_w$	time to 0.05% creep (hrs)	736 ± 9	3.05 ± 0.21
2124+SiC$_w$	minimum creep rate (in/in/sec)	559 ± 8	-13.68 ± 0.15
unreinforced 2124	time to 0.05% creep (hrs)	367 ± 43	12.30 ± 0.99
unreinforced 2124	minimum creep rate (in/in/sec)	728 ± 14	-11.59 ± 0.46

The equation defining the Manson-Haferd Parameter is:

$$P_{M-H} = \frac{(T - T_a)}{(\log t_{0.1\%} - \log t_a)} \tag{3}$$

Table 10. Creep stress exponents calculated from experimental creep data (slope of isothermal lines on log strain rate vs. log stress plot) as compared to stress exponents predicted using the Manson-Haferd parameter.

Unreinforced 2124		
Temperature (°F)	Empirical Stress Exponent, n	Manson-Haferd Stress Exponent, n_{M-H}
350	2.76 ± 0.81	3.74
400	6.94 ± 0.27	6.10
500	7.54 ± 0.42	8.00
2124+SiC$_w$		
Temperature (°F)	Empirical Stress Exponent, n	Manson-Haferd Stress Exponent, n_{M-H}
250	2.00 ± 0.62	2.88
350	3.20 ± 0.68	3.98
400	4.50 ± 0.69	4.61
450	6.22 ± 0.16	5.64
475	6.53	5.78
500	6.99 ± 0.67	7.38

Table 11. Activation energy for creep as calculated from slope of isostress lines on natural log minimum creep rate vs. inverse of absolute temperature plot. Empirical data from method *(2)* in Table 8 is shown in comparison to values predicted using the Manson-Haferd parameter.

Unreinforced 2124			
Stress (ksi)	Temperature Range (°F)	Empirical Activation Energy[2] (kcal/mol)	Manson-Haferd Activation Energy (kcal/mol)
10	450-500	42.4	17.9
17	350-400	29.0 ± 15.3	45.3
17	400-500	49.5 ± 3.3	44.1
25	350-400	64.3 ± 13.2	61.3
35	350-400	60.7	57.3
2124+SiC$_w$			
Stress (ksi)	Temperature Range (°F)	Empirical Activation Energy[2] (kcal/mol)	Manson-Haferd Activation Energy (kcal/mol)
10	400-450	21.7 ± 1.3	23.6
10	450-500	38.8 ± 16.6	27.2
17	250-400	20.5 ± 2.7	26.0
17	400-500	48.4 ± 1.9	40.8
25	300-350	30.0 ± 6.2	23.4
25	350-450	43.7 ± 3.8	41.3
35	200-250	20.7 ± 0.4	25.6
35	250-350	33.3 ± 0.7	34.6

FIGURES

LIST OF FIGURES

Figure 1. Skin temperature of a supersonic aircraft as a function of airspeed.
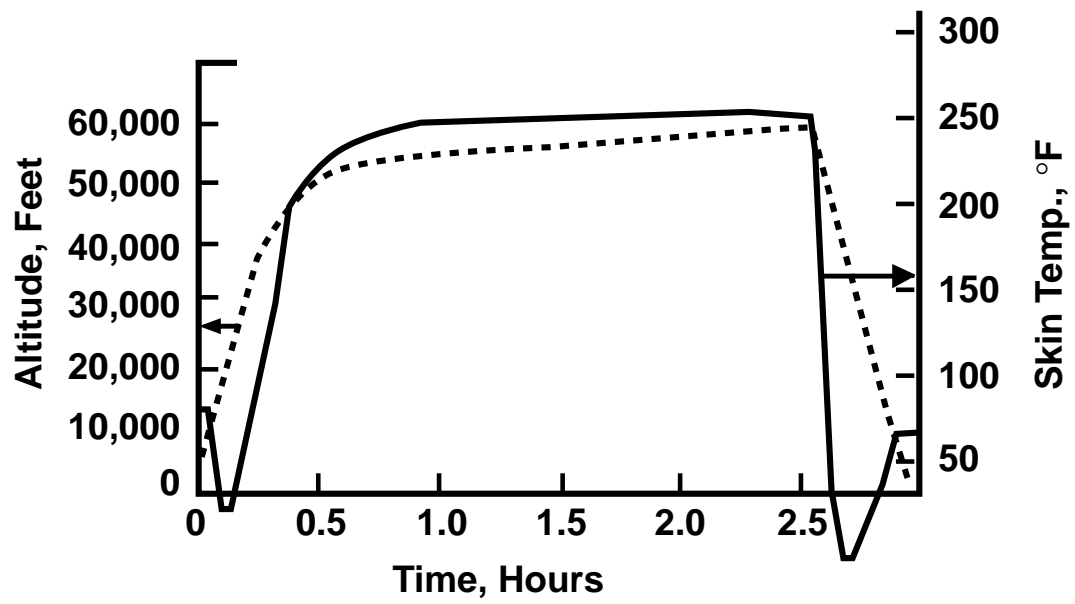
Figure 2. Thermal flight profile for a standard mission on the Concorde.
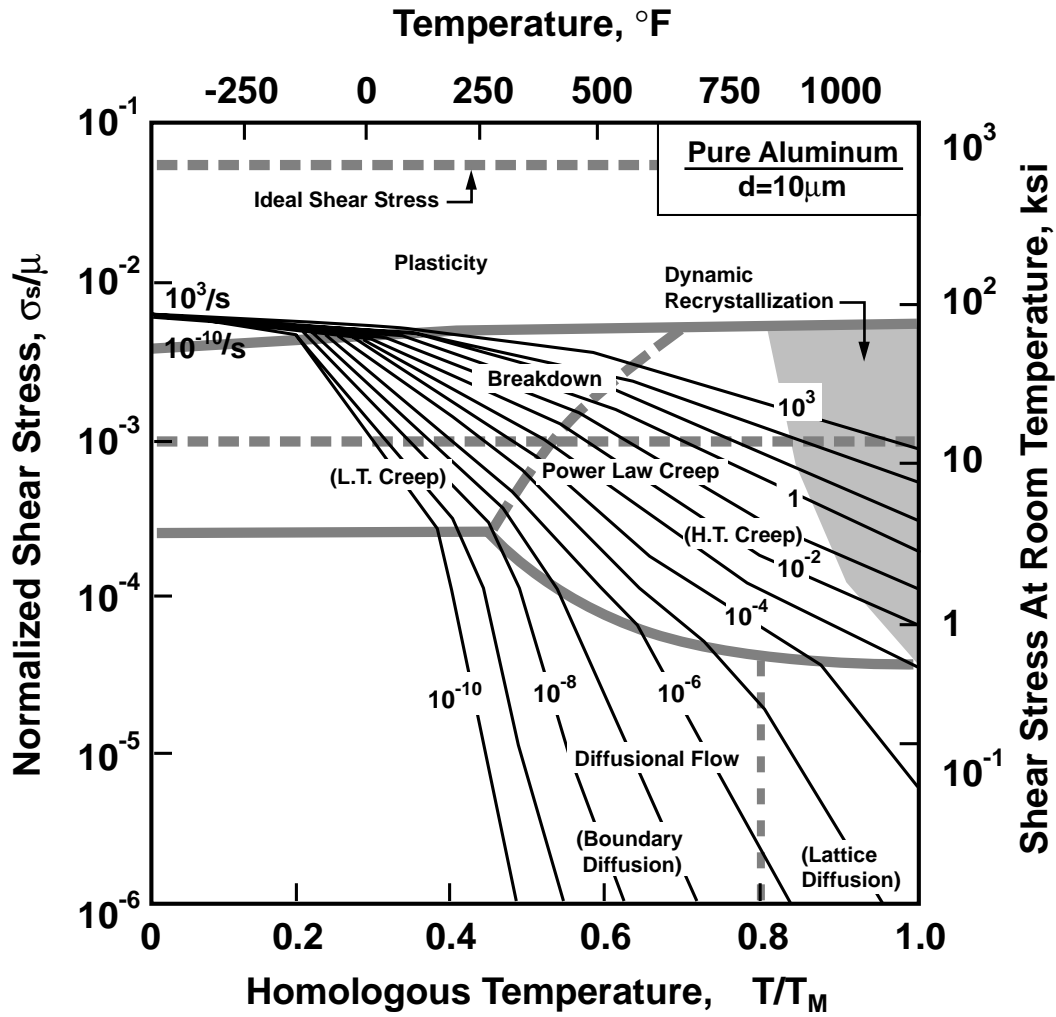
Figure 3. Creep deformation map for pure aluminum. (Frost & Ashby, 1982)
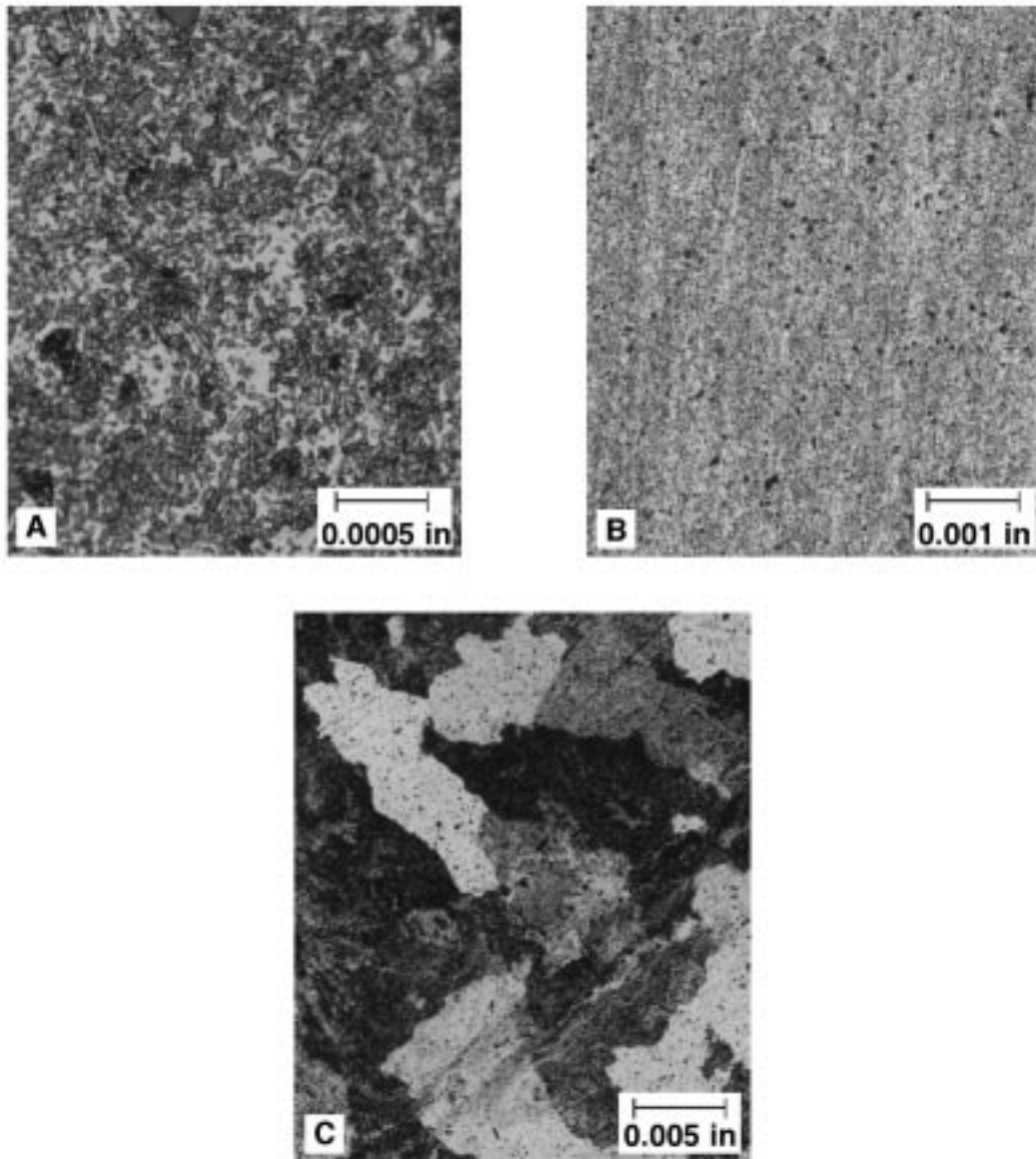
Figure 4. Optical micrographs of (a) and (b) 2124+SiCw at two different magnifications, and (c) unreinforced 2124. Shown is the L-T plane in the as-received condition, polished and chemical etched. (a) and (b) The grain size is indeterminant due to the dominance of the SiC whiskers, which are randomly oriented within the material due to cross-rolling. Some evidence of precipitates appearing as darker spots is also present. (c) Notice the grain size in the unreinforced material is clearly evident. The dark spots observed are precipitates.
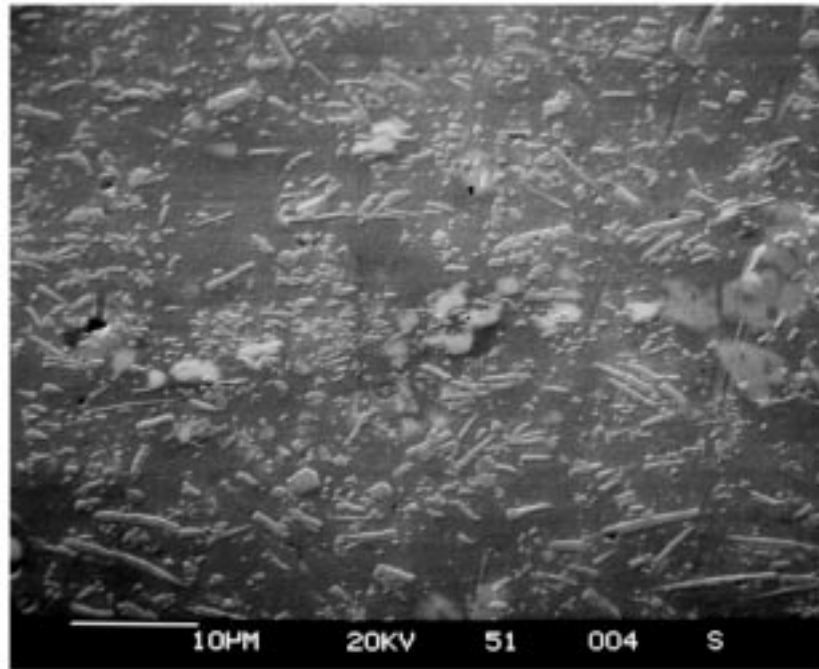
Figure 5. SEM micrograph of polished L-T cross-section of 2124+SiCw. The grains in the matrix are difficult to identify, due to the high loading fraction of silicon carbide whiskers.   Notice the random orientation and uniform distribution of whiskers throughout the material.
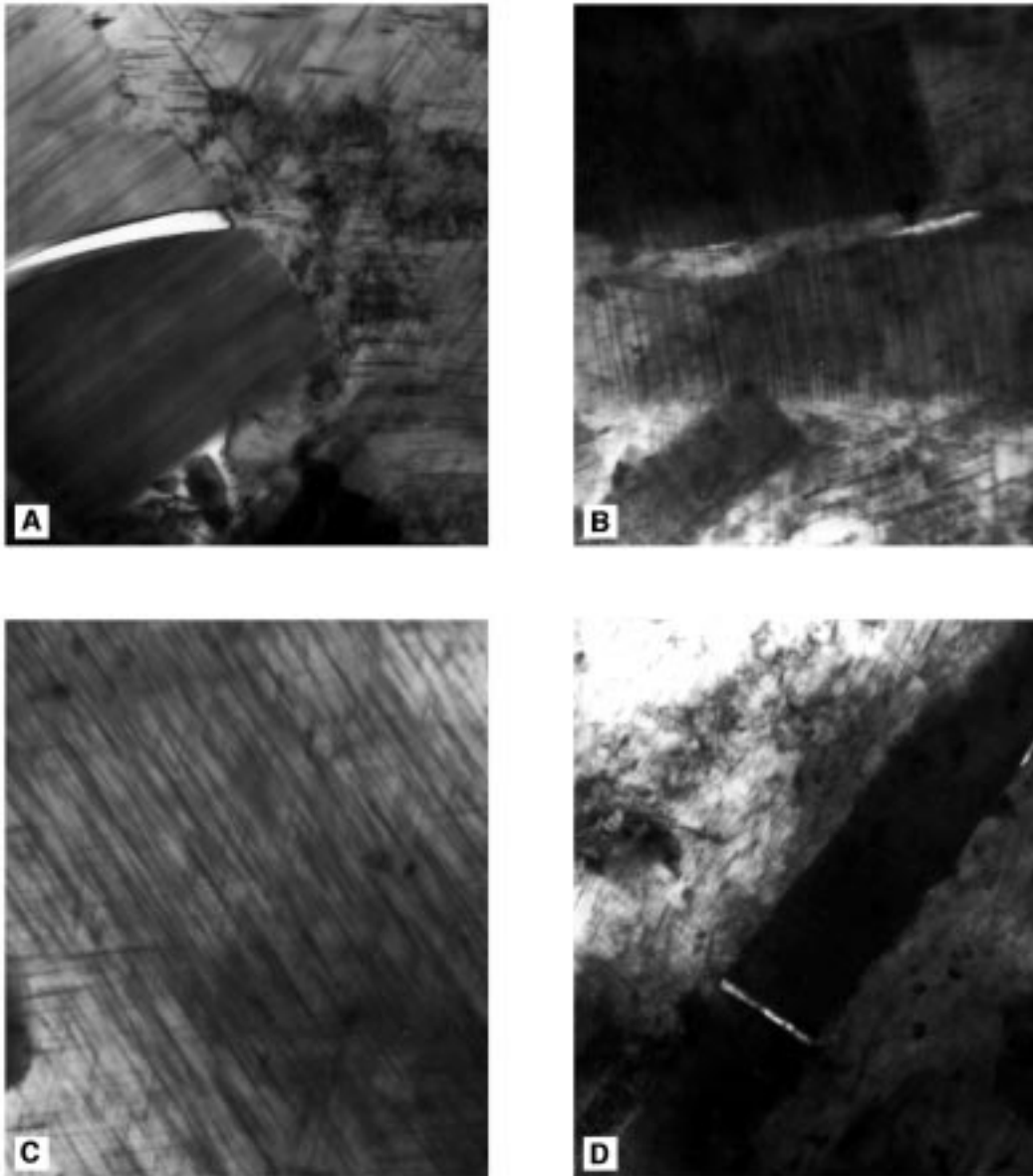
Figure 6.   TEM micrographs of 2124+SiCw after exposure to 143 hours at 350°F / 35 ksi. Stacking faults in the silicon carbide whiskers are visible in (a), (b), and (d). High dislocation densities occur in the matrix in the vicinity of the whisker ends in (a), (b), and (d). Voids are evident at the whisker-matrix interface in (b) and (d), and at cracks in the whiskers in (a) and (d). Precipitates appear in the matrix as dark, parallel lines in (a), (b), and (c).
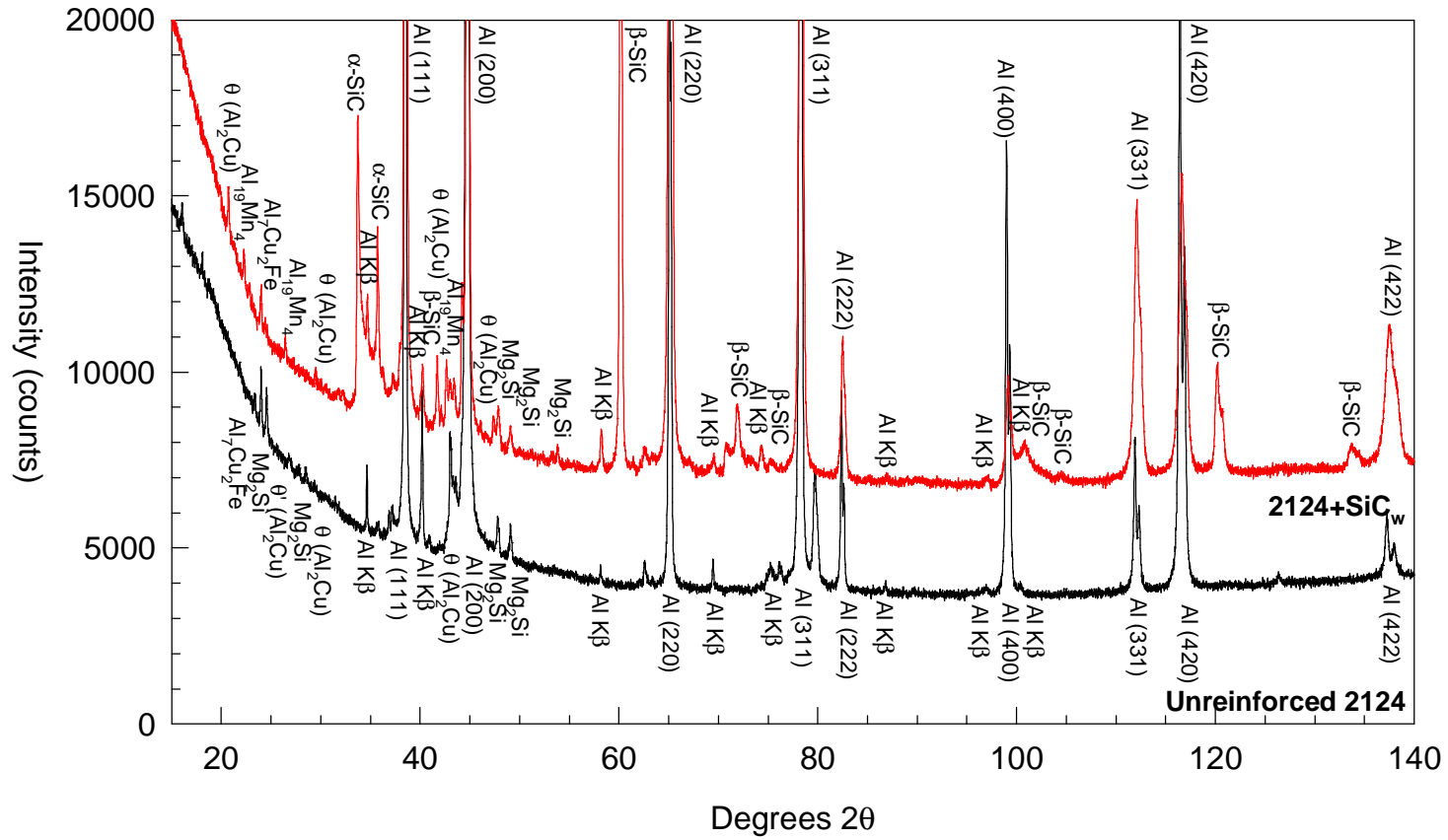
Figure 7. X-ray diffraction scans of unreinforced 2124 and 2124+SiC$_w$ in the as-received condition. Similar precipitates occur in both materials. The precipitates present include Θ' ($CuAl_2$), $(Al, Si)_{19}Mn_4$, Mg_2Si, and Al_7Cu_2Fe.
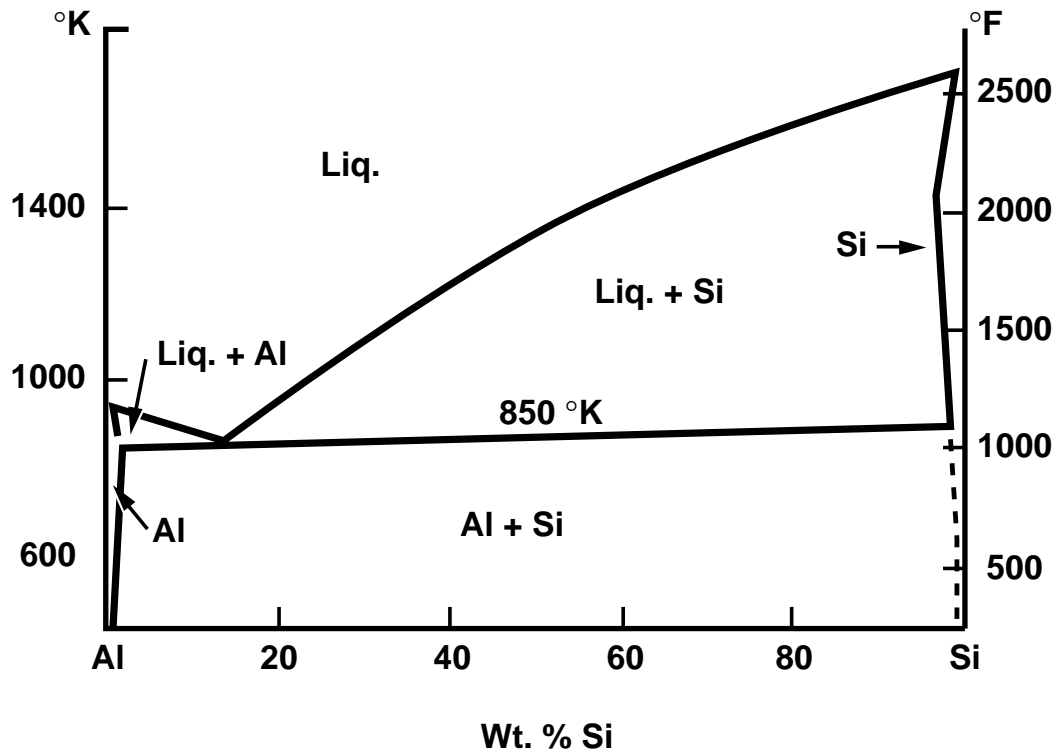
Figure 8.   Aluminum-silicon binary phase diagram. (Mondolfo, 1976) Aluminum
and silicon form solid solution alloys rather than aluminum silicide
compounds.
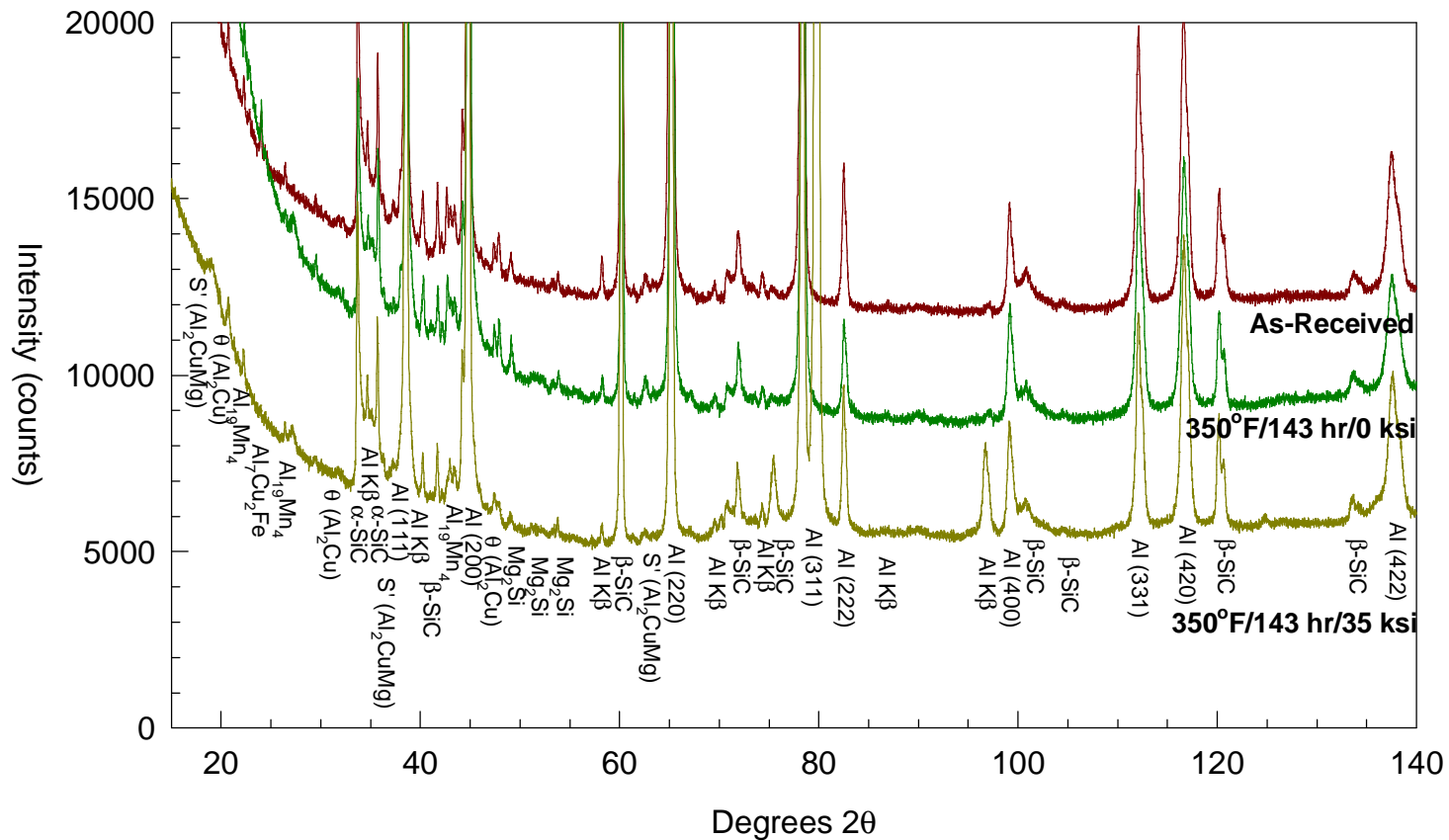
Figure 9.   X-ray diffraction scans of 2124+SiC$_w$ as-received and after 143 hrs at 350°F unstressed and 35 ksi. Near 350°F and above, S' (Al$_2$CuMg) is formed, in addition to Θ (CuAl$_2$). At lower temperatures, Θ is favored over S'.
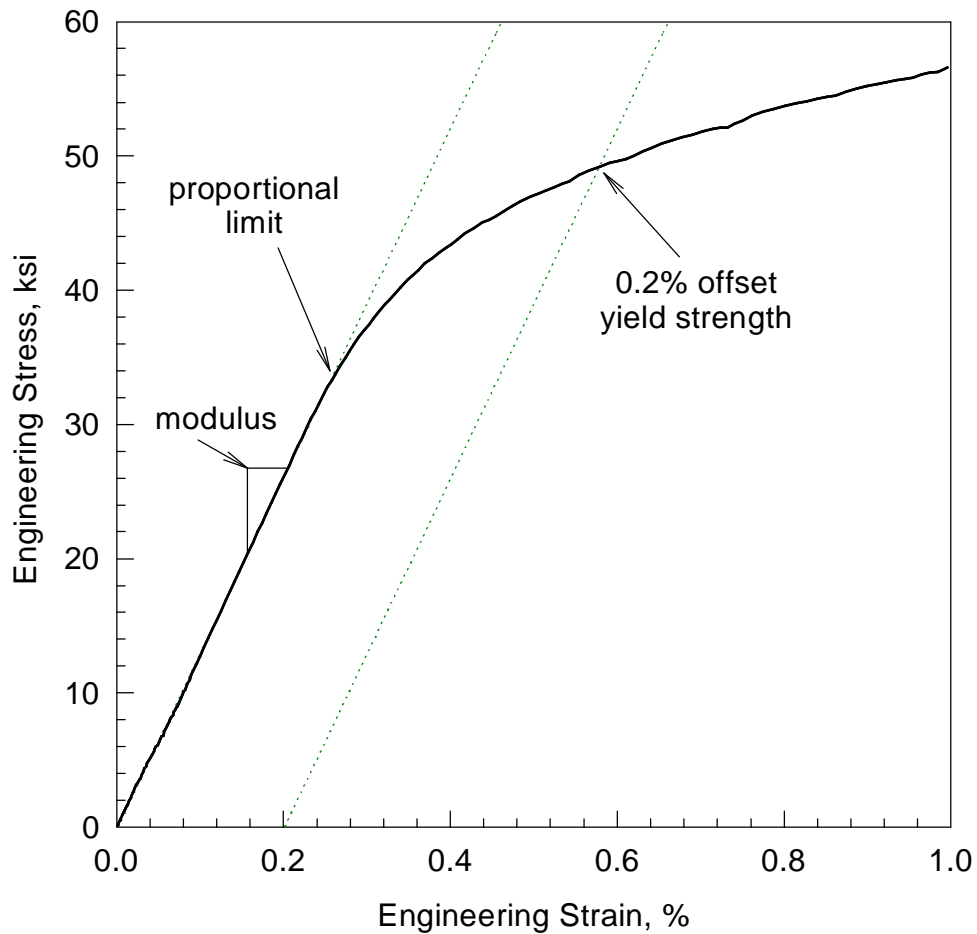
Figure 10.   Typical stress-strain curve at 300°F for 2124+SiC$_w$. Strain is based on the average of back-to-back strain gages. One line is constructed on top of the linear portion of the curve. The slope of this line is the modulus, and the point at which this line deviates from the stress-strain relationship identifies the proportional limit. Constructing a line parallel to this first line, shifted over 0.02% on the strain axis defines the yield strength of the material as the intersection between this second constructed line and the stress-strain relationship.
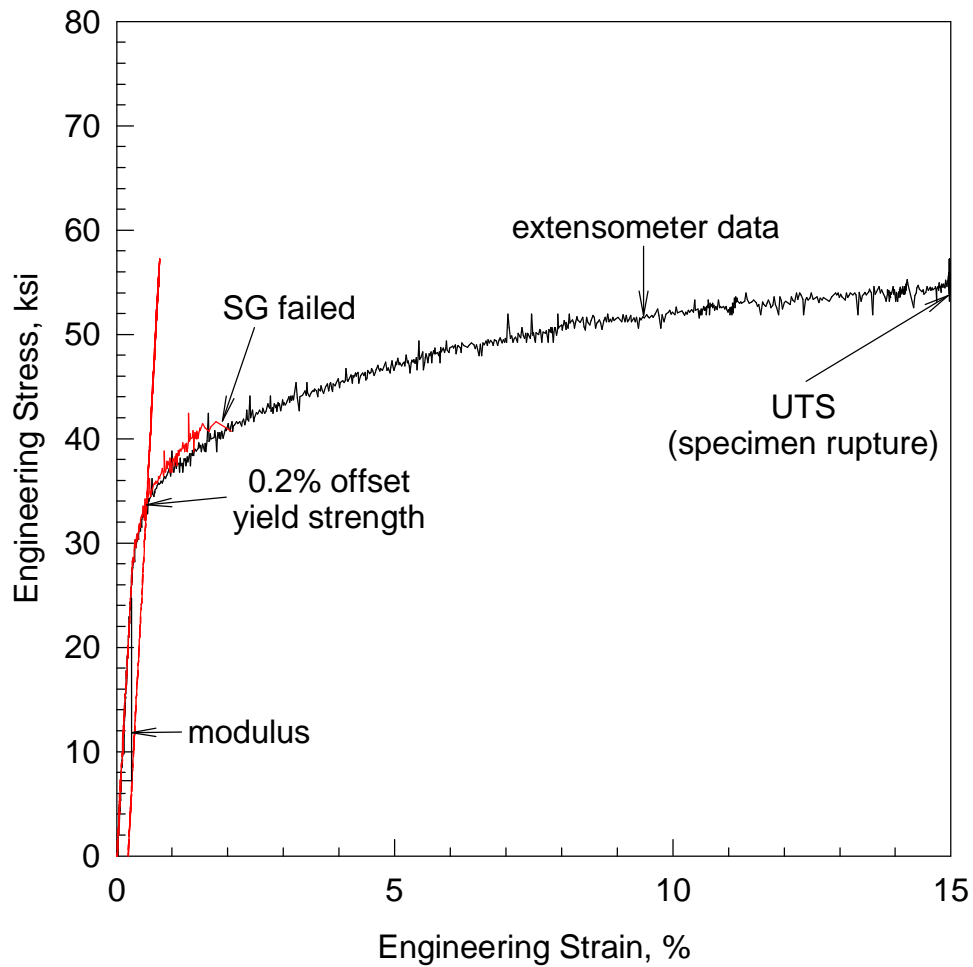
Figure 11.   Typical stress-strain curve at room temperature for unreinforced 2124. Two curves are shown, one for the average of back-to-back strain gages, and the second for the average of back-to-back extensometers.   The location where the strain gages failed is shown on the plot.   Total elongation to failure is based upon the extensometer data.
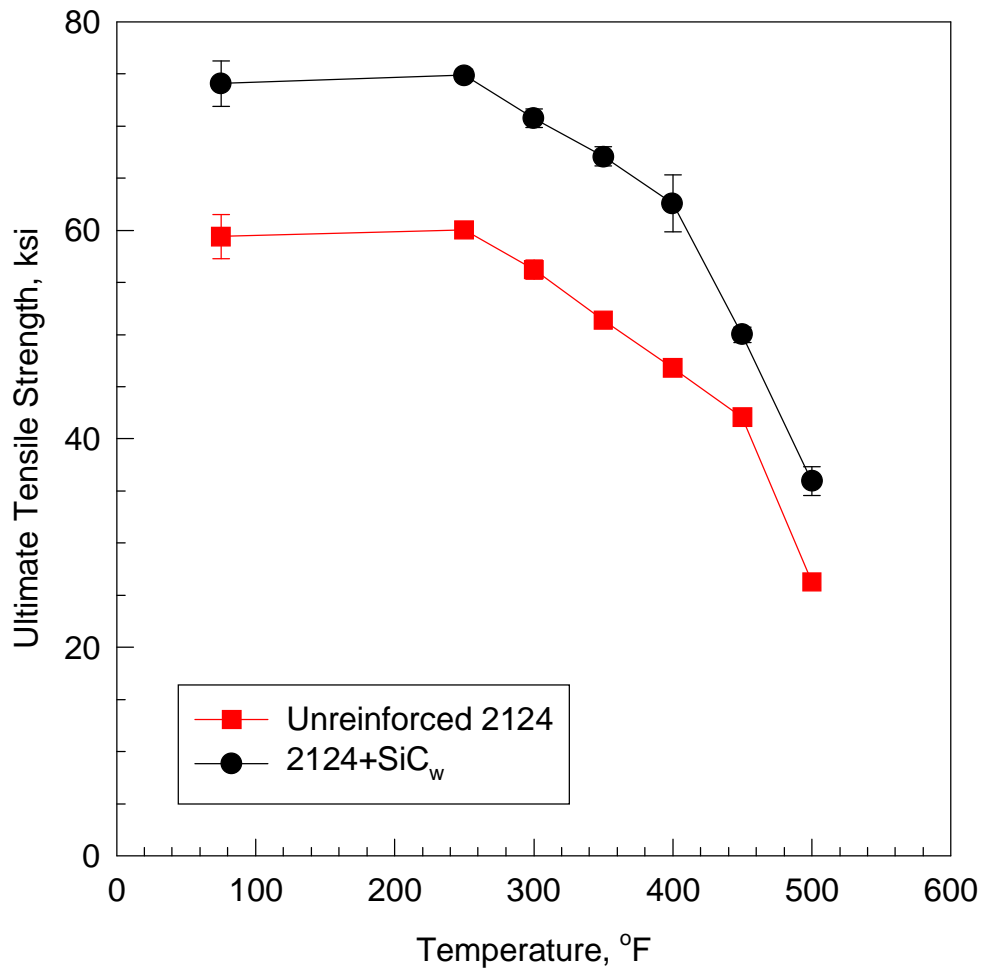
Figure 12.   Effect of temperature on the ultimate tensile strength of unreinforced 2124 and 2124+SiC$_w$. The range of data measured is shown by the error bars constructed at each temperature data point. All data is for the longitudinal direction.
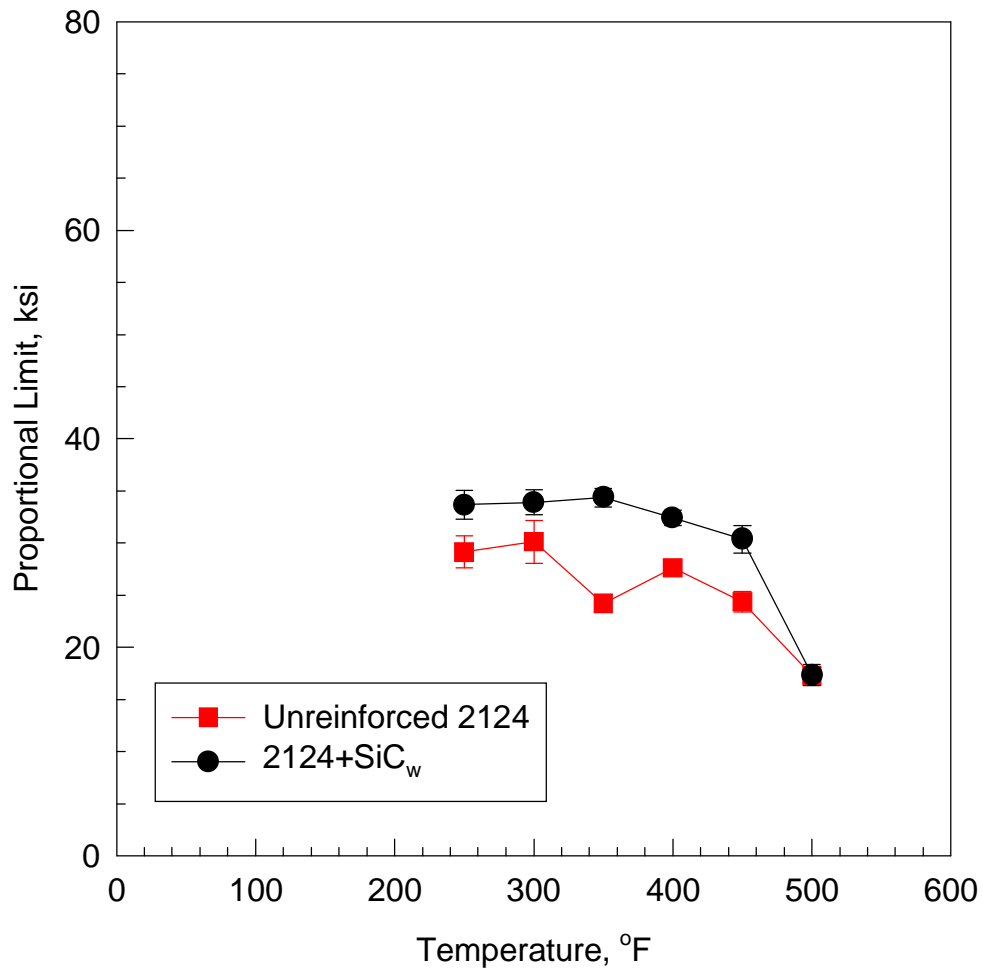
Figure 13.   Effect of temperature on the proportional limit of unreinforced 2124 and
2124+SiC$_w$.   The range of data measured is shown by the error bars
constructed at each temperature data point.   All data is for the longitudinal
direction.
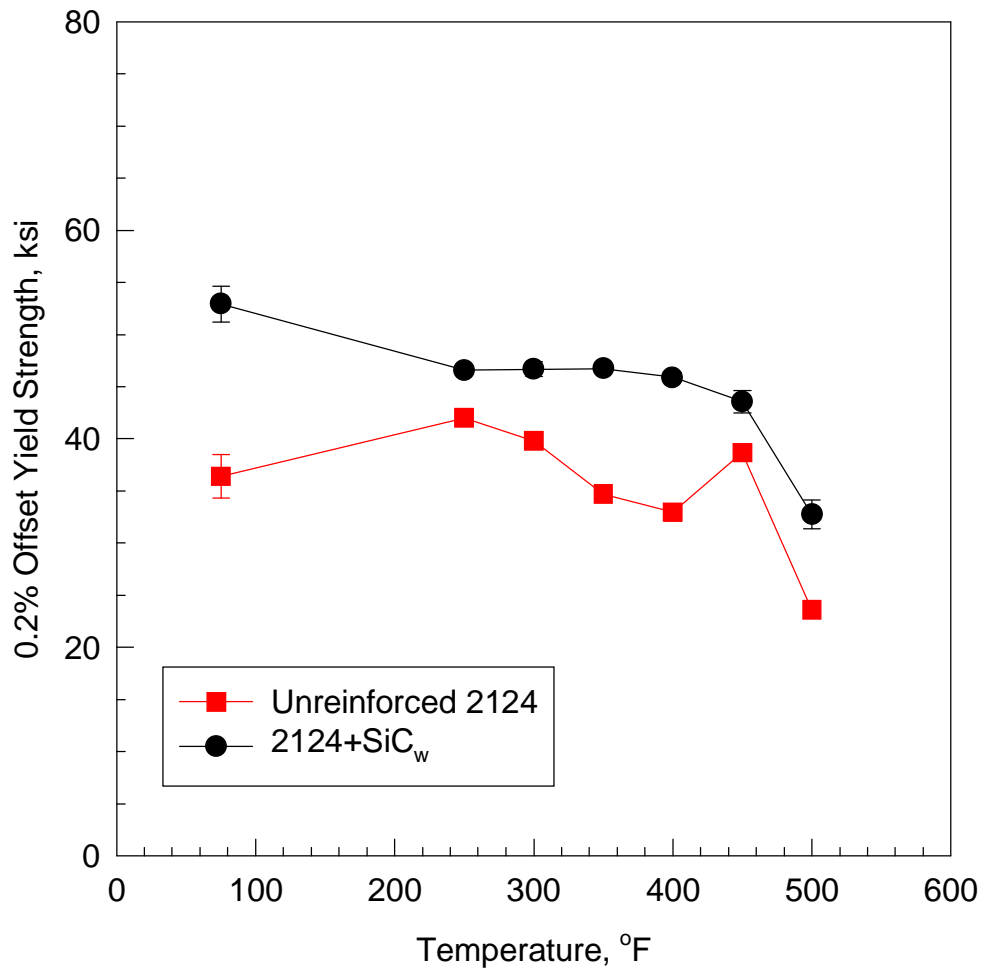
Figure 14.   Effect of temperature on the 0.02% offset yield strength of unreinforced 2124 and 2124+SiC$_w$. The range of data measured is shown by the error bars constructed at each temperature data point. All data is for the longitudinal direction.
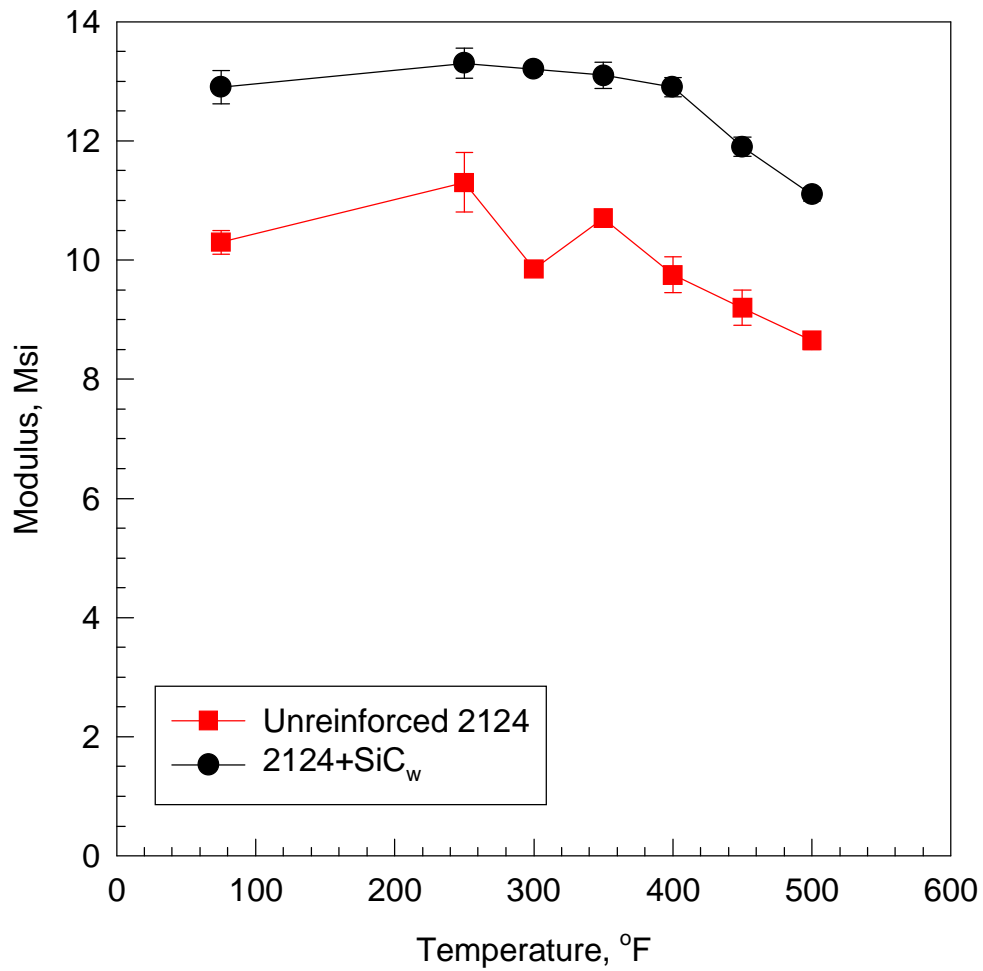
Figure 15. Effect of temperature on the modulus of unreinforced 2124 and 2124+SiC$_w$. The range of data measured is shown by the error bars constructed at each temperature data point. All data is for the longitudinal direction.
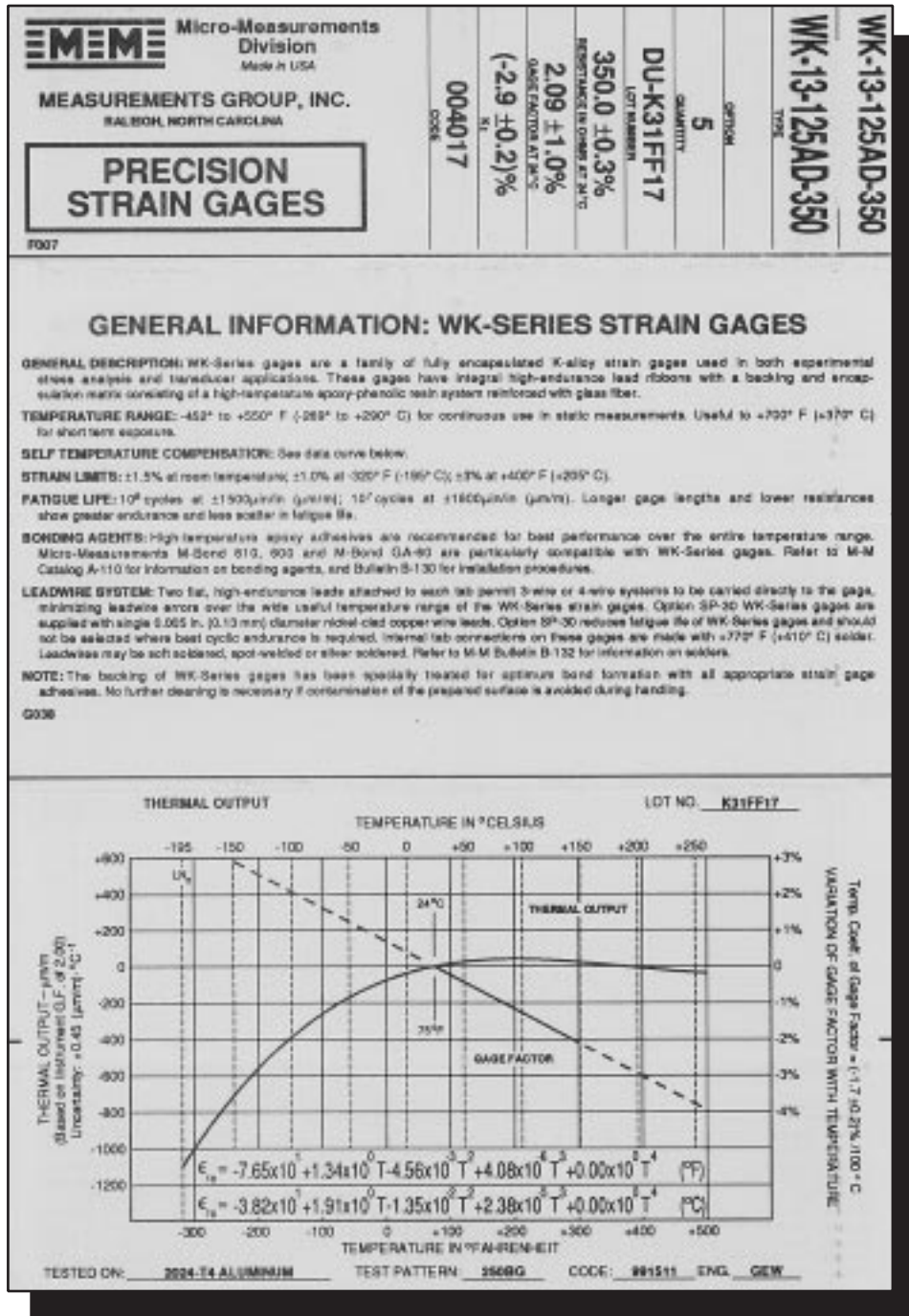
Figure 16. Strain gage information sheet.
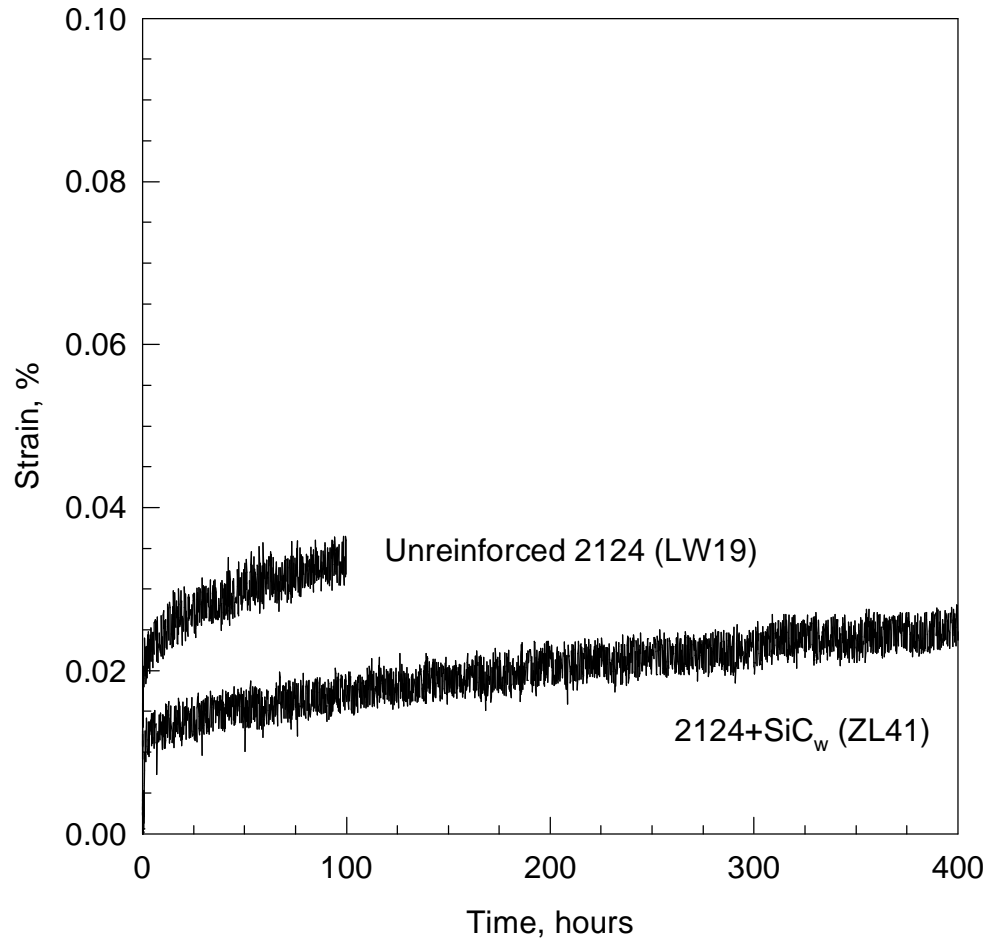
Figure 17. Creep of unreinforced 2124 and 2124+SiC$_w$ at 250°F and 37 ksi. The unreinforced specimen (LW19) was stopped after 100 hours and 0.037% strain. The 2124+SiC$_w$ specimen (ZL41) was stopped after 401 hours and 0.025% strain.
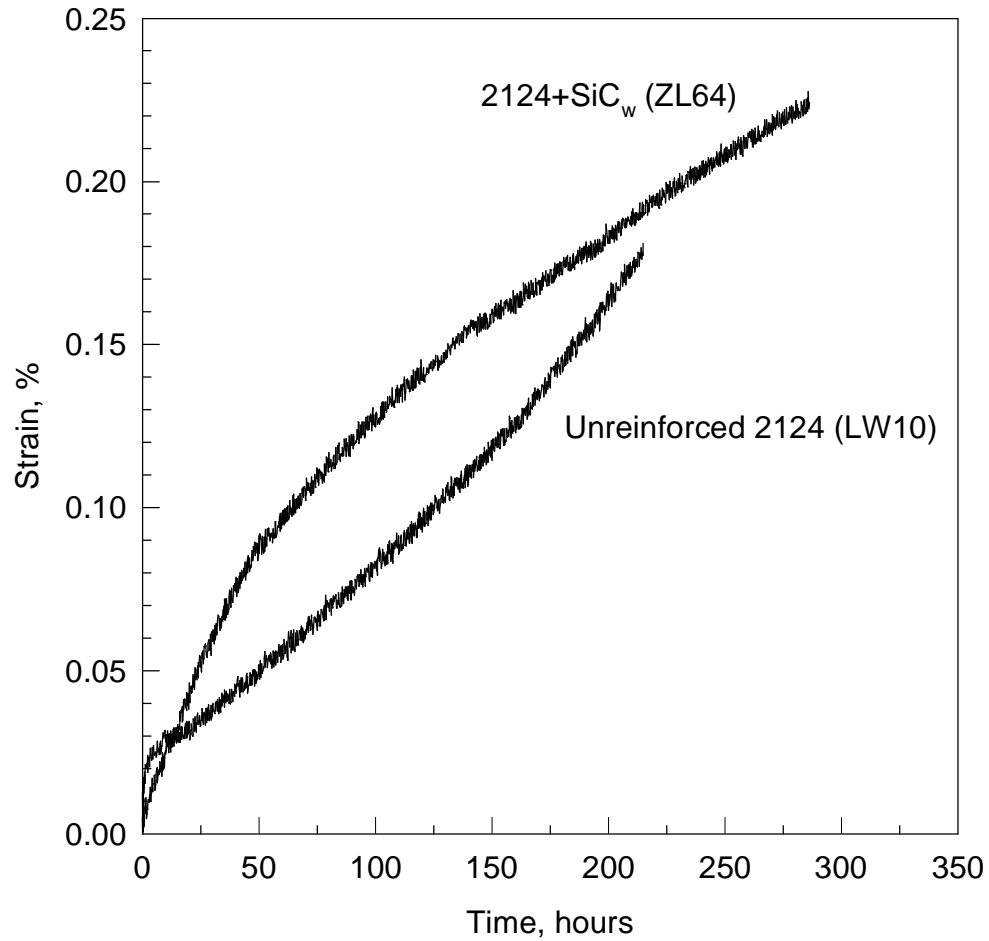
Figure 18.   Creep of unreinforced 2124 and 2124+SiC$_w$ at 350°F and 25 ksi. The unreinforced specimen (LW10) ruptured after 215 hours and 0.182% strain. The 2124+SiC$_w$ specimen (ZL64) was stopped after 286 hours and 0.224% strain.
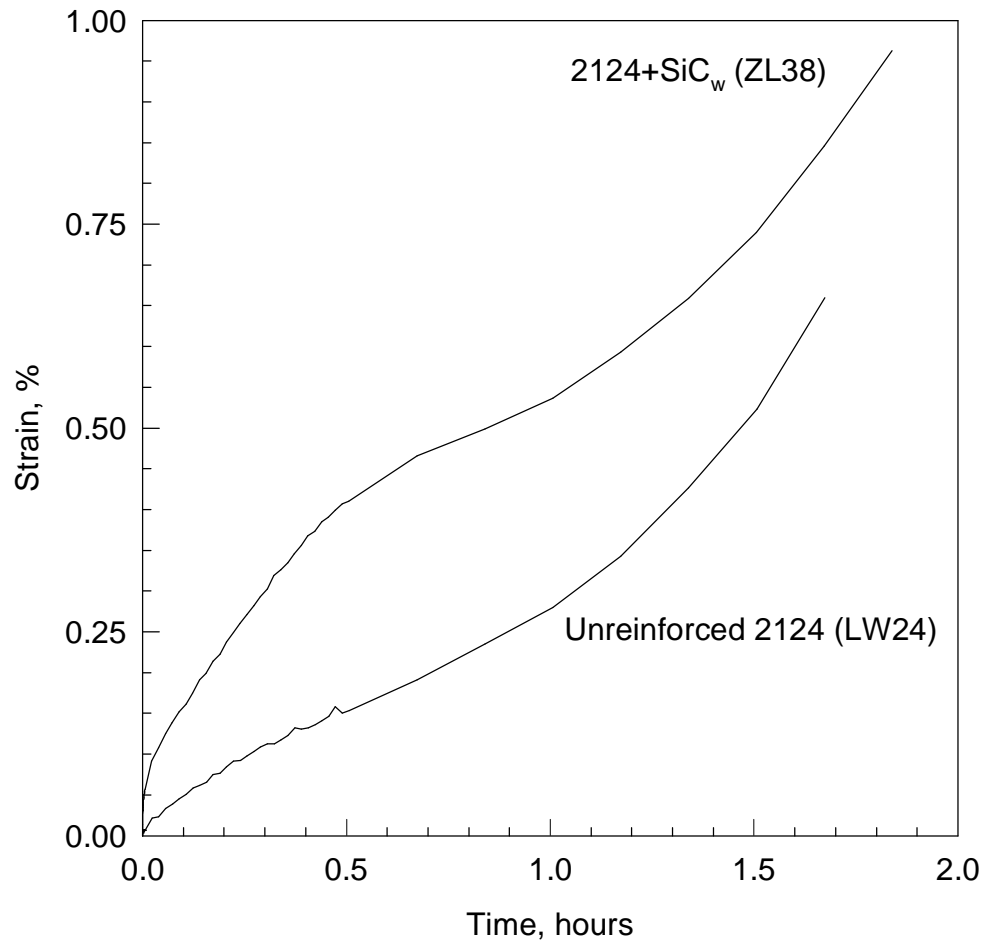
Figure 19.   Creep of unreinforced 2124 and 2124+SiC$_w$ at 500°F and 18 ksi. The unreinforced specimen (LW24) ruptured after 1.7 hours and 0.660% strain. The 2124+SiC$_w$ specimen (ZL38) ruptured after 3 hours and 0.955% strain.
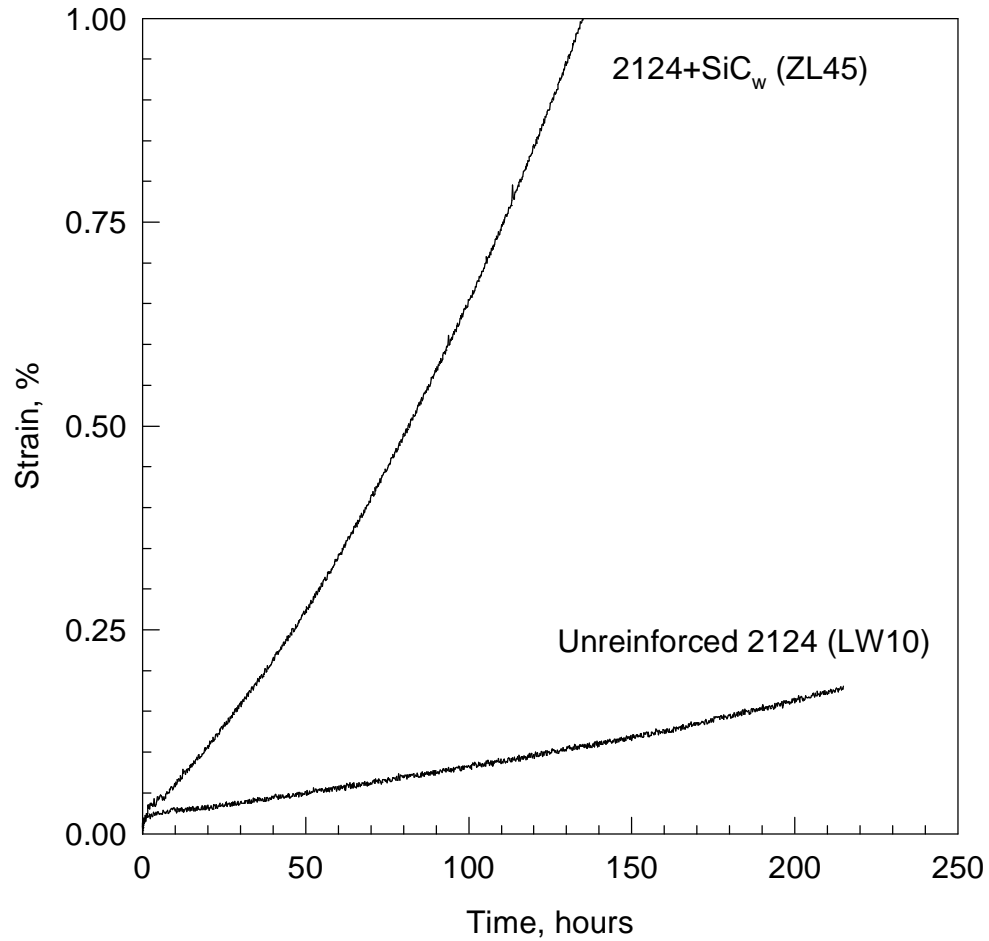
Figure 20. Creep of unreinforced 2124 and 2124+SiC$_w$ at 350°F and a stress ratio (applied stress to UTS at 350°F) of 0.5. The unreinforced specimen (LW10) ruptured after 215 hours and 0.182% strain. The 2124+SiC$_w$ specimen (ZL45) ruptured after 219 hours and greater than 1.99% strain.
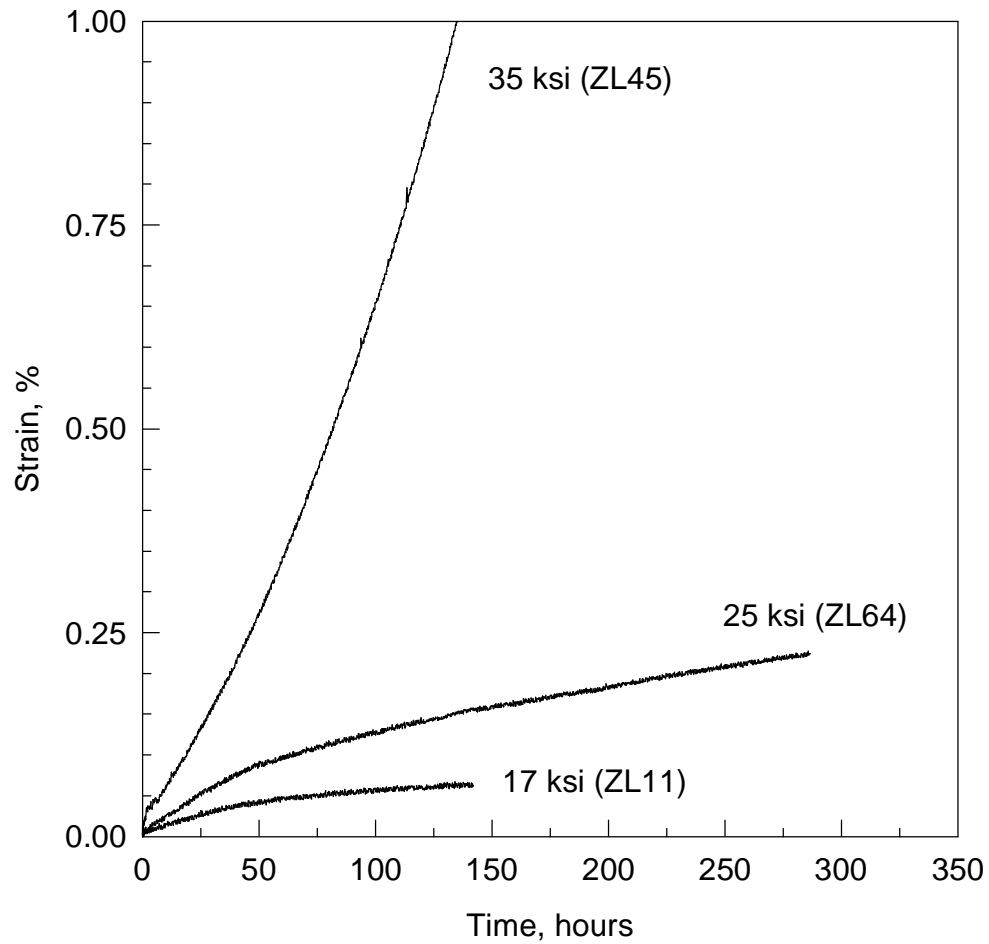
Figure 21.   Creep of 2124+SiC$_w$ at 350°F and 17, 25, and 35 ksi. The specimen at 17 ksi (ZL11) was stopped after 142 hours and 0.071% strain. The specimen at 25 ksi (ZL64) was stopped after 286 hours and 0.224% strain. The specimen at 35 ksi (ZL45) ruptured after 219 hours and greater than 1.99% strain.
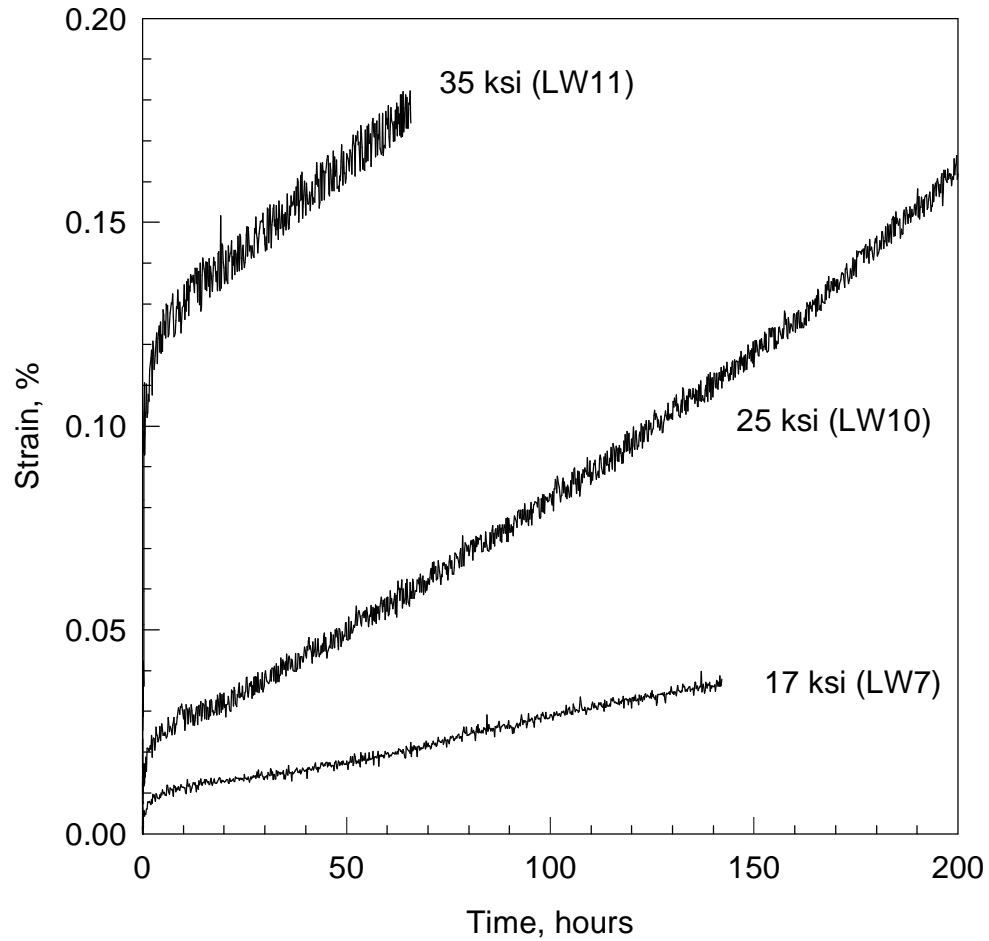
Figure 22.   Creep of unreinforced 2124 at 350°F and 17, 25, and 35 ksi. The specimen at 17 ksi (LW7) was stopped after 142 hours and 0.041% strain. The specimen at 25 ksi (LW10) ruptured after 215 hours and 0.182% strain. The specimen at 35 ksi (LW11) ruptured after 66 hours and 0.211% strain.
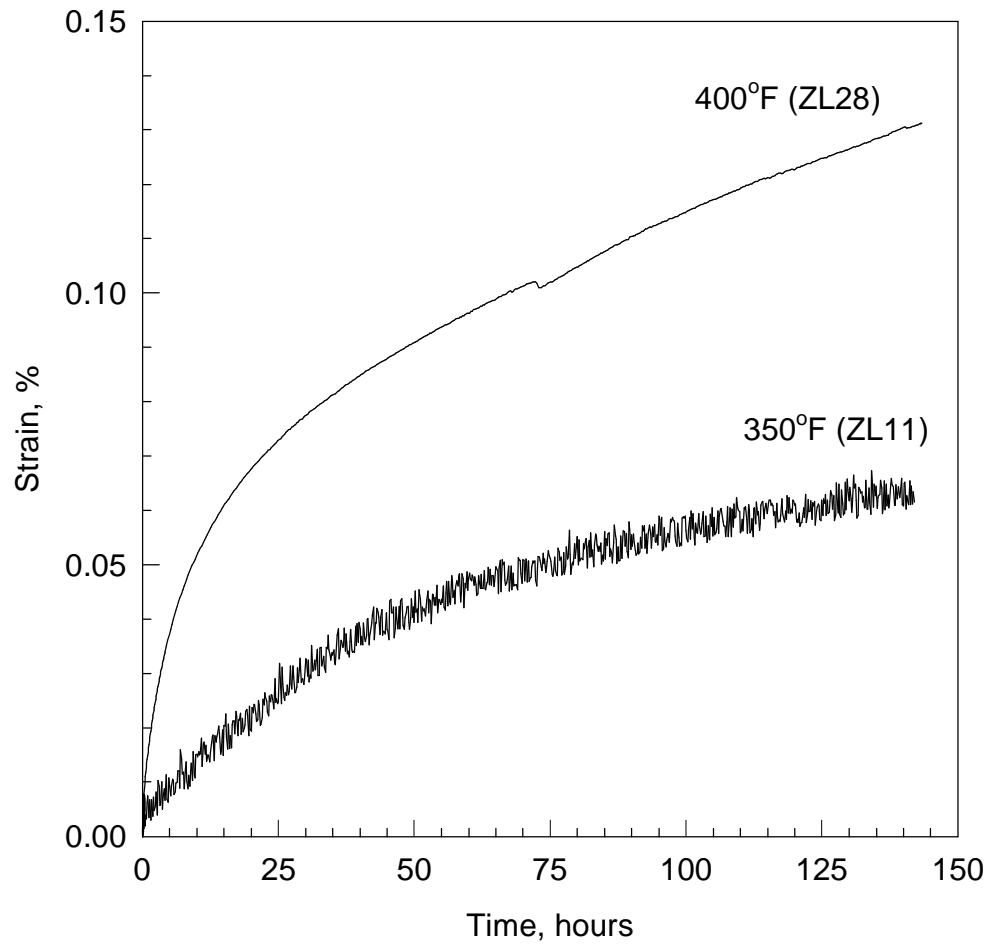
Figure 23.   Creep of 2124+SiC$_w$ at 17 ksi and 350°F and 400°F. The specimen at 350°F (ZL11) was stopped after 142 hours and 0.071% strain.   The specimen at 400°F (ZL28) was stopped after 143 hours and 0.131% strain. A specimen at 500°F and 17 ksi (ZL38), offscale on this chart, ruptured after 3 hours and 0.955% strain.
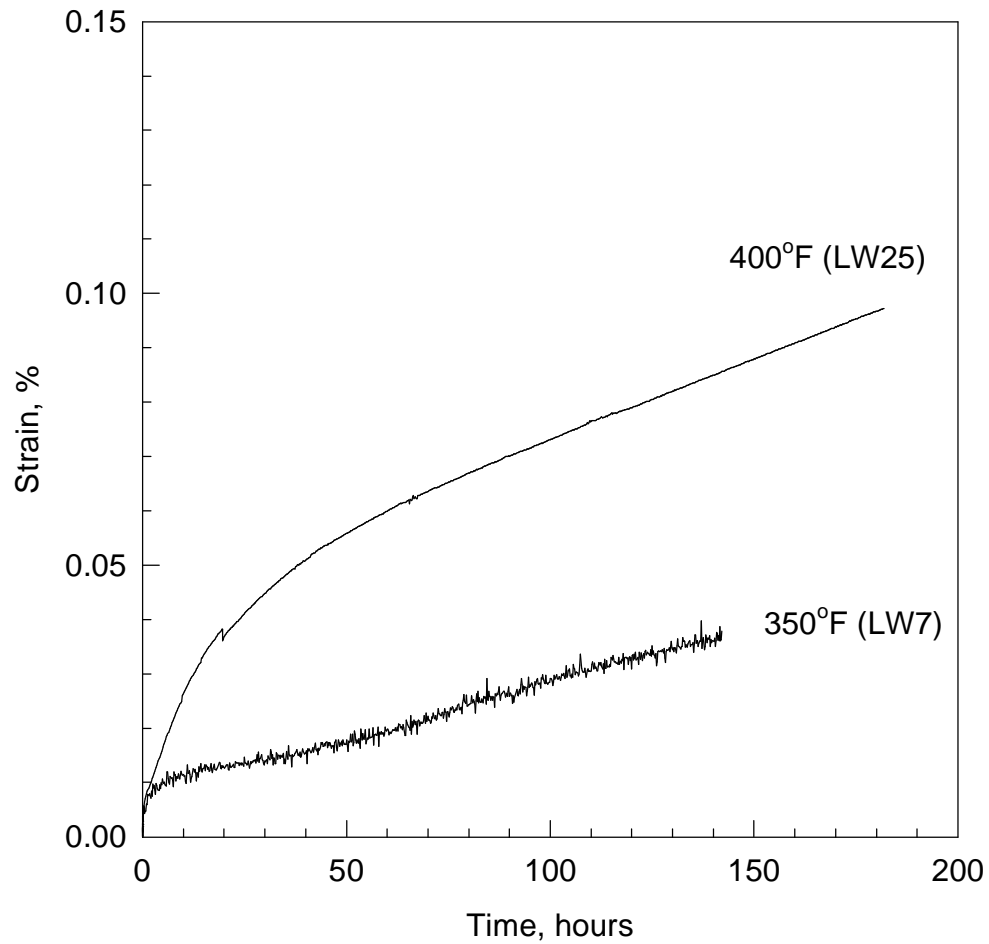
Figure 24.   Creep of unreinforced 2124 at 17 ksi and 350°F and 400°F. The specimen at 350°F (LW7) was stopped after 142 hours and 0.041% strain. The specimen at 400°F (LW25) ruptured after 182 hours and 0.097% strain. A specimen at 500°F and 17 ksi (LW24), offscale on this chart, ruptured after 1.7 hours and 0.660% strain.
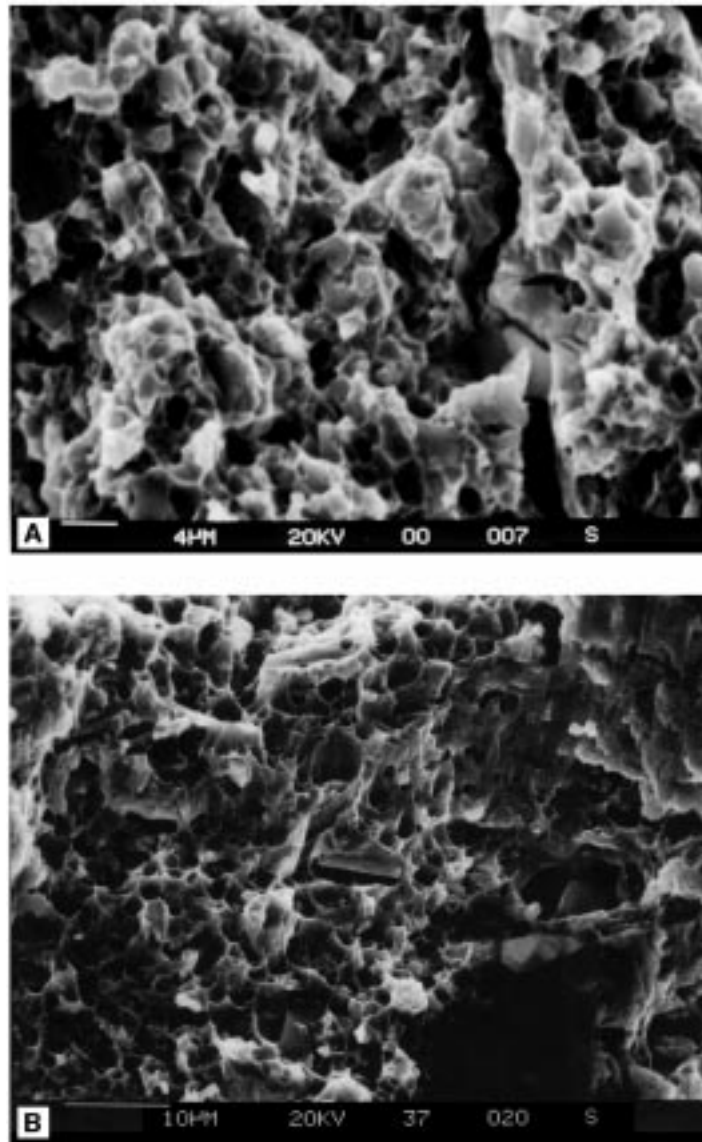
Figure 25. SEM fractographs of 2124+SiCw specimens tensile tested at (a) 300°F and (b)
500°F. The fracture surface in the matrix primarily consists of ductile dimples,
with whisker ends in the bottom of some dimples. The dimples are drawn up
more in (b) due to the higher test temperature. The large cracked particles on
the fracture surfaces are constituent intermetallics. The whiskers do not break
during the tensile test.
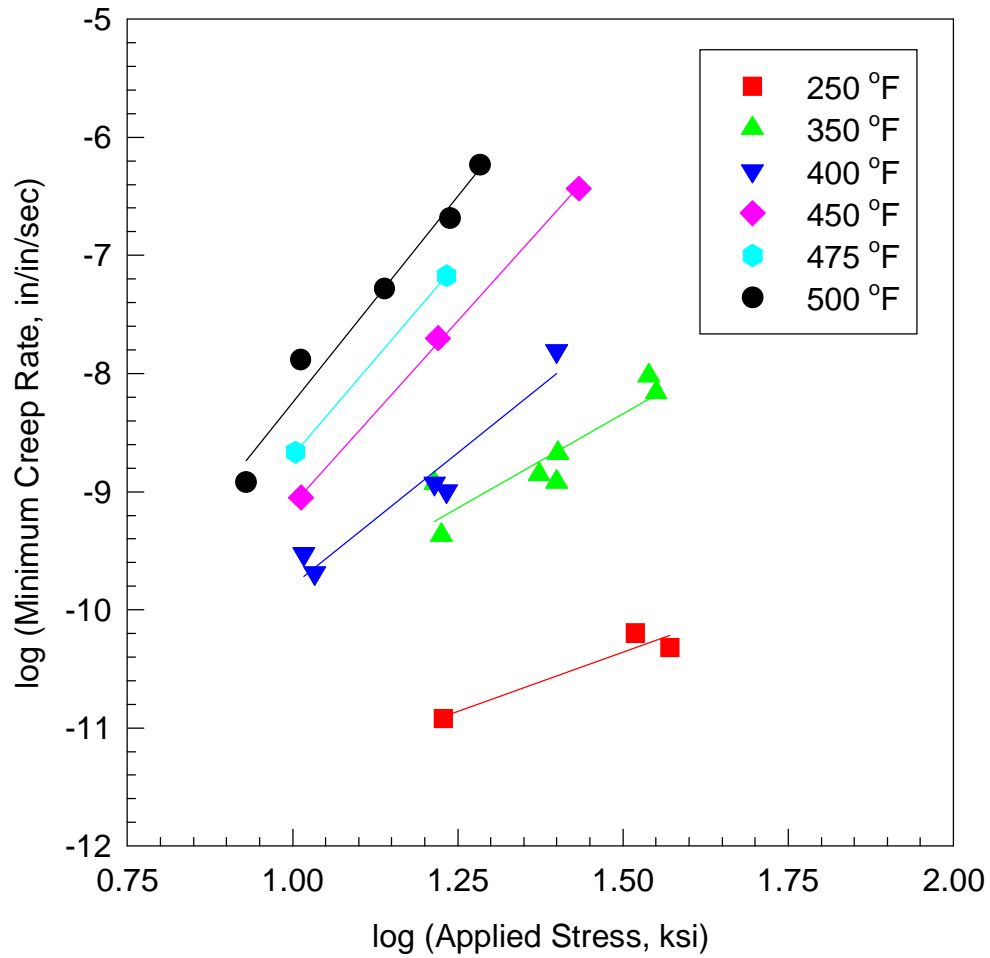
Figure 26.   Determination of creep stress exponent for 2124+SiC$_w$. The slope of the isothermal lines is the creep stress exponent, *n*. Values for creep stress exponents and standard deviations calculated for each temperature are shown in Table 7.
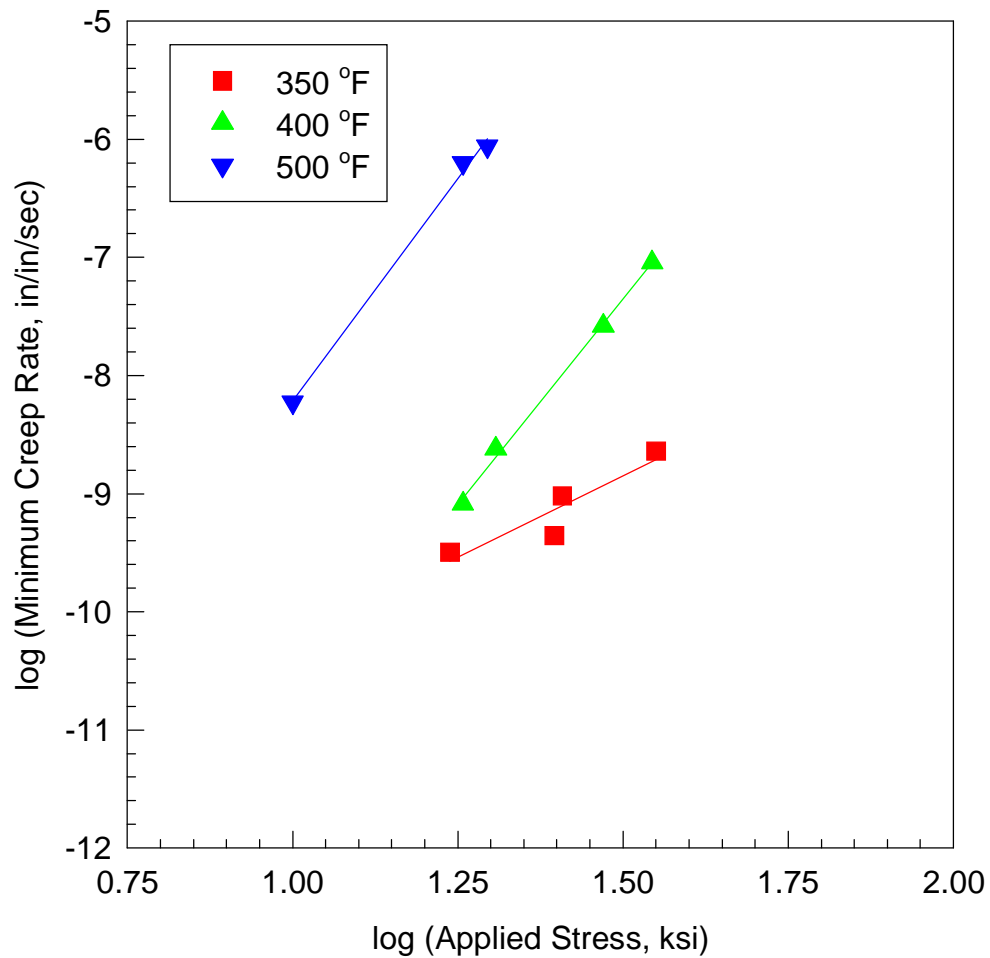
Figure 27.   Determination of creep stress exponent for unreinforced 2124. The slope of the isothermal lines is the creep stress exponent, *n*. Values for creep stress exponents and standard deviations calculated for each temperature are shown in Table 7.
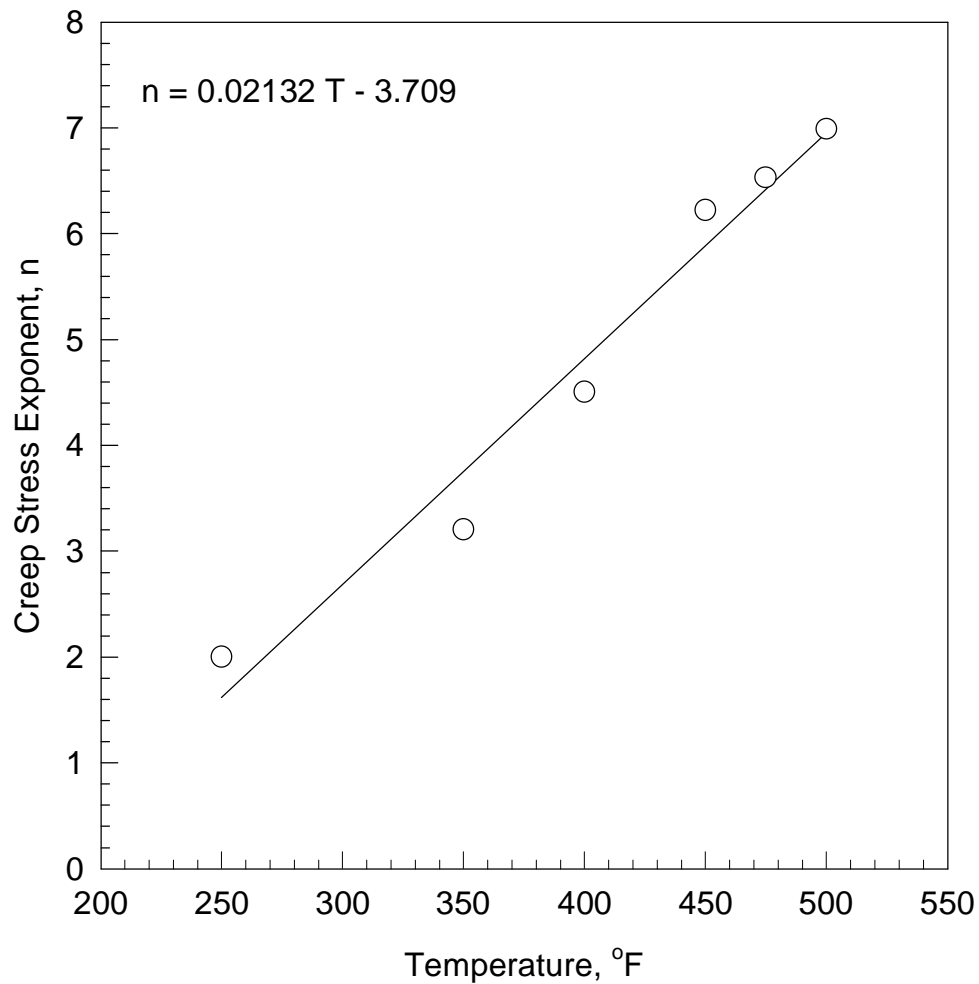
Figure 28.   Effect of temperature on creep stress exponent for 2124+SiC$_w$. Empirical values of stress exponent, determined in Figure 26 and listed in Table 7, are shown as a function of temperature. The best fit equation describing the relationship is a linear regression. The equation derived from a linear regression is shown on the figure.
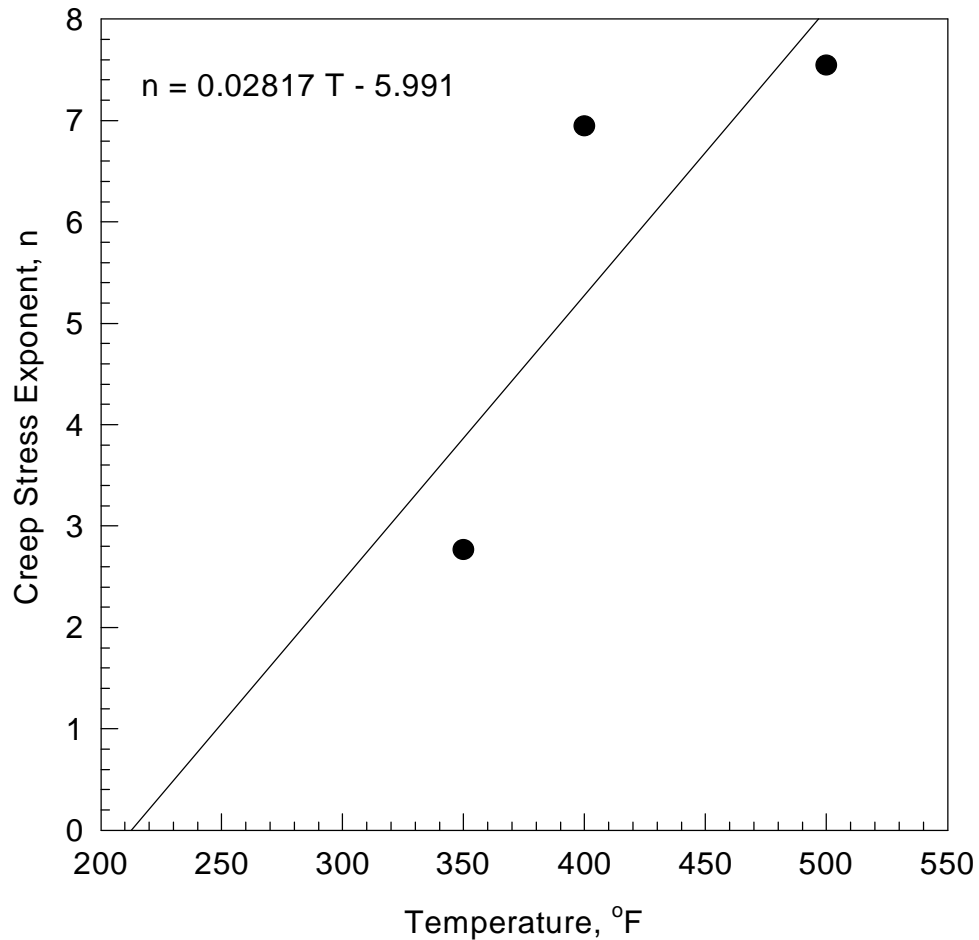
Figure 29.   Effect of temperature on creep stress exponent for unreinforced 2124. Empirical values of stress exponent, determined in Figure 27 and listed in Table 7, are shown as a function of temperature. The limited amount of data for the unreinforced 2124 made fitting this relationship problematic. Therefore, a linear regression was used to fit the data because the fit for the 2124+SiC$_w$ creep stress exponent demonstrated a linear relationship as a function of temperature. The equation derived from a linear regression is shown on the figure.
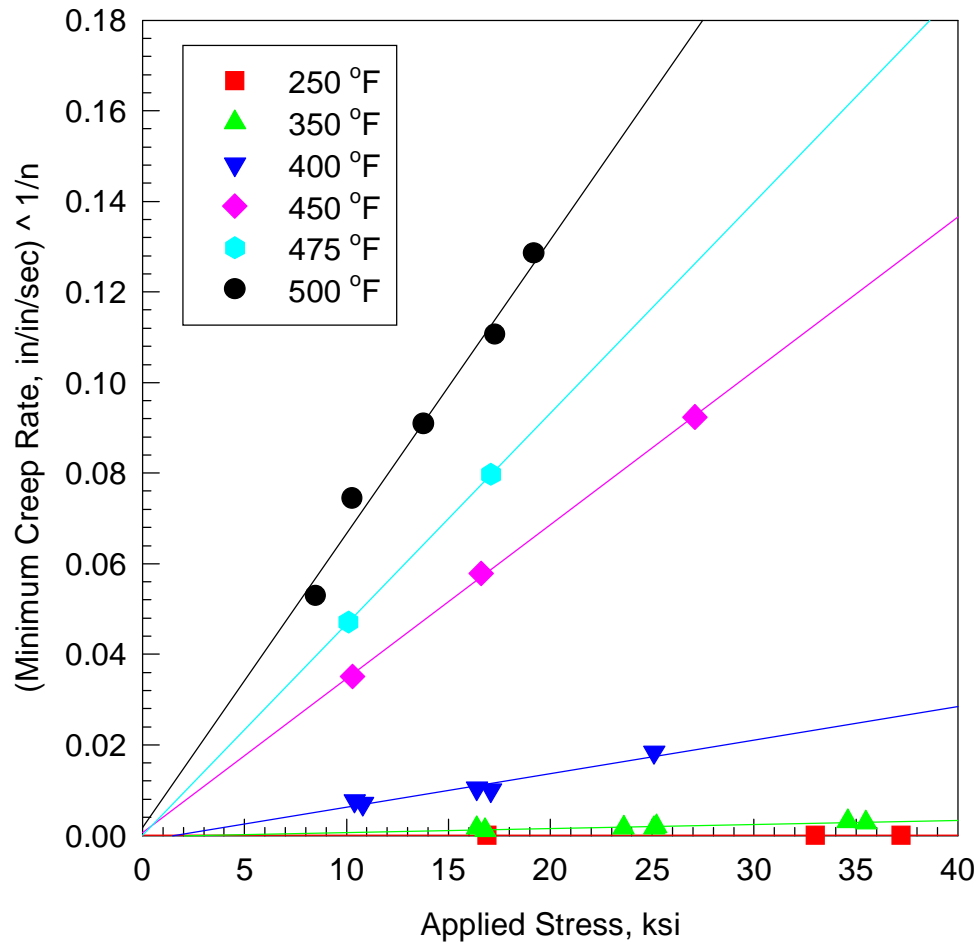
Figure 30. Determination of threshold stress for creep for 2124+SiC$_w$. The ordinate is based upon the creep stress exponents determined in Figure 26 and listed in Table 7. Isothermal lines are extrapolated back to the stress axis. Positive values of stress indicates the existence of a threshold stress. As can be seen from the data at all temperatures tested, the 2124+SiC$_w$ exhibits zero or slightly negative intercepts with the abscissa, indicating that a threshold stress does not exist.
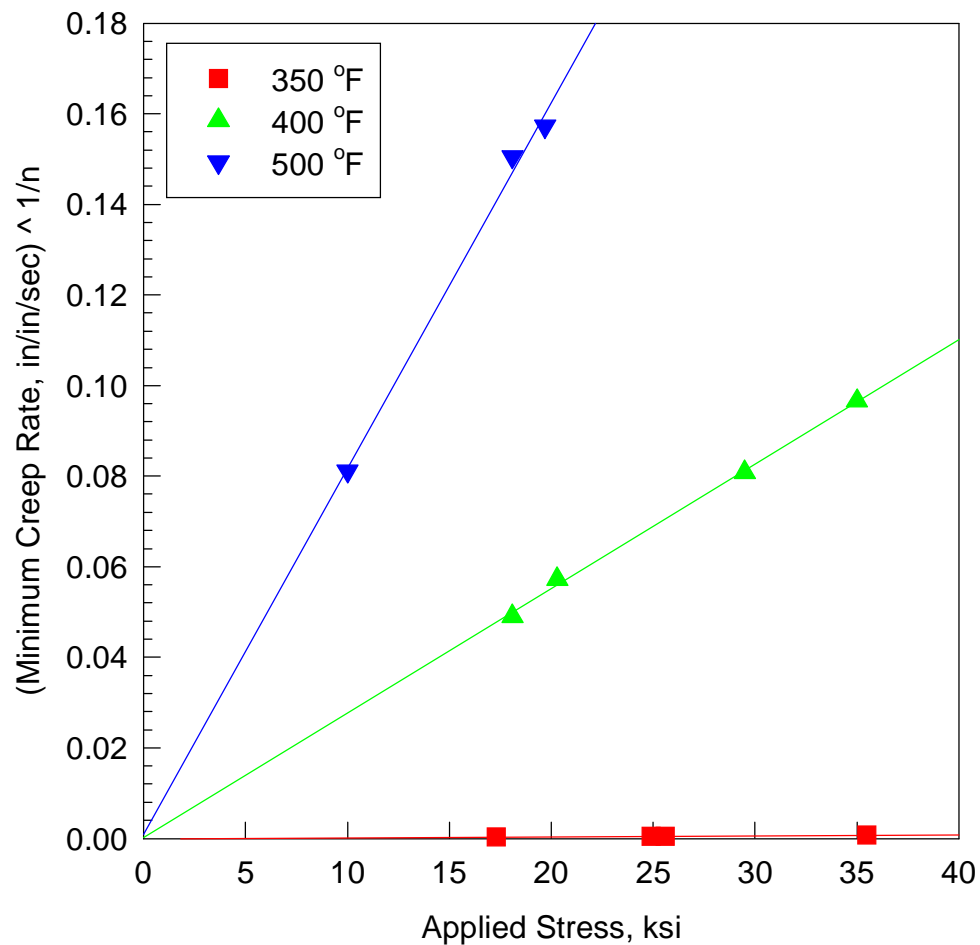
Figure 31. Determination of threshold stress for creep for unreinforced 2124. The ordinate is based upon the creep stress exponents determined in Figure 27 and listed in Table 7. Isothermal lines are extrapolated back to the stress axis. Positive values of stress indicates the existence of a threshold stress. As can be seen from the data at all temperatures tested, the unreinforced 2124 exhibits zero or slightly negative intercepts with the abscissa, indicating that a threshold stress does not exist.
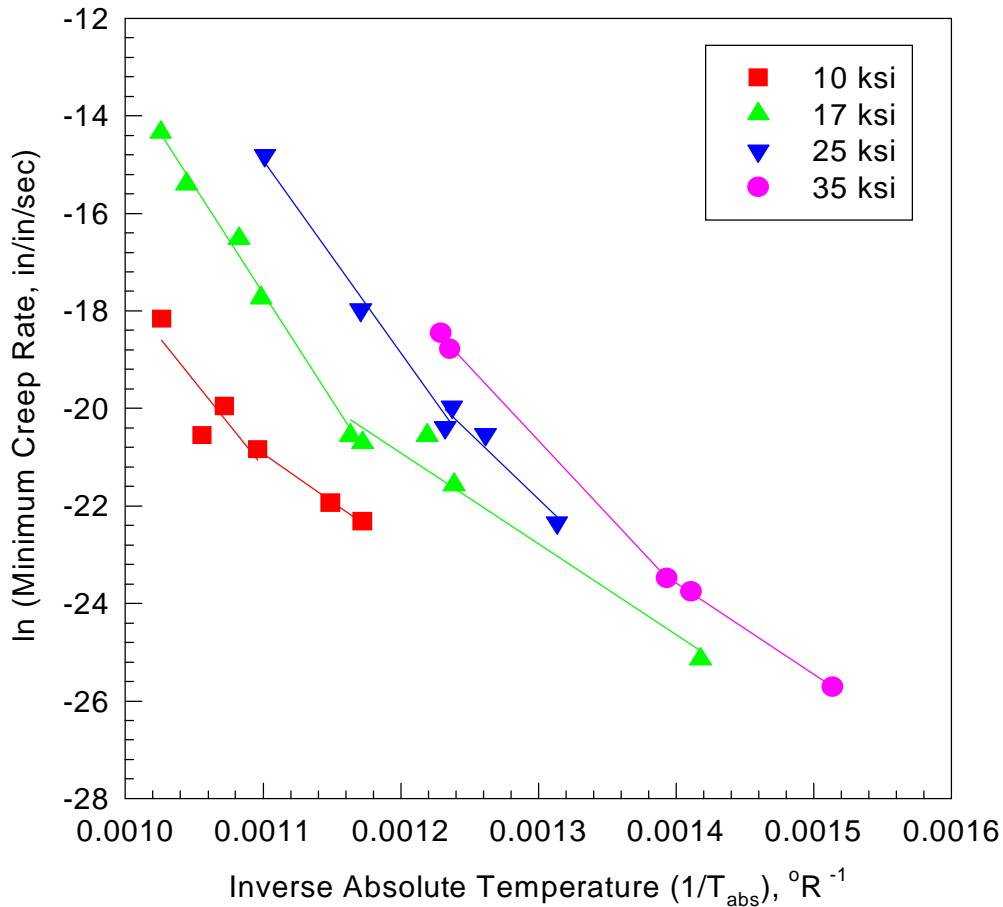
Figure 32.   Determination of apparent activation energy for creep for 2124+SiC$_w$. Isostress data demonstrates two distinct linear portions for each stress level. The slopes of these lines are the apparent activation energies for creep shown in Table 8; values based upon the slopes shown in this figure are identified as method (2). The break in the lines is a result of changes in deformation mechanisms, and therefore activation energies. Notice that the breaks in the lines at all stress levels except 35 ksi occur at approximately the same minimum creep rate.
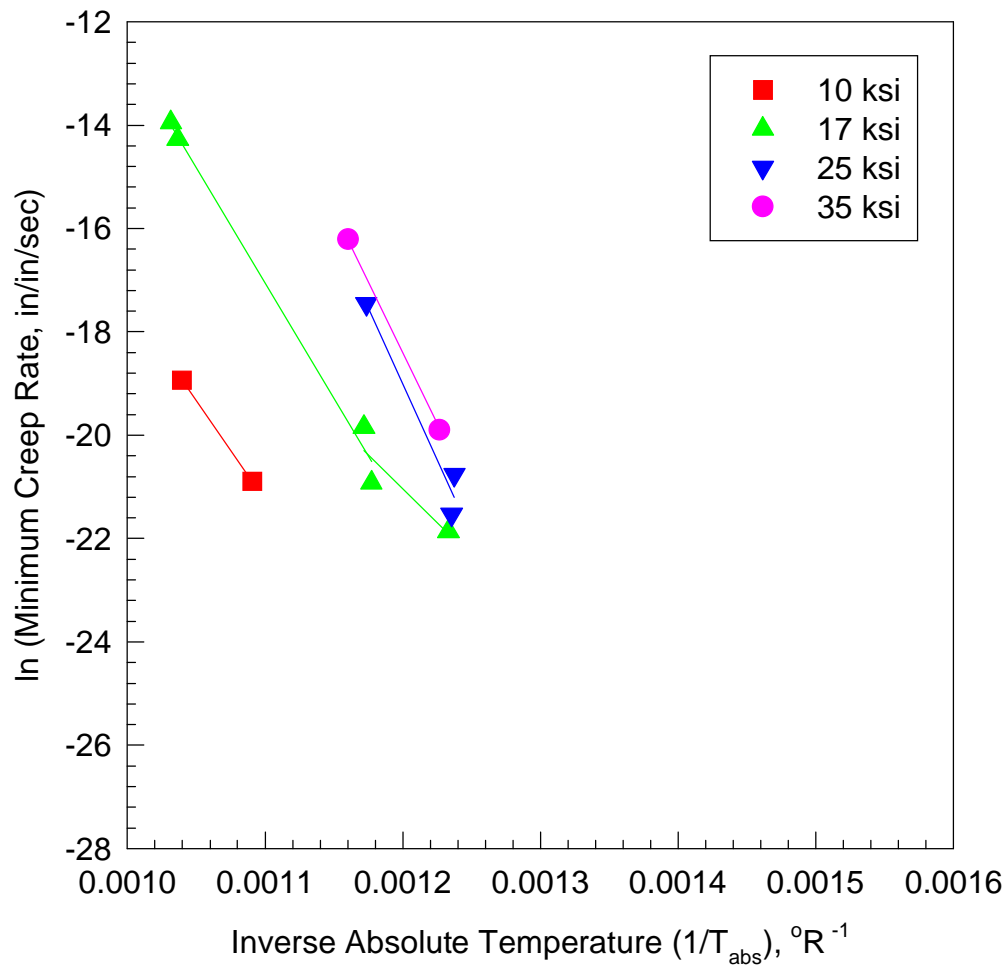
Figure 33. Determination of apparent activation energy for creep for unreinforced 2124. The slopes of isostress data are the apparent activation energies for creep shown in Table 8; values based upon the slopes shown in this figure are identified as method (2).
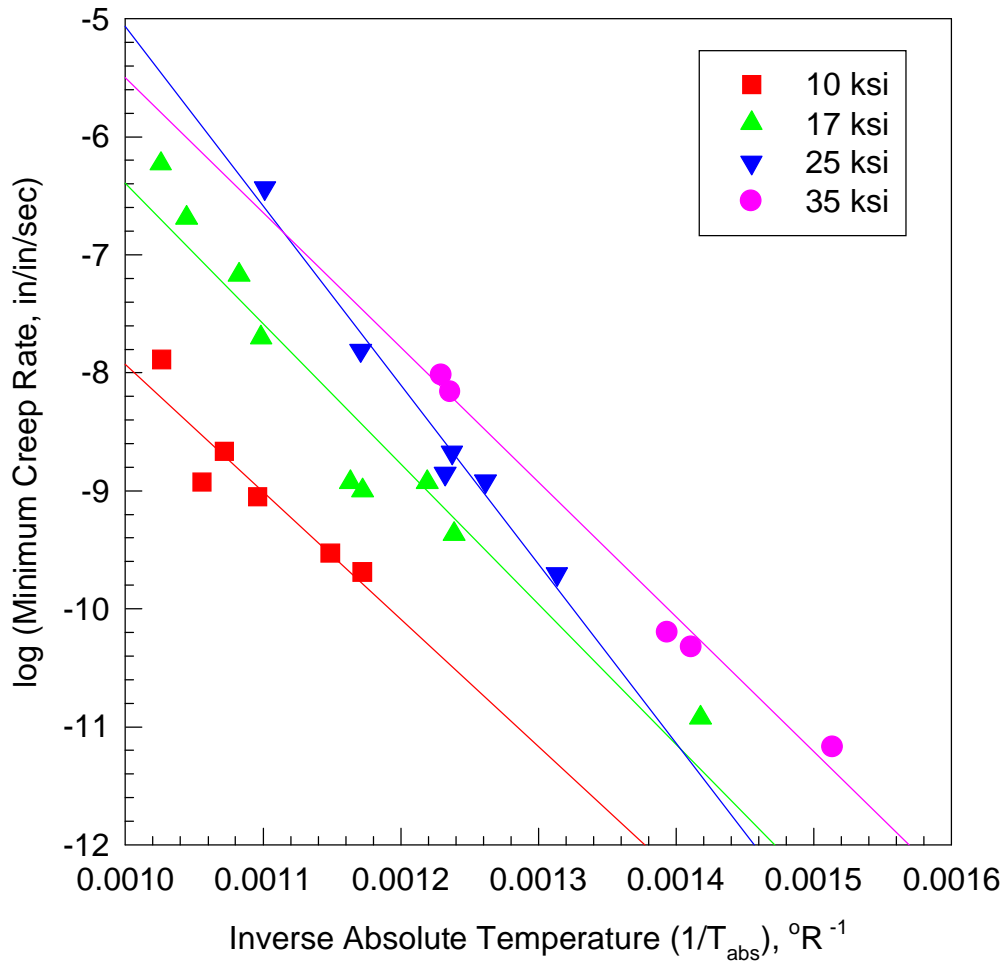
Figure 34.   Determination of Larson-Miller constant for 2124+SiC$_w$, based upon the minimum creep rate. This figure demonstrates that the 2124+SiC$_w$ creep data do not conform to the Larson-Miller parameter. The Larson-Miller constant is the point at which the isostress lines are supposed to converge at the ordinate. As can be seen in the data, the isostress lines converge before the ordinate, and therefore do not result in a useable value for the Larson-Miller constant.
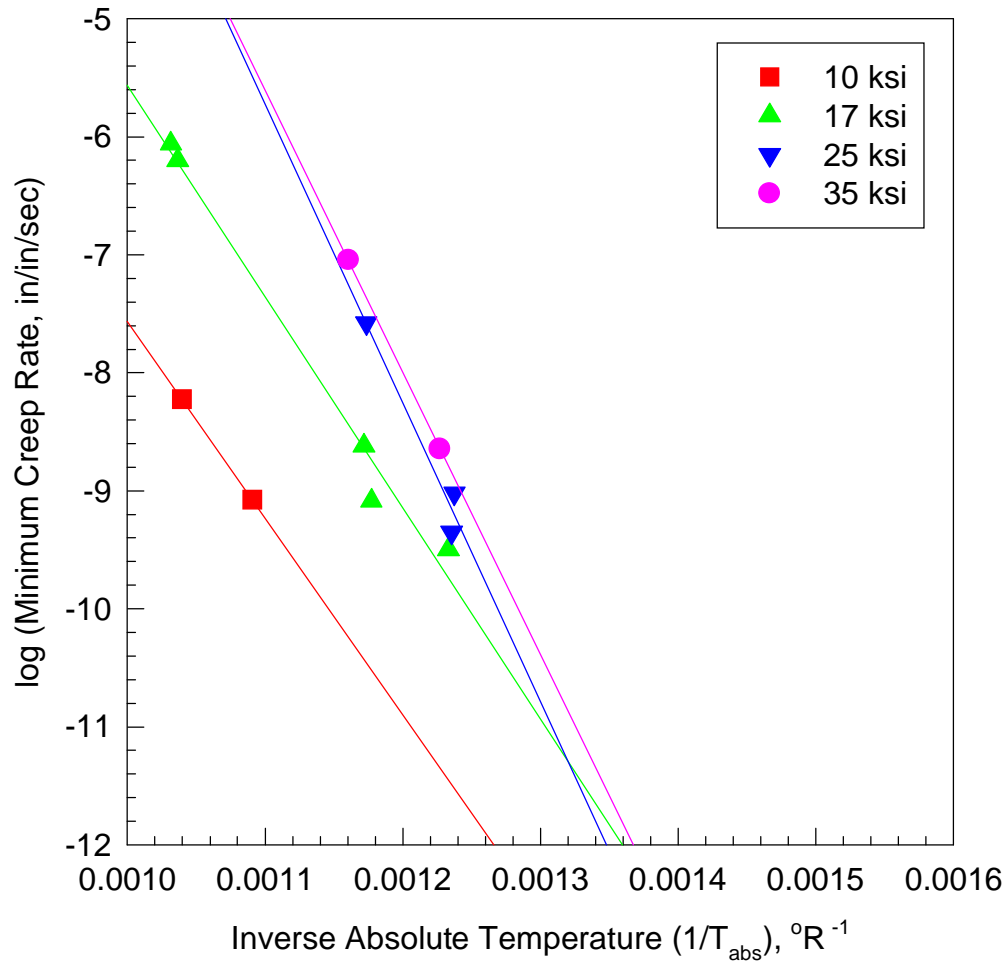
Figure 35.   Determination of Larson-Miller constant for unreinforced 2124, based upon the minimum creep rate. This figure demonstrates that the unreinforced 2124 creep data do not conform to the Larson-Miller parameter. The Larson-Miller constant is the point at which the isostress lines are supposed to converge at the ordinate. As can be seen in the data, the isostress lines converge before the ordinate, and therefore do not result in a useable value for the Larson-Miller constant.
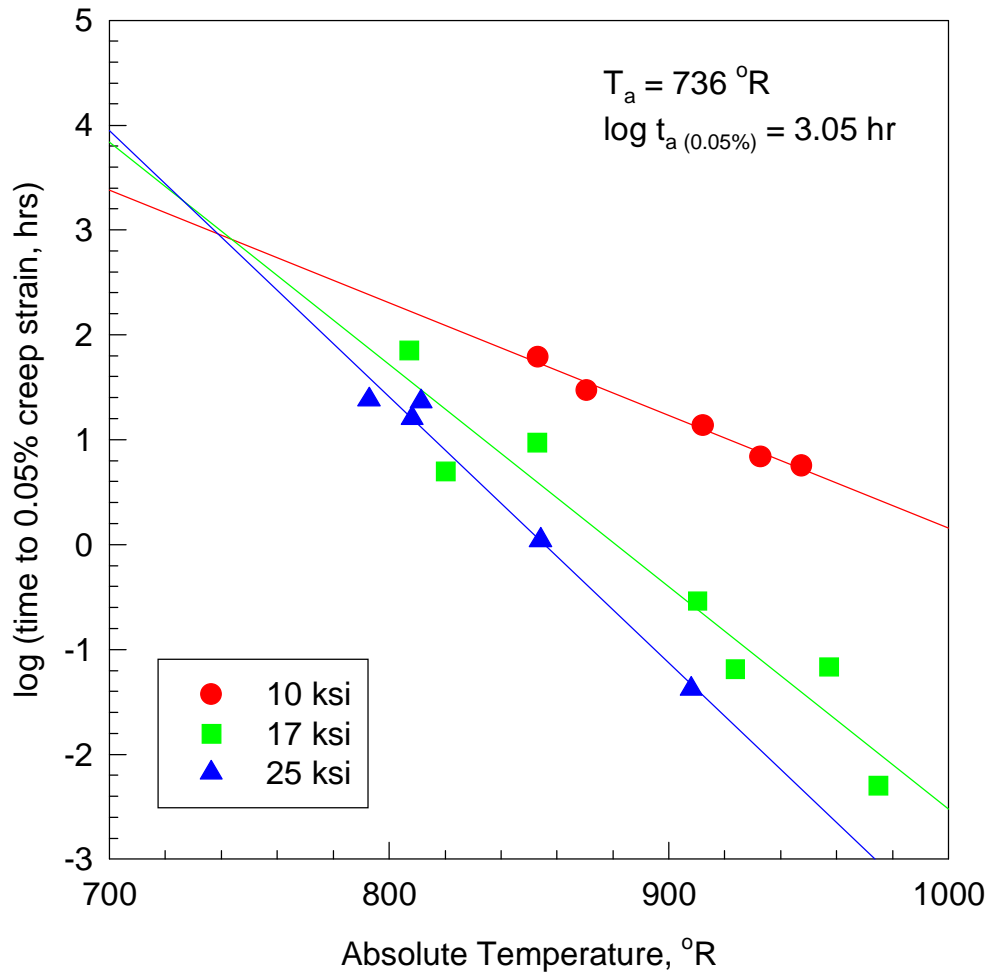
Figure 36. Determination of Manson-Haferd constant for 2124+SiC$_w$, based upon the time to 0.05% permanent creep strain. The Manson-Haferd constants are determined by the convergence point of the isostress lines. Values for the Manson-Haferd constants are shown on the figure and in Table 9.
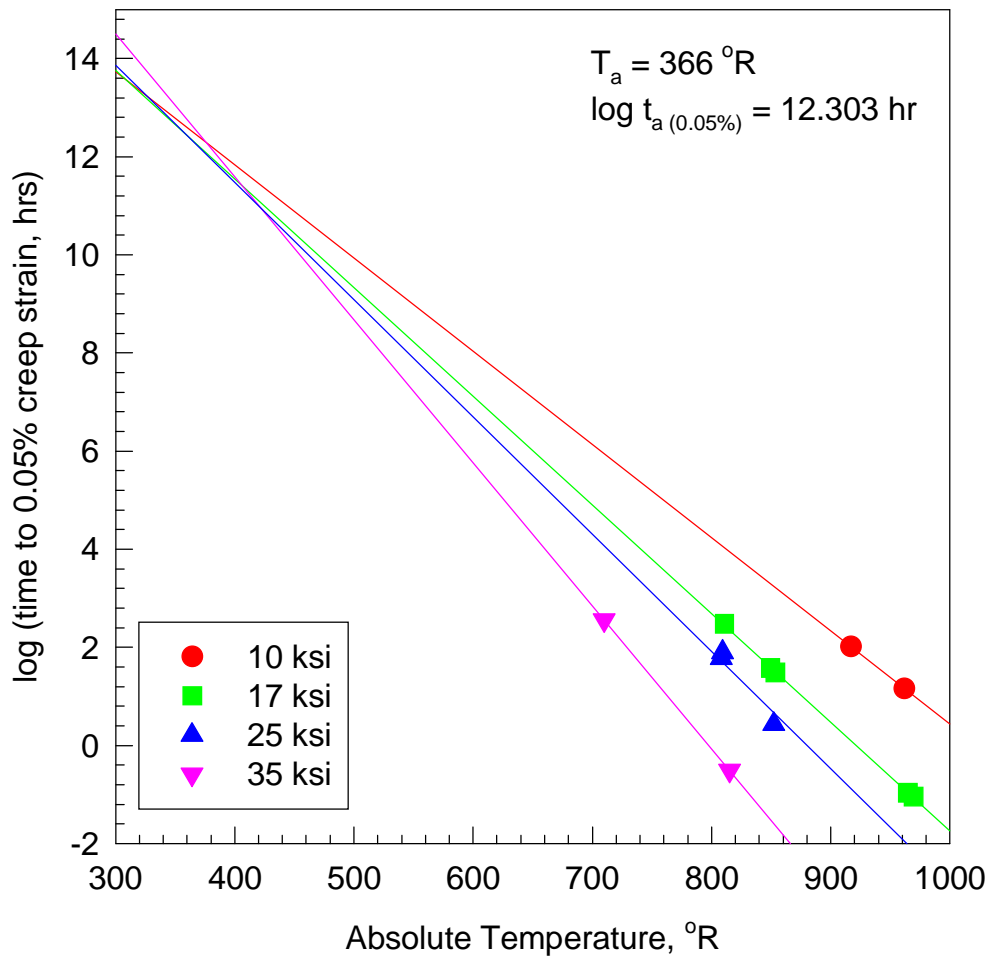
Figure 37.   Determination of Manson-Haferd constant for unreinforced 2124, based upon the time to 0.05% permanent creep strain. The Manson-Haferd constants are determined by the convergence point of the isostress lines. Values for the Manson-Haferd constants are shown on the figure and in Table 9.
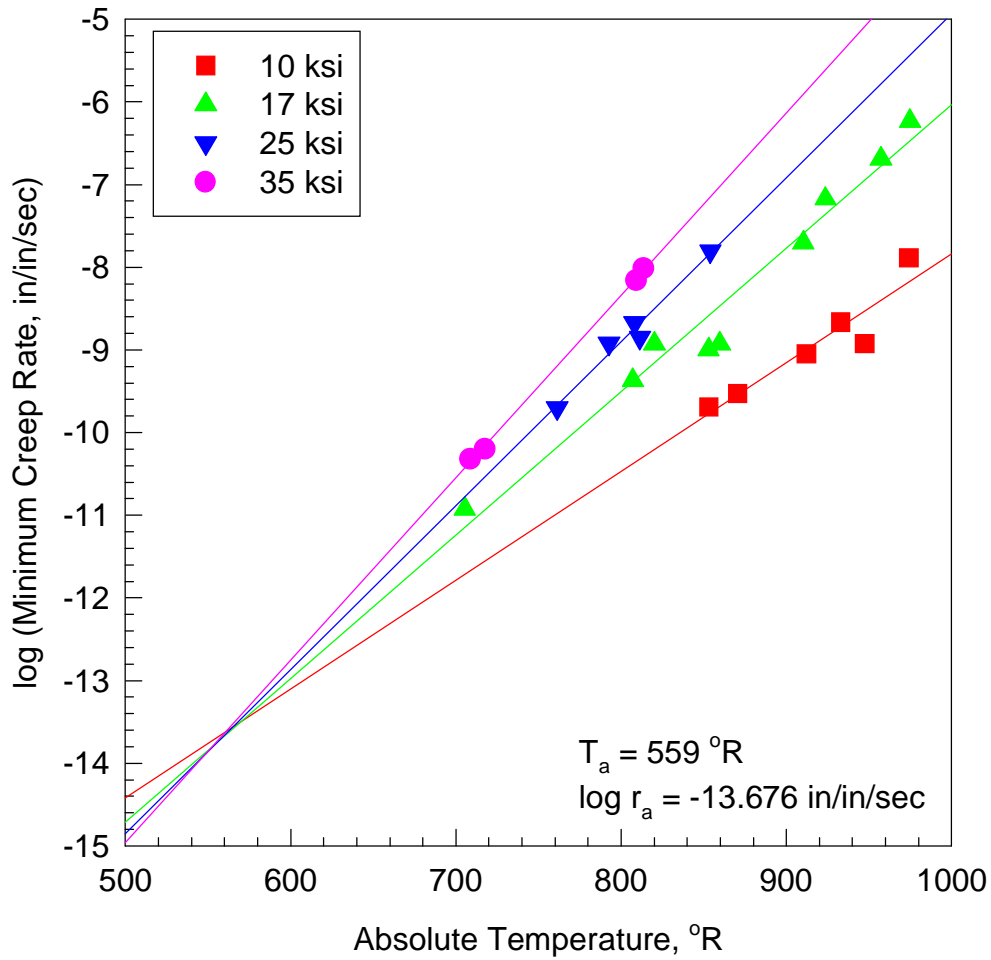
Figure 38. Determination of Manson-Haferd constant for 2124+SiC$_w$, based upon the minimum creep rate. The Manson-Haferd constants are determined by the convergence point of the isostress lines. Values for the Manson-Haferd constants are shown on the figure and in Table 9.
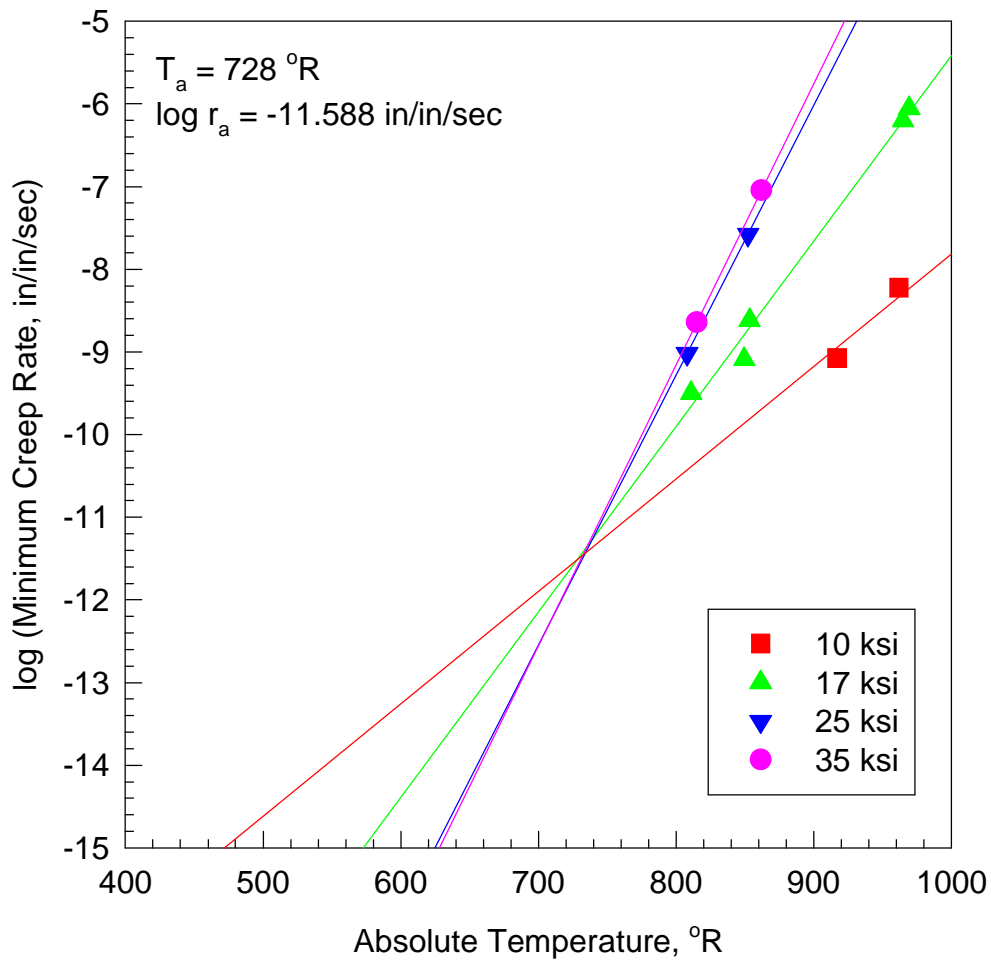
Figure 39.   Determination of Manson-Haferd constant for unreinforced 2124, based upon the minimum creep rate.   The Manson-Haferd constants are determined by the convergence point of the isostress lines. Values for the Manson-Haferd constants are shown on the figure and in Table 9.
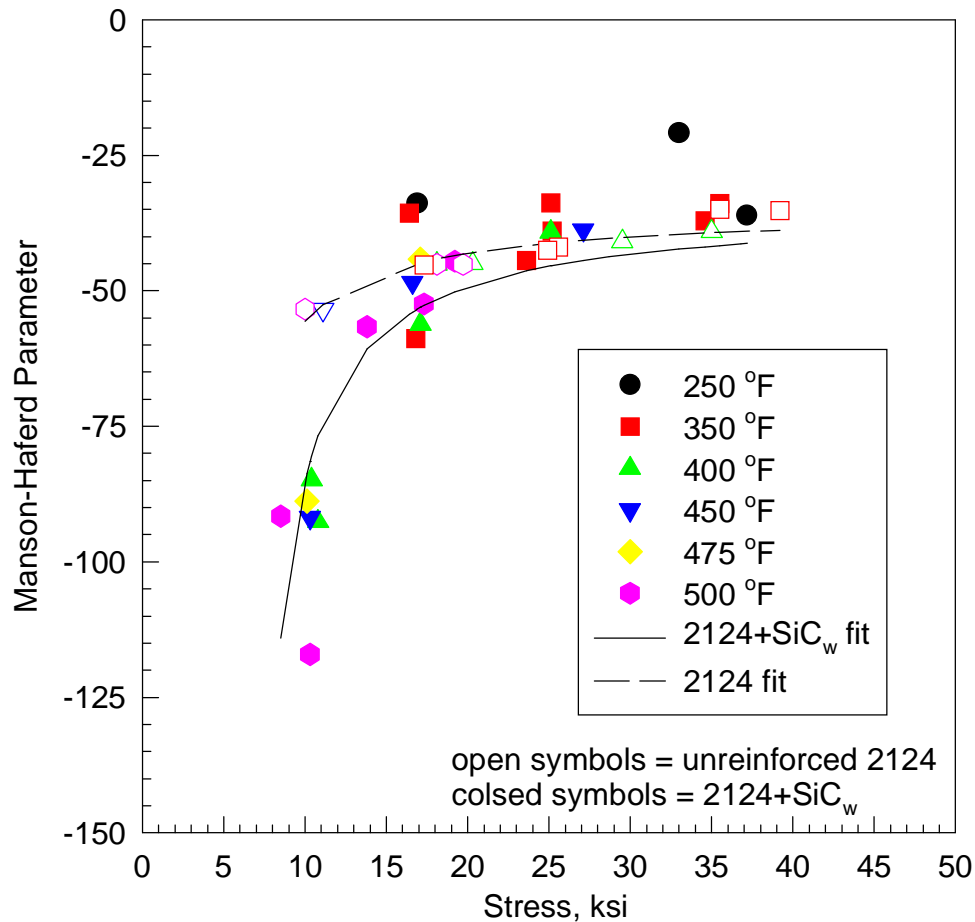
Figure 40.   Manson-Haferd master curves for time to 0.05% permanent creep strain. The open symbols and dashed line correspond to the unreinforced 2124 data, and the closed symbols and solid line correspond to the 2124+SiC$_w$ data. Notice that all temperatures and stresses collapse onto a single line for the master curve. This figure can be used to predict stresses, temperatures, or times, given the other two parameters. Alternately, the empirical equations (13) and (14), which are curve fits based on these master curves, can also be used for predicting creep data.
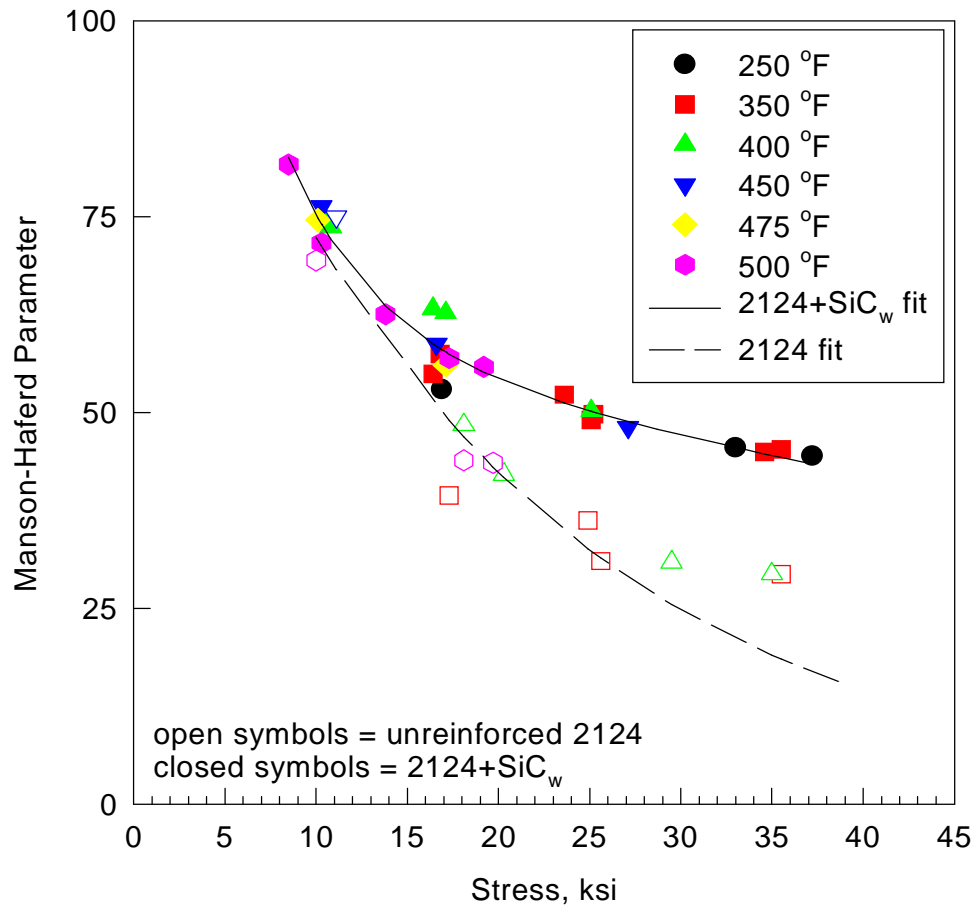
Figure 41.   Manson-Haferd master curves for minimum creep rate. The open symbols
              and dashed line correspond to the unreinforced 2124 data, and the closed
              symbols and solid line correspond to the 2124+SiC$_w$ data. Notice that all
              temperatures and stresses collapse onto a single line for the master curve.
              This figure can be used to predict stresses, temperatures, or creep rates,
              given the other two parameters. Alternately, the empirical equations (15)
              and (16), which are curve fits based on these master curves, can also be
              used for predicting creep data.
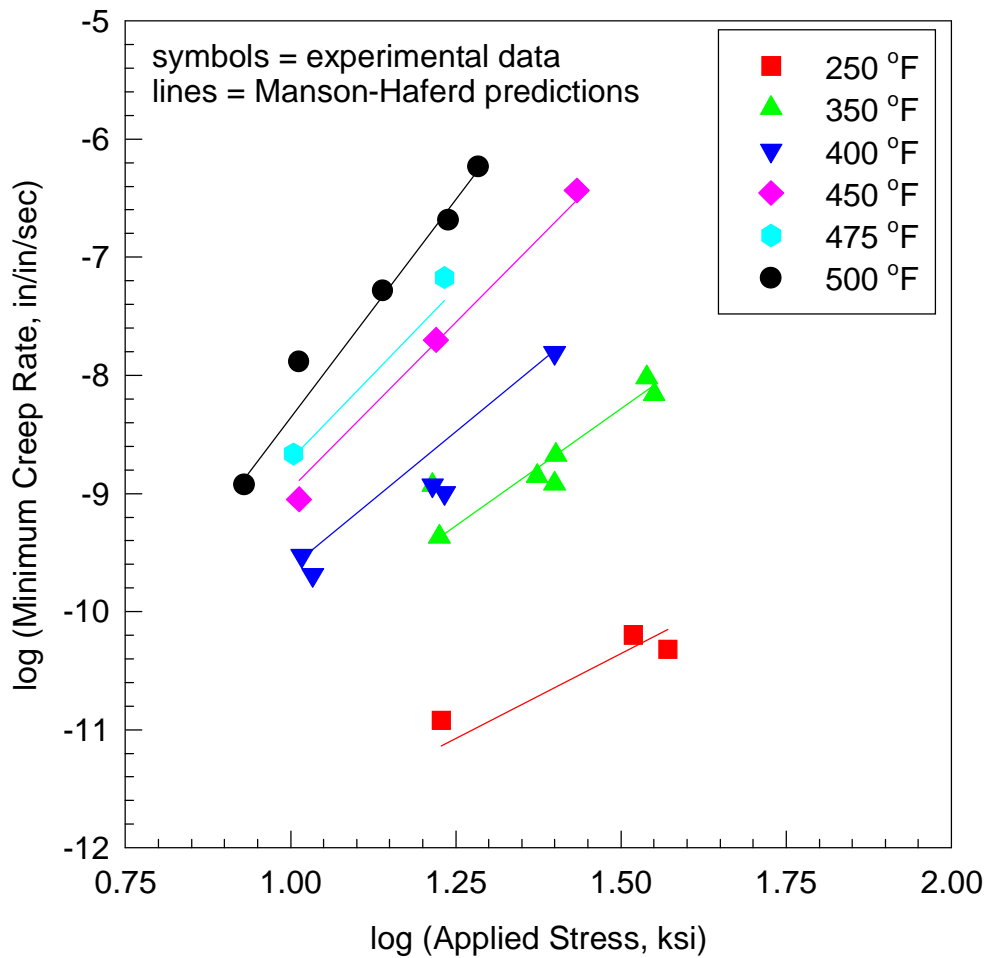
Figure 42.   Manson-Haferd predictions of creep stress exponents for 2124+SiC$_w$. The individual data points shown are experimental values. The lines represent the predictions based upon the Manson-Haferd analysis of the minimum creep rates. A comparison of experimental values to predicted values of creep stress exponents is shown in Table 10.
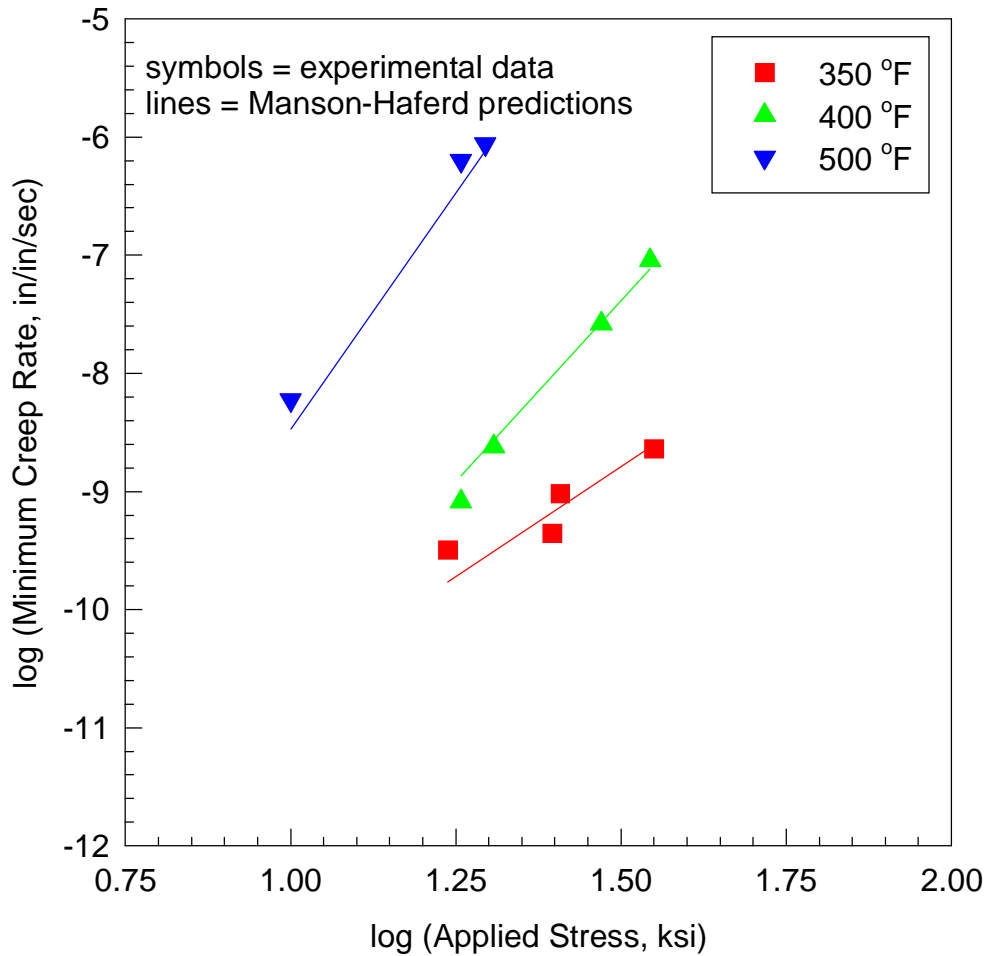
Figure 43.   Manson-Haferd predictions of creep stress exponents for unreinforced 2124. The individual data points shown are experimental values. The lines represent the predictions based upon the Manson-Haferd analysis of the minimum creep rates. A comparison of experimental values to predicted values of creep stress exponents is shown in Table 10 .
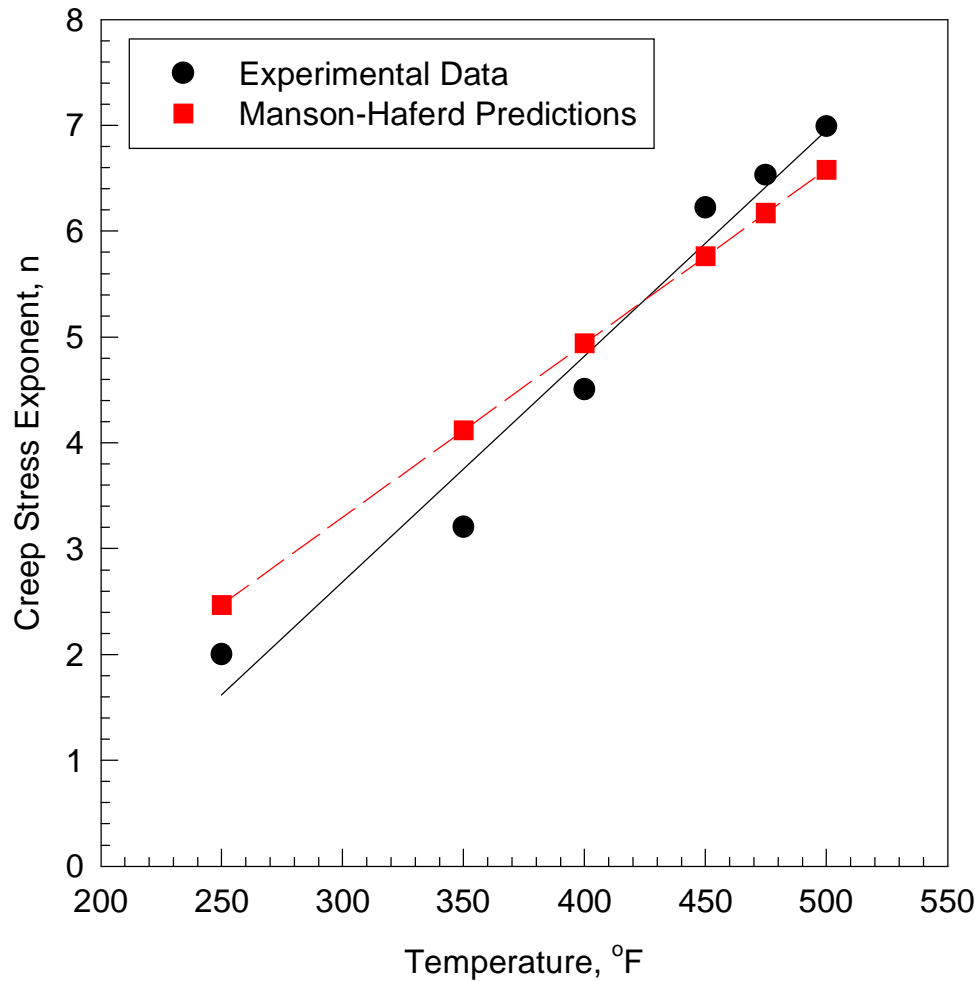
Figure 44.   Comparison of experimental and predicted temperature-dependence of stress exponents for 2124+SiC$_w$. The predicted values are based upon Manson-Haferd predictions of minimum creep rates. Notice that the predicted values of creep stress exponent fall mostly within the error bars for the experimental values. The relationship between stress exponent and temperature is linear for both experimental and predicted data sets.
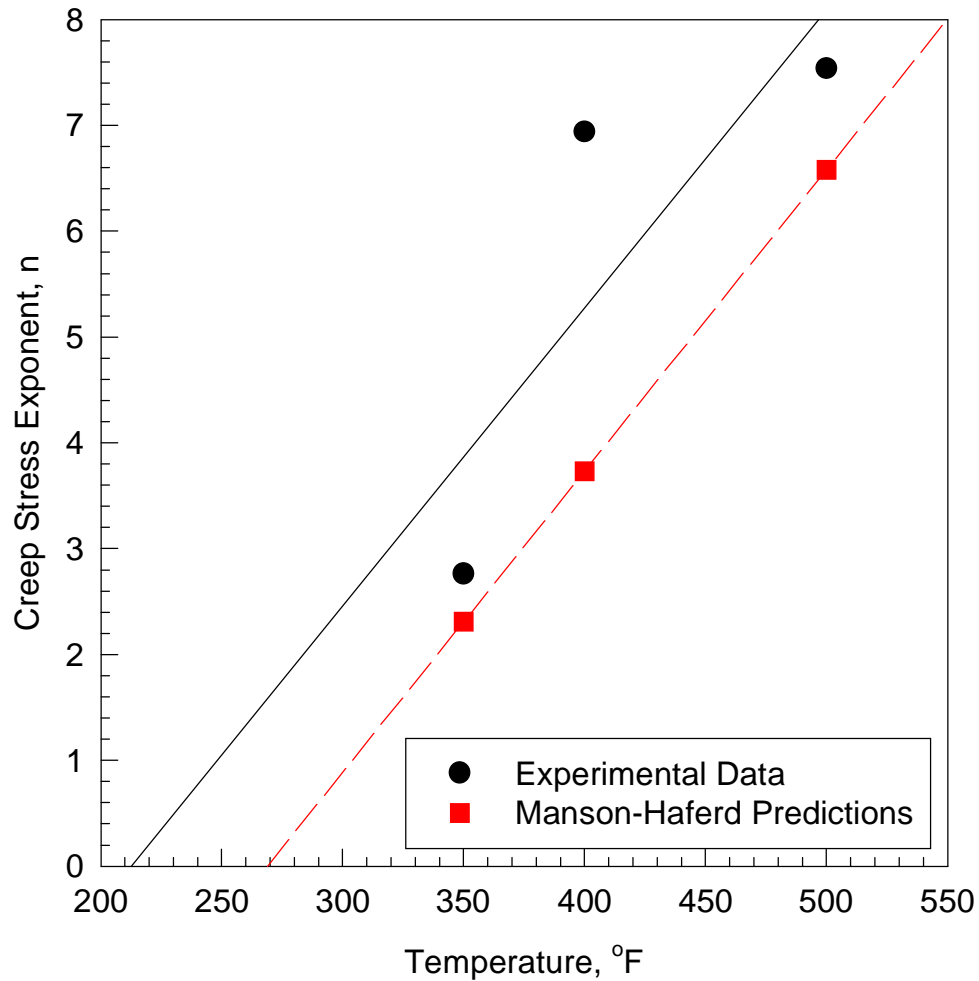
Figure 45.   Comparison of experimental and predicted temperature-dependence of stress exponents for unreinforced 2124. The predicted values are based upon Manson-Haferd predictions of minimum creep rates. Notice that the predicted values of creep stress exponent fall mostly within the error bars for the experimental values. The relationship between stress exponent and temperature is linear for both experimental and predicted data sets.
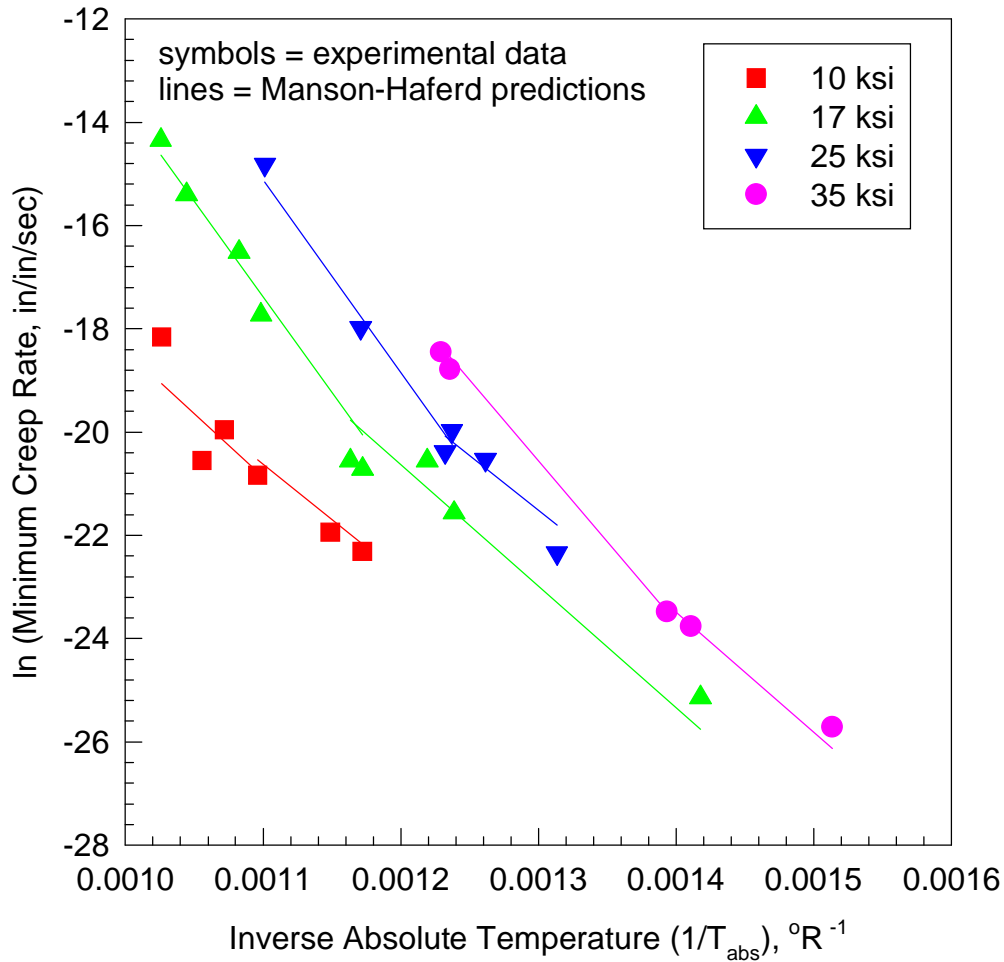
Figure 46.   Manson-Haferd predictions of apparent activation energies for creep for 2124+SiC_w. The individual data points shown are experimental values. The lines represent the predictions based upon the Manson-Haferd analysis of the minimum creep rates for the 2124+SiC_w. A comparison of experimental values to predicted values of apparent activation energies is shown in Table 11.
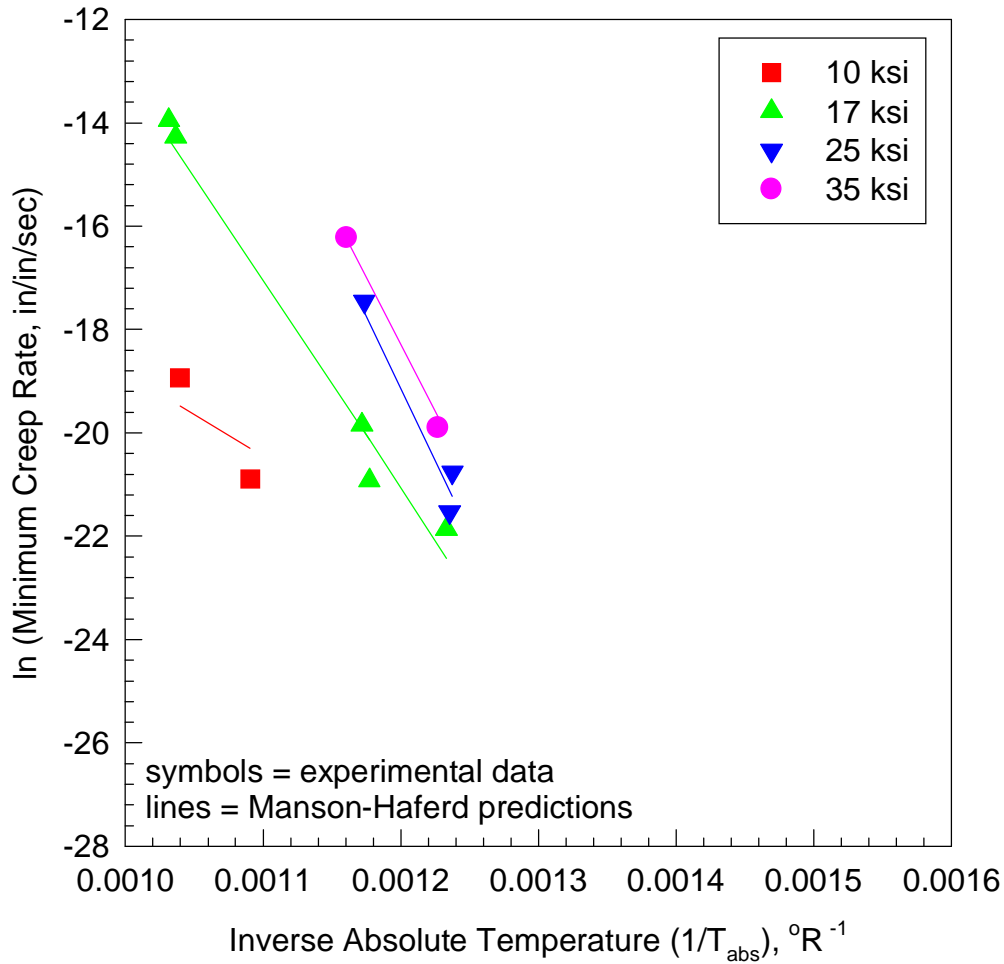
Figure 47. Manson-Haferd predictions of apparent activation energies for creep for unreinforced 2124. The individual data points shown are experimental values. The lines represent the predictions based upon the Manson-Haferd analysis of the minimum creep rates for the 2124+SiC$_w$. A comparison of experimental values to predicted values of apparent activation energies is shown in Table 11.

DEFINITION OF SYMBOLS

Symbol	Definition
A, A_1, A_2	Arrhenius constants for all stresses and temperatures
b	burgers vector
c_j	concentration of dislocation jogs
C	Larson-Miller constant, generally defined = 20
D_v	bulk self-diffusion coefficient
E	tensile modulus
$E(T)$	temperature-dependent elastic modulus
G	shear modulus
k	Boltzmann's constant
n	creep stress exponent
P_{L-M}	Larson-Miller parameter, defined in Equation (2)
P_{M-H}	Manson-Haferd parameter, defined in Equation (3)
Q_{app}	apparent activation energy for creep
Q_c	true activation energy for creep
Q_E	temperature-dependent modulus correction to activation energy for creep
r_a	Manson-Haferd constant for minimum creep rate
R	universal gas constant
t	time
$t_{0.05\%}$	time to 0.05% permanent creep strain
t_a	Manson-Haferd time constant to given creep strain level
T	temperature
T_a	Manson-Haferd temperature constant
$\dot{\varepsilon}_{ss}$	steady-state creep rate
$\dot{\varepsilon}_{min}$	minimum creep rate
σ	applied stress

TENSILE DATA

The following figures are representative stress-strain relationships for unreinforced 2124 and 2124+SiC$_w$ composite. Curves are shown for room temperature tests on unreinforced 2124. In addition, one curve is shown for 2124+SiC$_w$ for each of the temperatures tested. Tests were conducted at room temperature and at 50°F increments between 250°F and 500°F in the longitudinal direction (parallel to the extrusion direction). Tests were also conducted at room temperature on both materials in the transverse direction (perpendicular to the extrusion direction). Strain measuring devices are indicated in the figure captions; specimens tested using strain gages only show the stress-strain data up to the point of failure of the strain gages, not the entire stress-strain relationship.

LIST OF FIGURES

Figure B1.   Typical engineering stress-strain data from room temperature tensile test on unreinforced 2124 in the longitudinal orientation (specimen LW17). Strain measurement is based upon average of back-to-back extensometers, each with a 1.000" gage length.
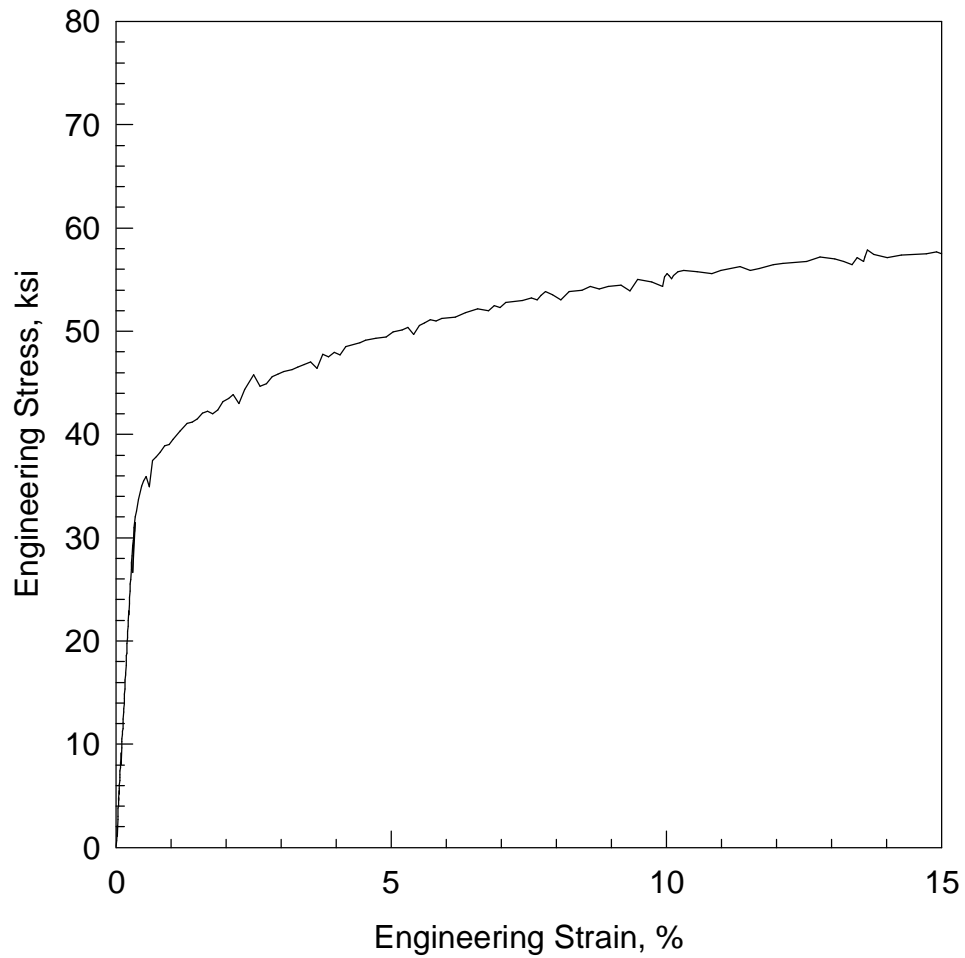
Figure B2.   Typical engineering stress-strain data from room temperature tensile test on unreinforced 2124 in the transverse orientation (specimen TW7). Strain measurement is based upon average of back-to-back extensometers, each with a 1.000" gage length.
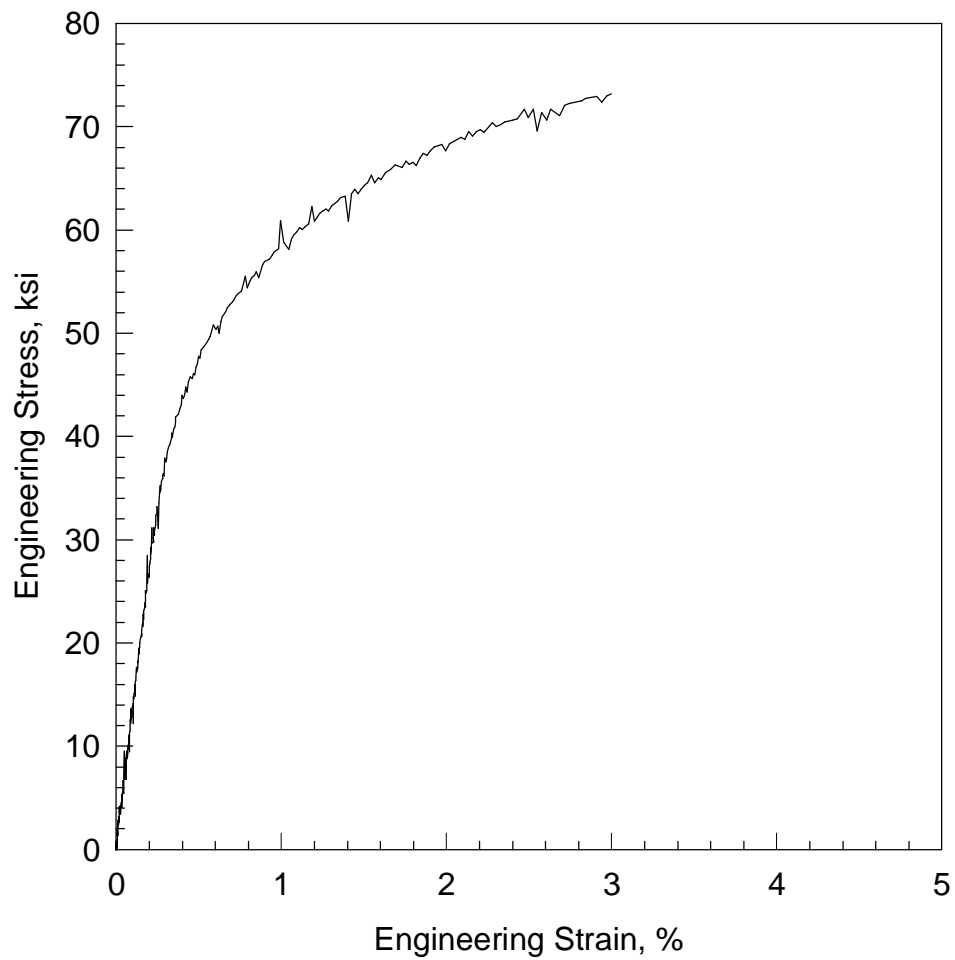
Figure B3.   Typical engineering stress-strain data from room temperature tensile test on 2124+SiC$_w$ in the longitudinal orientation (specimen ZL50). Strain measurement is based upon average of back-to-back extensometers, each with a 1.000" gage length.
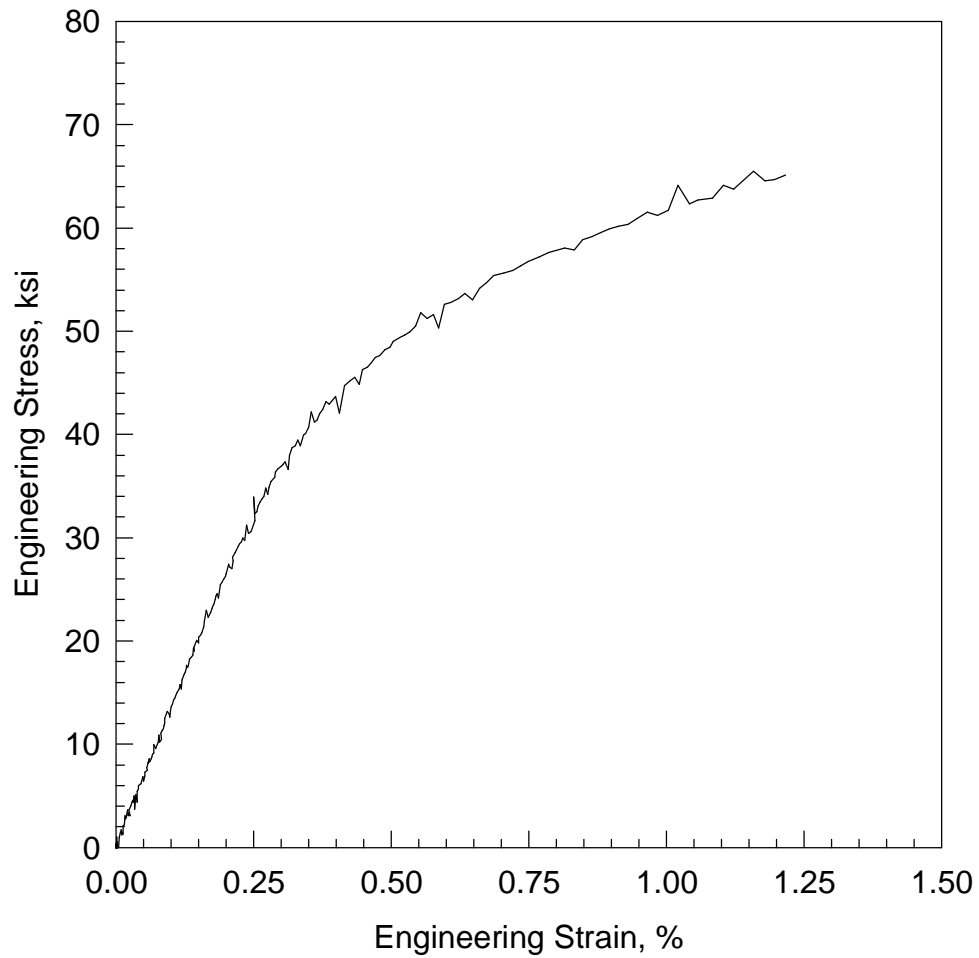
Figure B4.   Typical engineering stress-strain data from room temperature tensile test on 2124+SiC$_w$ in the longitudinal orientation (specimen ZL61). Strain measurement is based upon average of back-to-back strain gages which failed prior to the end of the test.
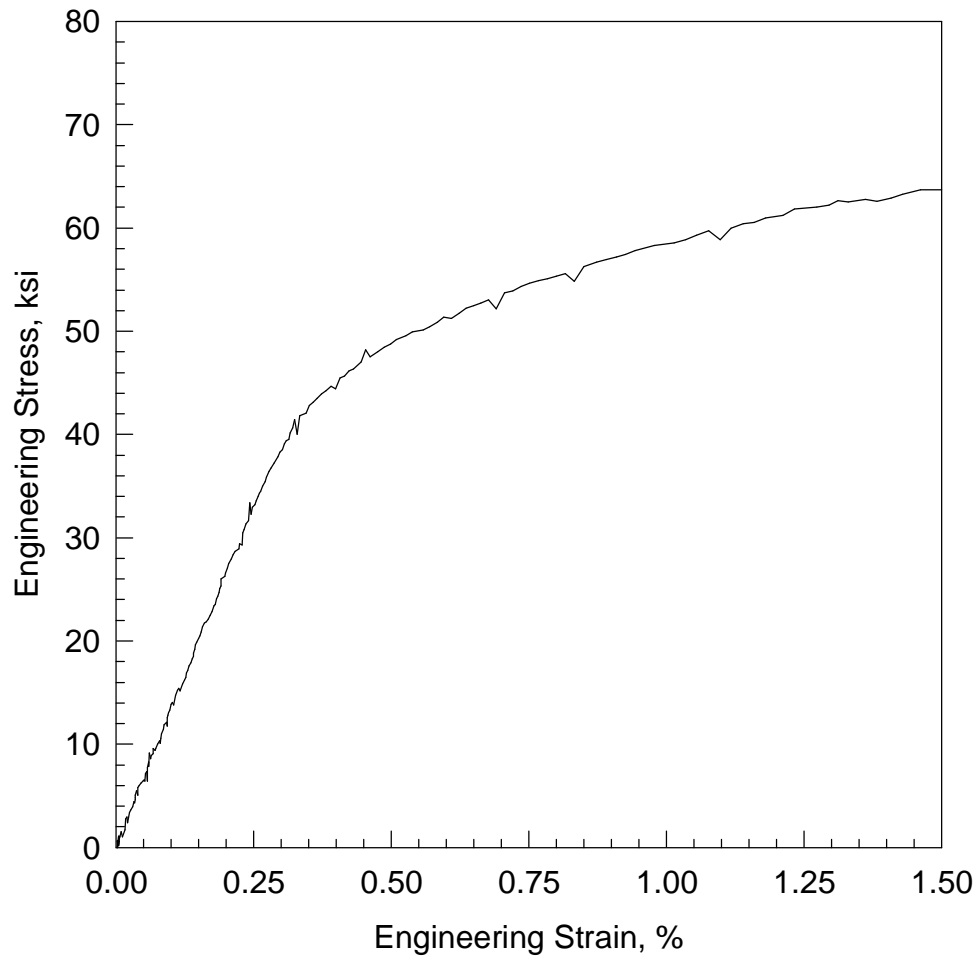
Figure B5.   Typical engineering stress-strain data from room temperature tensile test on 2124+SiC$_w$ in the transverse orientation (specimen TZ3). Strain measurement is based upon average of back-to-back strain gages which failed prior to the end of the test.
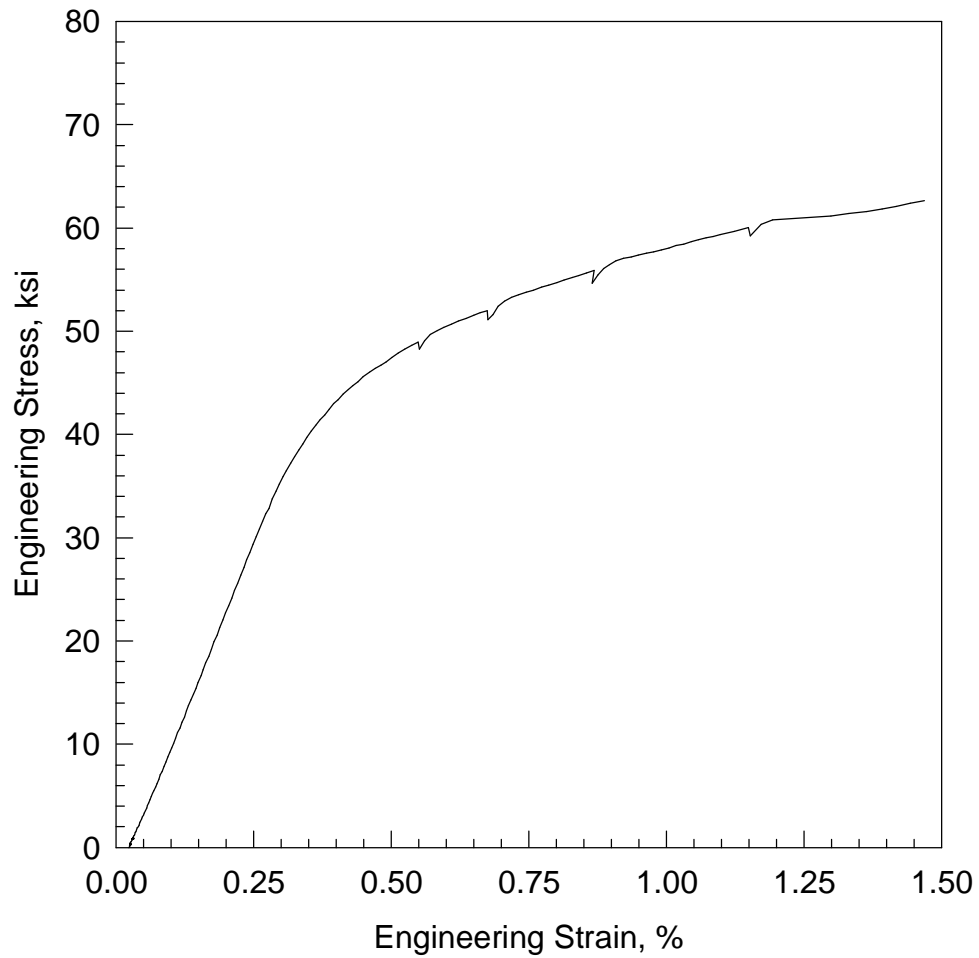
Figure B6.   Typical engineering stress-strain data from tensile test at 250°F on 2124+SiC$_w$ in the longitudinal orientation (specimen LZ104). Strain measurement is based upon average of back-to-back strain gages which failed prior to the end of the test.
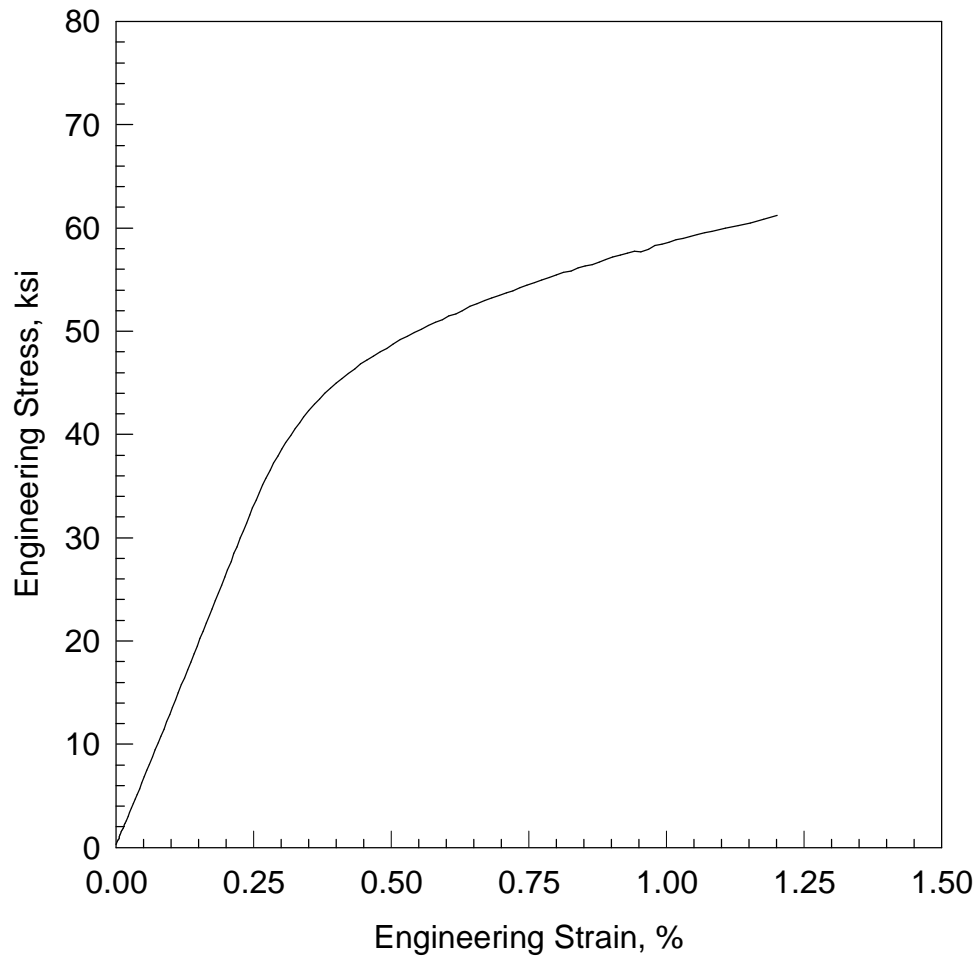
Figure B7.   Typical engineering stress-strain data from tensile test at 300°F on
2124+SiC$_w$ in the longitudinal orientation (specimen LZ109).   Strain
measurement is based upon average of back-to-back strain gages which
failed prior to the end of the test.
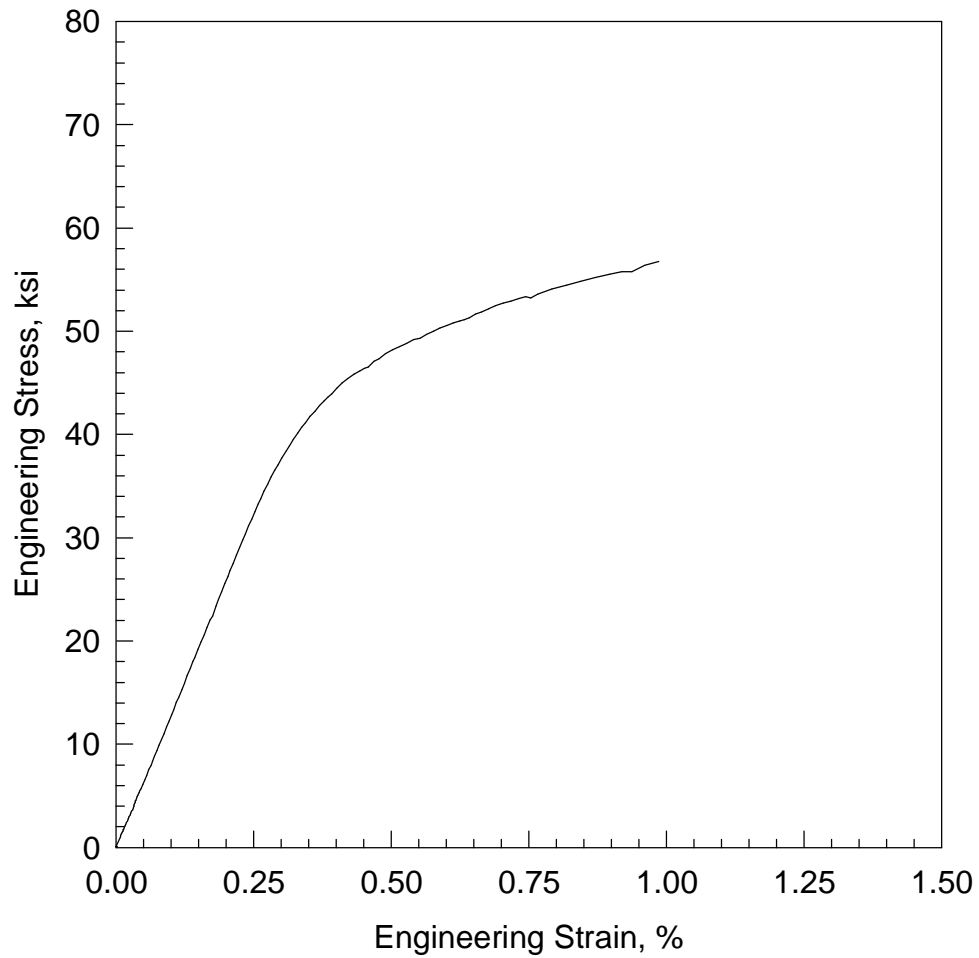
Figure B8.   Typical engineering stress-strain data from tensile test at 350°F on 2124+SiC$_w$ in the longitudinal orientation (specimen LZ114). Strain measurement is based upon average of back-to-back strain gages which failed prior to the end of the test.
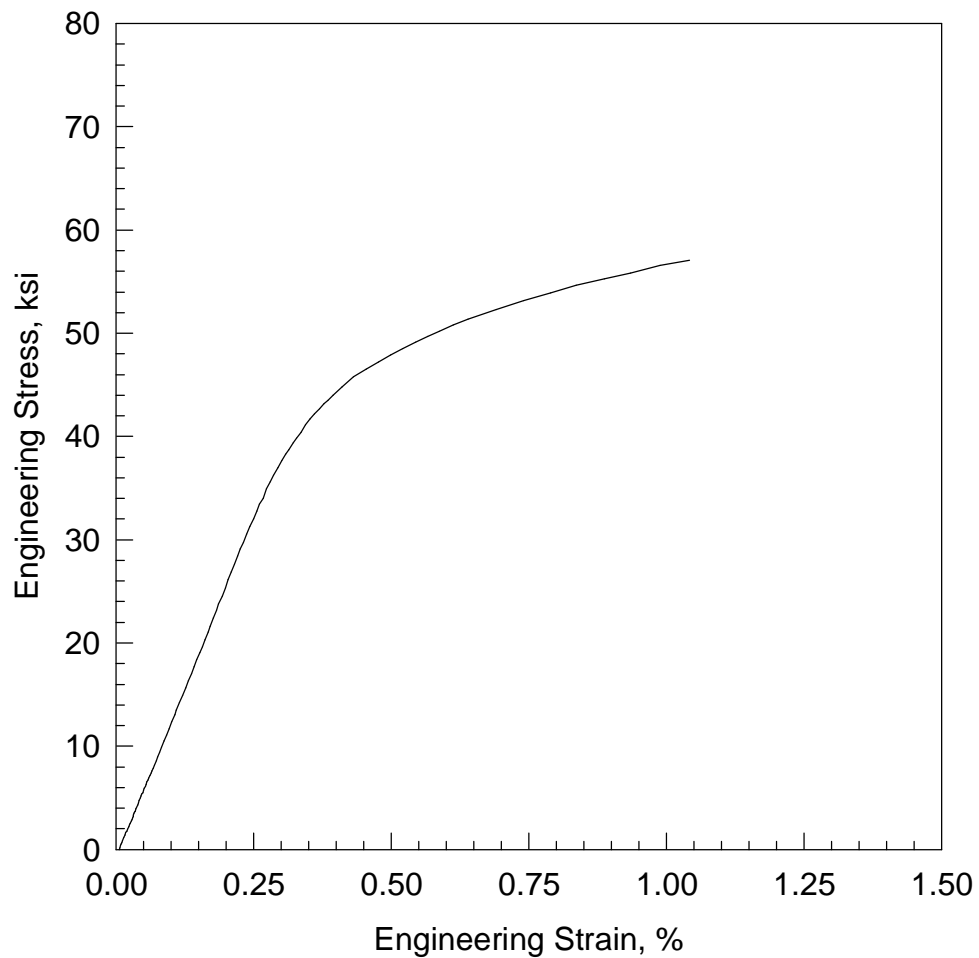
Figure B9.   Typical engineering stress-strain data from tensile test at 400°F on 2124+SiC$_w$ in the longitudinal orientation (specimen LZ119).   Strain measurement is based upon average of back-to-back strain gages which failed prior to the end of the test.
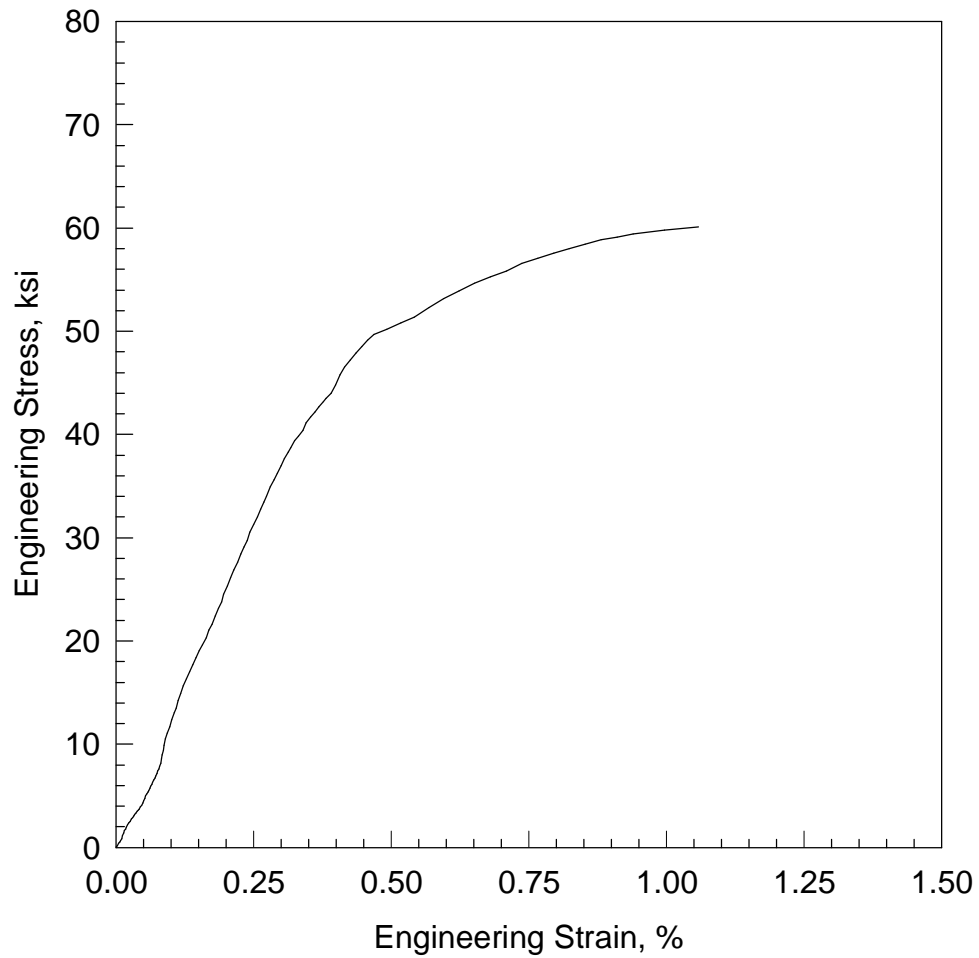
Figure B10.   Typical engineering stress-strain data from tensile test at 450°F on 2124+SiC$_w$ in the longitudinal orientation (specimen LZ124). Strain measurement is based upon average of back-to-back strain gages which failed prior to the end of the test.
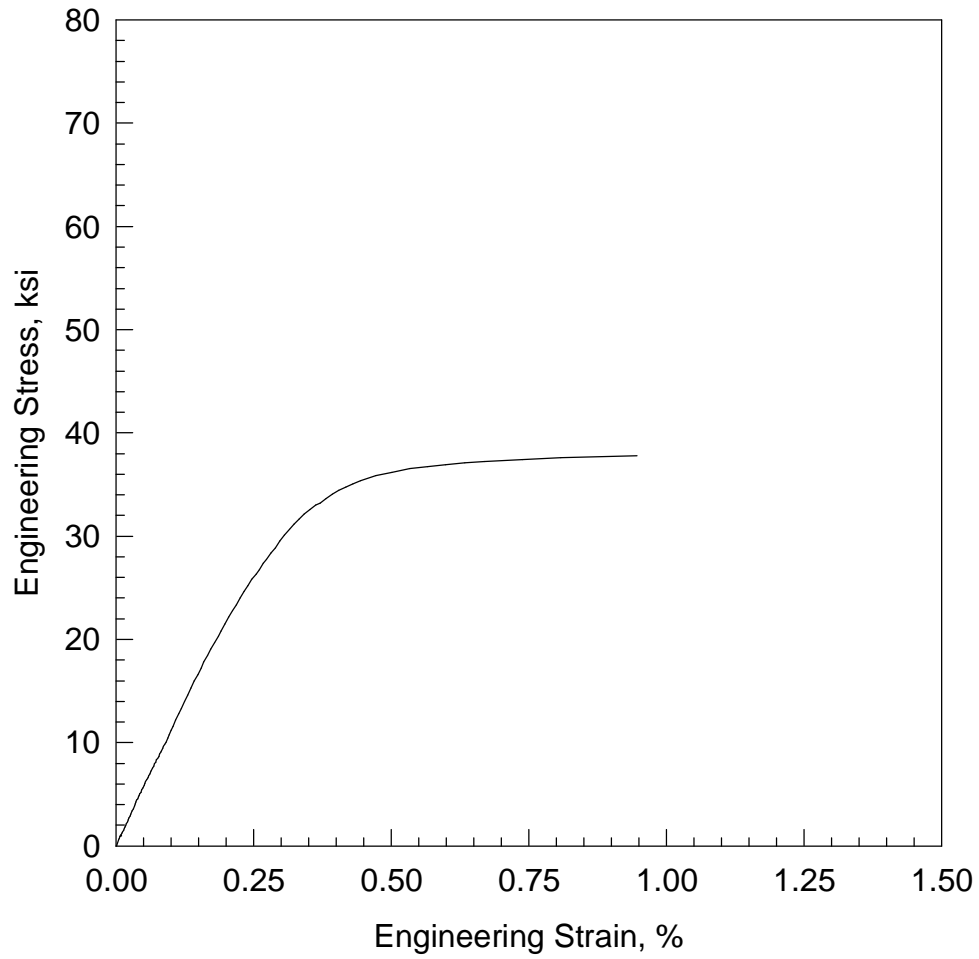
Figure B11.   Typical engineering stress-strain data from tensile test at 500°F on 2124+SiC$_w$ in the longitudinal orientation (specimen LZ129).   Strain measurement is based upon average of back-to-back strain gages which failed prior to the end of the test.

CREEP DATA

The following figures are creep curves from each test conducted on unreinforced 2124 and 2124+SiC$_w$ composite. The strain data are the average of strains from back-to-back strain gages plotted as a function of time. Each figure shows the creep relationship in addition to the linear regression construction for determination of minimum creep rate (slope). The figure captions include the slope, as well as the final time and strain for the test, and whether the test was terminated or ended due to creep rupture.

LIST OF FIGURES

ZL60

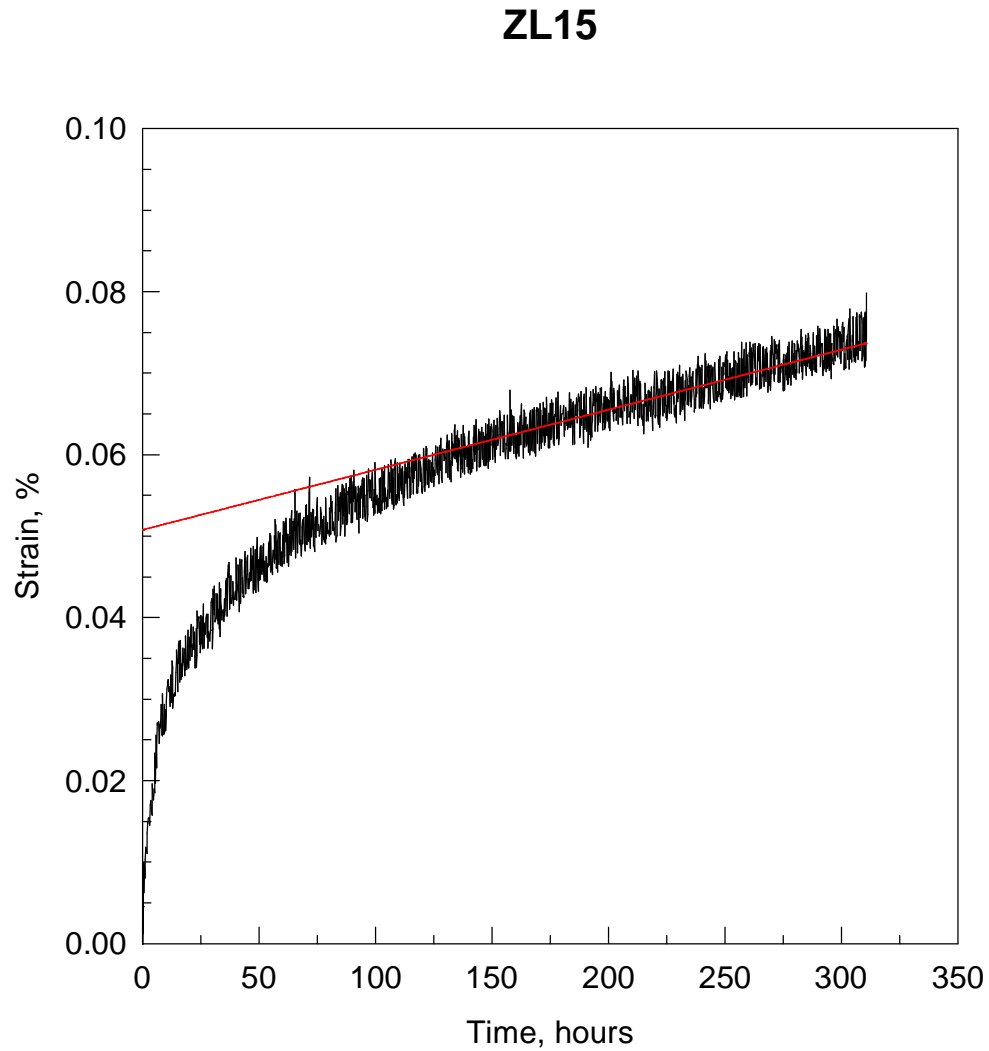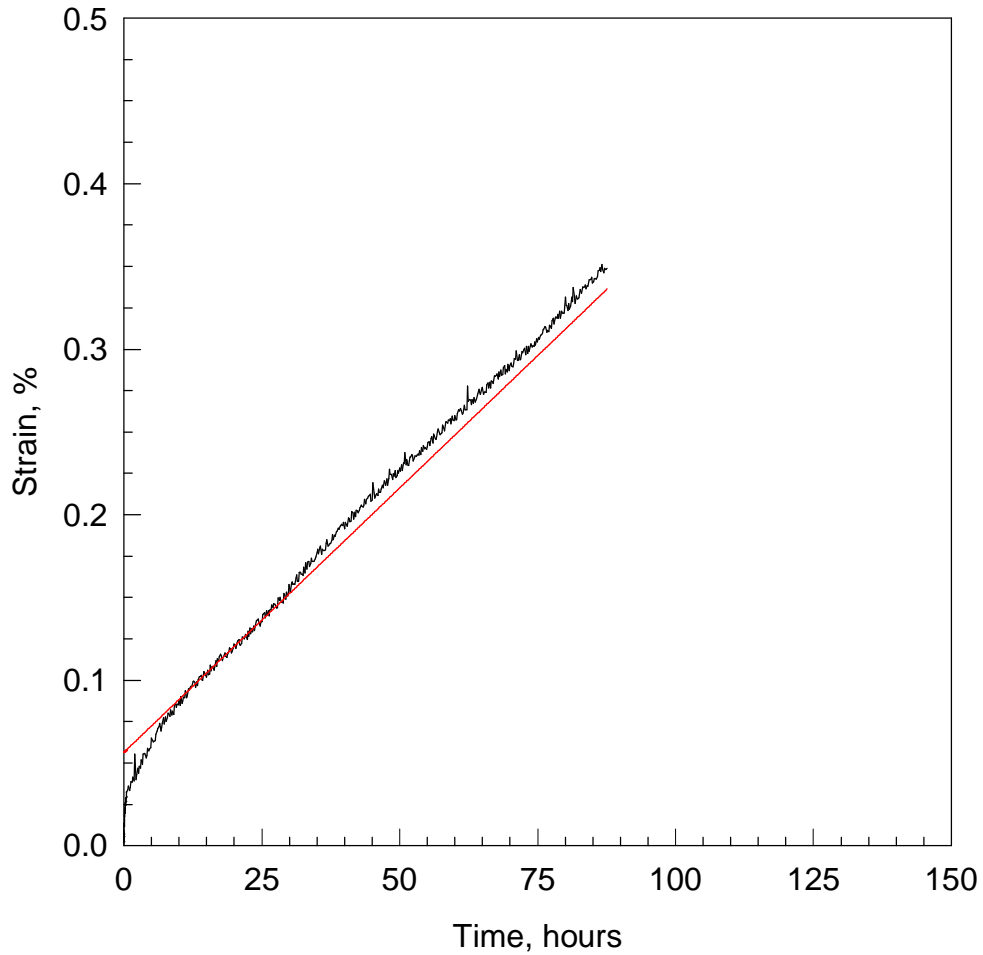Figure C1.   Creep of $2124+SiC_w$ at 200°F and 37 ksi (specimen ZL60). Test stopped after 1035 hours and 0.011% strain. Minimum creep rate shown is 6.81 x 10^{-12} in/in/sec. Gap in data is a data acquisition malfunction where part of the data was lost.

ZL32
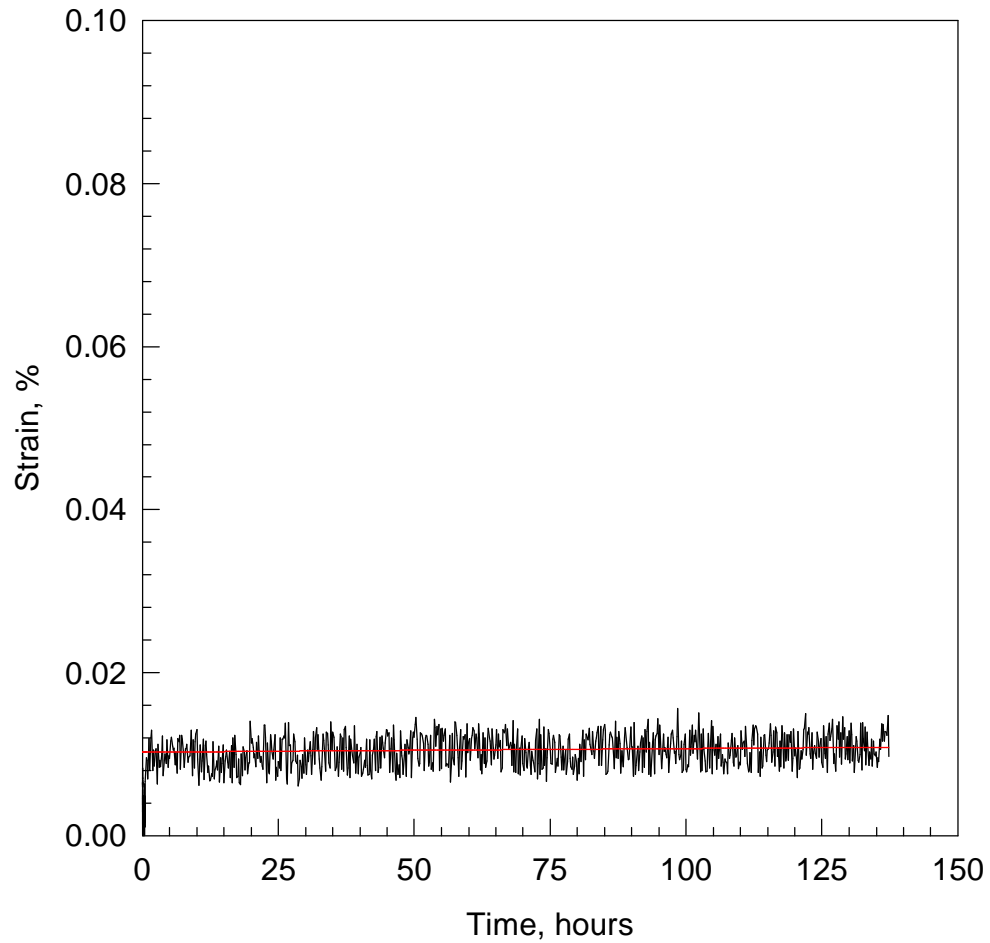
Figure C2.   Creep of 2124+SiC$_w$ at 250°F and 17 ksi (specimen ZL32). Test stopped after 137 hours and 0.013% strain. Minimum creep rate shown is 1.20 x 10^{-11} in/in/sec.
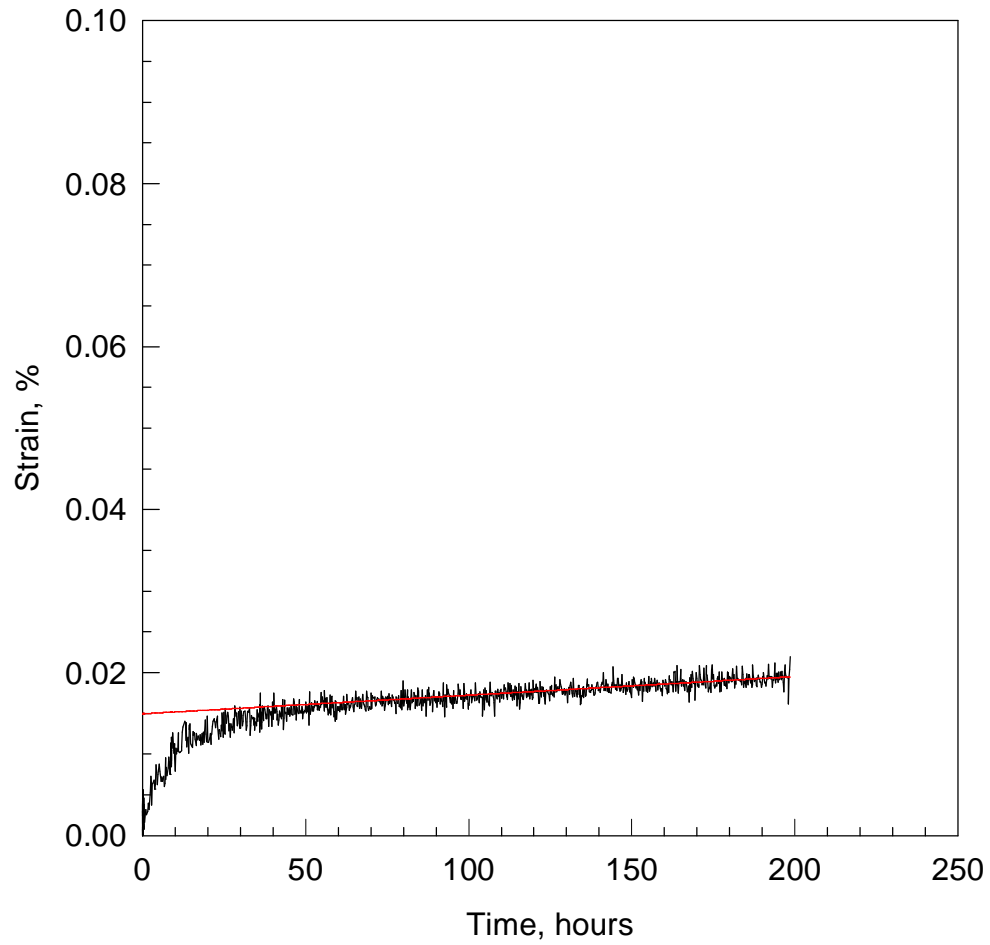
ZL47

Figure C3.   Creep of 2124+SiC$_w$ at 250°F and 35 ksi (specimen ZL47). Test stopped after 199 hours and 0.030% strain. Minimum creep rate shown is 6.35 x 10^{-11} in/in/sec.
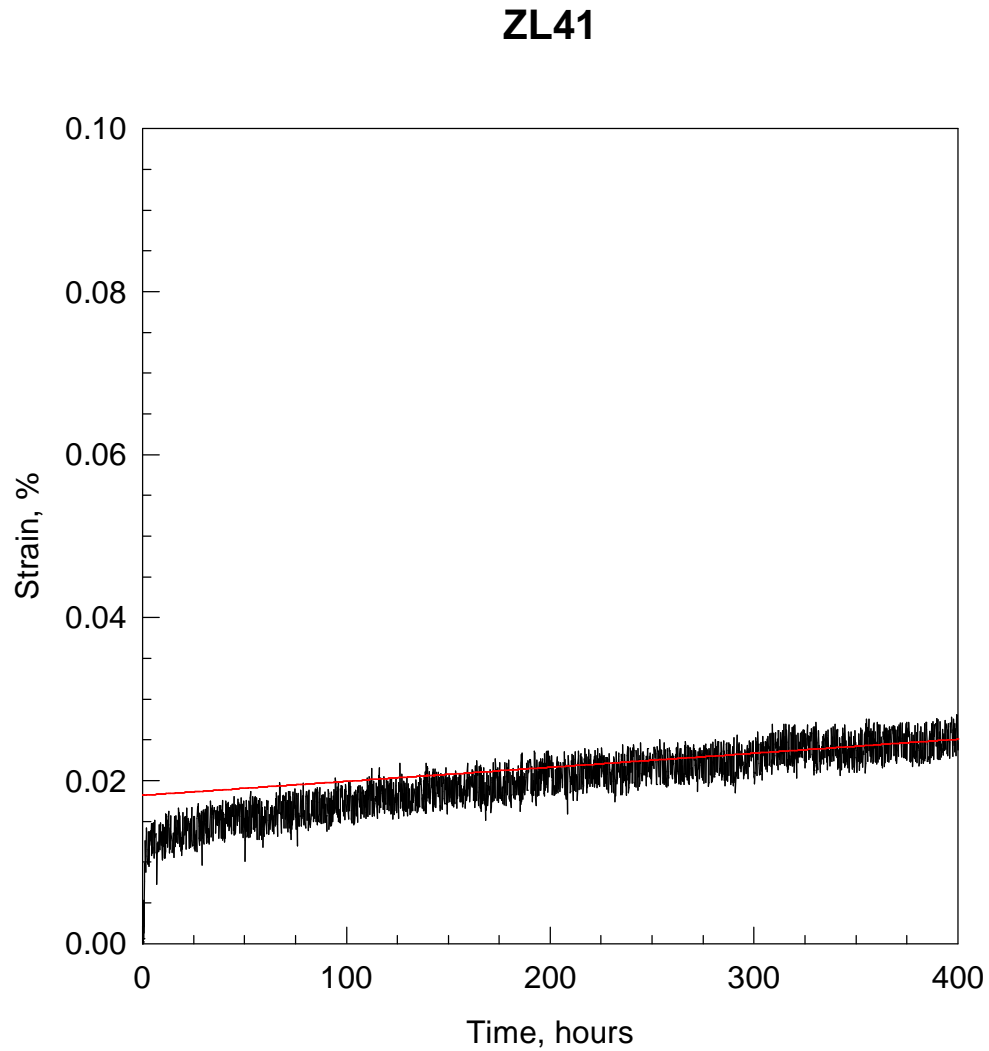
ZL41

Figure C4.   Creep of 2124+SiC$_w$ at 250°F and 37 ksi (specimen ZL41). Test stopped after 401 hours and 0.025% strain. Minimum creep rate shown is 4.78 x 10^{-11} in/in/sec.
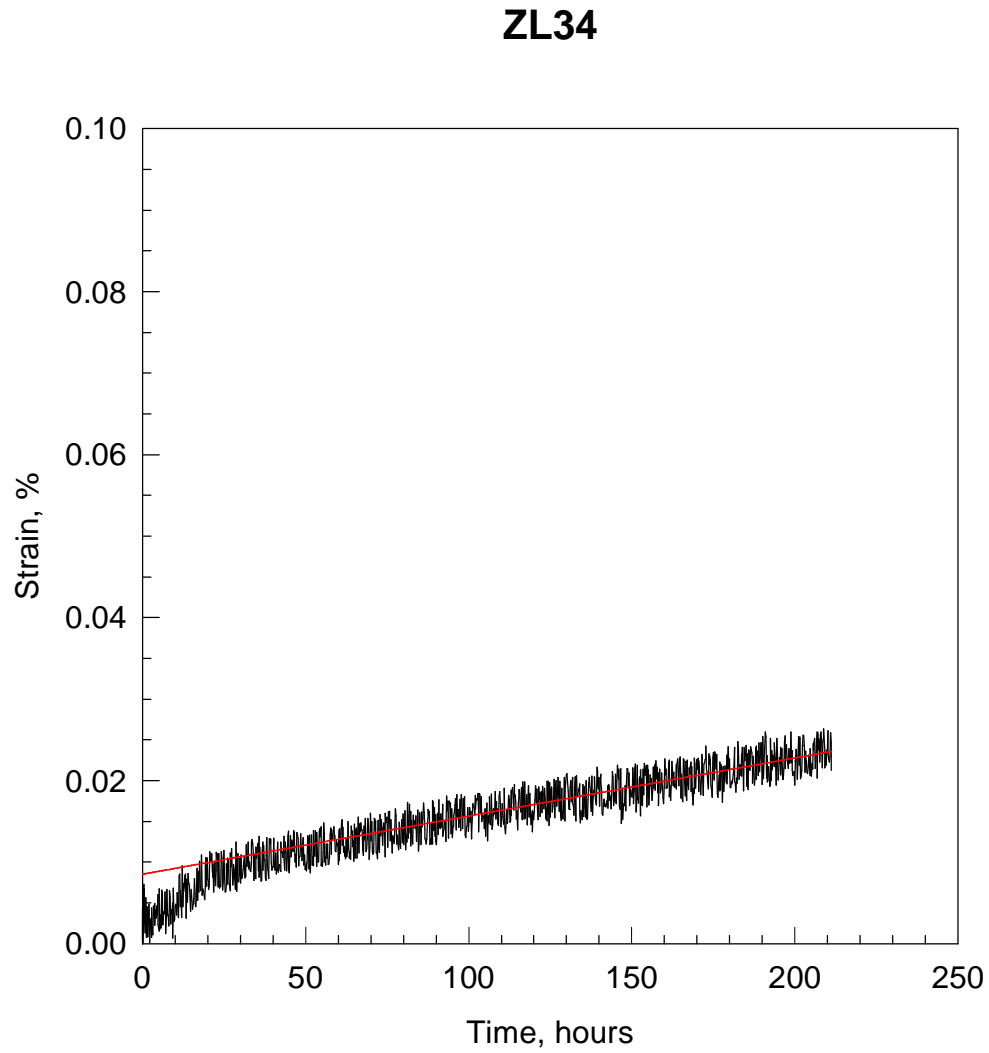
ZL34

Figure C5.   Creep of 2124+SiC$_w$ at 300°F and 25 ksi (specimen ZL34). Test stopped
after 211 hours and 0.059% strain. Minimum creep rate shown is 1.98 x
10^{-10} in/in/sec.
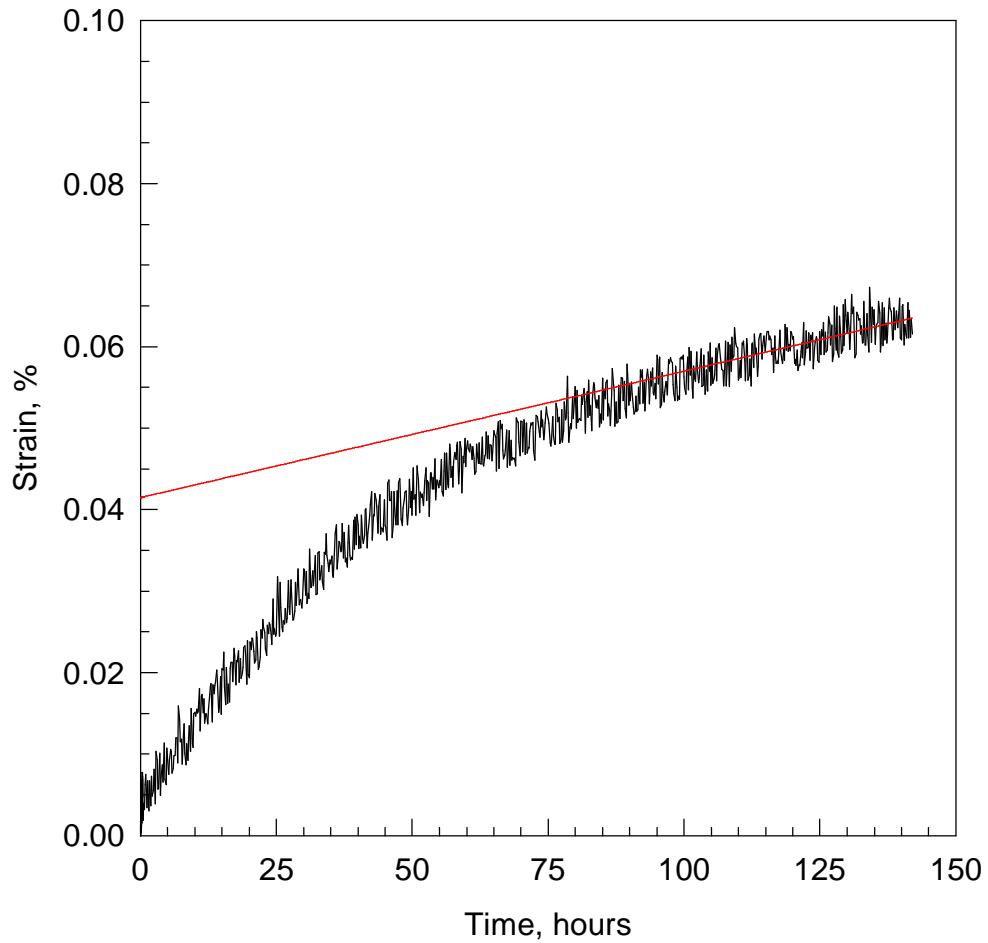
ZL11
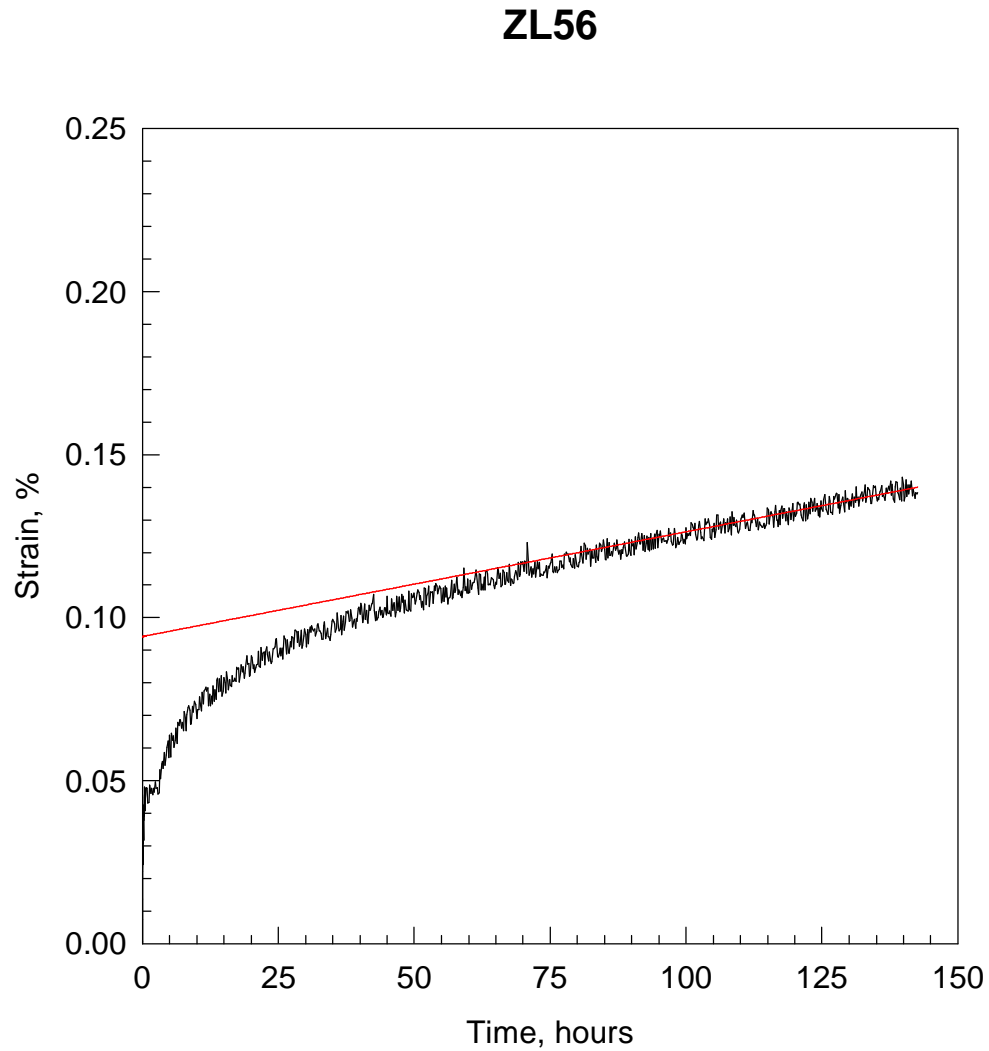

Figure C6.   Creep of 2124+SiC$_w$ at 350°F and 17 ksi (specimen ZL11). Test stopped after 142 hours and 0.071% strain. Minimum creep rate shown is 4.31 x 10^{-10} in/in/sec.
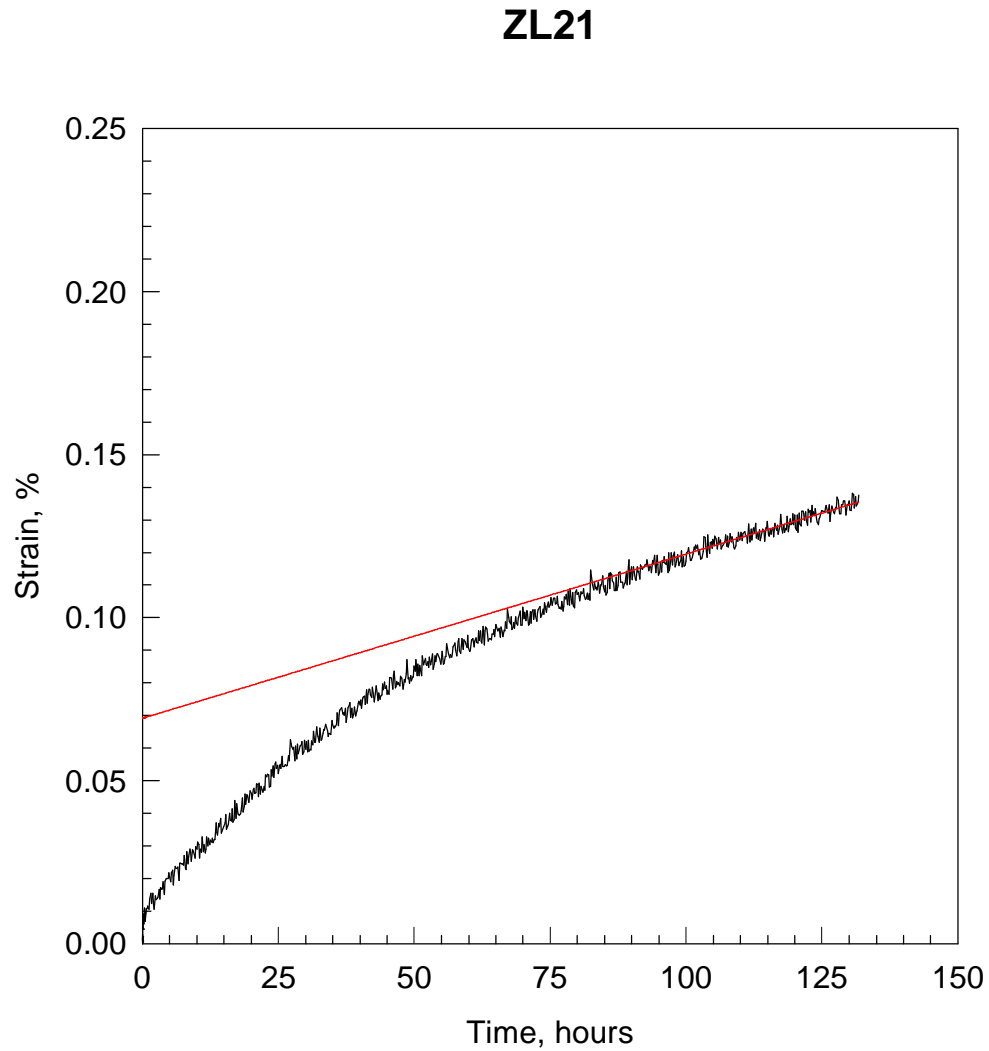
ZL21

Figure C7.   Creep of 2124+SiC$_w$ at 350°F and 25 ksi (specimen ZL21). Test stopped after 132 hours and 0.136% strain. Minimum creep rate shown is 1.40 x 10^{-9} in/in/sec.
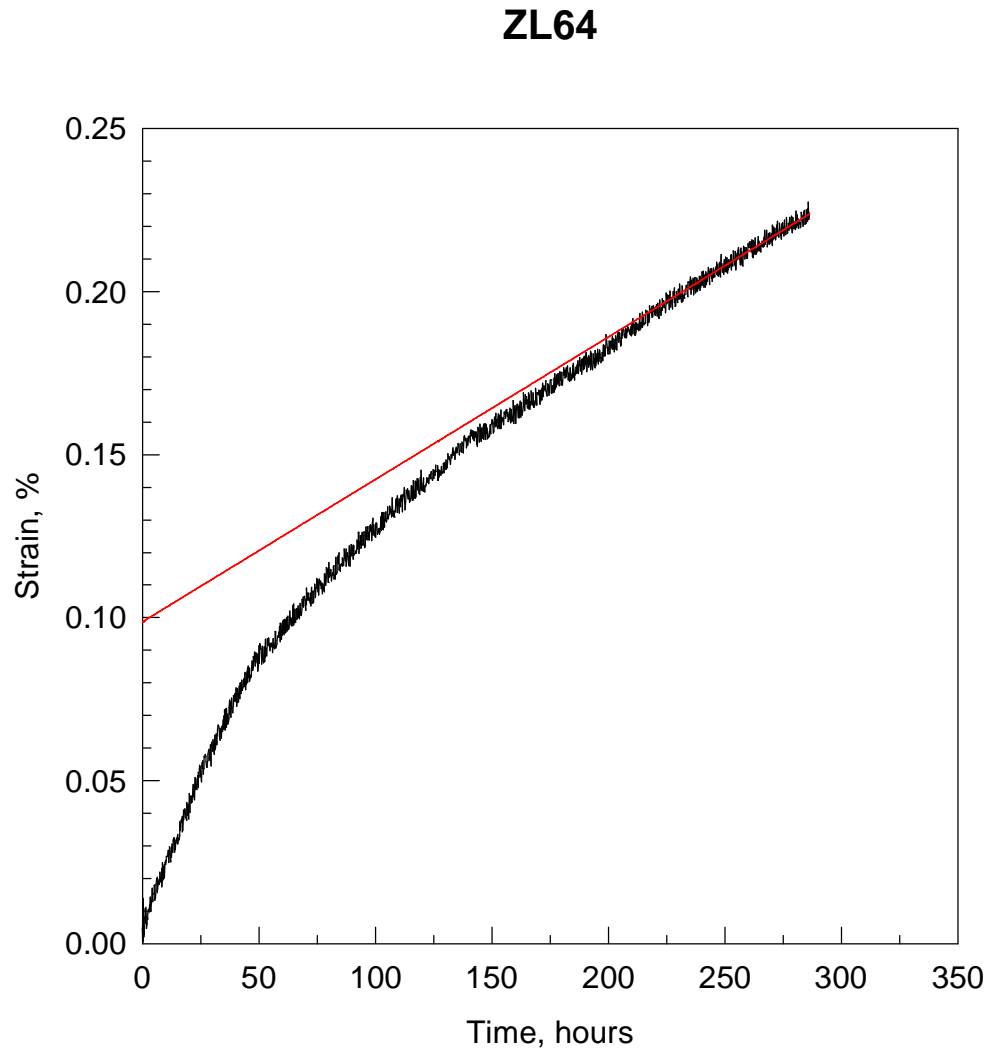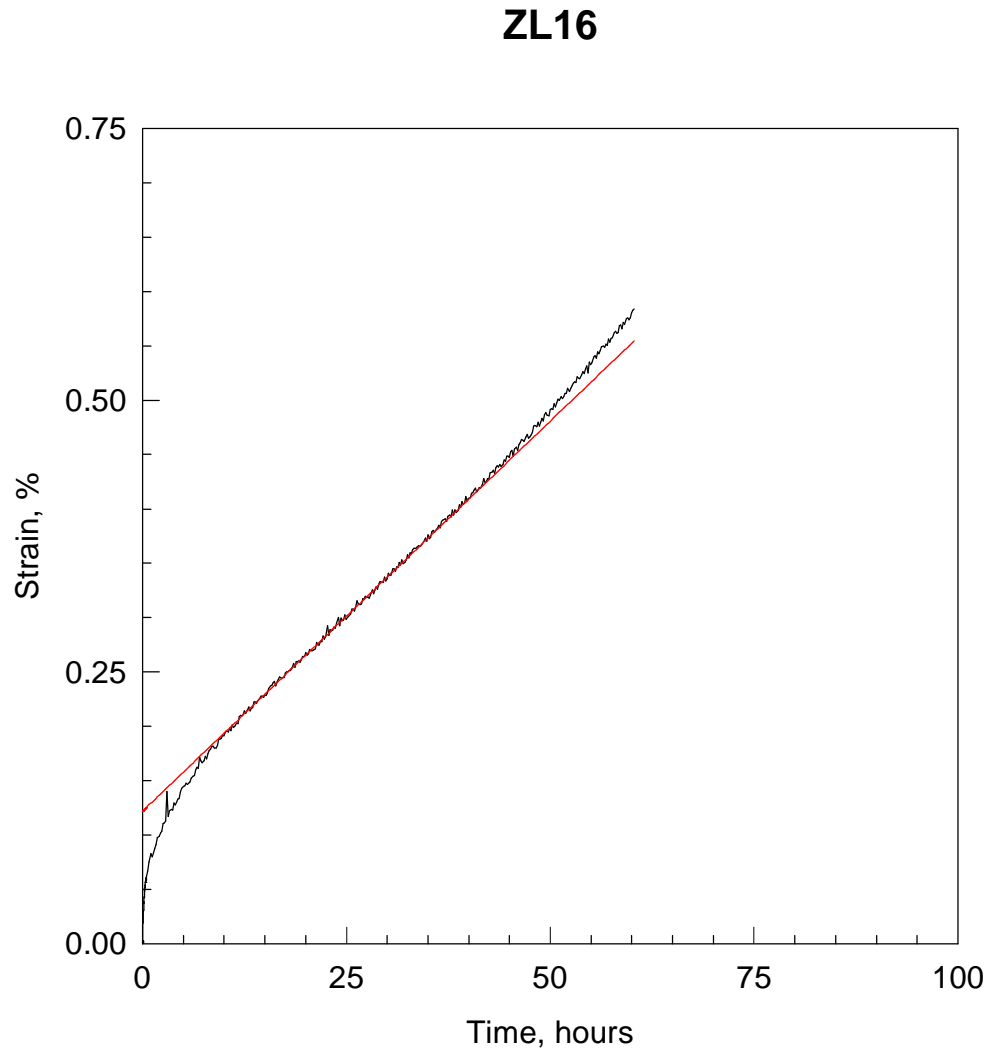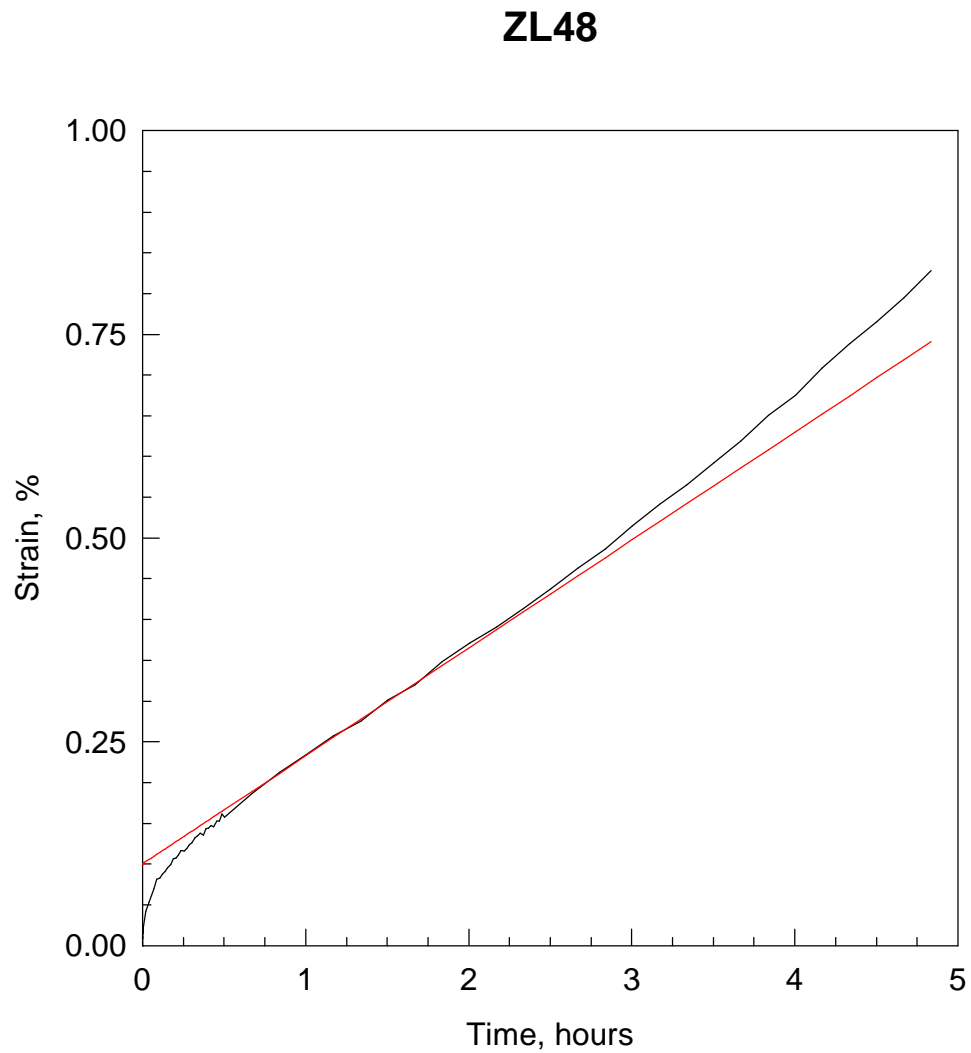
Figure C8.   Creep of 2124+SiC$_w$ at 350°F and 25 ksi (specimen ZL64). Test stopped
after 286 hours and 0.224% strain. Minimum creep rate shown is 1.21 x
10^{-9} in/in/sec.

TZ7
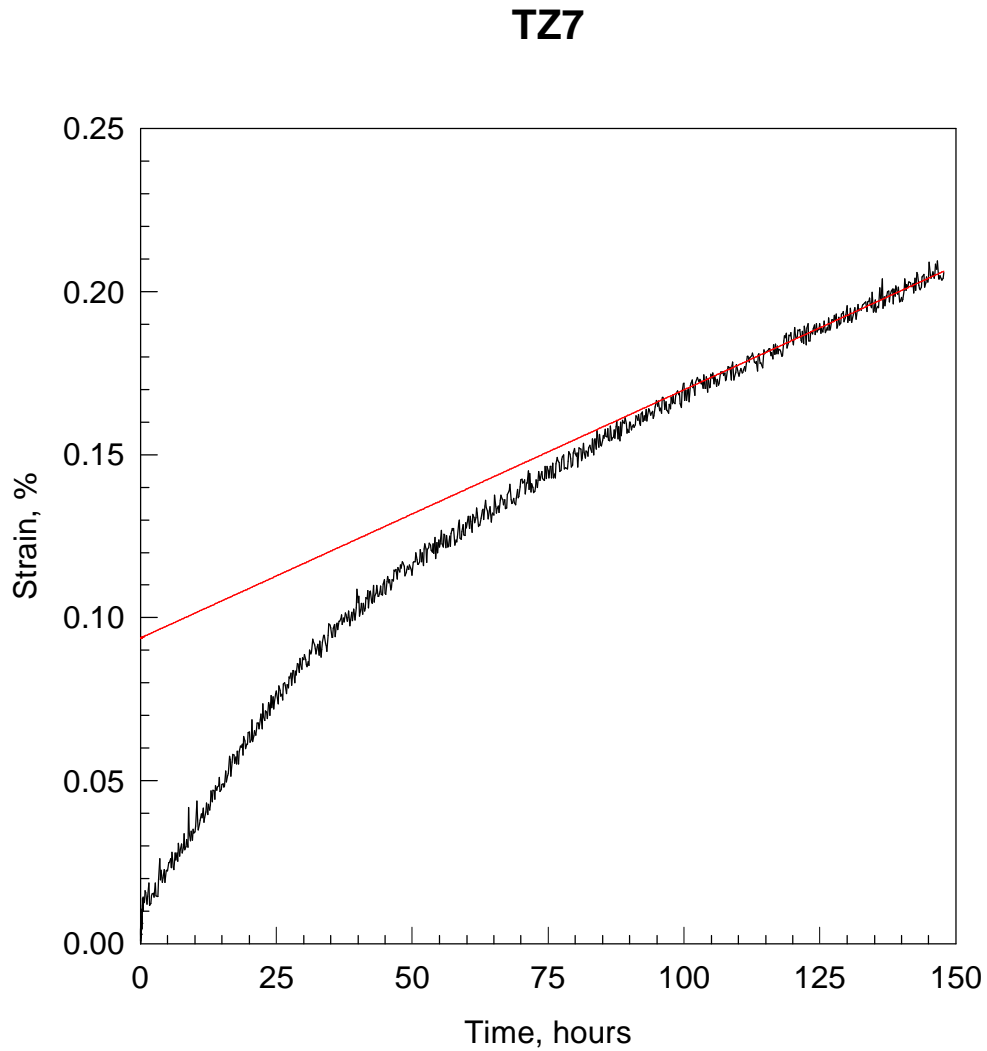
Figure C9.   Creep of 2124+SiC$_w$ at 350°F and 25 ksi (specimen TZ7). Test stopped
after 148 hours and 0.206% strain. Minimum creep rate shown is 2.12 x
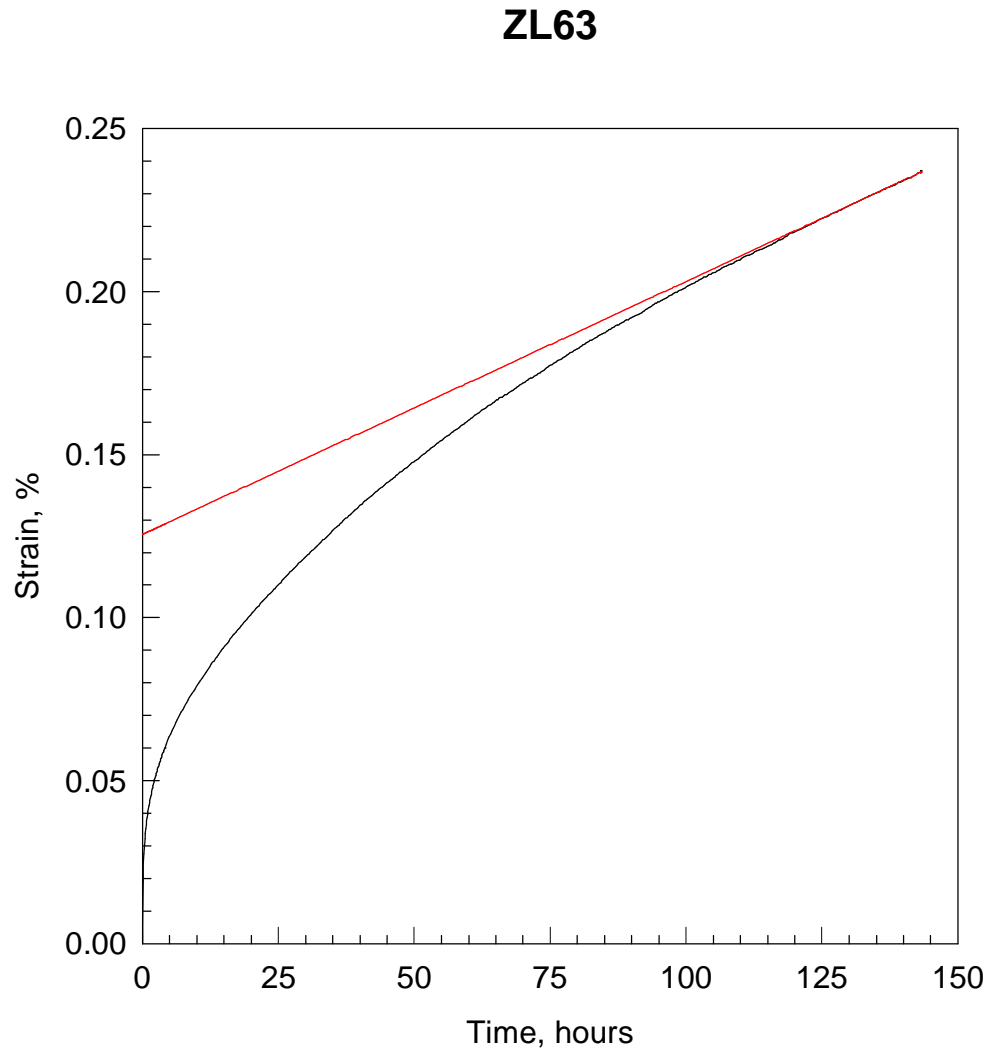10^{-9} in/in/sec.
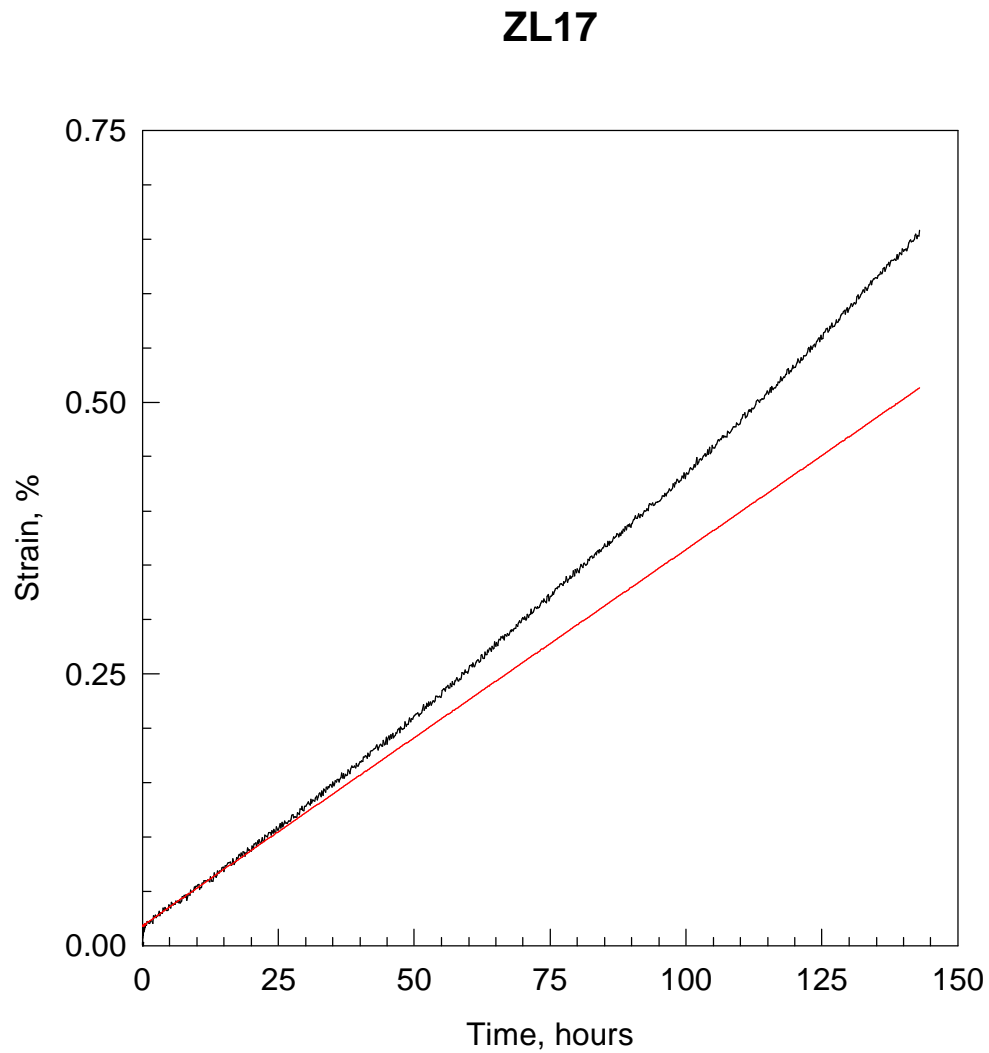
ZL17

Figure C10.   Creep of 2124+SiC$_w$ at 350°F and 35 ksi (specimen ZL17). Test stopped after 143 hours and 0.668% strain. Minimum creep rate shown is 9.62 x 10^{-9} in/in/sec.
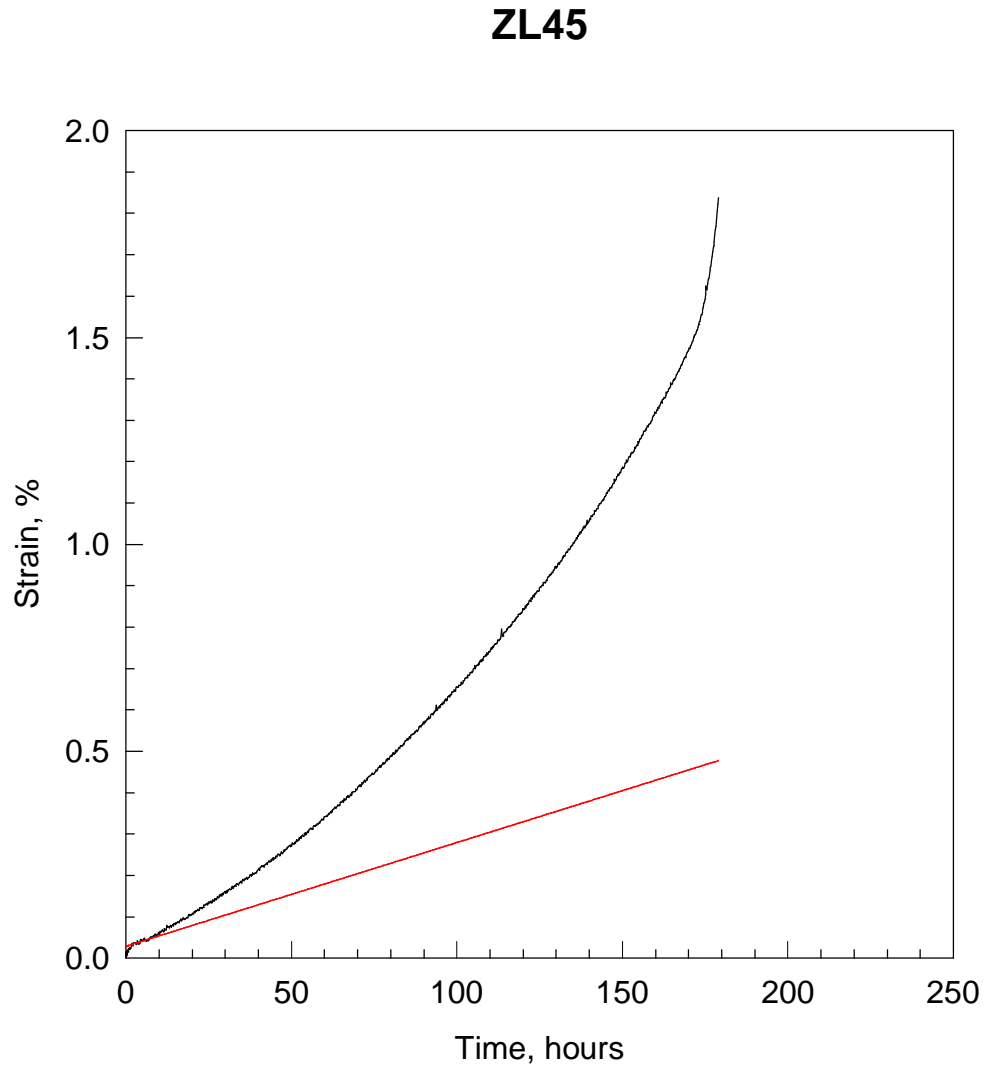
ZL45

Figure C11.   Creep of 2124+SiC$_w$ at 350°F and 35 ksi (specimen ZL45).   Specimen ruptured after 219 hours and greater than 1.99% strain (strain gages failed before specimen ruptured).   Minimum creep rate shown is 6.96 x 10^{-9} in/in/sec.
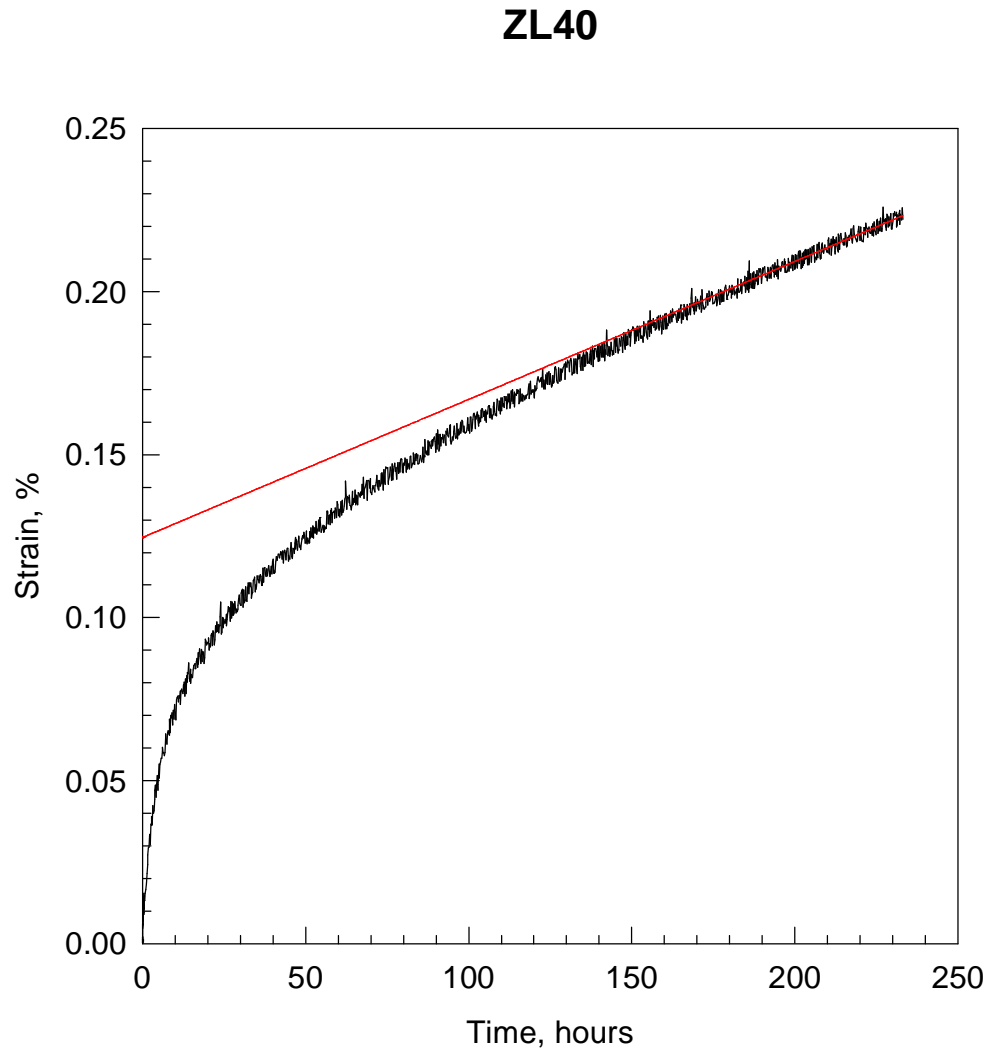
ZL40

Figure C12.   Creep of 2124+SiC$_w$ at 375°F and 17 ksi (specimen ZL40). Test stopped after 233 hours and 0.223% strain. Minimum creep rate shown is 1.18 x 10^{-9} in/in/sec.
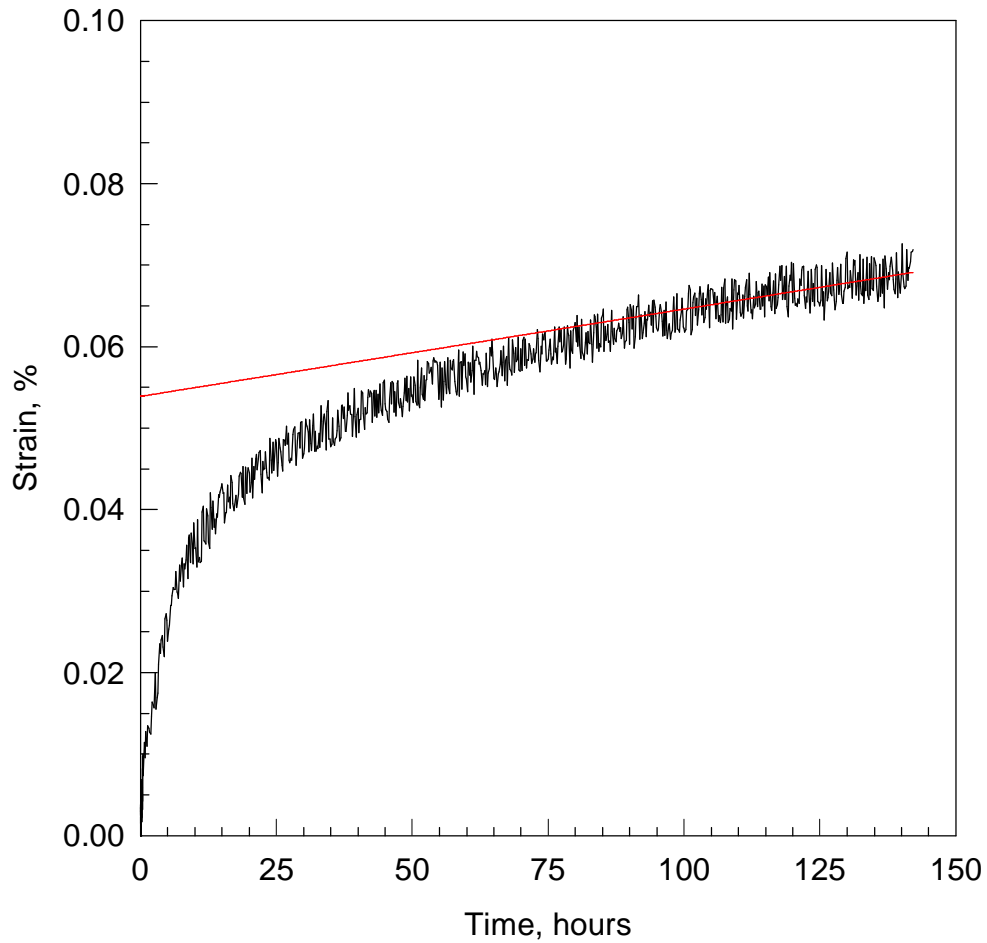
ZL39

Figure C13.   Creep of 2124+SiC$_w$ at 400°F and 10 ksi (specimen ZL39). Test stopped after 142 hours and 0.095% strain. Minimum creep rate shown is 2.97 x 10^{-10} in/in/sec.

ZL15

Figure C14.   Creep of 2124+SiC$_w$ at 400°F and 10 ksi (specimen ZL15). Test stopped after 311 hours and 0.089% strain. Minimum creep rate shown is 2.05 x 10^{-10} in/in/sec.

ZL8

Figure C15.   Creep of 2124+SiC$_w$ at 400°F and 17 ksi (specimen ZL8). Test stopped
                after 231 hours and 0.245% strain. Minimum creep rate shown is 1.18 x
   10^{-9} in/in/sec.
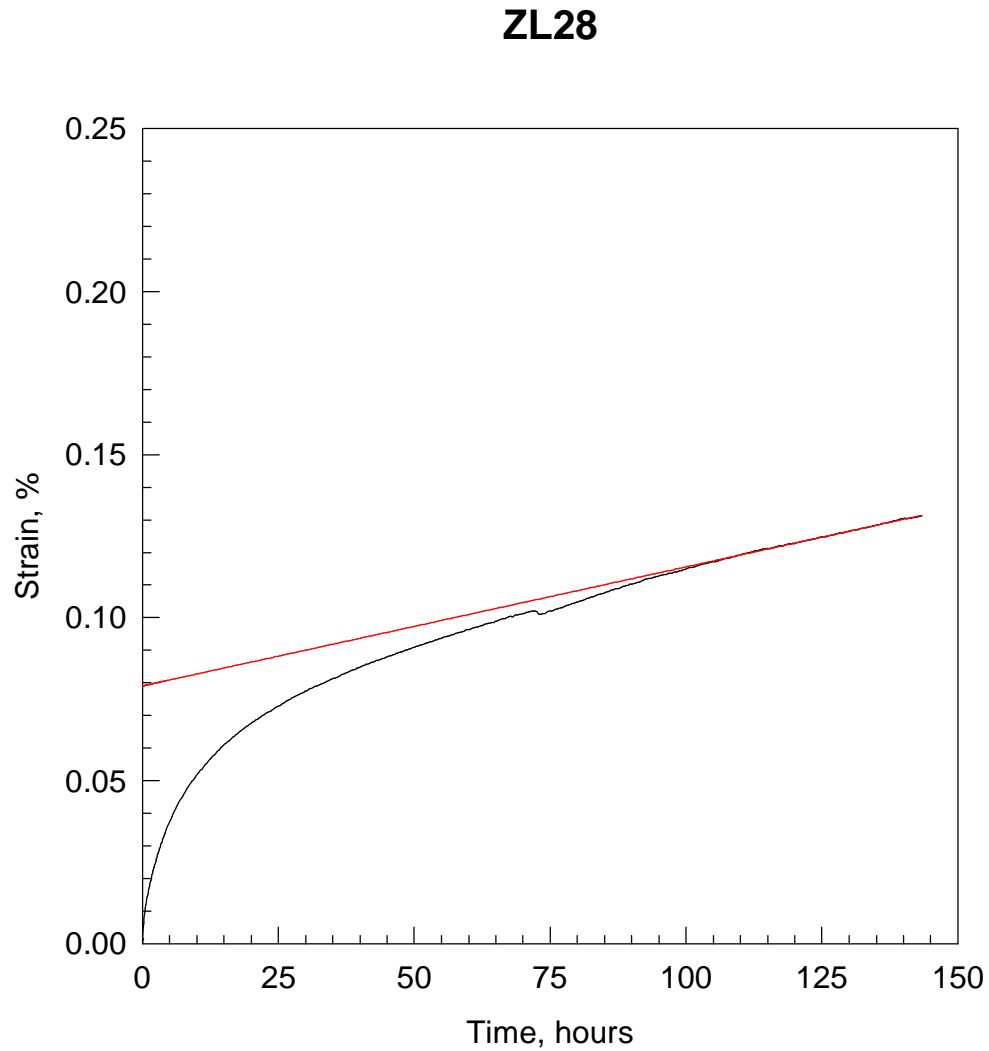
ZL28

Figure C16.   Creep of 2124+SiC$_w$ at 400°F and 17 ksi (specimen ZL28). Test stopped after 143 hours and 0.131% strain. Minimum creep rate shown is 1.01 x 10^{-9} in/in/sec.
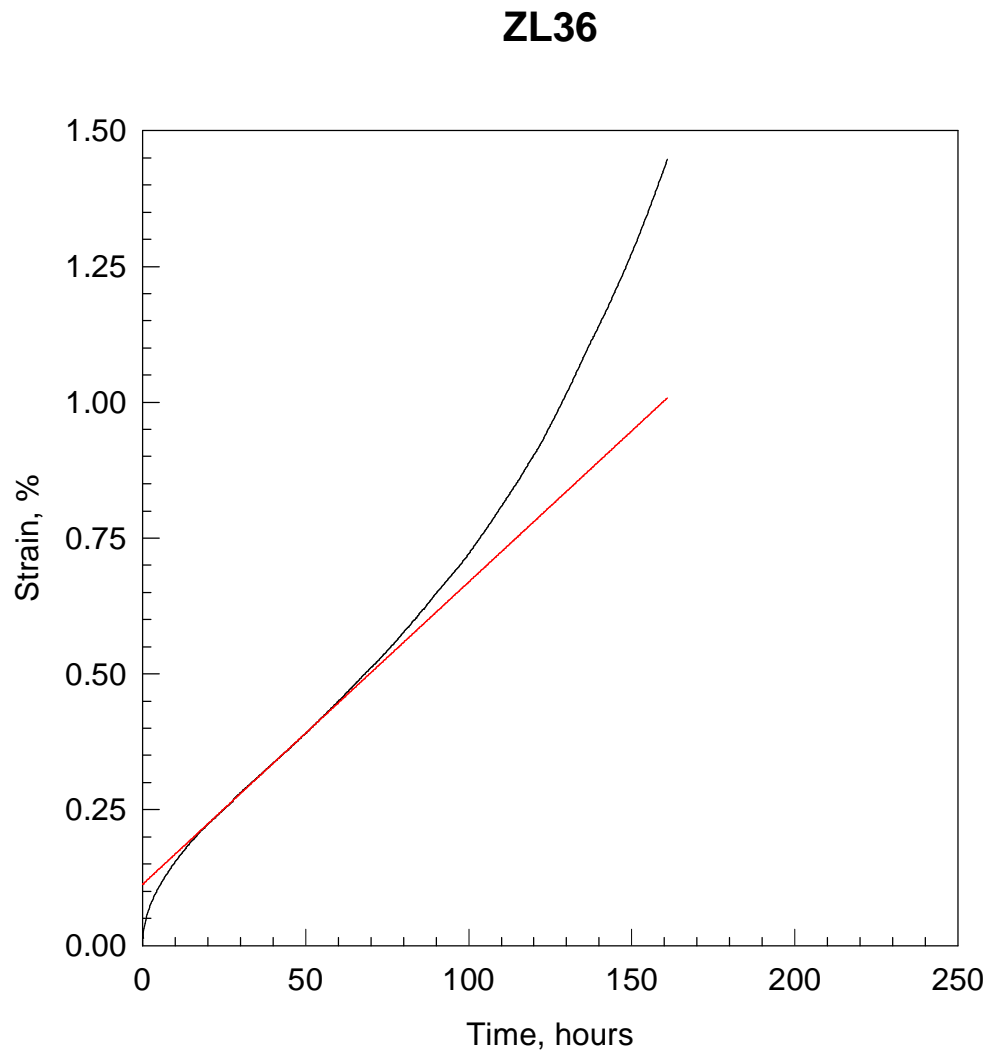
ZL36

Figure C17.   Creep of 2124+SiC$_w$ at 400°F and 25 ksi (specimen ZL36). Test stopped after 161 hours and 1.45% strain. Minimum creep rate shown is 1.55 x 10^{-8} in/in/sec.

ZL56

Figure C18. Creep of 2124+SiC$_w$ at 450°F and 10 ksi (specimen ZL56). Test stopped after 143 hours and 0.140% strain. Minimum creep rate shown is 8.92 x 10^{-10} in/in/sec.

ZL16

Figure C19.   Creep of 2124+SiC$_w$ at 450°F and 17 ksi (specimen ZL16). Specimen ruptured after 60 hours and 0.584% strain. Minimum creep rate shown is 1.99 x 10^{-8} in/in/sec.
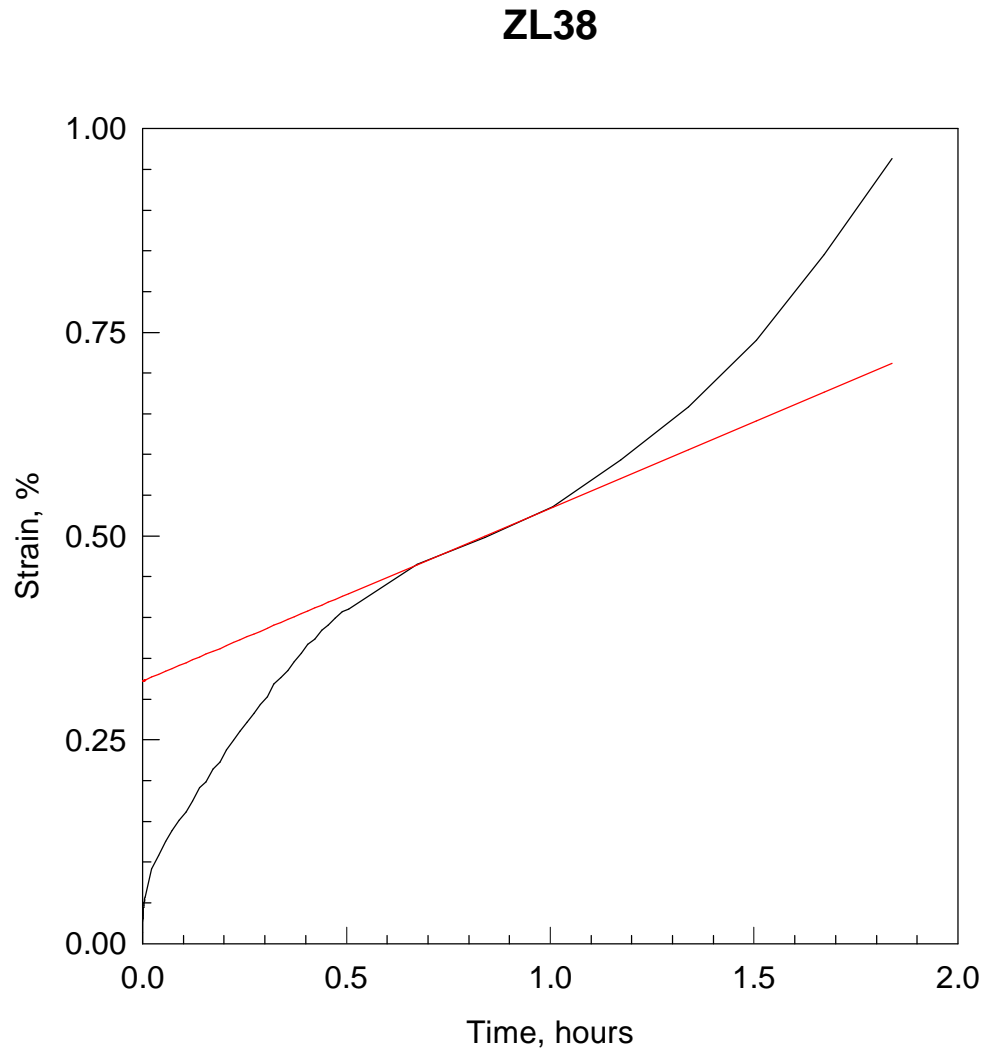
ZL48

Figure C20.   Creep of 2124+SiC$_w$ at 450°F and 25 ksi (specimen ZL48).   Specimen ruptured after 5 hours and 0.846% strain.   Minimum creep rate shown is 3.68 x 10^{-7} in/in/sec.

ZL63

Figure C21.   Creep of 2124+SiC$_w$ at 475°F and 10 ksi (specimen ZL63). Test stopped after 143 hours and 0.236% strain. Minimum creep rate shown is 2.16 x 10^{-9} in/in/sec.

ZL4
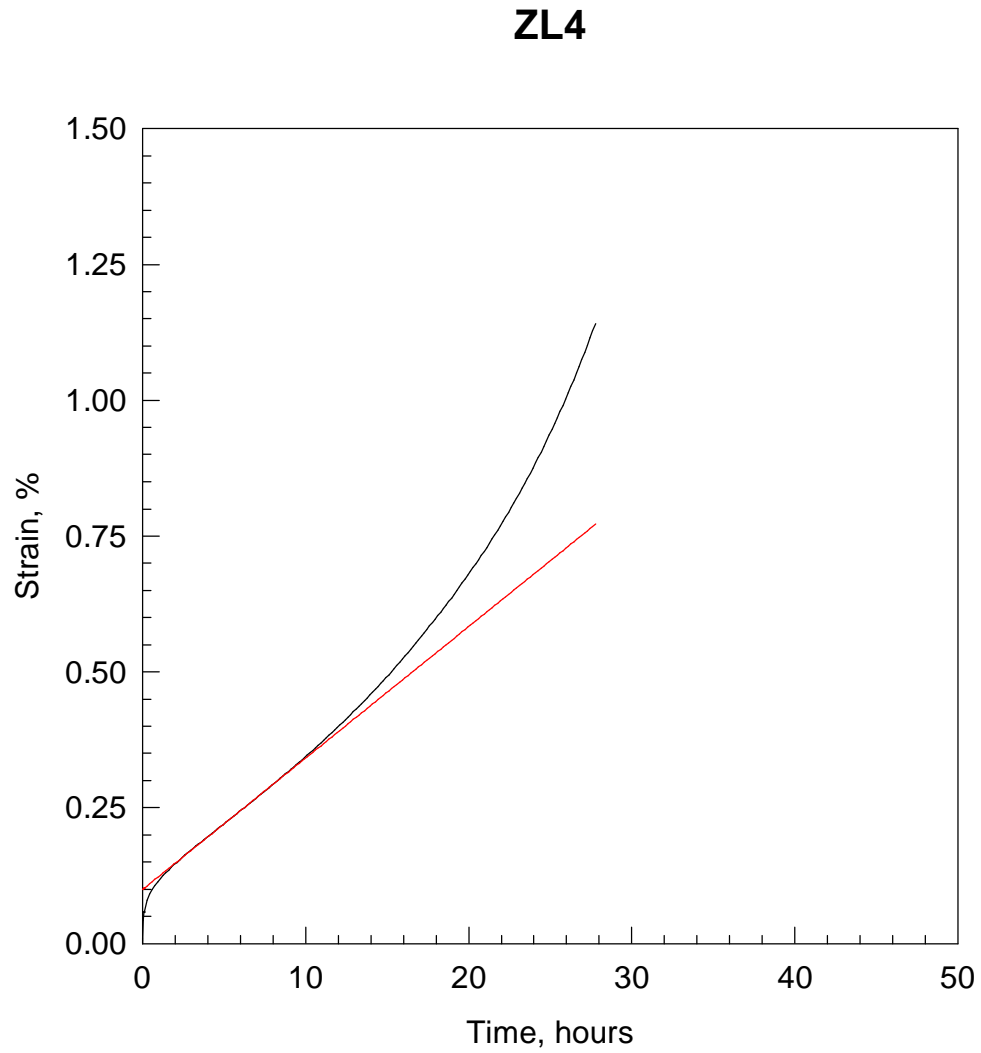
Figure C22.   Creep of 2124+SiC$_w$ at 475°F and 17 ksi (specimen ZL4).   Specimen ruptured after 28 hours and 1.14% strain.   Minimum creep rate shown is 6.72 x 10^{-8} in/in/sec.
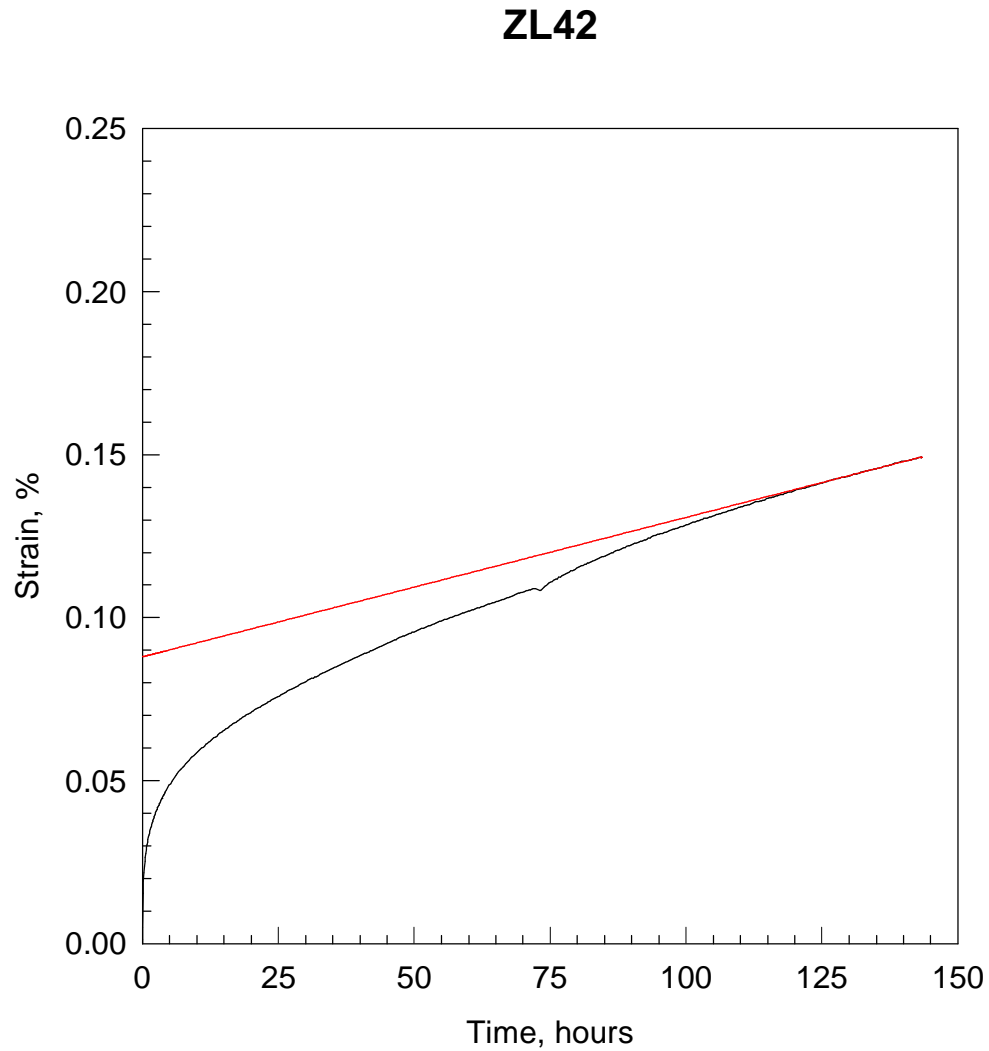
ZL42

Figure C23.   Creep of 2124+SiC$_w$ at 500°F and 10 ksi (specimen ZL42). Test stopped after 143 hours and 0.145% strain. Minimum creep rate shown is 1.19 x 10^{-9} in/in/sec.
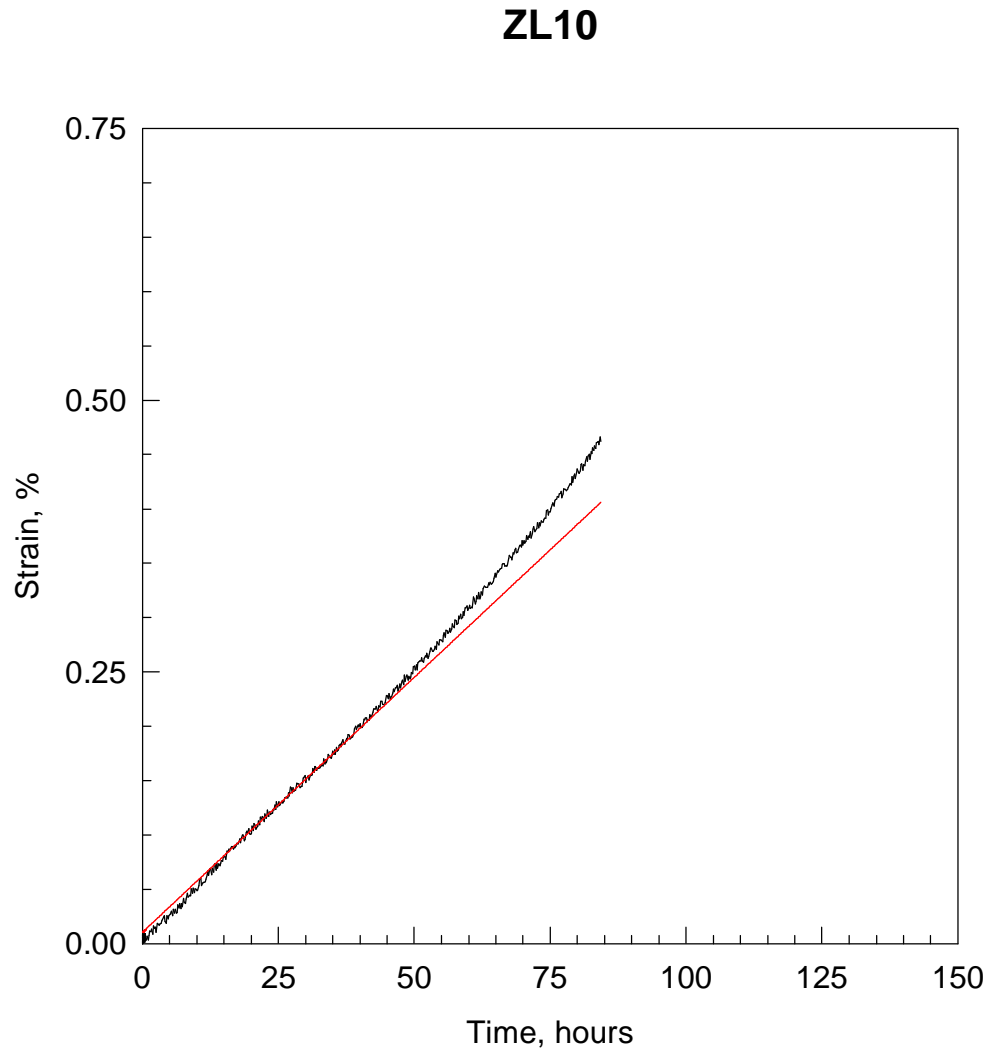
ZL10

Figure C24.   Creep of 2124+SiC$_w$ at 500°F and 10 ksi (specimen ZL10). Specimen ruptured after 84 hours and 0.573% strain. Minimum creep rate shown is 1.30 x 10^{-8} in/in/sec.
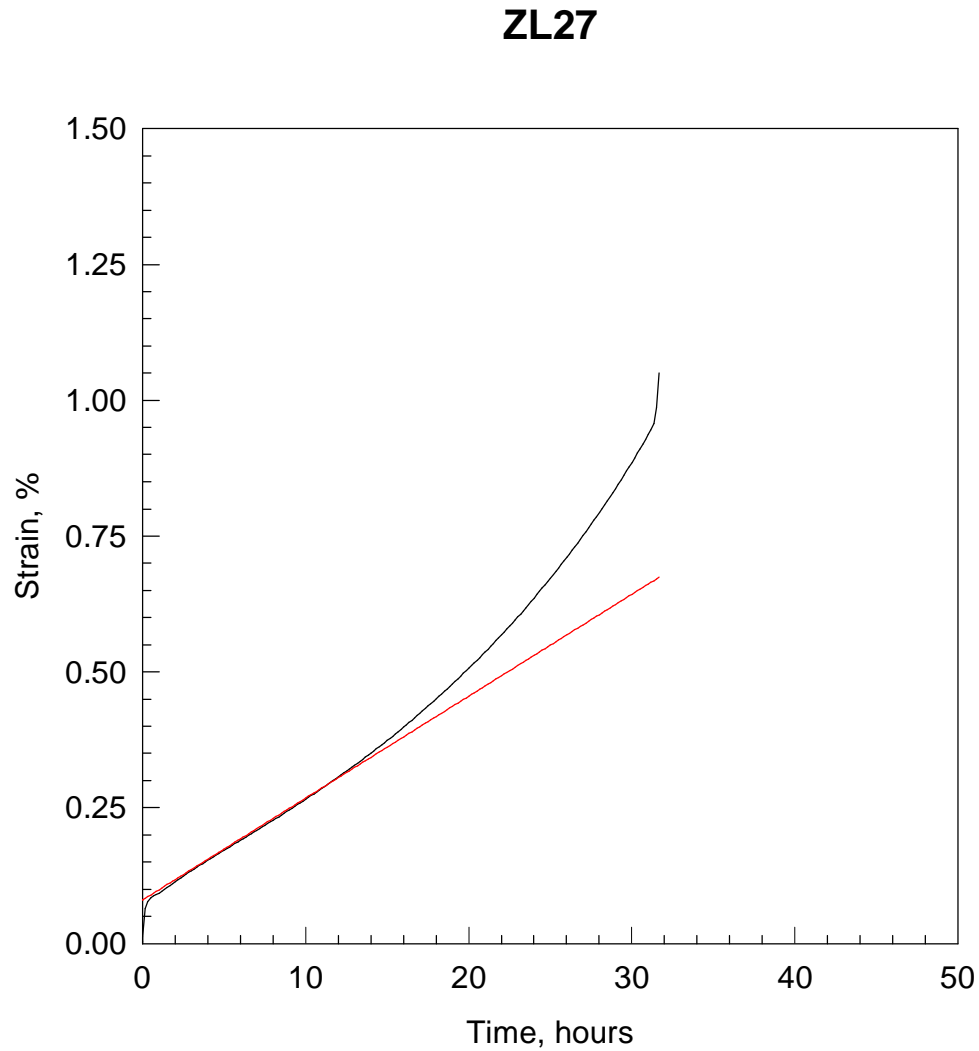
ZL27

Figure C25.   Creep of 2124+SiC$_w$ at 500°F and 14 ksi (specimen ZL27). Specimen ruptured after 36 hours and 1.07% strain. Minimum creep rate shown is 5.21 x 10^{-8} in/in/sec.
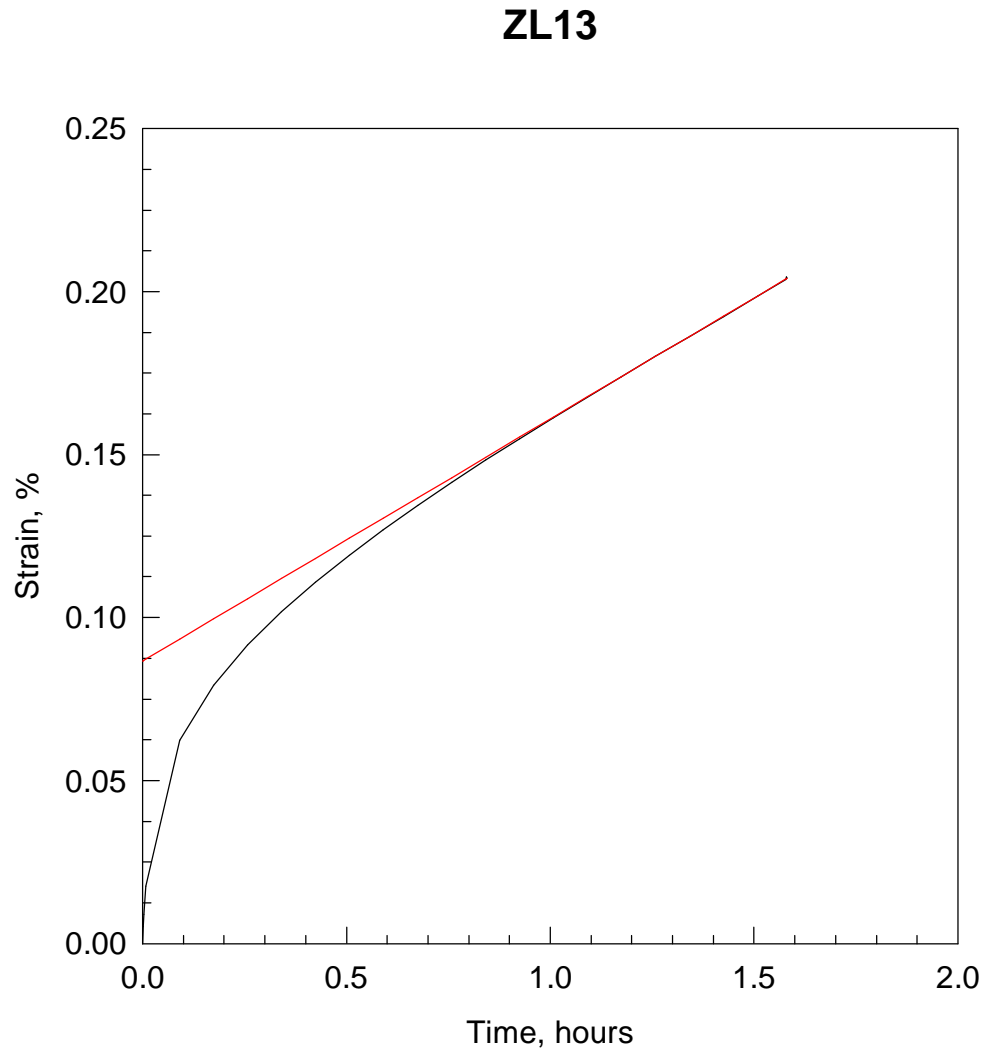
ZL13

Figure C26.   Creep of $2124+SiC_w$ at 500°F and 17 ksi (specimen ZL13). Test stopped after 1.6 hours and 0.204% strain in the steady state creep regime. Minimum creep rate shown is 2.06 x 10^{-7} in/in/sec.

ZL38

Figure C27.   Creep of 2124+SiC$_w$ at 500°F and 20 ksi (specimen ZL38). Specimen ruptured after 3 hours and 0.955% strain. Minimum creep rate shown is 5.89 x 10^{-7} in/in/sec.
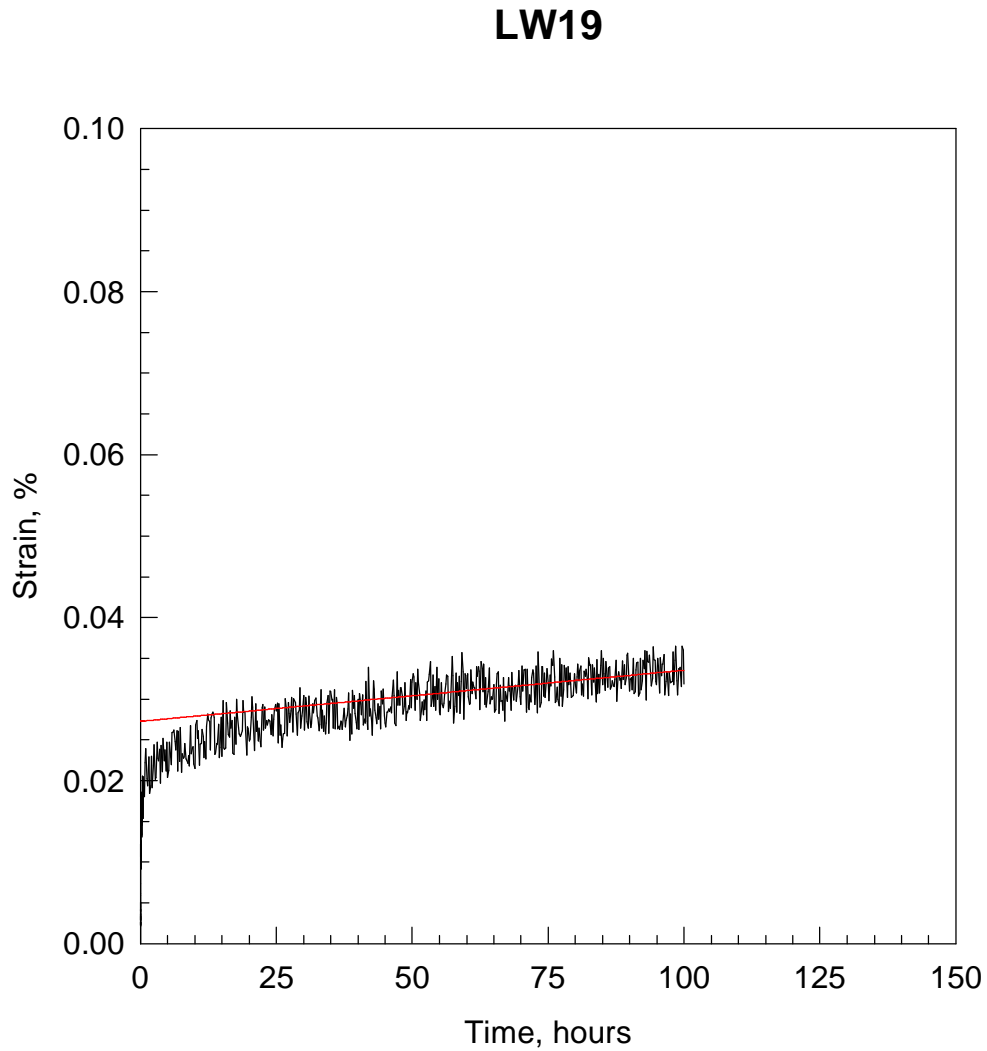
LW19

Figure C28.   Creep of unreinforced 2124 at 250°F and 39 ksi (specimen LW19). Test stopped after 100 hours and 0.037% strain. Minimum creep rate shown is 1.74 x 10^{-10} in/in/sec.
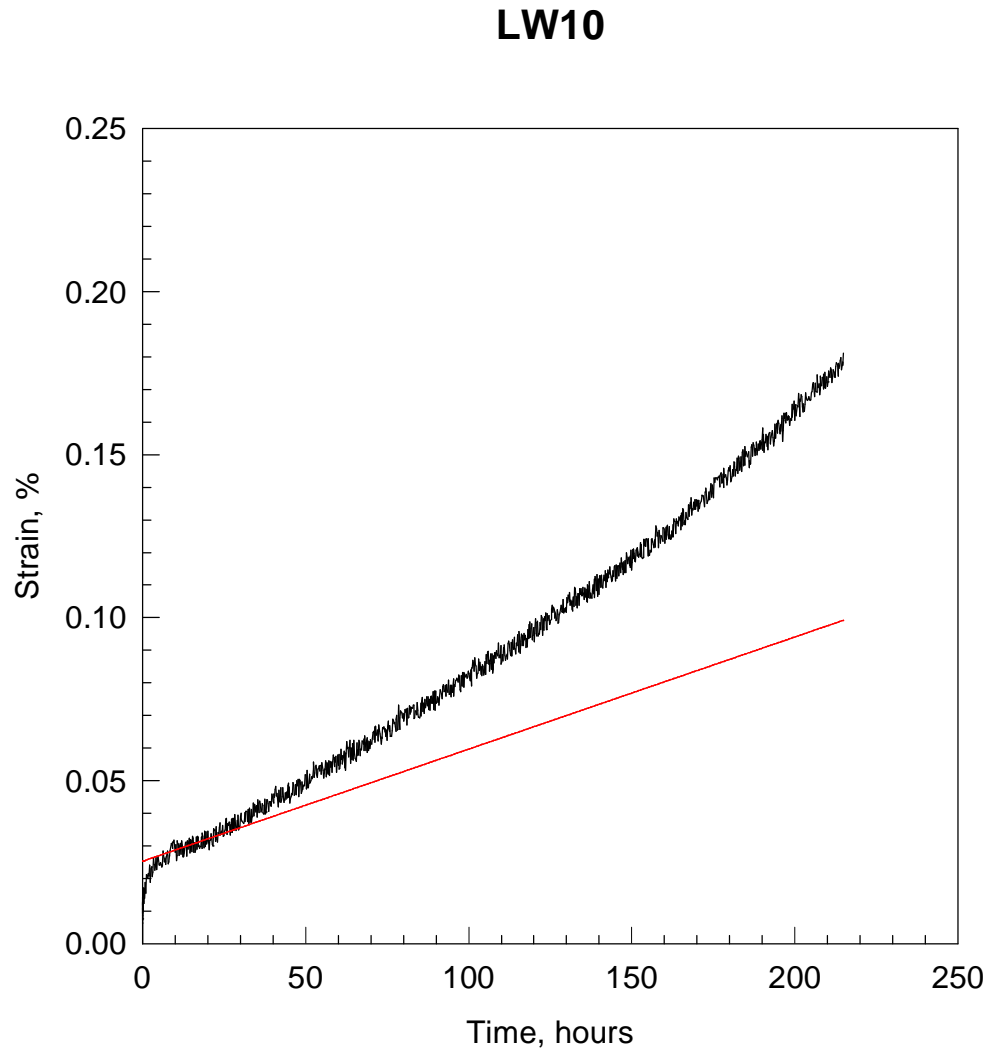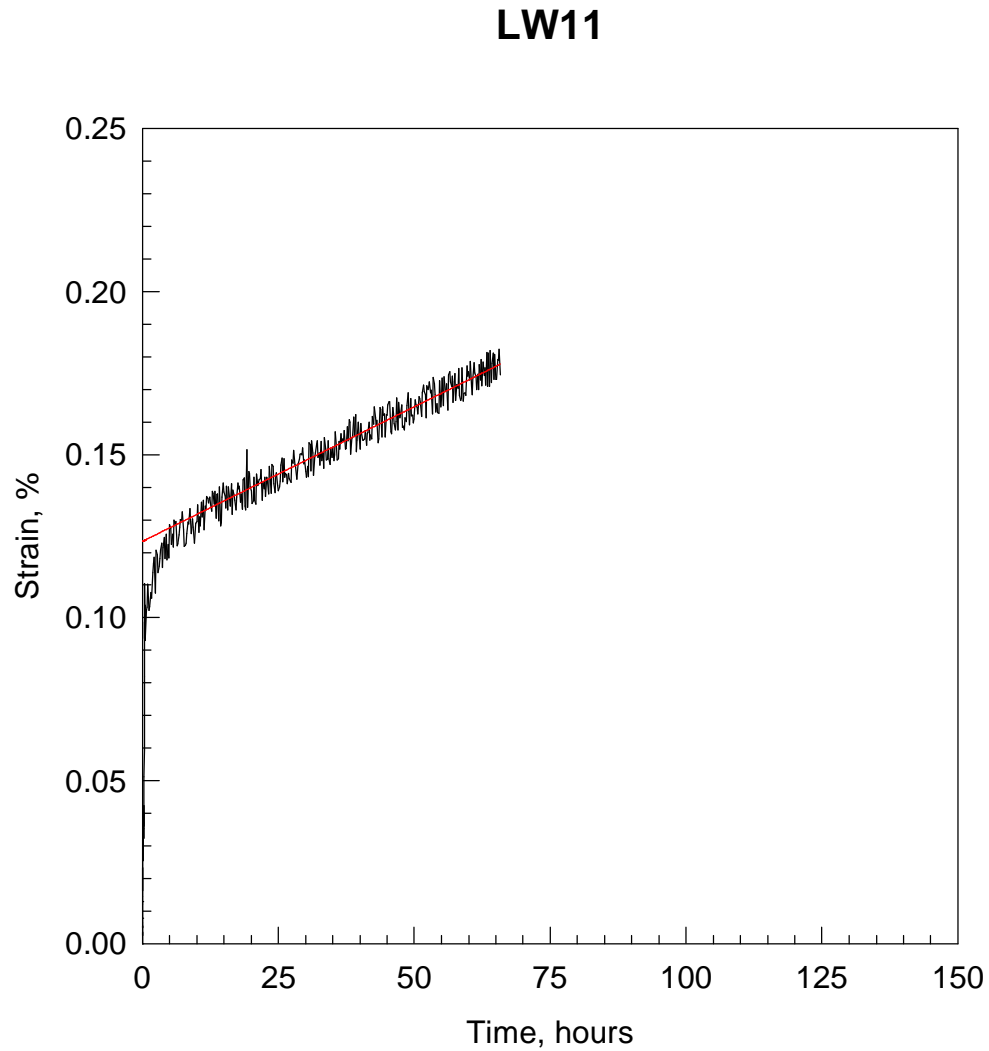
LW7
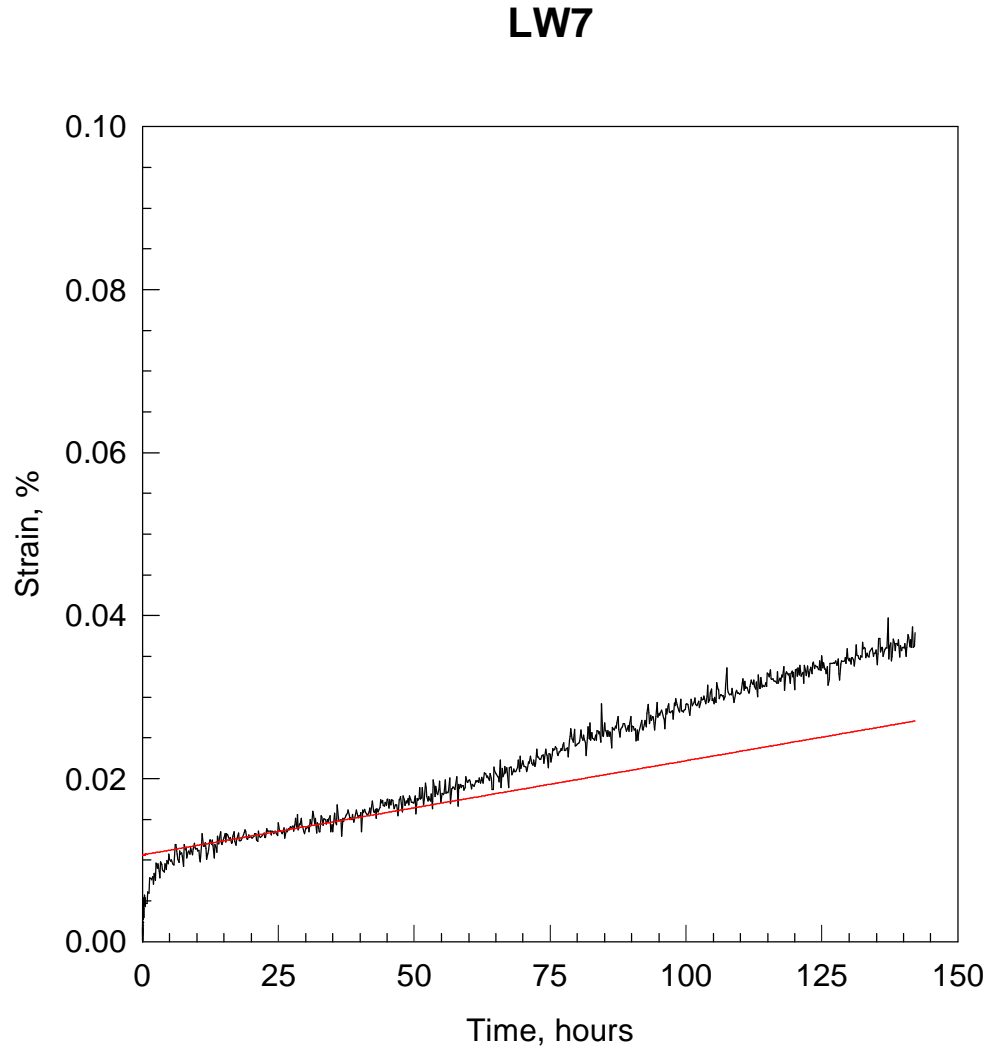
Figure C29.   Creep of unreinforced 2124 at 350°F and 17 ksi (specimen LW7). Test stopped after 142 hours and 0.041% strain. Minimum creep rate shown is 3.19 x 10^{-10} in/in/sec.
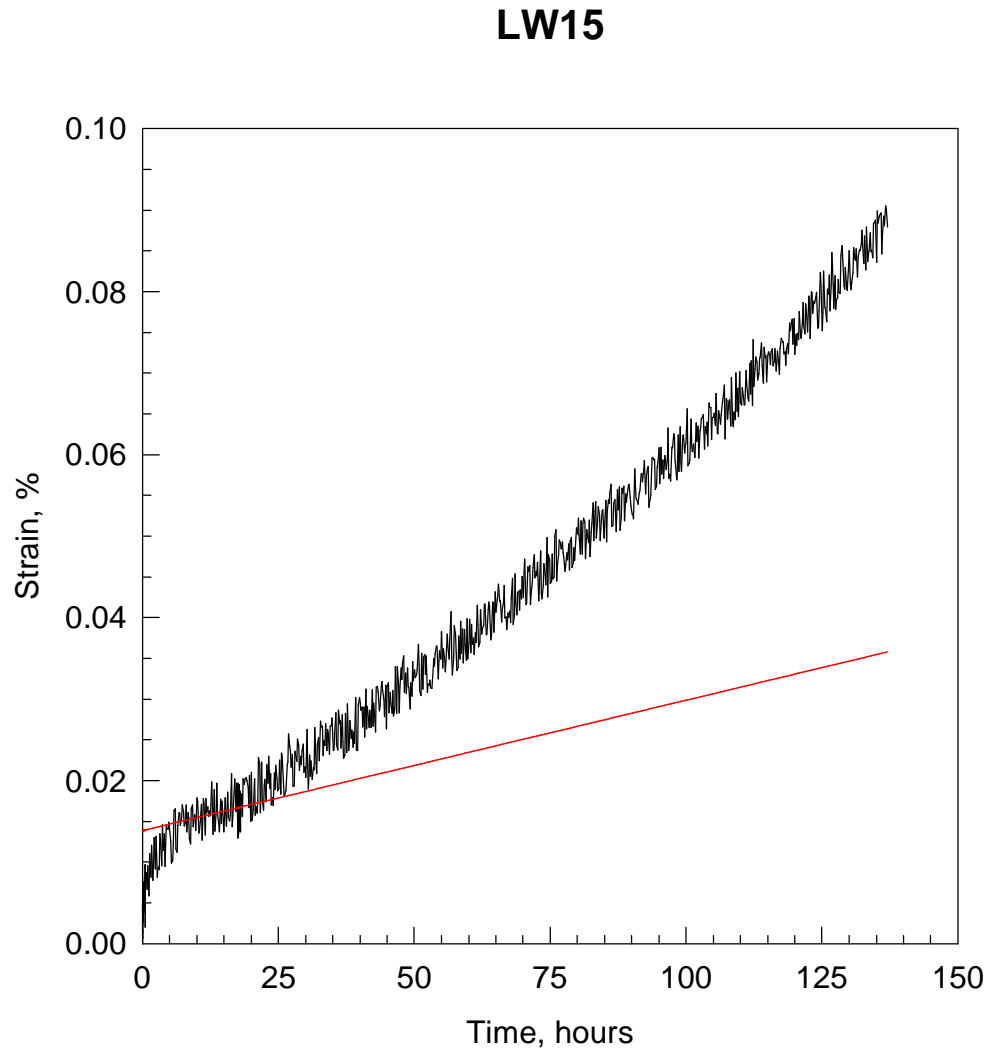
LW15

Figure C30.   Creep of unreinforced 2124 at 350°F and 25 ksi (specimen LW15). Test stopped after 137 hours and 0.091% strain. Minimum creep rate shown is 4.44×10^{-10} in/in/sec.
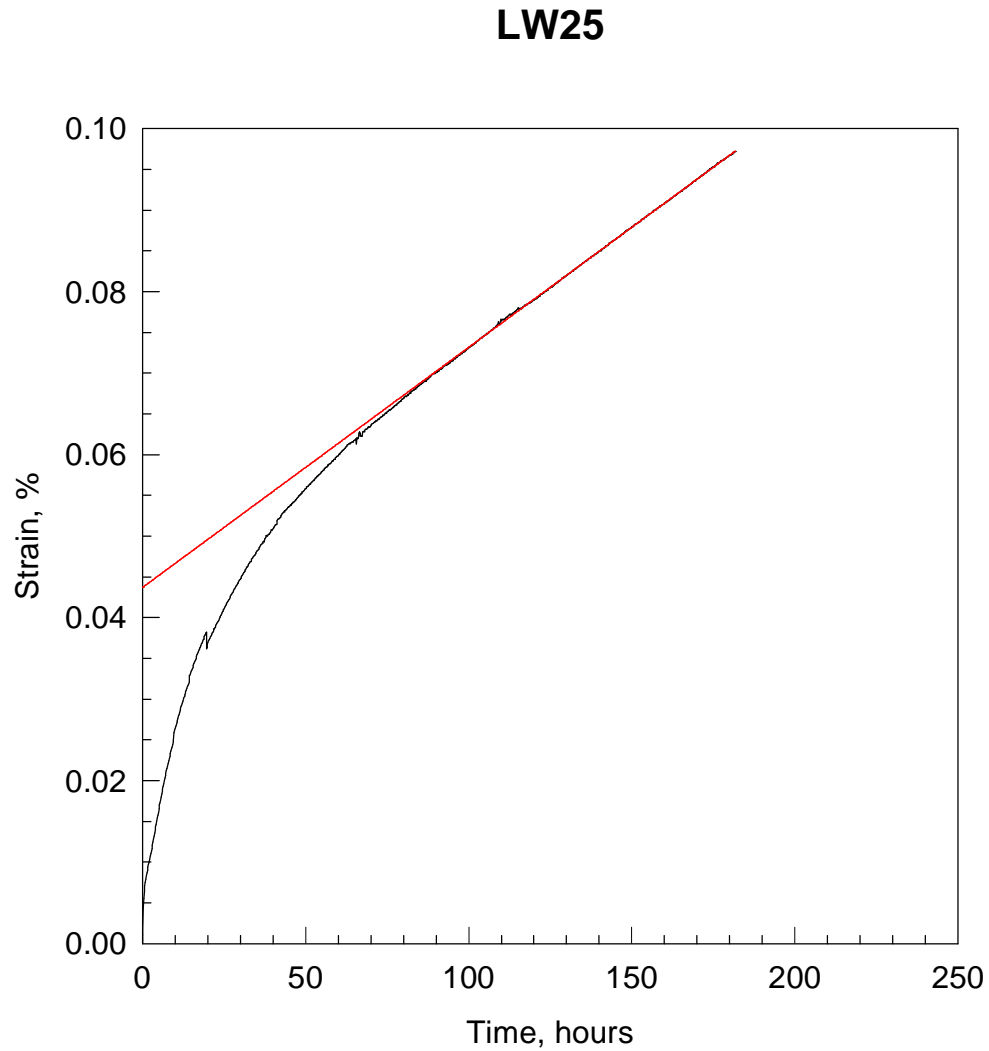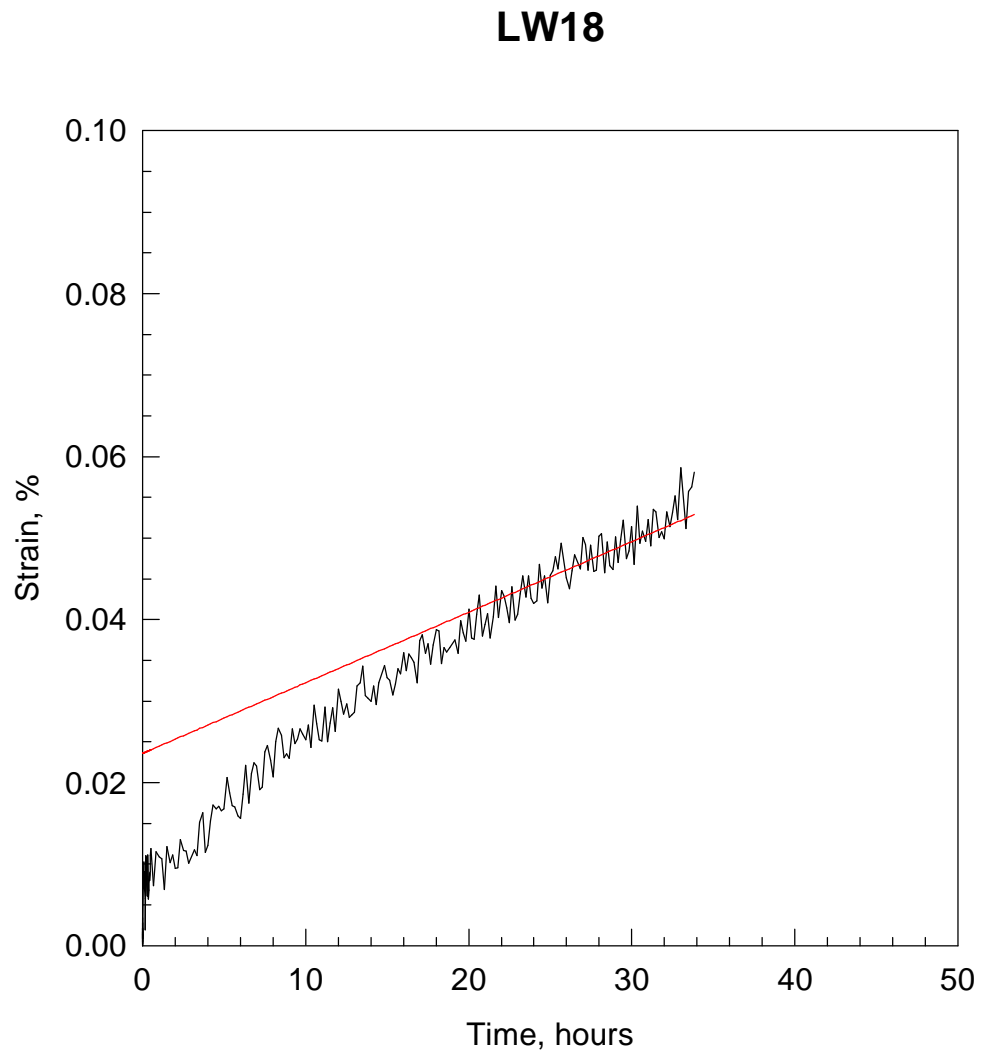
LW10

Figure C31.   Creep of unreinforced 2124 at 350°F and 25 ksi (specimen LW10). Specimen ruptured after 215 hours and 0.182% strain. Minimum creep rate shown is 9.55 x 10^{-10} in/in/sec.

LW11

Figure C32.   Creep of unreinforced 2124 at 350°F and 35 ksi (specimen LW11). Specimen ruptured after 66 hours and 0.211% strain. Minimum creep rate shown is 2.29 x 10^{-9} in/in/sec.

LW25

Figure C33.   Creep of unreinforced 2124 at 400°F and 17 ksi (specimen LW25). Specimen ruptured after 182 hours and 0.097% strain. Minimum creep rate shown is 8.18 x 10^{-10} in/in/sec.

LW18

Figure C34.   Creep of unreinforced 2124 at 400°F and 20 ksi (specimen LW18). Specimen ruptured after 34 hours and 0.058% strain. Minimum creep rate shown is 2.40 x 10^{-9} in/in/sec.
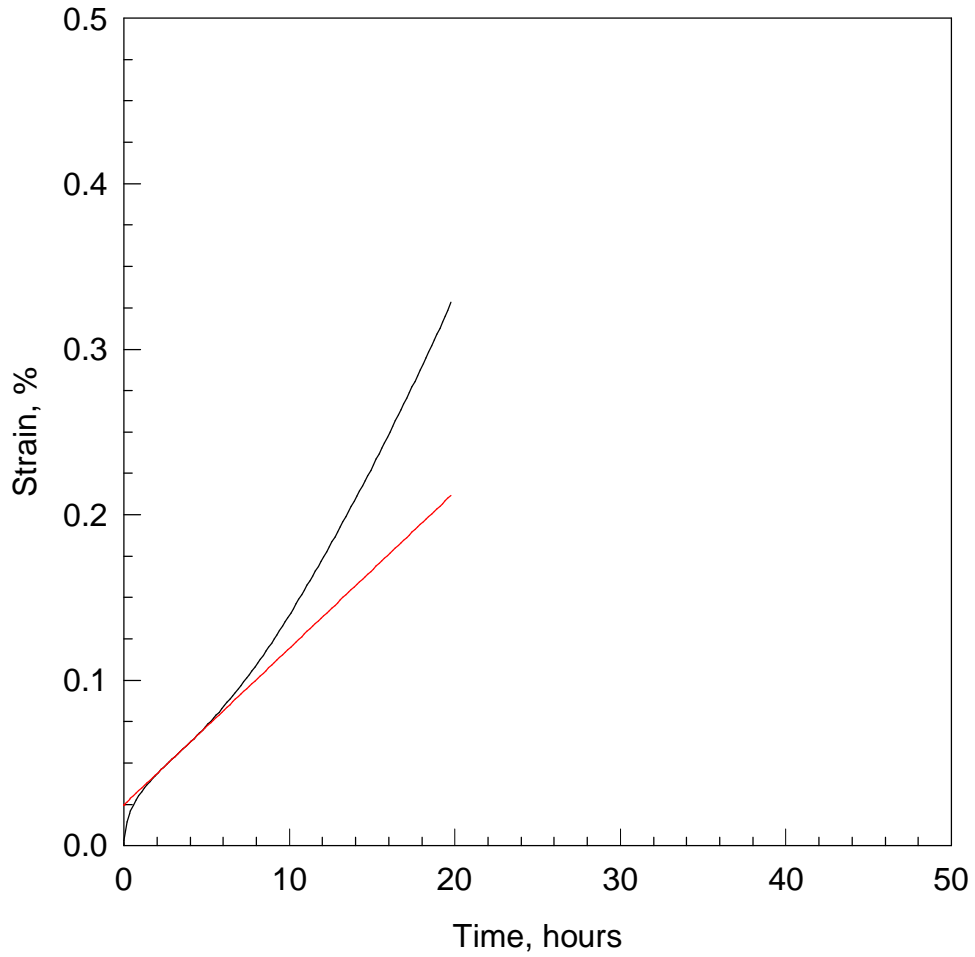
TW10

Figure C35.   Creep of unreinforced 2124 at 400°F and 25 ksi (specimen TW10). Specimen ruptured after 19.8 hours and 0.328% strain. Minimum creep rate shown is 2.63 x 10^{-8} in/in/sec.
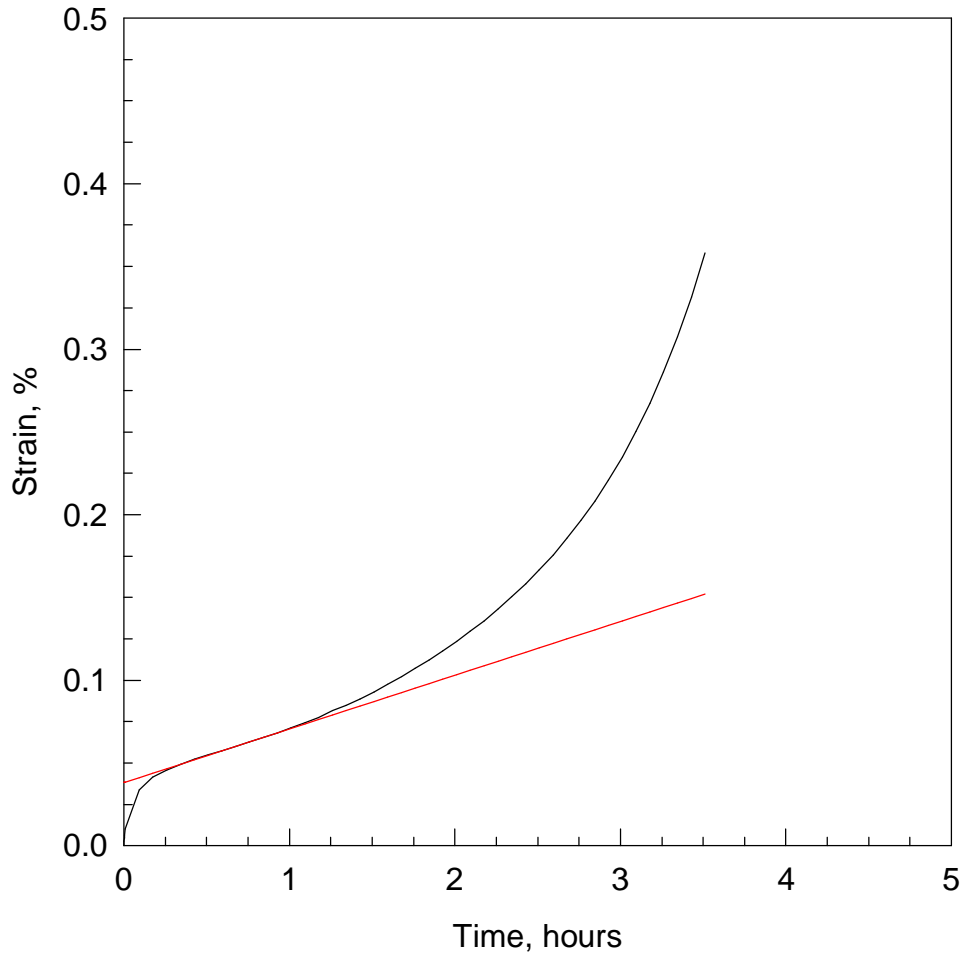
LW1

Figure C36. Creep of unreinforced 2124 at 400°F and 35 ksi (specimen LW1). Specimen ruptured after 3.5 hours and 0.358% strain. Minimum creep rate shown is 9.01 x 10^{-8} in/in/sec.
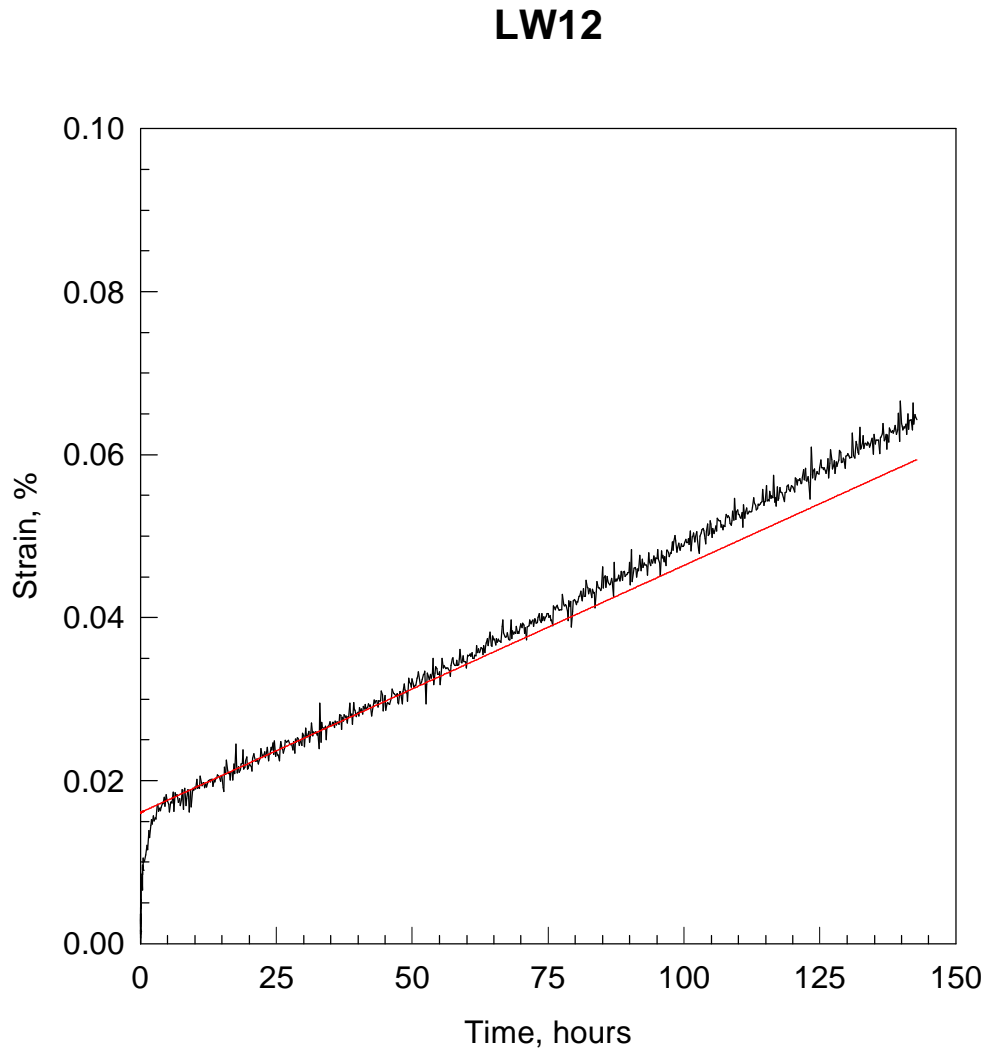
LW12

Figure C37.   Creep of unreinforced 2124 at 450°F and 10 ksi (specimen LW12). Test stopped after 142 hours and 0.079% strain. Minimum creep rate shown is 8.42 x 10^{-10} in/in/sec.
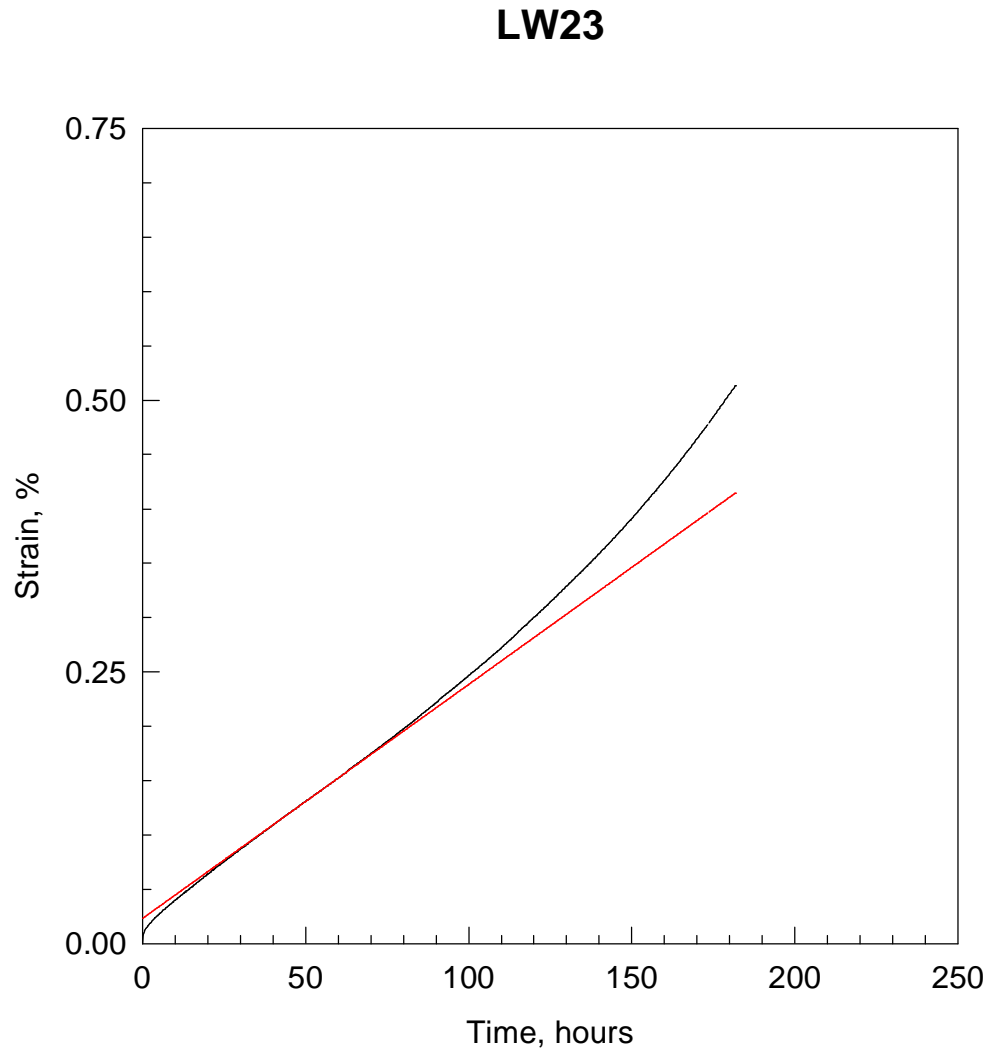
LW23

Figure C38.   Creep of unreinforced 2124 at 500°F and 10 ksi (specimen LW23).   Test stopped after 182 hours and 0.512% strain. Minimum creep rate shown is 5.98 x 10^{-9} in/in/sec.
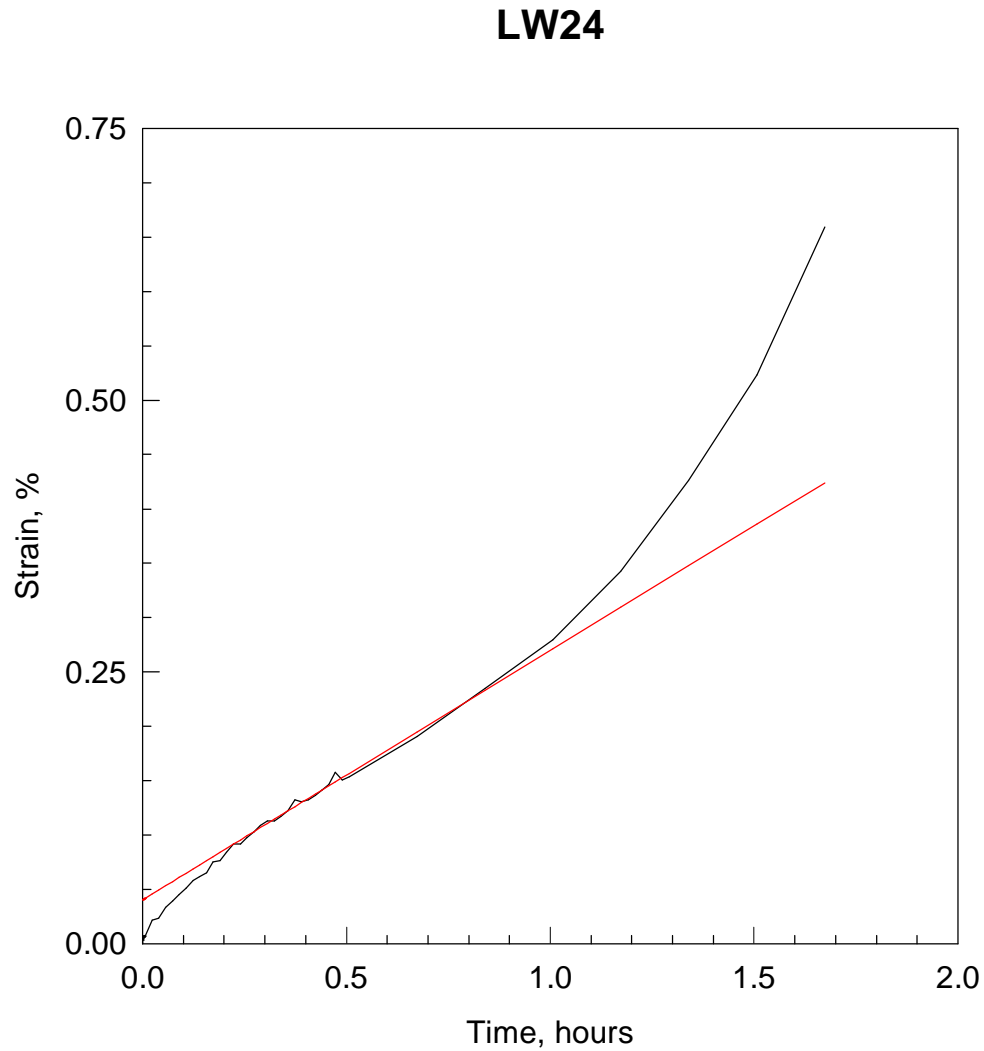
LW24

Figure C39.   Creep of unreinforced 2124 at 500°F and 17 ksi (specimen LW24). Specimen ruptured after 1.7 hours and 0.660% strain. Minimum creep rate shown is 6.30 x 10^{-7} in/in/sec.
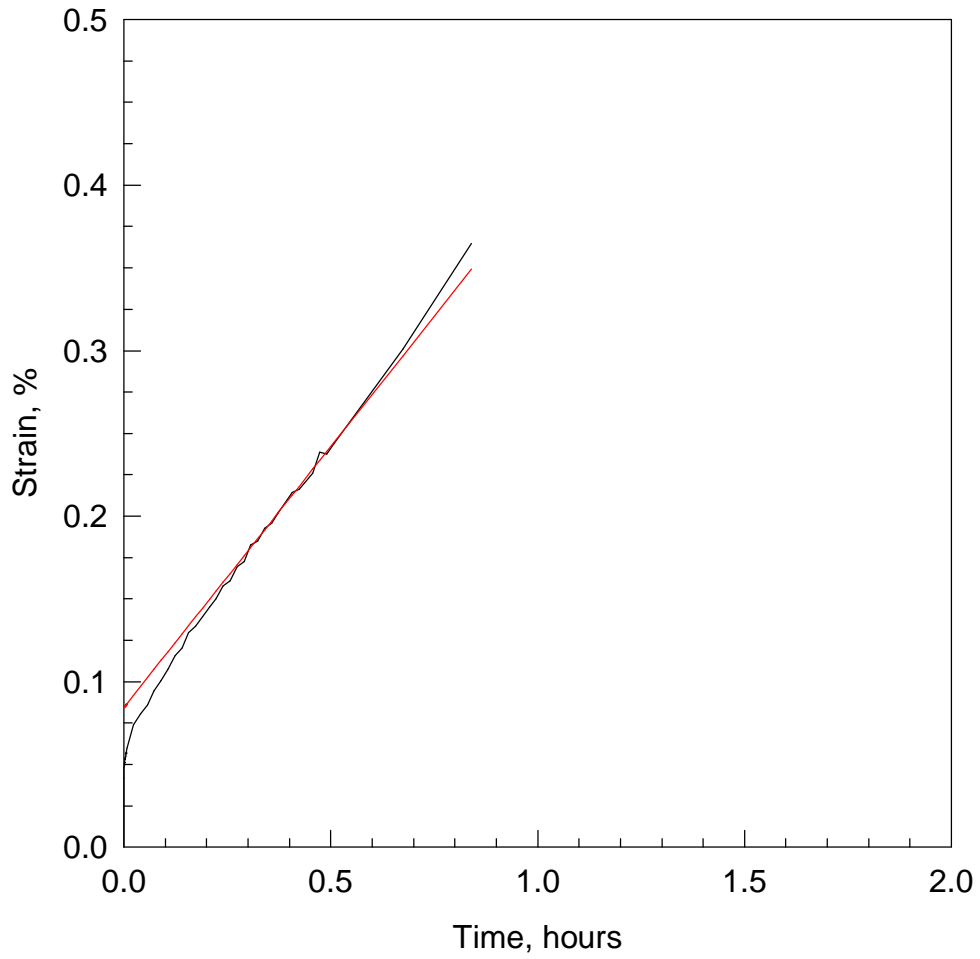
LW8

Figure C40.   Creep of unreinforced 2124 at 500°F and 20 ksi (specimen LW8). Specimen ruptured after 0.8 hours and 0.365% strain. Minimum creep rate shown is 8.76×10^{-7} in/in/sec.

KAREN M. B. TAMINGER

VITA

The author was born Karen M. Brown in 1966. While in high school, she attended the Virginia Governor's School for the Gifted at NASA Langley Research Center. In the fall of 1984 she entered Virginia Polytechnic Institute and State University (Virginia Tech), to major in Materials Engineering. In January 1986, she was accepted into the co-operative education program with NASA Langley Research Center. As a co-operative education student, she worked in each of the four main areas of materials research at NASA Langley: mechanics of materials, polymeric materials, applied materials, and metallic materials. She was inducted into several honor societies during her five years at Virginia Tech, including *Tau Beta Pi* (national engineering honor society), *Omicron Delta Kappa* (national leadership honor society), and *Alpha Sigma Mu* (national metallurgy honor society). She also served as secretary and chairman of the local student chapter of the American Society for Metals. She received a Bachelors Degree in the Honors program, graduating *Magna Cum Laude* in May 1989. She accepted her current position as a Materials Research Engineer in the Metallic Materials Branch, Materials Division at NASA Langley Research Center in Hampton, VA in July 1989. Her primary research area is focused on evaluating advanced light alloys and metal matrix composites, with emphasis on understanding the effects of creep, long term thermal exposure, and simulated mission exposure on the microstructures and mechanical properties of emerging metallic materials and structures. She has presented 15 technical talks and co-authored more than 28 papers and reports on her research at NASA Langley. She has been very active in the Hampton Roads Chapter of ASM International, serving as membership chairman, treasurer, vice chairman, and chairman. She married and changed her name to Karen M. B. Taminger, and currently lives in Yorktown, VA with her family. She completed all of the requirements for the degree Masters of Science in Materials Science and Engineering in the spring of 1999.